S. Krivovichev
(Ed.)

Minerals as Advanced Materials I

Springer

Minerals as Advanced Materials I

Sergey V. Krivovichev (Ed.)

Minerals as Advanced Materials I

Springer

Editor

Prof. Dr. Sergey V. Krivovichev
Department of Crystallography, Faculty of Geology
St. Petersburg State University
University Emb. 7/9
St. Petersburg
Russia 199034
skrivovi@mail.ru

ISBN: 978-3-540-77122-7 e-ISBN: 978-3-540-77123-4

Library of Congress Control Number: 2007942593

Cover illustration: Yakovenchukite-(Y), a new yttrium silicate with unique microporous structure discovered in Khibiny massif, Kola peninsula, Russia (Krivovichev S.V., Pakhomovsky Ya.A., Ivanyuk G.Yu., Mikhailova J.A., Men'shikov Yu.P., Armbruster T., Selivanova E.A., Meisser N. (2007): Yakovenchukite-(Y) K3NaCaY2[Si12O30](H2O)4, a new mineral from the Khibiny massif, Kola Peninsula, Russia: A novel type of octahedral-tetrahedral open-framework structure. Amer Mineral 92:1525-1530)

Cover design: deblik, Berlin

Printed on acid-free paper

9 8 7 6 5 4 3 2 1

springer.com

Foreword

This book contains chapters presented at the International workshop 'Minerals as Advanced Materials I' that was held in the hotel of the Russian Academy of Sciences on the Imandra lake, Kola peninsula, one of the most beautiful places of the Russian North, during 8–12 July, 2007. The idea of the workshop originated from the necessity of interactions between mineralogy and material science, including all aspects of both these disciplines. Many important materials that dominate modern technological development were known to mineralogists for hundreds years, though their properties were not fully recognized. Mineralogy, on the other hand, needs new impacts for the further development in the line of modern scientific achievements, including novel insights provided by development of bio- and nanotechnologies as well as by the understanding of a deep role that information plays in the formation of natural structures and definition of natural processes.

Thematically, the book can be separated into several parts dedicated to some specific ideas: zeolites and microporous materials (contributions by Armbruster, Pekov et al., Peters et al., Yakovenchuk et al., Merlino et al., Zubkova and Pushcharovsky, Spiridonova et al., Khomyakov, Zolotarev et al., Grigorieva et al., Olysych et al., Organova et al.), crystal chemistry of minerals with important properties (chapters by Yakubovich, Filatov and Bubnova, Krzhizhanovskaya et al., Britvin, Siidra and Krivovichev, Selivanova et al., Karimova and Burns), mineral nanostructures (chapters by Ferraris, Kovalevski, Voytekhovsky, Krivovichev), minerals as actinide host matrices (chapters by Livshits and Yudintsev, Burakov et al., Tananaev), and biominerals and biomineralogy (chapters by Chukanov et al., Izatulina and Elnikov, Frank-Kamenetskaya). Thus, the chapters in this book touch almost all important points where mineralogy intersects with material science and related disciplines.

We hope that the workshop series 'Minerals as Advanced Materials' will initiate interesting and fruitful discussions that will help us to achieve deeper understanding of inorganic natural matter.

Thanks are due to the Swiss National Science Foundation for the support of the first workshop of the series.

Contents

List of Contributors

Atali A. Agakhanov
Fersman Mineralogical Museum, Moscow, Russia

Thomas Armbruster
Institute of Geological Sciences, Research Group: Mineralogical Crystallography, University of Bern, Freiestr. 3, CH-3012 Bern, Switzerland, e-mail: Thomas.Armbruster@krist.unibe.ch

Elena Bonaccorsi
Dipartimento di Scienze della Terra, Università di Pisa, Via S. Maria 53, 56126 Pisa, Italy

Sergey N. Britvin
Department of Crystallography, Faculty of Geology, St. Petersburg State University, University Emb. 7/9, St. Petersburg, Russia, e-mail: SBritvin@gmail.com

Igor A. Bryzgalov
Faculty of Geology, Moscow State University, 119991 Moscow, Russia

Rimma S. Bubnova
Institute of Silicate Chemistry of Russian Academy of Sciences, St. Petersburg, Russia, e-mail: Rimma_Bubnova@mail.ru

Boris E. Burakov
Laboratory of Applied Mineralogy and Radiogeochemistry, V.G. Khlopin Radium Institute, 2-nd Site, KIRSI-branch, 1, Roentgen Street, 197101 St. Petersburg, Russia, e-mail: Burakov@peterlink.ru

Peter C. Burns
Department of Civil Engineering and Geological Sciences, University of Notre Dame, 156 Fitzpatrick Hall, Notre Dame, IN 46556-0767, USA

Nikita V. Chukanov
Institute of Problems of Chemical Physics Russian Academy of Sciences, Chernogolovka, Moscow region, Russia, e-mail: Chukanov@icp.ac.ru

Wulf Depmeier
Universität Kiel, Institut fuer Geowissenschaften, Olshausenstrasse 40, D-24098 Kiel, Germany

Yana V. Domracheva
Laboratory of Applied Mineralogy and Radiogeochemistry, V.G. Khlopin Radium Institute, 2-nd Site, KIRSI-branch, 1, Roentgen Street, 197101 St. Petersburg, Russia

Vera N. Ermolaeva
Institute of Geochemistry and Analytical Chemistry, 119991 Moscow, Russia

Giovanni Ferraris
Dipartimento di Scienze Mineralogiche e Petrologiche, Università di Torino – Istituto di Geoscienze e Georisorse, CNR – Via Valperga Caluso 35, I-10125 Torino, Italy, e-mail: giovanni.ferraris@unito.it

Stanislav K. Filatov
Department of Crystallography, St. Petersburg State University, St. Petersburg, Russia, e-mail: filatov@crystalspb.com

Walter Garra
Dipartimento di Chimica e Chimica Industriale, Università di Pisa, Via Risorgimento 35, 56126 Pisa, Italy

Vladimir M. Garbuzov
Laboratory of Applied Mineralogy and Radiogeochemistry, V.G. Khlopin Radium Institute, 2-nd Site, KIRSI-branch, 1, Roentgen Street, 197101 St. Petersburg, Russia

Arina A. Grigorieva
Faculty of Geology, Moscow State University, 119991 Moscow, Russia, e-mail: arina1984@bk.ru

Gregory Yu. Ivanyuk
Geological Institute, Kola Science Centre of the Russian Academy of Sciences, Apatity, Russia, e-mail: ivanyuk@geoksc.apatity.ru

Alina R. Izatulina
Department of Crystallography, Faculty of Geology, St. Petersburg State University, University Emb. 7/9, St. Petersburg, Russia, e-mail: Alina.Izatulina@mail.ru

Oxana Karimova
Department of Mineralogy, Institute of Geology of Ore Deposits Russian Academy of Sciences, 35 Staromonetny, 119017 Moscow, Russia, e-mail: oksa@igem.ru

Alexander P. Khomyakov
Institute of Mineralogy, Geochemistry, and Crystal Chemistry of Rare Elements, Moscow, Russia, e-mail: noomineral@noomin.msk.ru

Alexander A. Kitsay
Laboratory of Applied Mineralogy and Radiogeochemistry, V.G. Khlopin Radium Institute, 2-nd Site, KIRSI-branch, 1, Roentgen Street, 197101 St. Petersburg, Russia

Karsten Knorr
Universität Kiel, Institut fuer Geowissenschaften, Olshausenstrasse 40, D-24098 Kiel, Germany

Ekaterina V. Kolesnikova
Laboratory of Applied Mineralogy and Radiogeochemistry, V.G. Khlopin Radium Institute, 2-nd Site, KIRSI-branch, 1, Roentgen Street, 197101 St. Petersburg, Russia

Vladimir V. Kovalevski
Institute of Geology, Karelian Research Center, Russian Academy of Sciences, Pushkinskaya St. 11, Petrozavodsk 185610, Russia, e-mail: kovalevs@krc.karelia.ru

Sergey V. Krivovichev
Department of Crystallography, Faculty of Geology, St. Petersburg State University, State University Emb. 7/9, 199034 St. Petersburg, Russia, e-mail: SKrivovi@mail.ru

Maria G. Krzhizhanovskaya
Department of Crystallography, St. Petersburg State University, St. Petersburg, Russia, e-mail: Krzhizhanovskaya@mail.ru

Tatiana Livshits
Institute of Geology of Ore Deposits, Moscow, Russia

Ekaterina V. Lovskaya
Faculty of Geology, Moscow State University, 119991 Moscow, Russia

Fabio Marchetti
Dipartimento di Chimica e Chimica Industriale, Università di Pisa, Via Risorgimento 35, 56126 Pisa, Italy

Yurii P. Men'shikov
Geological Institute, Kola Science Centre of the Russian Academy of Sciences, Apatity, Russia

Marco Merlini
Dipartimento di Scienze della Terra "A. Desio", Università di Milano, Via Botticelli 23, 20133 Milano, Italy

Stefano Merlino
Dipartimento di Scienze della Terra, Università di Pisa, Via S. Maria 53, 56126 Pisa, Italy, e-mail: Merlino@dst.unipi.it

Larisa D. Nikolaeva
Laboratory of Applied Mineralogy and Radiogeochemistry, V.G. Khlopin Radium Institute, 2-nd Site, KIRSI-branch, 1, Roentgen Street, 197101 St. Petersburg, Russia

Lyudmila V. Olysych
Faculty of Geology, Moscow State University, Moscow, Russia, e-mail: Olyssych@mail.ru

Natalia I. Organova
Institute of Geology of Ore Deposits, Petrology, Mineralogy, Russian Academy of Scienses, Staromonetny per.35, 109017 Moscow, Russia, e-mail: Natalia@igem.ru

Yakov A. Pakhomovsky
Geological Institute of the Kola Science Center of the Russian Academy of Sciences, Apatity 184200, Russia

Igor V. Pekov
Faculty of Geology, Moscow State University, 119991 Moscow, Russia, e-mail: IgorPekov@mail.ru; Institute of Geochemistry and Analytical Chemistry, 119991 Moscow, Russia

Lars Peters
Universität Kiel, Institut fuer Geowissenschaften, Olshausenstrasse 40, D-24098 Kiel, Germany, e-mail: wd@min.uni-kiel.de; Present address: Chemistry Department, University of Durham, Durham, UK

Marina A. Petrova
Laboratory of Applied Mineralogy and Radiogeochemistry, V.G. Khlopin Radium Institute, 2-nd Site, KIRSI-branch, 1, Roentgen Street, 197101 St. Petersburg, Russia

Dmitrii Yu. Pushcharovsky
Geology Department, Moscow State University, 119992 Moscow, Russia

Nouri-Said Rahmoun
Universität Kiel, Institut fuer Geowissenschaften, Olshausenstrasse 40, D-24098 Kiel, Germany

Ekaterina A. Selivanova
Geological Institute, Kola Science Centre of the Russian Academy of Sciences, Apatity, Russia

Zoya V. Shlyukova
Institute of Geology of Ore Deposits, Petrology, Mineralogy, Russian Academy of Scienses, Staromonetny per.35, 109017 Moscow, Russia

Oleg I. Siidra
Department of Crystallography, St. Petersburg State University, University Emb. 7/9, 199034 St. Petersburg, Russia, e-mail: siidra@mail.ru

Dar'ya V. Spiridonova
Department of Crystallography, Faculty of Geology, St. Petersburg State University, University Emb. 7/9, St. Petersburg, Russia, e-mail: dasha@crystalspb.com

Ivan G. Tananaev
Vernadsky Institute of Geochemistry and Analytical Chemistry, Russian Academy of Sciences, Moscow, Russia; Frumkin Institute of Physical Chemistry and Electrochemistry, Russian Academy of Sciences, Moscow, Russia, e-mail: Tananaev@geokhi.ru

Yurii L. Voytekhovsky
Geological Institute, Kola Scientific Centre, Russian Academy of Sciences, Apatity, Russia, e-mail: voyt@geoksc.apatity.ru

Maria A. Yagovkina
Laboratory of Applied Mineralogy and Radiogeochemistry, V.G. Khlopin Radium Institute, 2-nd Site, KIRSI-branch, 1, Roentgen Street, 197101 St. Petersburg, Russia

Viktor N. Yakovenchuk
Geological Institute, Kola Science Centre of the Russian Academy of Sciences, Apatity 184200, Russia, e-mail: yakovenchuk@geoksc.apatity.ru

Olga V. Yakubovich
Moscow State Lomonosov University, Moscow, Russia, e-mail: yakubol@geol.msu.ru

Vladislav Yu. Yelnikov
Department of Crystallography, Faculty of Geology, St. Petersburg State University, University Emb. 7/9, St. Petersburg, Russia

Sergey Yudintsev
Institute of Geology of Ore Deposits, Moscow, Russia, e-mail: syud@igem.ru

Maria V. Zamoryanskaya
Laboratory of Applied Mineralogy and Radiogeochemistry, V.G. Khlopin Radium Institute, 2-nd Site, KIRSI-branch, 1, Roentgen Street, 197101 St. Petersburg, Russia

Vladimir A. Zirlin
Laboratory of Applied Mineralogy and Radiogeochemistry, V.G. Khlopin Radium Institute, 2-nd Site, KIRSI-branch, 1, Roentgen Street, 197101 St. Petersburg, Russia

Andrey A. Zolotarev
Department of Crystallography, Faculty of Geology, St. Petersburg State University, St. Petersburg, Russia, e-mail: AAZolotarev@gmail.com

Natalia V. Zubkova
Geology Department, Moscow State University, 119992 Moscow, Russia, e-mail: Nata_Zubkova@rambler.ru

Natural Zeolites: Cation Exchange, Cation Arrangement and Dehydration Behavior

Thomas Armbruster

Introduction

Still 50 years ago natural zeolites mainly from vugs and fissures of volcanic rocks were considered a rare curiosity of nature. About 100 years ago chemists recognized that these minerals with a tetrahedral framework structure, characterized by internal porous space in form of cavities and connecting channels, can be used for ion exchange, molecular sieving, and catalytic reactions. Thus in the 1950s the chemical industry became engaged in the synthesis of these minerals. The industry aimed for chabazite but the synthesis failed and instead the most important synthetic zeolite LTA (Linde Type A) was produced. Simultaneously, geologists discovered huge deposits of natural zeolites mainly in altered volcanic tuffs. Whole mountain ranges on all continents consist of clinoptilolite, phillipsite, chabazite, and analcime with zeolite concentrations above 60%. Since this discovery there is a continuous competition between the pure but expensive synthetic products and the "dirty" but inexpensive natural zeolites. About 3.6 Mio tons of natural zeolites are annually produced. In contrast, 1.3 Mio tons of synthetic zeolites are annually consumed for detergents, catalysts, desiccation, and separation. Main applications (Armbruster, 2001) for natural zeolites are as soil conditioner, animal feed addition, ion exchanger for industrial-, agricultural-, and municipal- wastewater treatment, absorber of Sr and Cs radioisotopes in the nuclear industry and for clean up of nuclear accidents (Chernobyl), soil replacement (ZEOPONICS) in horticulture and also as cat litter. Even veterinary and medical applications are under investigation. In general, products from each natural zeolite deposit have a different favorable application depending on structure and chemistry of the zeolite. A sodian zeolite is not good for potable water production or horticultural applications but excellent for ammonia, Cs, Sr, Pb, Cd exchange in wastewater. A potassian zeolite is favorable for soil amendment

Thomas Armbruster
Institute of Geological Sciences, Research Group: Mineralogical Crystallography, University of Bern, Freiestr. 3, CH-3012 Bern, Switzerland, e-mail: Thomas.Armbruster@krist.unibe.ch

whereas a calcian zeolite is excellent for animal feed addition. The mechanical properties are of special interest for cat litter applications. Not only the benefits of the porous structure are used. Natural zeolites from altered volcanic tuffs are fine-crystalline (about 1 μm) – also responsible for their late discovery – and thus possess a large external surface of high activity. In modern applications such zeolites are surface treated (SMZ: Surface Modified Zeolite) with organic molecules (e.g. HDTMA) used for retention of harmful anions, cations, and non-polar organics such as PCE's and benzene in polluted industrial areas.

Principles of Cation Exchange

In the context of cation exchange on natural zeolites there are several fundamental questions, which are only qualitatively understood. Why do certain natural zeolites easily absorb large cations (Cs, Ba, Sr) from solutions but behave extremely sluggish in their absorption behavior for small cations (Li, Na, Mg)? The key parameters for this property are the hydration energies of the ions in solution and of those already occupying the structural channels, and the difference of electrostatic bonding energy of the competing ions to the inner cavity surface (Eisenman, 1962; Sherry, 1969). Understanding of these relationships originates mainly from studies of ion-sensitive electrodes. However, we do not know yet how a cation diffuses through a narrow bottle-neck (e.g., an eight-membered ring of tetrahedra) to reach a structural cavity. Does the ion diffuse with its coordinating water shell or parts of it, or is H_2O stripped off to allow successful passage of the relatively narrow windows. These differences will certainly influence the kinetic behavior and choice of proper hydration energy values for successful prediction of cation exchange.

Structural Disorder in Natural Zeolites

Single-crystal X-ray structure-analysis allows determining the preferred structural sites of various cations and H_2O molecules within the internal open space of a zeolite structure. However, most natural zeolites are highly disordered:

(1) The negative charge on the inner surface of a cavity is determined by the concentration of Al^{3+} tetrahedra within the tetrahedral silicate-framework. The amount of substituting Al is often non-stoichiometric (e.g., clinoptilolite) and there are tetrahedral sites with lower and higher Al preference leading to strong occupational disorder of Al (Alberti, 1972). In X-ray diffraction studies, the Si/Al ratio in a tetrahedron (T) is usually derived from the mean T–O bond length. However, in conventional structure refinements based on diffraction experiments, only the Si, Al distribution averaged over the whole crystal is resolved.

(2) The disordered Al distribution has direct bearing on the arrangement of the extraframework cations. For charge balance reasons, cations within the cavities will always nestle close to Al-occupied tetrahedral framework sites leading to distributional cation disorder within the open cavity space. The situation becomes even more complex if two or more different types of cations have to be considered as cavity or channel occupants.
(3) Two types of H_2O molecules in the structural channels can be distinguished: (a) H_2O molecules coordinating the extraframework cations and (b) "space-filling" H_2O molecules bonded by hydrogen bonds to the cavity surface. The H_2O space-fillers are not coordinated to cations. Both types of H_2O molecules will be disordered following the distribution pattern of the cations.

The Compromise in Basic Research

When applying X-ray diffraction methods to explore cation and H_2O arrangement in such strongly disordered natural zeolite structures, we have to accept some compromises:

(1) We cannot work on the fine-grained natural material, which is commonly used for technical and environmental applications. Powder materials would limit diffraction experiments to powder methods, which have not sufficient resolution to resolve the expected disorder. Instead of clinoptilolite, the most important natural zeolite for technical applications, we use coarse crystalline heulandite from fissures of volcanic rocks. Clinoptilolite and heulandite have the same structural topology and symmetry (Coombs et al., 1997). The second advantage of heulandite (Si/Al < 4) is the higher Al concentration compared to clinoptilolite (Si/Al > 4). The more Al, the higher is the occupation of the extraframework sites.
(2) Natural heulandites are mainly Ca-dominant but also contain significant Na, K, Mg, which additionally increase the distributional disorder within the cavities. Thus, we first produce heulandite–Na crystals by cation exchange of the natural samples using 1N NaCl solution at elevated temperature. Even after regular replacement of the NaCl stock solution, this exchange takes about 30 days at 100°C to be nearly complete for crystals with dimensions of 0.1–0.3 mm. The long duration of the exchange experiments is a consequence of the crystal size (Yang et al., 1997). Unfortunately, the crystals also mechanically suffer from this procedure.
(3) In the final preparation step we perform a second cation-exchange run to incorporate the cations, which we aim to study by single crystal X-ray diffraction.

The "heulandite compromise" has also one big advantage. When working on fine-grained powders one is never sure whether the observed properties are caused by outer surface "adsorption" or by "absorption" on the inner surface. In case of a single crystal (0.1–0.3 mm) the surface of the inner open space by far exceeds the

outer crystal surface. In addition, conventional X-ray single crystal experiments are "blind" for surface effects. Thus we clearly limit our experiment to the bulk of the crystal.

The Diffraction Experiment

The goal of the diffraction experiment is an exploration of the extraframework cation distribution depending on the degree of hydration, combined with an analysis of the accompanying distortion of the tetrahedral framework upon dehydration. Special care has to be taken in crystal mounting on glass fibers reducing the amount of glue in order to allow easy de- and re-hydration of the crystal. Another applied mounting technique uses unsealed glass capillaries where the crystal is fixed by glass padding above and below. The standard experiment is performed at low temperature, characteristically between 100 and 150 K, using a conventional N_2-chiller. Low temperature is only necessary to preserve a chosen degree of hydration. A typical experiment starts at room temperature at which the zeolite is equilibrated at high humidity. The crystal is subsequently quenched to low temperature for X-ray data collection. After data collection the chiller is switched off and instead a temperature regulated hot air blower is started. The crystal is brought to increased temperature (e.g., 50°C) and is allowed to equilibrate at this condition (ca. 1h). Subsequently, the crystal is chilled for X-ray data collection. In general, this procedure is repeated in several temperature steps as long as the crystal quality allows data collection. With each step crystal quality degrades and X-ray reflections become increasingly diffuse.

Interpretation of the Results

First experiments following the above procedure were performed on natural (untreated) heulandites (Armbruster and Gunter, 1991; Armbruster, 1993). It was found that H_2O released first is bonded to extraframework Na, followed by "space filling" – hydrogen bonded H_2O. H_2O released last is bonded to Ca. This shows that the interpretation of zeolitic water: continuous release with increasing temperature, is only partly correct. The nearly continuous H_2O release is an artifact due to the complex extraframework composition and cation arrangement. Each cation on a specific cavity site has an individual H_2O bonding energy. Furthermore, for each cation site dehydration proceeds stepwise. The H_2O coordination of a cation is gradually reduced and instead the cation adopts increasing coordination by oxygen from the surface of the cavity walls. The consequences are intra-cavity cation-diffusion accompanied by distortion of the tetrahedral framework structure. In particular, in case of small divalent extraframework cations (e.g., Ca, Cd) dehydration and accompanied migration of small cations to other bonding partners may lead to disruption of the tetrahedral framework with formation of an altered tetrahedral connectivity.

Other trend-setting results (Gunter et al., 1994; Yang and Armbruster, 1996; Döbelin and Armbruster, 2003) were derived from structural analyses of heulandites with only one type of heavy element (e.g., Cd^{2+}, Pb^{2+}, Cs^{+}). In case of heulandite–Cd^{2+} the diffraction pattern clearly revealed additional diffuse features associated with intensity modulation along the streaks. This is interpreted in terms of some correlated long-range Cd order among adjacent cavities. Such effects can only be seen for heavy elements increasing the sensitivity of the diffraction experiments for extraframework sites. In case of Cd- and Pb-exchanged heulandite the corresponding structure was found to be acenteric, space group *Cm* and not centro-symmetric *C*2/*m* as generally assumed for heulandite. Due to the relative high anomalous dispersion behavior of Cd and Pb for Mo-X-radiation, acentricity of the structure becomes obvious, which is obscured for heulandite with light elements (Na, Mg, K, Ca) as channel occupants. These results indicate that Al substitution in the tetrahedral framework and associated extraframework cation substitution is not as disordered as originally assumed.

Conclusions

Natural zeolites are applied for their highly active outer surface and their porous bulk structure. For many technical applications it remains dubious, which of these properties is dominant. Due to its periodicity the bulk structure may easily be investigated. However, even diffraction experiments with well-chosen procedures and conditions indicate that detailed knowledge of the true structure of zeolites, in particular of the clinoptilolite- heulandite group, is very limited. Our diffraction experiments gave qualitative evidence that long- and short range Si, Al disorder and associated extraframework cation disorder is not as random as originally believed. However, the question whether Al tetrahedra occur correlated, e.g. enriched around certain cavities but depleted around others, is fundamental for understanding selectivity behavior of clinoptilolite–heulandite.

References

Alberti A (1972) On the crystal structure of the zeolite heulandite. Mineral Petrol 18:129–146

Armbruster T (1993) Dehydration mechanism of clinoptilolite and heulandite: single-crystal X-ray study of Na-poor, Ca-, K-, Mg-rich clinoptilolite at 100 K. Am Mineral 78:260–264

Armbruster T (2001) Clinoptilolite–heulandite: applications and basic research. In: Galarnau A, Di Renzo F, Faujula F, Vedrine J (eds) Studies in surface science and catalysis, vol 135. Zeolites and Mesoporous Materials at the Dawn of the 21st Century. Elsevier Science BV, Amsterdam, pp 13–27

Armbruster T, Gunter ME (1991) Stepwise dehydration of heulandite-clinoptilolite from Succor Creek, Oregon, USA: a single-crystal X-ray study at 100 K. Am Mineral 76:1872–1883

Coombs DS, Alberti A, Armbruster T, Artioli G, Colella C, Galli E, Grice JD, Liebau F, Minato H, Nickel EH, Passaglia E, Peacor DR, Quartieri S, Rinaldi R, Ross M, Sheppard RA, Tillmanns E,

Vezzalini G (1997) Recommended nomenclature for zeolite minerals: report of the subcommittee on zeolites of the International Mineralogical Association, Commission on New Minerals and Mineral Names. Can Mineral 35:1571–1606

Döbelin N, Armbruster T (2003) Stepwise dehydration and change of framework topology in Cd-exchanges heulandite. Micropor Mesopor Mat 61:85–103

Eisenman J (1962) Cation selective glass electrodes and their mode of operation. Biophys J Suppl 2:259–323

Gunter ME, Armbruster T, Kohler T, Knowles ChR (1994) Crystal structure and optical properties of Na- and Pb-exchanged heulandite-group zeolites. Am Mineral 79:675–682

Sherry HS (1969) The ion exchange properties of a zeolites. In: Marinsky JA (ed) Ion exchange, a series of advances, vol 2. Marcel Dekker, New York, pp 89–133

Yang P, Armbruster T (1996) Na, K, Rb, and Cs exchange in heulandite single-crystals: X-ray structure refinements at 100 K. J Solid State Chem 123:140–149

Yang P, Stolz J, Armbruster T, Gunter ME (1997) Na, K. Rb, and Cs exchange in heulandite single crystals: diffusion kinetics. Am Mineral 82:517–525

Natural Ion Exchange in Microporous Minerals: Different Aspects and Implications

Igor V. Pekov, Arina A. Grigorieva, Anna G. Turchkova and Ekaterina V. Lovskaya

Introduction

The ion exchange phenomenon is well-known for crystalline materials including minerals. It has been confirmed experimentally that many microporous minerals representing different chemical classes are capable of cation exchange with salt solutions, including dilute ones, even under room conditions. No doubt that microporous minerals show ion-exchange properties also in nature. Numerous works are devoted to the experimental study and practical use of ion-exchange properties of minerals, especially microporous aluminosilicates (zeolites, clay minerals, *etc*.), whereas reactions and products of natural ion exchange were almost non-studied to recent time.

Background Information and Research Subject

For a crystalline substance, the ion exchange is its capacity to exchange cations or anions with a liquid or gaseous phase (electrolyte) without destruction of the crystal structure. This property is characteristic for microporous crystals in which strong

Igor V. Pekov
Faculty of Geology, Moscow State University, 119991 Moscow, Russia, e-mail: IgorPekov@mail.ru
Institute of Geochemistry and Analytical Chemistry, 119991 Moscow, Russia

Arina A. Grigorieva
Faculty of Geology, Moscow State University, 119991 Moscow, Russia

Anna G. Turchkova
Faculty of Geology, Moscow State University, 119991 Moscow, Russia

Ekaterina V. Lovskaya
Faculty of Geology, Moscow State University, 119991 Moscow, Russia

(essentially covalent, forming stable structure fragments) and weak (ionic, hydrogen) chemical bonds take place together. Steric factor plays also an important role: if the exchangeable ion is located in open cage or wide channel then is favourable for exchange but if it is situated in isolated cage with small windows that exchange can be difficult or impossible.

More than 500 minerals including many widespread species have the structure features making the ion exchange possible. They are characterized by framework, layer or tubular stable structure fragments. Minerals with wide channels show strong ion-exchange properties even under room conditions: there are, in particular, wide-pore aluminosilicate zeolites, silicates with low-dense heteropolyhedral frameworks (consisting of the Si tetrahedra and the octahedra centered by atoms of Zr, Ti, Nb and other transition elements: Chukanov & Pekov, 2005), smectites, vermiculite, pyrochlores and layered sulfides with large atoms. The second group (ion exchange at 60–300°C) includes narrow-pore zeolites, feldspathoids of the cancrinite and sodalite groups, majority of silicates with heteropolyhedral frameworks, *etc*. Under the temperature $\geq$400°C, feldspars, nepheline, micas, apatites and some other minerals become ion-exchangers (Barrer, 1962; Chelishchev, 1973; Breck, 1974; our data). From the structure features, strong ion-exchange capacity can be predicted for natural zeolite-like borates, beryllophosphates, "uranium micas", tobermorite-like silicates, sulfides and Mn oxides with tunnel structures and some other minerals.

Ion-exchange transformations, including ones in nature, can be considered as special case of a metasomatism. The main distinctive feature of ion exchange from "classic" metasomatic reactions is as follows: a crystal has not undergo strong changes in the energetic (only weak chemical bonds break with further formation of new such bonds), structural-geometric (no changes of stable structure fragment or its insignificant deformations), space and morphological (volume and morphology of a crystal remain or change very slightly) aspects.

We examine a problem of natural ion exchange on "macroscopic" ($\geq$0.1 mm) crystals of microporous minerals mainly from peralkaline rocks and granitic pegmatites. Smectites and other fine-grained minerals were not involved for two reasons: (1) it is very difficult to divide the phenomena of ion exchange and surface sorption; (2) study of inner structure of so tiny individuals are very difficult.

Peralkaline rocks seem one of the best objects for study of the natural ion exchange phenomenon. They contain the most diversity of microporous minerals, firstly zeolites (Pekov et al., 2004) and zeolite-like Ti-, Nb- and Zr-silicates (Pekov & Chukanov, 2005). Some of these minerals are unstable: we can observe both initial and replacing secondary phases (the latters typically with relics of the formers) and alteration processes can be easily modelled in laboratory.

In accordance with numerous experimental data and the theory of clathrate formation (Belov, 1976; Barrer, 1982), zeolites and zeolite-like compounds can crystallize in their full-cationic forms only. In peralkaline rocks, such forms are minerals "saturated" by Na or/and K. Alkali-depleted microporous crystals enriched by cations with higher valency (Ca, Sr, Ba, Pb, U, *etc*.) have been considered by us as the products of the ion-exchange reactions with late hydrothermal or/and supergene low-alkaline solutions. Direct exchange "cation-for-cation": $\boldsymbol{nA^+ \rightarrow A'^{n+} + (n-1)\square}$, or $\boldsymbol{nA^+ \rightarrow A'^{n+} + (n-1)H_2O}$, is not excluded. However the well-known

from experimental data for aqueous solutions (Donnay et al., 1959; Zhdanov & Egorova, 1968; Breck, 1974) way including the intermediate stage: $A^+ \rightarrow H^+$, or $A^+ \rightarrow (H_3O)^+$, with further exchange of cations H^+ or $(H_3O)^+$ to other metal cations: $nH^+ \rightarrow A'^{n+} + (n-1)\square$, or $n(H_3O)^+ \rightarrow A'^{n+} + (n-1)H_2O$, seems more probable. For non-aluminosilicate minerals, a protonation of bridge oxygen atoms and, correspondingly, the formation of stable hydroxyl-bearing modifications with deficiency of exchangeable metal cations is typical: $nA^+ + O^{2-} \rightarrow \square + (OH)^-$; in some cases, hydrous forms result: $nA^+ + O^{2-} \rightarrow H_2O + (OH)^-$.

Evidence of Ion Exchange in Nature: Methodology and Modelling Experiments

The main problem in the study of natural ion exchange is reliable identification of its products. Thus, we have the main task as the determination of signs for reliable (or at least highly probable) conclusion: is the studied natural crystal ion-exchanged or not.

The analysis of distribution of chemical constituents in a crystal has been used as the main methodological instrument for answer this question. We have studied two representative groups of samples: (1) natural ones, with unknown "history"; (2) ones certainly cation-exchanged in our modelling experiments (several hundreds experiments with more than 30 microporous minerals in aqueous solutions of salts of Na, K, Rb, Cs, Ca, Sr, Ba and Pb). The distribution of constituents was examined in polished sections using scanning electron microscopy (BSE images and images with characteristic X-ray radiation for different chemical elements) and quantitative electron microprobe analysis. The patterns for natural samples and samples after the experiments were in comparison. Note that for the experiments we have selected crystals maximally homogeneous in the initial distribution of exchangeable cations. Natural samples and samples used in the experiments were represented by the same mineral species or at least members of the same mineral groups.

Similarity of patterns of the distribution of chemical constituents in samples after the ion-exchange experiments and natural samples seems the major argument for the conclusion that the latters were ion-exchanged in nature. It is very important that the chemistry of a stable structure fragment could not be different in neighbouring parts of a crystal, both having undergone and not undergone the ion exchange, if they were chemically identical initially.

As our experiments show, the morphology and distribution of ion-exchanged zones in crystals are different in different cases. Location of areas with maximum concentration of exchanged ions in the peripheral parts of a crystal and along big cracks is the most common. In other cases, the ion-exchanged areas are observed in zones saturated by microcracks (including cleavage microcracks). Strong ion exchange occurs in porous zones of a crystal. In some cases, we observe the maximum concentration of exchanged ions in inner fractured and/or porous areas of a crystal whereas its peripheral parts and zones along big cracks and twin boundaries are not

so enriched by them. It may be caused by the capillar effect. In some samples the maximum content of exchanged ions "marks" margins between concentric growing zones of a crystal imitating a rhytmic growing zonation. "Chamber" distribution of ion-exchanged areas not connected with macroscopic defects in a crystal is not rare.

If the ion-exchange equilibrium is attained in all space of a crystal and exchanged ions are evenly distributed in it (or their distribution is in concordance with a primary zonation) then the problem to determine: is this crystal ion-exchanged or no? is generally unsolvable. For evidence that ion exchange really took place, it is necessary to find a crystal in which this process was interrupted before the ion-exchange equilibrium attainment in all its space. Thus, it would be chemically heterogeneous crystal containing both areas which could be considered as (1) ion-exchanged and (2) relics of initial or relatively slightly altered phase.

Thus, there are the **topochemical signs** which seem only direct evidence that a crystal has undergone ion exchange.

Several other signs could be used as indirect evidences.

Geochemical signs: if a microporous mineral occurs in the mineral assemblage indicating the physico-chemical conditions under which it (or its hypothetic protophase) can not be formed (examples: pyrochlores or titanosilicates together with supergene minerals; zirconosilicates associated with only alkali-free minerals). Location of probable source of exchanged ions close to the crystal for which an ion exchange has been supposed seems convincing "geochemical sign".

Presence of significant amount of weakly bonded cations H^+ or/and hydronium, $(H_3O)^+$, in a microporous mineral can be considered as the **chemical sign**: it is typical for the intermediate stage of the cation-exchange process.

High disorder of extra-framework cations and anions (and water molecules, if they are present) is, in some cases, **crystallochemical sign** of interrupted ion exchange.

Note that in nature an ion-exchange process can be interrupted by different ways. Examples are: (1) withdraval of the electrolyte from the system: solution or gas leaving, melt hardening, insulation of a crystal from electrolyte; (2) temperature decrease; (3) pressure increase; (4) decrease of concentration of exchangeable ions in the electrolyte to the ion-exchange equilibrium constant $K = 1$.

Examples of Natural Ion Exchange in Microporous Minerals

No doubt that natural cation exchange is typical for aluminosilicate zeolites. For example, strong potassium enrichment of the latest zeolites, firstly **chabazite**, detected by us (Pekov et al., 2004) in alkaline complexes of Kola Peninsula (Russia) was initially considered as paradoxical. However it is typical not only for the K-rich Khibiny complex but also the hypersodic Lovozero complex and the Kovdor and Afrikanda massifs with general strong Ca prevailing over K. This phenomenon is easily explained using ion-exchange mechanism: our experiments with mixed salt solutions demonstrate very strong affinity of chabazite to potassium in cation exchange.

Pyrochlore group members, generally $A_{2-x}B_2(O,OH,F)_7$ with B = Nb, Ta, Ti and A = Ca, Na, Sr, Ba, U, *REE*, Pb, Bi, *etc*. are the most well-known ion-exchangers among oxide minerals. The composition of "fresh" pyrochlore from the Khibiny and Lovozero alkaline complexes is stable and close to $NaCaNb_2O_6(OH,F)$. In pegmatites and metasomatic rocks altered by low-temperature hydrothermal solutions, pyrochlores become *A*-deficient (x up to 1.6), Ca- and especially Na-depleted and enriched by Sr, Ba, Pb, Y, *Ln*, U, Th and, in some cases, K and H_3O. Their crystals show significant heterogeneity in distribution of the *A* cations unlike the *B* cations, with typical signs of the ion exchange. In granitic pegmatites of the Lipovka (Urals, Russia) we have found crystals with a microlite core and *A*-deficient uranmicrolite, plumbomicrolite or bismutomicrolite rim. In section, the border between core and rim looks a curve arched to the core; it is considered as a projection of the front of the ion-exchange reaction.

The oxosilicate minerals with pyrochlore-like modules in the structure, namely **komarovite series** members and **fersmanite**, show exchange properties for the same cations as pyrochlore: Sr, Ba, Pb, Th, U and K. These minerals from hydrothermally altered alkaline pegmatites, unlike "fresh" samples, are Na- or/and Ca-depleted and enriched by above-listed metals. In one of altered Khibiny pegmatites, we have found very bright example of natural ion exchange: aggregates of Na-poor and Pb-rich (8–13 wt.% PbO) komarovite located very close to significantly corroded large galena crystals.

In crystals of minerals of the vuoriyarvite subgroup (**labuntsovite group**), large cations K and Ba are typically concentrated in peripheral parts and in zones along cracks and other defects. These patterns are absolutely the same as ones obtained in above-discussed experiments and no doubt that we have observed a result of the natural ion exchange.

Ion exchange with hydrothermal solutions is probable cause of abnormal enrichment of **micas** in granitic pegmatites of Voron'i Tundry (Kola Peninsula) by rubidium and cesium. In lepidolite crystals, Rb- and Cs-enriched and K-depleted areas are located along cleavage microcracks close to cross big cracks fulfilled by pollucite.

An example of natural ion exchange in sulfides is formation of **cronusite** in the Norton County enstatite achondrite under terrestrial conditions. Meteoritic caswellsilverite, $NaCrS_2$, a microporous mineral with layered structure, easily looses about 70% Na during its weathering and hydrates to schöllhornite, $Na_{0.3}CrS_2{\cdot}H_2O$. Further, residual Na easily exchanges to Ca and K with entry of second layer of water molecules forming cronusite, $(Ca,K)_{0.2}CrS_2{\cdot}2H_2O$ (Britvin et al., 2001).

Natural ion exchange is typical for **eudialyte group** minerals in alkaline pegmatites altered by low-alkaline solutions. Evidently, the enrichment of aqualite, a Na-depleted strongly hydrated member of the group, at the Inagli (Sakha-Yakutia, Russia) and Kovdor massifs by K and Ba, unusual constituents of "fresh" eudialyte of these localities, is a result of the ion exchange. A Na-deficient hydrated eudialyte containing several wt.% SO_3 was found in the Lovozero complex. It occurs in a pegmatite hydrothermally altered under oxidizing conditions and is considered by us as a product of natural anion exchange.

Enrichment of majority of microporous sodium and potassium zirconosilicates by alkaline-earth cations in nature seems result of the ion exchange. In unaltered agpaitic pegmatites these minerals are charascterized by almost pure-alkaline composition of extra-framework cations whereas pegmatites strongly altered by late low-alkaline hydrothermal solutions contain their alkali-deficient varieties enriched typically by Ca and sometimes Ba and Sr. The examples are Ca-dominant analogue of **gaidonnayite** from the Khibiny (Belyaevskaya et al., 1991), **calciohilairite** and Ca-rich varieties of **catapleiite**, **elpidite**, **paraumbite** and some other minerals found by us in several alkaline massifs.

The ion-exchange transformations involving H^+ or H-bearing cationic and anionic groups seem usual in nature. This phenomenon is very important for comprehension of post-crystallization processes in minerals under hydrothernmal (especially low-temperature) and supergene conditions.

The mechanism of complex ion exchange in wide-pore zeolite-like zirconosilicates of the **hilairite group** was reconstructed using structural data on calciohilairite from Lovozero (Pushcharovsky et al., 2002). The scheme of alteration of hilairite to cation-deficient calciohilairite is: $\mathbf{2Na^+ + H_2O \rightarrow 0.5Ca^{2+} + 1.5\square + (H_3O)^+}$.

Entry of hydronium cation instead of Na ($\mathbf{Na^+ \rightarrow (H_3O)^+}$) is found in three other zeolite-like silicates with heteropolyhedral frameworks, namely tsepinite-Na, a member of the **labuntsovite group**, and two representatives of the **eudialyte group**: ikranite and aqualite. In heterophyllosilicate **hydroastrophyllite**, hydronium is located instead of K and Na. All these minerals are products of natural ion exchange.

The capacity of anhydrous zircono- and titanosilicates of the **lovozerite group** to loose more than half Na with partial hydration is well-known (Chernitsova et al., 1975; Khomyakov, 1995). We have studied the mechanism of this process basing on the modelling experiments and exact determination of the character of occupancy of different sites in zeolitic channels and cages (Pekov & Chukanov, 2005): complete leaching of Na from the *B* sites takes place whereas only its insignificant amount leaves the *A* sites. The transformation of Na-rich lovozerite-type minerals to H-rich members of the group is considered as an exchange reaction involving both cations and anions: $\mathbf{Na^+ + O^{2-} \rightarrow (\square,H_2O)^0 + (OH)^-}$.

The substitution of O^{2-} by OH^- on the bridges between framework-forming octahedra (centered by Ti, Nb, Ta and Sb atoms) is the major charge-balance compensation mechanism when large cations are leached from framework oxides of the **perovskite group** (Na-deficient "metaloparite") and **pyrochlore group** in nature. Among silicates with heteropolyhedral frameworks, it can occur in **labuntsovite group** and **komarovite series** minerals, **zorite**, **vinogradovite**, **sitinakite**, **fersmanite**, *etc*.

The ion exchange scheme $\mathbf{\mathit{A}^+ \rightarrow H^+}$ (*A* = Na, K) is also known in nature. A presence of "free" H^+ as cation was found by us, using the IR spectroscopy, in **astrophyllite group** minerals from the Darai-Pioz alkaline massif (Tadjikistan) and **paranatrolite** and **chabazite** from Khibiny (Pekov et al., 2004).

Ion Exchange in Nature: Significance and Geological Implications

From our viewpoint, significance of natural ion exchange for the genetic mineralogy and geochemistry resides mainly in the two following unique features.

1. Many microporous phases have ultra-high selectivity with respect to some elements, includes very rare ones. That allows catching and concentrating these elements from solutions or gases, even in traces. It is very important that a crystal can act as ion exchanger for an unlimited time, whereas its action as element incorporator during growing is limited in time; thus, such crystals can extract selected elements from solutions (fluids) for a very long time, playing a role of filtering.
2. Ion exchange allows microporous minerals to enrich in some elements under conditions not favorable to the direct crystallization from solutions or melts (that happens under low temperature and/or deficiency of framework-forming elements in the medium).

Several important geological consequences result from these two features.

Selective concentration of deficient chemical constituents. For example, micas and other layered silicates with large low-valent cations, namely K and Na, can concentrate Rb, Cs, NH_4 and Tl by ion exchange. In supergene natural systems, also phosphate, arsenate and vanadate "uranium micas" can play the same role.

Formation of rare-metal deposits with a participation of ion-exchange processes can be demonstrated on the example of pyrochlores. At present time, the main source of Nb in the world is Araxá bariopyrochlore deposit (Brazil) located in the weathered zone of a Ba-bearing carbonatites. In unaltered carbonatites of the Araxá complex, usual Na, Ca pyrochlore occurs. During the weathering, it transforms to bariopyrochlore by cation exchange with solutions enriched by Ba mainly from decomposed Ba-bearing carbonates. The same situation is at other huge niobium deposits of Brazil, namely Cataläo I and II, Tapira, *etc*. In our mind, Th- and Pb-bearing uranpyrochlore, the main ore mineral of the complex Nb-Ta-U deposits of the north-eastern contact zone of the Lovozero complex was formed by ion exchange from earlier albititic pyrochlore.

Increase of mineral diversity. Selectively concentrating certain constituents in crystals, natural ion-exchange processes play important role in increase of diversity of mineral species and especially their chemical varieties. Some microporous minerals can be formed only by this way.

Expansion of stability fields of minerals (structure types). A capacity to exchange ions when conditions (firstly chemistry of the medium) change is important property allowing microporous minerals an advantage in stability over other phases. For example, many minerals formed in "dry" hyperagpaitic pegmatites become unstable when temperature and Na activity decrease and H_2O activity increases. The ionite minerals such as zirsinalite, parakeldyshite, *etc*. "smoothly" exchange significant part of Na to H-bearing groups and preserve their structure types whereas

alkali-rich minerals with dense structures (natrosilite, fenaksite, phosinaite, *etc*.) disappear being replaced by phases with different structure types.

It is important to take into account natural ion exchange working on some geological tasks.

Reconstruction of geochemical history. The ion exchange properties of minerals give a unique possibility of knowing the chemistry of the latest residual solutions that did not produce their own minerals. For example, the cation composition of late wide-pore zeolites show that residual solutions in Kola alkaline complexes were rich of K (and, less, Ca), unlike Mont Saint-Hilaire (Quebec, Canada) and Ilímaussaq (Greenland) where they were Na-rich (Pekov et al., 2004).

Study of mineral equilibria. When a mineral equilibrium is in study (including the geothermometry and geobarometry) that chemical compositions of involved minerals are the most important. If some of the minerals are potential ion exchangers then it can not be excluded that their composition can be "distorted".

Study of liquid and gas inclusions. If a crystal containing liquid and/or gas inclusions is potential ion exchanger then the temperature evolution of the system can provoke the ion exchange between the inclusion and host crystal. In this case, composition of the liquid (gas) phase of the inclusion is determined by the ion-exchange equilibrium at last stage of the exchange process.

Isotope geology (geochronology, determination of source of matter, etc.). Many methods in geology are based on the measurements of isotope concentrations. Some of these methods use elements forming exchangeable ions. In geochronology, there are K, Rb, Sr, U, Th and Pb; for the determination of source of matter, isotopes of O, S and some other elements are in use. In mineral ionites, the "distortion" of the composition by natural ion exchange processes seems very probable.

Acknowledgements We are grateful to N.N. Kononkova, I.A. Bryzgalov, E.V. Guseva and N.N. Korotaeva for their help in SEM and electron probe study of our samples and N.V. Chukanov for discussion. This work was supported by grants of President of Russian Federation MD-7230.2006.5, NSh-4964.2006.5 and NSh-4818.2006.5, grant RFBR 06-05-90626-BNTS_a and grant of Russian Science Support Foundation (for IVP).

References

Barrer RM (1962) Some features of ion exchanges in crystals. Chem Ind 1258–1266

Barrer RM (1982) Hydrothermal Chemistry of Zeolites. Academic Press, London

Belov NV (1976) Ocherki po Strukturnoy Mineralogii (Essays on Structural Mineralogy). Nedra Publishing, Moscow (in Russian)

Belyaevskaya GP, Borutskiy BE, Marsiy IM, Vlasova EV, Sivtsov AV, Golovanova TI, Vishnev AI (1991) Potassium-calcium gaidonnayite, $(Ca,Na,K)_{2-x}ZrSi_3O_9 \cdot nH_2O$, a new mineral variety from the Khibiny massif. Dokl RAN 320:5:1220–1225 (in Russian)

Breck DW (1974) Zeolites Molecular Sieves: Structure, Chemistry and Use. John Wiley & Sons, New York

Britvin SN, Guo YS, Kolomenskiy VD, Boldyreva MM, Kretser YuL, Yagovkina MA (2001) Cronusite, $Ca_{0.2}(H_2O)_2CrS_2$, a new mineral from the Norton County enstatite achondrite. Zapiski VMO 3:29–36 (in Russian)

Chelishchev NF (1973) Ionoobmennye Svoystva Mineralov: (Ion-Exchange Properties of Minerals). Nauka Publishing, Moscow (in Russian)
Chernitsova NM, Pudovkina ZV, Voronkov AA, Kapustin YuL, Pyatenko YuA (1975) On a new lovozerite crystallochemical family. Zapiski VMO 1:18–27 (in Russian)
Chukanov NV, Pekov IV (2005) Heterosilicates with tetrahedral-octahedral frameworks: mineralogical and crystal-chemical aspects. Rev Miner Geochem 57:105–143
Donnay G, Wyart J, Sabatier G (1959) Structural mechanism of thermal and compositional transformations in silicates. Z Kristallogr 112:161–168
Khomyakov AP (1995) Mineralogy of Hyperagpaitic Alkaline Rocks. Clarendon Press, Oxford
Pekov IV, Chukanov NV (2005) Microporous framework silicate minerals with rare and transition elements: minerogenetic aspects. Rev Mineral Geochem 57:145–171
Pekov IV, Turchkova AG, Lovskaya EV, Chukanov NV (2004) Tseolity Shchelochnykh Massivov (Zeolites of Alkaline Massifs). Ekost, Moscow (in Russian)
Pushcharovsky DYu, Pekov IV, Pasero M, Gobechiya ER, Merlino S, Zubkova NV (2002) Crystal structure of cation-deficient calciohilairite and probable decationization mechanisms in minerals with mixed frameworks. Kristallografiya 47(5):814–818 (in Russian)
Zhdanov SP, Egorova EN (1968) Khimiya Tseolitov (Chemistry of Zeolites). Nauka Publishing, Leningrad (in Russian)

Why Do Super-Aluminous Sodalites and Melilites Exist, but Not so Feldspars?

Lars Peters, Nouri-Said Rahmoun, Karsten Knorr and Wulf Depmeier

Microporous structures not only continue to raise great scientific interest, but, in addition, several representatives bear high technical importance and have commercial value as functional materials. Their functionality depends on both, particular features of their structure and their actual chemical composition. Many microporous structure types with a wide variety of chemical compositions are currently known, and new ones are discovered in short intervals, see (Baerlocher and McCusker, http://www.iza–structure.org/databases/). Various experimental parameters are at the disposal of the experimentalist when he attempts to find synthesis methods for the preparation of materials with new topological or geometrical features, e.g. heteropolyhedral topology, larger pores, wider rings, ... or having superior physical or chemical properties. An obvious strategy to follow is variation of the chemical composition. A particular case which is in the focus of the present contribution is constituted by the aluminosilicate frameworks, i.e. three-dimensional frameworks built from corner–connected $[SiO_4]$– and $[AlO_4]$–tetrahedra. The development in this field has been given impetus by real technical demands. Many natural, and also many as-synthesized, aluminosilicate zeolites have a Si:Al ratio close to 1. However, one of the most important technical applications of zeolites is their use as catalysts in crude oil refining. The underlying chemical processes necessitate high degrees of thermal stability, hydrophobicity and resistivity to low pH.

Lars Peters
Universität Kiel, Institut fuer Geowissenschaften, Olshausenstrasse 40, D-24098 Kiel, Germany, e-mail: wd@min.uni-kiel.de
Present address: Chemistry Department, University of Durham, Durham, UK

Nouri-Said Rahmoun,
Universität Kiel, Institut fuer Geowissenschaften, Olshausenstrasse 40, D-24098 Kiel, Germany

Karsten Knorr
Universität Kiel, Institut fuer Geowissenschaften, Olshausenstrasse 40, D-24098 Kiel, Germany

Wulf Depmeier
Universität Kiel, Institut fuer Geowissenschaften, Olshausenstrasse 40, D-24098 Kiel, Germany

This can be achieved by pushing the Si:Al ratio to values much higher than 1.0, up to the compositions of highly siliceous or even pure silica zeolites.

Striking the opposite path, i.e. decreasing the Si:Al ratio below 1.0, has only rarely been considered, most probably for the following two reasons:

(i) an alleged uselessness of such low–Si/high–Al microporous materials for practical applications,
(ii) a widely believed doctrine in the community that Si:Al ratios beyond 1.0 were forbidden, because of Loewenstein's rule (Loewenstein, 1954).

We consider both objections as arguable. Ad (i): One can conceive of possible applications. For example, each Al-atom substituting for Si, requires the addition of a positive charge to the structure in order to maintain charge balance. Usually, this happens by incorporation of extra cations into the pores of the microporous framework. Therefore, the capacity of an aluminosilicate zeolite to incorporate guest cations will increase with its Al content, provided the pores are sufficiently large and also accessible. Such materials could be of interest for absorbing, and thus rendering harmless, dangerous volatile radioactive species, like ^{137}Cs and ^{90}Sr. Other possible applications of Al-rich microporous materials include gas storage, or rely on the inclusion of species having a particular property or function, e.g. if they carry a magnetic moment or an electric dipole, or act as a luminophore. Thus, despite the fact that superaluminous microporous materials most probably would not be very useful for the established petrochemical processes, this does not necessarily imply that such materials would lack any potential in other fields of technical application. Even the diminishing hydrophobicity could be turned into an asset, if applications based on the hydrophilic character of superaluminous microporous compounds were found.

Ad (ii): Loewenstein's rule was first formulated more than fifty years ago (Loewenstein, 1954). Since then, it has developed into a popular rationale used in the crystal chemistry of aluminosilicates in general, and of zeolites in particular. Several recent publications deal with various experimental and theoretical aspects of this rule and bear witness to its ongoing scientific interest, see e.g. (Bosenick et al., 2001) and literature cited therein. Loewenstein (1954) claimed that "whenever two tetrahedra are linked by an oxygen bridge, the center of only one of them can be occupied by aluminium; the other center must be occupied by silicon. . . " and ". . . , whenever two aluminium ions are neighbours to the same oxygen anion, at least one of them must have a coordination number larger than four, . . . ". He goes on: "These rules explain the maximum substitution of 50% of the silicon in three–dimensional frameworks and plane networks .." and "For 50% substitution, rigorous alternation between silicon and aluminium tetrahedra becomes necessary; . . . ". Loewenstein based his arguments on the crystal chemical particularities of the Al^{3+} cation compared with Si^{4+}; this is why Loewenstein's rule is also known as aluminium avoidance rule. Loewenstein had to build his empirical finding on the rather small set of structural data which was at his disposal at that time. Since then, the number of known aluminosilicate structures has increased enormously, and the progress of experimental techniques and theory allows more well-founded statements on the

validity of Loewenstein's rule to be made. For many room temperature structures of 1:1 aluminosilicates one finds, indeed, alternation between silicon and aluminium, as supposed by Loewenstein. However, it should not come as a big surprise that at higher temperatures entropy prevails and disorder occurs. Note, that in this case Al–O–Al connections are unavoidable, clearly in contradiction to Loewenstein's rule. If Al/Si < 1, various local ordering schemes become possible which, however, allow global Al/Si disorder, such that the structure remains in accordance with aluminium avoidance. The temperature at which the Al/Si order–disorder transition sets in shows a remarkably wide range. A number of profound investigations into these problems took advantage of the progress in computer simulation techniques over the years (e.g., Winkler et al., 1991, 2004; Dove et al., 1993, 1996; Thayaparam et al., 1994; Myers et al., 1998). In early work it could be demonstrated that the enthalpy of formation of two Al–O–Si linkages is, indeed, slightly favoured over that of forming one Al–O–Al and one Si–O–Si linkage (Dove et al., 1993). Recently, the basic reason for the validity of the tendencies cast in Loewenstein's rule has been attributed to the cost in elastic energy which becomes due, when a bigger Al-cation substitutes for a smaller Si, thus giving rise to a local deformation of the structure (Bosenick et al., 2001).

The diligence which has been exercised in the investigation of Loewenstein's aluminium avoidance rule, including its entropically stabilised exceptions, is in striking contrast with the compliancy of wide parts of the community to accept the claim that only a maximum of 50% of silicon may be substituted for by aluminium in aluminosilicates. However, even in his original chapter Loewenstein (1954) had mentioned an exception to that rule, viz. $KAlO_2$, which has a stuffed cristobalite-type structure with a framework of all-corner-connected AlO_4–tetrahedra. Subsequently, several other framework aluminates were discovered (see, e.g. Dent Glasser et al. 1982; Depmeier, 1988a). Taken literally, all these compounds would violate Loewenstein's rule, because clearly Al:Si > 1.0. However, in view of the results of Bosenick et al. (2001), the formation of all-alumina frameworks does not require extra costs in elastic energy, because all Al-atoms have the same size. Therefore, all-alumina frameworks are not within the scope of Loewenstein's rule, and their existence cannot be considered to be counter-examples to its validity.

But what about aluminosilicates with $1 <$ Al:Si $< \infty$? Admittedly, there were only very few cases known until recently, but their number has considerably increased by our recent work. In the following we will confine ourselves on discussing two different topologies. The first one is that of the mineral gehlenite, $Ca_2Al_2SiO_7$, which belongs to the melilite structure type (Warren, 1930). Despite its ratio Al:Si = 2.0, gehlenite is not considered as an exception to Loewenstein's rule, because the two Al atoms in the formula unit occupy two topologically distinct positions, and direct linkage between them is therefore considered admissible (Thayaparam et al., 1994). A more appropriate formulation of gehlenite is therefore $Ca_2Al[AlSiO_7]$, where the Al- and Si-atoms within the brackets are in accordance with both claims of Loewenstein's rule, i.e. Al:Si ≤ 1.0, and strict alternance of Al and Si for Al:Si = 1.0. The situation is clearly different in the second case represented by the rare sodalite-type mineral bicchulite, $|Ca_8(OH)_8|[Al_8Si_4O_{24}]$–**SOD**

(Sahl and Chatterjee, 1977; Gupta and Chatterjee, 1978; Sahl, 1980). In contrast to gehlenite, Al and Si occupy the same topological position. Since Al:Si > 1.0, and Al and Si are statistically distributed (Winkler et al., 2004), the formation of Al–O–Al linkages is unavoidable. Hence, both claims of Loewensteins's rule are violated in this compound. A similar situation is found for the synthetic compound $|Dy_4(MoO_4)_2|[Al_8Si_4O_{24}]$–**SOD** (Roth et al., 1989), and its relatives. From this and from our previous experience with aluminate sodalites, e.g. $|Ca_8(WO_4)_2|[Al_{12}O_{24}]$–**SOD** (Depmeier, 1988a) we were fully convinced that Loewenstein's rule, while being by and large obeyed, cannot claim generality, in particular not with respect to the alleged maximum value of 1.0 for Al:Si. We therefore decided to attempt the synthesis of members of the sodalite family having variable Al:Si ratios > 1. The general idea was to use the coupled substitution $(Ca^{2+} + Si^{4+}) \leftrightarrow (Ln^{3+} + Al^{3+})$ to prepare members of the sodalite family that are richer in Al than bicchulite, i.e. Al:Si > 2; Ln^{3+} representing rare earth cations. If successful, the existence of such compounds would also indicate that the conspicuous 2:1 Al/Si ratio in the above-mentioned bicchulite and $|Dy_4(MoO_4)_2|[Al_8Si_4O_{24}]$–**SOD** does not represent a hypothetical isolated island of extraordinary stability in the composition range $1 \leq$ Al/Si $\leq \infty$. A direct synthesis of the envisaged sodalites was not successful. Instead, a two-step procedure had to be developed. The first step consisted of the preparation of superaluminous melilite-type compounds $(Ln_xCa_{2-x})Al[Al_{1+x}Si_{1-x}O_7]$, $0 \leq x \leq 1$. $Ln = La^{3+}$, Eu^{3+} and Er^{3+}, were used, and x was varied in steps of $\Delta x = 0.125$. The products were single-phased; their structures were successfully Rietveld-refined (Rietveld, 1967) in space group P-42_1m with disordered Al and Si in the so-called double tetrahedra. Figure 1 illustrates the lattice parameters of the melilite-type compounds as a function of x.

Note the non-uniform deviations from Vegard's rule (Vegard and Dale, 1928) for the different Ln^{3+} cations. By the successful synthesis of the Al-rich melilites with $x > 0$ in the above formula the systematic violation of Loewenstein's rule in the melilite structure type has been documented.

The sodalite-type compounds $|Eu_xCa_{8-x}(OH)_8|[Al_{8+x}Si_{4-x}O_{24}]$–**SOD** could be obtained from the corresponding Eu-containing melilites $Eu_xCa_{2-x}Al[Al_{1+x}Si_{1-x}O_7]$, with $\Delta x = 0.125$, by hydrothermal treatment ($T = 810$ ($x < 0.5$), $T = 910$ K ($0.5 \leq x \leq 1.0$), $p_{H2O} = 0.1$ GPa, run time up to 1000 h). The procedure was inspired by the preparation of bicchulite from gehlenite (Gupta and Chatterjee, 1978). The sodalites obtained were successfully Rietveld–refined in space group I–43m, with both, disordered Al/Si and Ca/Eu. Figure 2 shows the normalized lattice parameter of the Eu-bearing sodalites as a function of the composition.

For a full discussion of structural details the reader is referred to the literature (Peters, 2005; Peters et al., 2006a,b). In short, the results of our studies can be summarized as follows. Loewenstein's rule can be broken systematically and continuously in the melilite- and sodalite-type structures via coupled substitutions of $(Al^{3+} + Ln^{3+})$ for $(Si^{4+} + Ca^{2+})$. In both structure types the substitution of Al^{3+} for Si^{4+} results in a similar extension of the average T–O-bond length. The observed linear dependence of the T–O-bond length on the Al molar fraction follows exactly Jones' (1968) extrapolation from aluminosilicates in the compositional range 'allowed' by Loewenstein's rule, see Fig. 3. This behaviour lends support to our

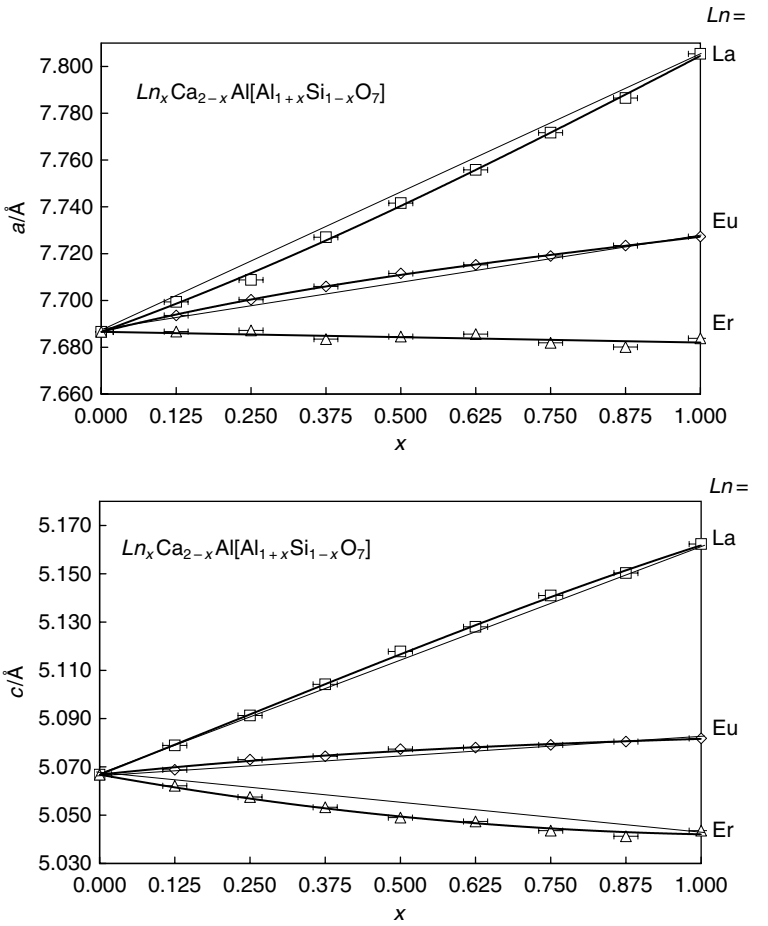

Fig. 1 Change of the tetragonal lattice parameters a and c of the melilite-type solid solution $Ln_xCa_{2-x}Al[Al_{1+x}Si_{1-x}O_7]$ with Ln = La (*squares*), Eu (*diamonds*) and Er (*triangles*). Bold lines correspond to polynomial fits, while thin lines represent a behaviour corresponding to Vegard's rule. The error bars of the relative changes are smaller than the symbols used

conjecture that no significant difference exists between the mixing properties of Al and Si on both sides of the alleged borderline with Al/Si = 1. Contrary to an intuitive expectation that a breach of Loewenstein's rule might result in some spectacular structural conspicuities, no structural phase transitions, superstructures or miscibility gaps were observed in the studied phases. On the other hand, the coupled substitution primarily evokes stronger electrostatic interactions between the partial structures. This behaviour can easily be rationalized in terms of classical crystal chemistry. The stronger electrostatic interactions with increasing content in Ln^{3+} is demonstrated by measurements of the thermal expansion, which clearly show a prevailing three-dimensional character for the melilite-type aluminates

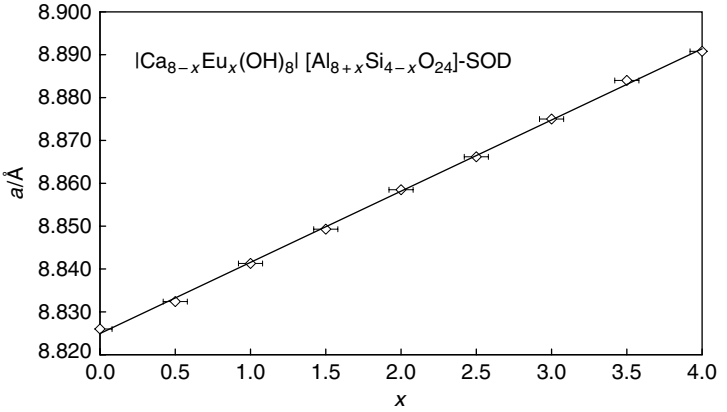

Fig. 2 Relative change of the cubic lattice parameter a of the Eu–bearing sodalite-type solid solution. The bold line corresponds to a linear fit. The error bars of the relative changes are smaller than the symbols used

$TbCaAl[Al_2O_7]$ and $SmCaAl[Al_2O_7]$ compared with gehlenite, $Ca_2Al[AlSiO_7]$ (Peters et al., 2005). A significant reduction of the thermal expansion coefficient due to stronger electrostatic interactions was also observed for $|Eu_2Ca_6(OH)_8|[Al_{10}Si_2O_{24}]$–**SOD** as compared with bicchulite, $|Ca_8(OH)_8|[Al_8Si_4O_{24}]$–**SOD** (Peters et al., 2006c).

As an interesting aside, we have observed increasing thermal stability with increasing x in the series $|Eu_xCa_{8-x}(OH)_8|[Al_{8+x}Si_{4-x}O_{24}]$–**SOD**, $0 \leq x \leq 4$. This

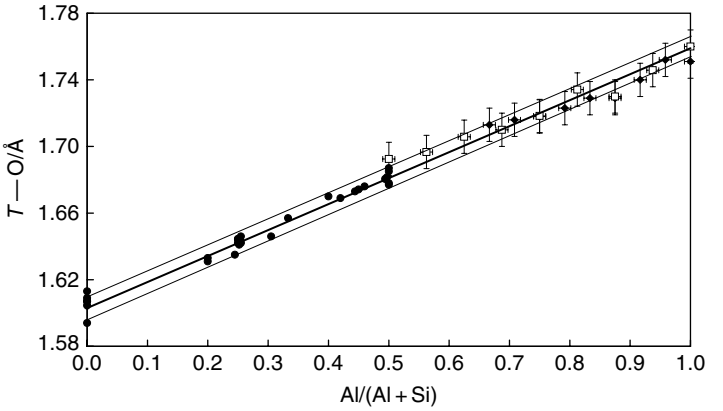

Fig. 3 Mean T–O bond lengths for superaluminous melilites $Ln_xCa_{2-x}Al[Al_{1+x}Si_{1-x}O_7]$ (*open squares*), superaluminous sodalites $|Eu_xCa_{8-x}(OH)_8|[Al_{8+x}Si_{4-x}O_{24}]$–**SOD** (*filled diamonds*) as a function of the Al molar fraction. Their behaviour extrapolates linearly from that of aluminosilicates with Al $\leq$ Si (filled circles, after Jones, 1968). The thick line corresponds to Jones' linear fit, thin lines indicate the error margin to Jones' fit

contrasts with the behaviour of aluminosilicates with Al/Si ≤ 1, where one normally observes decreasing thermal stability with increasing Al-content.

Admittedly, our present results concerning the sodalite structure type are confined on species with $2.0 < \text{Al/Si} \leq \infty$ and bicchulite type materials, i.e. containing hetero-cubane-like $\mathbf{M}_4(\text{OH})_4$ polyhedra ($\mathbf{M} = Ca^{2+}$, Eu^{3+}) in the sodalite cages. It remains to be shown that other cage contents are also compatible with frameworks violating Loewenstein's rule. In particular, such sodalites should be prepared and investigated which contain tetrahedral cage anions, as such materials seem to be prone to interesting ferroic phase transitions (Depmeier, 1988b). Another presently unresolved issue is the range $1.0 < \text{Al/Si} < 2.0$. This range is currently the subject of synthetic work.

Finally, we would like to briefly comment on the question raised in the title and on the possibility to synthesize superaluminous "real" zeolites. The melilite-type, as well as the sodalite-type are well-known for both, their chemical and conformational flexibility. Of course, both are related with each other. The high conformational flexibility has been demonstrated by the occurrence of at least one rigid-unit-mode (RUM) for each wave-vector **k** in the fresnoite structure type (Höche, 2004) (the structure of fresnoite is closely related with the melilite-structure), and in the sodalite structure type (Dove et al., 1995). Rigid unit modes have very low or vanishing frequency, thus, the energy, which is needed for a conformational distortion of the underlying structure is minimal or zero. This leads us to conclude that in both structural families local lattice deformations, which are caused by substitution, are released on a very short length scale via RUMs. Our results suggest that the existence of a large number of RUMs qualify a given aluminosilicate as candidate for systematic and continuous violations of Loewenstein's rule. Thus, in order to find "real" zeolites with $\text{Al/Si} > 1.0$, it seems to be a good strategy to look for candidates with very flexible frameworks, suitable candidates being natrolite (Meier, 1960) or zeolite Rho (McCusker and Baerlocher, 1984).

In a review of the flexibilities of aluminosilicate tectosilicates Baur (1992, 1995) has shown that highly flexible frameworks are less common than inflexible ones. We note that the most frequent minerals of the Earth's crust, viz. feldspars, belong to the inflexible framework types. According to the arguments given above, one should not be too much surprised that feldspars obey Loewenstein's rule, i.e. superaluminous feldspars should not exist.

Acknowledgements Financial support by the Deutsche Forschungsgemeinschaft under contract number De 412/27-1,2 and DE 412/31-1 is gratefully acknowledged.

References

Baerlocher Ch, McCusker LB Database of Zeolite Structures: http://www.iza–structure.org/databases/

Baur WH (1992) Self–limiting distortion by antirotating hinges is the principle of flexible but noncollapsible frameworks. J Solid State Chem 97:243–247

Baur WH (1995) Why the open framework of zeolite A does not collapse, while the dense framework of natrolite is collapsible. In: Rozwadowski M (ed) Proceedings of the 2nd Polish–German Zeolite Colloquim. Nicholas Copernicus University Press, Toruń, pp 171–185

Bosenick A, Dove MT, Myers ER, Palin EJ, Sainz–Diaz CI, Guiton BS, Warren MC, Craig MS, Redfern SAT (2001) Computational methods for the study of energies of cation distributions: applications to cation-ordering phase transitions and solid solutions. Mineral Mag 65:193–219

Dent Glasser LS, Henderson AP, Howie RA (1982) Refinement of the structure of a framework aluminate. Acta Crystallogr B38:24–27

Depmeier W (1988a) Structure of cubic aluminate sodalite $Ca_8[Al_{12}O_{24}](WO_4)$ in comparison with its orthorhombic phase and with cubic $Sr_8[Al_{12}O_{24}](CrO_4)$. Acta Crystallogr B44: 204–207

Depmeier W (1988b) Aluminate Sodalites–A family with strained structures and ferroic phase transitions. Phys Chem Miner 15:419–426

Dove MT, Cool T, Palmer DC, Putnis A, Salje EKH, Winkler B (1993) On the role of Al–Si ordering in the cubic–tetragonal phase transition of leucite. Am Mineral 78:486–492

Dove MT, Heine V, Hammonds KD (1995) Rigid unit modes in framework silicates. Mineral Mag 59:629–639

Dove MT, Thayaparam S, Heine V, Hammonds KD (1996) The phenomenon of low Al–Si ordering temperatures in aluminosilicate framework structures. Am Mineral 81:349–362

Gupta AK, Chatterjee ND (1978) Synthesis, composition, thermal stability, and thermodynamic properties of bicchulite, $Ca_2[Al_2SiO_6](OH)_2$. Am Mineral 63:58–65

Höche T (2004) Incommensurate structural modulations in fresnoite framework structures. Habilitation Thesis, University of Leipzig

Jones JB (1968) Al–O and Si–O Tetrahedral distances in aluminosilicate framework structures. Acta Crystallogr B 24:355–358

Loewenstein W (1954) The distribution of aluminium in the tetrahedra of silicates and aluminates. Am Mineral 39:92–98

McCusker LB, Baerlocher Ch (1984) The effect of dehydration upon the crystal structure of zeolite rho. Proceedings of the 6th International Zeolite Conference 812–822

Meier WM (1960) The crystal structure of natrolite. Zeitschrift fuer Kristallographie 113:430–444

Myers ER, Heine V, Dove MT (1998) Thermodynamics of Al/Al avoidance in the ordering of Al/Si tetrahedral framework structures. Phys Chem Miner 25:457–464

Peters L (2005) Gekoppelte Substitutionen im Melilith–und Sodalith–Strukturtyp. PhD Thesis, University of Kiel, http://e–diss.uni–kiel.de/diss_1519/

Peters L, Knorr K, Knapp M, Depmeier W (2005) Thermal expansion of gehlenite, $Ca_2Al[AlSiO_7]$, and the related aluminates $LnCaAl[Al_2O_7]$ with Ln = Tb, Sm. Phys Chem Miner 32:460–465

Peters L, Knorr K, Depmeier W (2006a) Structural variations in the solid–solution series $Ln_xCa_{2-x}Al[Al_{1+x}Si_{1-x}O_7]$, with $0 \leq x \leq 1$ and Ln = La, Eu, Er. Z Anorg Allg Chem 632:301–306

Peters L, Knorr K, Fechtelkord M, Appel P, Depmeier W (2006b) Structural variations in the solid solution series of sodalite-type $|(Eu_xCa_{2-x})_4(OH)_8|[(Al_{2+x}Si_{1-x})_4O_{24}]$–**SOD** with Δx = 0.125, determined by X-ray powder diffraction and ^{27}Al MAS NMR spectroscopy. Z Kristallogr 221:643–648

Peters L, Knorr K, Katzke H, Knapp M, Depmeier W (2006c) The transformation mechanism of the sodalite- to the melilite-topology: Thermal expansion and decomposition of bicchulite-type to melilite-type compounds. Z Kristallogr 221:198–205

Rietveld H (1967) Line profiles of neutron powder–diffraction peaks for structure refinements. Acta Crystallogr 22:151–152

Roth G, Pentinghaus H, Wanklyn BM (1989) Eine neue Variante in der Sodalith–Strukturfamilie: $Dy_2Al_4Si_2O_{12}\cdot MoO_4$, mit dreiwertigen großen Kationen. Z Kristallogr 186:251–252

Sahl K (1980) Refinement of the crystal structure of bicchulite, $Ca_2[Al_2SiO_6](OH)_2$. Z Kristallogr 152:13–21

Sahl K, Chatterjee ND (1977) The crystal structure of bicchulite, $Ca_2[Al_2SiO_6](OH)_2$. Z Kristallogr 146:35–41

Thayaparam S, Dove MT, Heine V (1994) A Computer simulation study of Al/Si ordering in gehlenite and the paradox of the low transition temperature. Phys Chem Miner 21:110–116

Vegard L, Dale H (1928) Untersuchungen über Mischkristalle und Legierungen. Z Kristallogr 67:148–162

Warren BE (1930) The structure of melilite $(Ca,Na)_2(Mg,Al)_1(Si,Al)_2O_7$. Z Kristallogr 74: 131–138

Winkler B, Dove MT, Leslie M (1991) Static lattice energy minimization and lattice dynamics calculations on aluminosilicate minerals. Am Mineral 76:313–331

Winkler B, Milman V, Pickard CJ (2004) Quantum mechanical study of Al/Si disorder in leucite and bicchulite. Mineral Mag 68:819–824

First Natural Pharmacosiderite-Related Titanosilicates and Their Ion-Exchange Properties

Viktor N. Yakovenchuk, Ekaterina A. Selivanova, Gregory Yu. Ivanyuk, Yakov A. Pakhomovsky, Dar'ya V. Spiridonova and Sergey V. Krivovichev

Introduction

In 1990, Chapman and Roe prepared a number of titanosilicate analogues of pharmacosiderite, including Cs, Rb and exchanged protonated phases. Harrison et al. (1995) reported structure of $Cs_3H[Ti_4O_4(SiO_4)_3](H_2O)_4$. Behrens et al. (1996), Behrens and Clearfield (1997) and Dadachov and Harrison (1997) provided data on preparation, structures and properties of $A_3H[Ti_4O_4(SiO_4)_3](H_2O)_n$ (A = H, Na, K, Cs). Structures and ion-exchanged properties of $HA_3[M_4O_4(XO_4)_3](H_2O)_4$ (A = K, Rb, Cs; M = Ti, Ge; X = Si, Ge) were reported by Behrens et al. (1998). These compounds were considered as perspective materials for the selective removal of Cs and Sr from wastewater solutions. However, no natural titanosilicates with pharmacosiderite topology have been reported so far. In this article, we report for the first time occurrence of four pharmacosiderite-type titanosilicates in Nature and their cation-exchange properties.

Viktor N. Yakovenchuk,
Geological Institute, Kola Science Centre of the Russian Academy of Sciences, Apatity, Russia, e-mail: yakovenchuk@geoksc.apatity.ru

Ekaterina A. Selivanova,
Geological Institute, Kola Science Centre of the Russian Academy of Sciences, Apatity, Russia

Gregory Yu. Ivanyuk,
Geological Institute, Kola Science Centre of the Russian Academy of Sciences, Apatity, Russia

Yakov A. Pakhomovsky,
Geological Institute, Kola Science Centre of the Russian Academy of Sciences, Apatity, Russia

Dar'ya V. Spiridonova
Department of Crystallography, Faculty of Geology, St. Petersburg State University, University Emb. 7/9, St. Petersburg, Russia

Sergey V. Krivovichev
Department of Crystallography, Faculty of Geology, St. Petersburg State University, University Emb. 7/9, St. Petersburg, Russia

All four minerals were found in a natrolitized microcline–aegirine–sodalite lens in orthoclase-bearing urtite at Mt. Koashva (the Khibiny massif), where they form differently coloured well-shaped cubic crystals (up to 1 mm diameter, Fig. 1) grown in voids on microcline, vinogradovite, sazykinaite-(Y) and natrolite crystals. Other associated minerals are catapleiite, chkalovite, djerfisherite, fluorapatite, galena, nepheline, pectolite, pyrite, solid organics, sphalerite and villiaumite. Pharmacosiderite-type minerals are different in colour, which permits us easily detect them in the vein.

Chemical composition of these minerals corresponds to the next empirical formulas:

Phase-1 (colourless) – $(Na_{1.82}K_{0.95}Ca_{0.03}Ba_{0.01})_{\Sigma=2.81}[(Ti_{3.68}\ Nb_{0.17}Fe^{3+}_{0.06}\ Mn_{0.01})_{\Sigma=3.92}(Si_{2.99}Al_{0.01})_{\Sigma=3.00}O_{14.59}(OH)_{1.41}] \cdot 7.27H_2O$;

Phase-2 (orange) – $(Na_{1.17}K_{0.94}Ca_{0.03})_{\Sigma=2.15}[(Ti_{3.32}Fe^{3+}_{0.21}Nb_{0.15}Mn_{0.03})_{\Sigma=3.71}\ (Si_{2.97}Al_{0.03})_{\Sigma=3.00}O_{12.89}(OH)_{3.11}] \cdot 5.90H_2O$;

Phase-3 (blue) – $(K_{1.16}Cu_{0.21}Ca_{0.13}Na_{0.07}Sr_{0.01})_{\Sigma=1.58}[(Ti_{3.49}Nb_{0.21}Fe^{3+}_{0.04}\ Mn_{0.07})_{\Sigma=3.81}(Si_{2.97}Al_{0.03})_{\Sigma=3.00}O_{13.19}(OH)_{2.81}] \cdot 9.30H_2O$;

Phase-4 (green) – $(Cu_{0.62}K_{0.43}Na_{0.04}Ca_{0.03})_{\Sigma=1.12}[(Ti_{3.48}Nb_{0.17}Fe^{3+}_{0.07}Mn_{0.03})\ _{\Sigma=3.75}(Si_{2.99}\ Al_{0.01})_{\Sigma=3.00}O_{12.88}(OH)_{3.08}(SO_4)_{0.02}] \cdot 7.11H_2O$.

Na-dominant phase-2, K-dominant phase-3 and Cu-dominant phase-4 are cubic with *P*-43*m* space group, and Na-dominant phase-1 has a slightly distorted cubic cell with *R*3*m* space group. Dadachov and Harrison (1997) noted the same distortion in synthetic $Na_4(TiO)_4(SiO4)_3 \cdot 6H_2O$ and explain it by the selective position of additional Na-atom, located at [111] axis of the crystal structure of the phase. Really, sodium content in the phase-1 is higher than in phase-2 (Fig. 2). Colourless phase-1 is mostly abundant in the vein. Orange phase-2 occurs in voids enriched in solid organics and is a result of partial decationization of phase-1.

Blue phase-3 and green phase-4 are probably results of natural ion-exchange of phase-1 or phase-2 near dissolved chalcopyrite and djerfisherite grains.

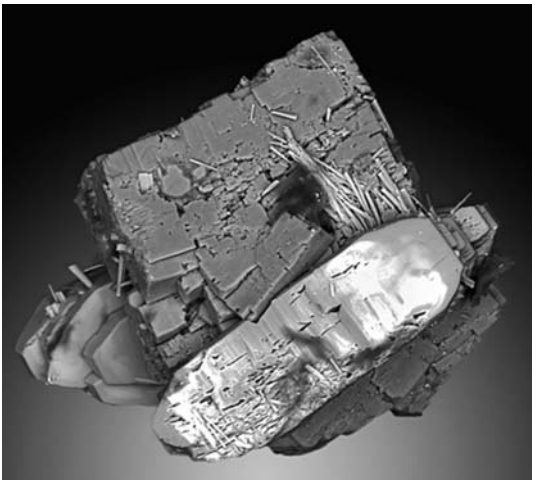

Fig. 1 Mosaic crystal of phase-1 (250 μm diameter), with vinogradovite, from a natrolitized microcline–aegirine–sodalite lens in orthoclase-bearing urtite at Mt. Koashva

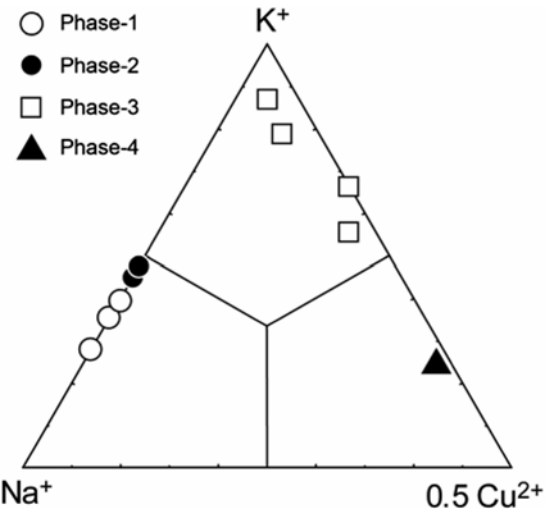

Fig. 2 Composition of natural pharmacosiderite-related titanosilicates

By analogy with synthetic pharmacosiderite-type compounds and in accordance with natural diversity of composition of considered minerals, we supposed that these minerals must have ion-exchange properties and performed a series of experiments to study these properties.

Experimental

In our experiments separate crystals of phase-1 were loaded in 1*M* solutions of NH_4Cl, CsCl, RbCl, $CuSO_4$, $SrCl_2$,and Clerichi liquid at ambient temperature during 12–48 h. The chemical composition of original and treated crystals (Table 1) has been studied by wave-length dispersion spectrometry using a Cameca MS-46 electron microprobe (Geological Institute, Kola Science Centre of the Russian Academy of Sciences, Apatity) operating at 20 kV and 20–30 nA. The following standards were used: lorenzenite (Na, Ti), pyrope (Mg, Al), diopside (Si, Ca), wadeite (K), synthetic $MnCO_3$ (Mn), hematite (Fe), celestine (Sr), metallic niobium (Nb), barite (Ba), lepidolite (Ru), pollucite (Cs) and atacamite (Cl). Water content was calculated as 100 wt.% minus SUM of oxides of analyzed elements.

Examination of polished sections of treated crystals made using Leo-1450 scanning electron microscope with Röntec EDS-analyzer. The powder X-ray-diffraction patterns of treated crystals were obtained by means of the URS–1 instrument operated at 40 kV and 30 mA with a 114.7 mm Debye–Scherrer camera and Fe$K\alpha$ radiation.

It was established that in aqueous solutions of NH_4Cl, CsCl, RbCl, $CuSO_4$ and Clerichi liquid phase-1 easily looses excessive Na and transforms into more stable cubic phase-2, whereas in solution of $SrCl_2$ crystal structure of the phase-1 remains

Table 1 Chemical composition (wt.%) and unit formula (*apfu*, Si+Al = 3) of phase-1 treated with solutions of Clerichi liquid, CsCl, RbCl and $SrCl_2$ at ambient temperature during 48 h

	Original	Treated with				
		Clerichi	CsCl	RbCl	RbCl+CsCl	$CuSO_4$
Na_2O	7.12	0.13	0.39	0.84	0.99	0.10
Al_2O_3	0.12	–	–	–	–	–
SiO_2	23.34	14.36	22.45	22.65	20.15	25.20
K_2O	5.96	–	1.63	0.16	1.88	3.36
CaO	0.08	0.28	0.21	0.11	0.15	–
TiO_2	39.48	24.08	32.24	34.26	33.07	41.56
MnO	–	0.08	–	–	–	–
FeO	0.43	0.34	0.41	0.36	0.38	0.55
CuO						1.58
Rb_2O	–	–	–	29.09	10.78	–
Nb_2O_5	2.53	2.11	3.83	3.81	3.19	4.14
Cs_2O	–	–	37.71	–	19.58	–
BaO	0.23	–	–	–	–	–
Tl_2O	–	56.22	–	–	–	–
SUM	405	2560	482	416	503	323
H_2O=100-SUM	20.71	2.40	1.13	8.72	9.83	23.51
K	0.97	–	0.28	0.03	0.36	0.51
Na	1.76	0.05	0.10	0.21	0.28	0.02
Ca	0.01	0.06	0.03	0.02	0.02	–
Ba	0.01	–	–	–	–	–
Cu	–	–	–	–	–	0.14
Rb	–	–	–	2.48	1.03	–
Cs	–	–	2.15	–	1.24	–
Tl	–	3.32	–	–	–	–
Ti	3.79	3.79	3.24	3.41	3.70	3.72
Nb	0.15	0.20	0.23	0.23	0.22	0.22
Fe^{3+}	0.05	0.06	0.05	0.04	0.05	0.06
Mn	–	0.01	–	–	–	–
Si	2.98	3.00	3.00	3.00	3.00	3.00
Al	0.02	–	–	–	–	–
H	17.67	3.36	1.02	7.69	9.77	18.67

unchanged. As regards as the solutions of CsCl, RbCl, $CuSO_4$ and Clerichi liquid, both phase-1 and phase-2 have extremely strong ion-exchange properties, which permits them to obtain up to 57 wt.% Tl_2O, 37 wt.% Cs_2O, 29 wt.% Rb_2O and 1.6 wt.% CuO during 12 h (see Table 1):

Original phase: $(Na_{1.76}K_{0.97}Ca_{0.01}Ba_{0.01})_{\Sigma=2.76}[(Ti_{3.79}Nb_{0.15}Fe^{3+}_{0.05})_{\Sigma=3.99}Si_3O_{14.81}(OH)_{1.19}]\cdot 8.2H_2O$, Tl-exchanged phase: $(Tl_{3.32}Ca_{0.06}Na_{0.05})_{\Sigma=3.44}[(Ti_{3.79}Nb_{0.20}Fe^{3+}_{0.06}Mn_{0.01})_{\Sigma=4.06}Si_3O_{15.85}(OH)_{0.16}]\cdot 1.6H_2O$, Cs-exchanged phase: $(Cs_{2.15}K_{0.28}Na_{0.10}Ca_{0.03})_{\Sigma=2.56}[(Ti_{3.24}Nb_{0.23}Fe^{3+}_{0.05})_{\Sigma=3.52}Si_3O_{12.84}(OH)_{3.16}]$, Rb-exchanged phase: $(Rb_{2.48}Na_{0.21}K_{0.03}Ca_{0.02})_{\Sigma=2.73}(Ti_{3.41}Nb_{0.23}Fe^{3+}_{0.04})_{\Sigma=3.68}[Si_3O_{13.67}(OH)_{2.33}]\cdot 2.7\ H_2O$, Cu-exchanged phase: $(K_{0.51}Cu_{0.14}Na_{0.02})_{\Sigma=0.67}(Ti_{3.72}Nb_{0.22}Fe^{3+}_{0.06})_{\Sigma=4.00}[Si_3O_{12.98}(OH)_{3.02}]\cdot 7.8\ H_2O$.

Ion-exchanged forms have exclusively clear powder X-ray diffraction patterns, which show improvement in their crystallinity in comparison to the original material. Cu-exchanged phase is an analogue of natural K-dominant phase-3. Crystal structure of Rb-substituted phase-1 is 'intermediate' between structures of natural phase-2 and anhydrous $Cs_3H(TiO)_4(SiO_4)_3$ (Table 2). Tl- and Cs-substituted phases are anhydrous and are structural analogues of synthetic $Cs_3H(TiO)_4(SiO_4)_3$. At powder X-ray diffraction pattern of Tl-exchanged phase such substitution accompanies by decreasing (up to disappearing) of the (100) reflex intensity (see Table 2), whereas intensities of (110), (111) and (200) reflections sufficiently increase. Such changes indicate that crystal structure of Tl-exchanged phase became Tl-centered. Unit cell parameters of all exchanged phases are smaller than those of original ones: 7.856(9) Å for phase-2, 7.832(4) Å for Tl-exchanged phase and 8.843(6) Å for Rb- and Cs-exchanged phases.

Table 2 X-ray powder diffraction data for Rb-, Tl- and Cu-exchanged phase-1 and for phase-2 (naturally decationized phase-1)

hkl	Phase-1 treated with						Phase-2	
	RbCl		Clerichi liquid		$CuSO_4$			
	I_{obs}	d_{obs}(Å)	I_{obs}	d_{obs}(Å)	I_{obs}	d_{obs}(Å)	I_{calc}	d_{calc}(Å)
100	100	7.85			100	7.88	100	7.88
110			20	5.55				
111	60	4.55	100	4.54	30	4.57	30	4.53
200	80	3.92	100	3.92	30	3.95	20	3.96
210	30	3.54	30	3.52	30	3.57		
211	90	3.20	90	3.20	90	3.21	80	3.205
220	80	2.77	100	2.77	60	2.79	30	2.774
221, 300	60	2.61	60	2.61	60	2.63	40	2.622
310	60	2.47	60	2.47	60	2.50	40	2.478
311	30*b*	2.36	60	2.36	30	2.37	20*b*	2.367
222	40	2.26	50	2.26	20	2.27	10	2.26
320			10	2.161				
321	30	2.100	30	2.093	10	2.107	10	2.093
400	10	1.957			20	1.969	30	1.96
322, 410	40	1.898	50	1.894	50	1.906	20	1.905
330, 411	50	1.848	50	1.840	50	1.850	30	1.843
331			20	1.795				
420	50	1.751	60	1.748	40	1.759	10	1.752
422	30	1.597	40	1.593	30	1.606	20*b*	1.598
430, 500	30	1.564	30	1.566	40	1.572	20*b*	1.561
333, 511	10	1.504	10	1.504	20	1.512		
521	20	1.426	10	1.427	30	1.435		
440	50	1.382	50	1.381	50	1.390	20	1.377
441, 522			10	1.361	30	1.369		
433, 530					20	1.350		

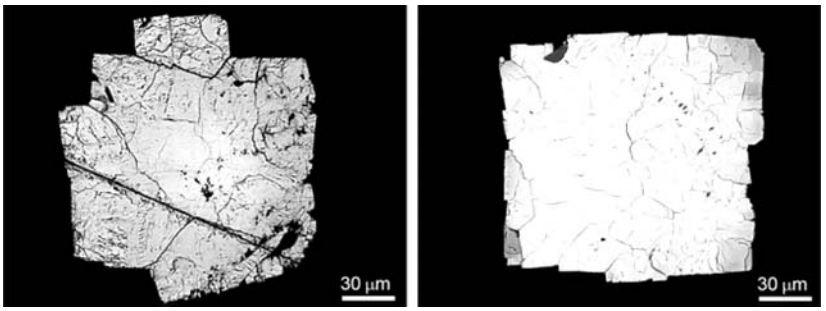

Fig. 3 BSE-images of the phase-1 crystals exchanged by Tl (**a**) and Rb (**b**)

Distribution of Tl and Rb within the exchanged crystals is homogeneous (Fig. 3), only that Rb can be leached often from the crystal corners during washing treated grains.

Content of Cu and Cs decrease from marginal part inside the crystals step by step at the expense of Na and K (Fig. 4). In core of a Cs-exchanged crystal, Na and H_2O contents became higher than in original state, and here the mineral structure again obtains rhombohedral distortion (retransformation into phase-1).

When we use solutions of both RbCl and CsCl, cations of Cs and Rb replace Na and K along boundaries of the crystal and along blocks within the crystal (Fig. 5, Table 1), whereas block cores also became sufficiently enriched in Na and H_2O (with corresponding rhombohedral distortion of crystal structure):

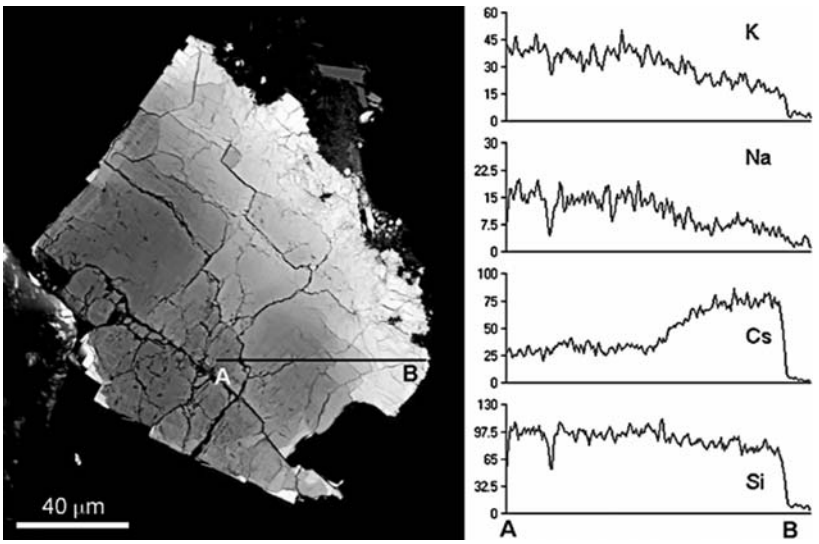

Fig. 4 BSE-image of the phase-1 crystal exchanged by Cs and concentration curves of indicated elements along the line A–B

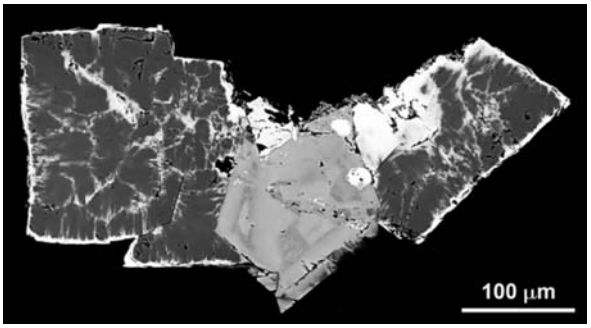

Fig. 5 BSE-image of blocked crystals of phase-1 (growing on sazykinaite-(Y) crystal) treated with solution of RbCl+CsCl

Block rims: $(Cs_{1.24}Rb_{1.03}\ K_{0.36}Na_{0.28}Ca_{0.02})_{\Sigma=2.93}(Ti_{3.70}Nb_{0.22}Fe^{3+}_{0.05})_{\Sigma=3.97}[Si_3O_{15}(OH)_{1.00}]\cdot 4.39\ H_2O$;

Block cores: $(Na_{2.44}K_{1.10})_{\Sigma=3.54}(Ti_{3.76}Nb_{0.23}Fe^{3+}_{0.03})_{\Sigma=4.02}[Si_3O_{15.81}(OH)_{2.19}]\cdot 10.04\ H_2O$.

All investigated crystals are strongly mosaic as one shown in Fig. 5 and the crystal structures of these minerals have not been studied in detail because of a highly diffuse character of their X-ray diffraction patterns obtained from single crystals. In order to check their identity with the synthetic material reported previously (see above), we have performed hydrothermal synthesis experiments.

Synthesis

Pharmacosiderite-related titanosilicate of sodium has been prepared hydrothermally from mixtures of titanyl sulphate, sodium silicate, potassium hydroxide, sodium hydroxide, and deionised water. The synthesis mixture was formed by combining two precursor solutions, one containing titanyl sulphate, deionised water, and another containing sodium silicate hydrate, sodium hydroxide, potassium hydroxide, and deionised water. In solution-1, a total weight of 3.238 g of sodium silicate (18–23% Na_2O, 19–21% SiO_2) was mixed with 15 ml of deionised water, 0.320 g of sodium hydroxide (98% NaOH, Vekton), 0.224 of potassium hydroxide (86% KOH, Vekton) (Sol. 1). This mixture was stirred slightly. Solution-2 was prepared by mixing 0.392 g of titanyl sulphate ($TiOSO_4$, Vekton), and 10 ml of deionised water. After that solution-2 was added to solution-1 by slight stirring. Finally, white synthesis mixture was obtained and then transferred into 50 ml Teflon-lined stainless steel autoclave. Crystallization was carried out at 180°C for 11 days.

After cooling, the content of the autoclave was filtered and washed by deionised water, followed by overnight drying at room temperature in ambient air.

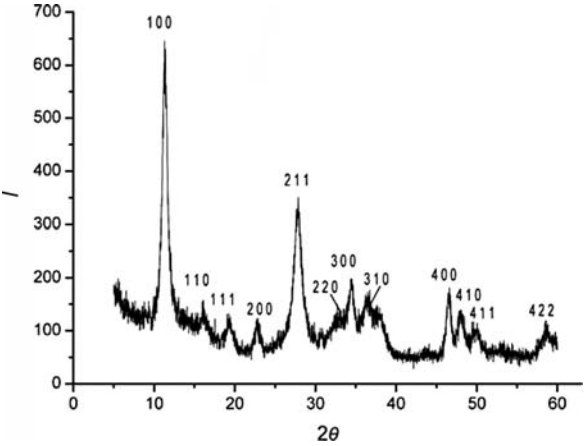

Fig. 6 Powder diffraction pattern of a synthetic K–Na pharmacosiderite-type titanosilicate

X-ray powder diffraction pattern was obtained using DRON-2 powder diffractometer with CuKα-radiation (Fig. 6). The pattern is similar to those reported for pharmacosiderite-type titanosilicates reported previously and the mineral phases reported herein.

Discussion

Since the K content in the minerals under consideration is about 1 and the minerals are highly hydrated, we believe that the K^+ cations occupy the large cavities in the titanosilicate framework. Monovalent cations larger than Na^+ and K^+ easily replace both K^+ and H_2O and the unit cell parameters decrease by 0.04–0.05 Å. Taking into account some deficiency of Ti in the structure (see Table 1), such re-equilibrium seems to be much more reliable.

Divalent copper can be separated from a hydrothermal solution due to its affinity to hydration. However, under ambient conditions, we were unable obtain a Cu-exchanged phase.

Trigonal modifications of the minerals under consideration, obviously, exist under ultraalkaline conditions only. Consequently, decreasing of solutions alkalinity with time causes its transformation into a cubic modification. However, sometimes rhombohedral crystal structure can be stabilized – for example, if hydrothermal solutions are enriched in Sr^{2+} or in the case when Na is pumped into the central part of crystals during substitution of Cs^+ for Na^+, K^+ and H_2O. The last effect blocks structure channels and interrupts phase transition to a cubic modification.

It is important that small (<20 μm diameter) crystals can be fully Cs-exchanged, and we can not decationize them under ambient conditions. It means that the

minerals considered are selective cation-exchangers for Cs and can be used for the removal of ^{137}Cs from radioactive waste solutions.

Acknowledgements We thank Swiss National Foundation (SNF) for financial support in the framework of the SCOPES program. D.V.S. and S.V.K. thank Russian federation Ministry of Science and Education for financial support through the RNP grant (2.1.1.3077) and 'Molecular geochemistry and biogeochemistry' project of the program 'Innovative education environment in a classical University'.

References

Behrens EA, Clearfield A (1997) Titanium silicates, $M_3HTi_4O_4(SiO_4)_3 \cdot 4H_2O$ (M = Na^+, K^+), with three-dimensional tunnel structures for the selective removal of strontium and cesium from wastewater solutions. Micropor Mater 11:65–75

Behrens EA, Poojary DM, Clearfield A (1996) Syntheses, crystal structures, and ion-exchange properties of porous titanosilicates, $HM_3Ti_4O_4(SiO_4)_3 \cdot 4(H_2O)$ (M = H^+, K^+, Cs^+), structural analogues of the mineral pharmacosiderite. Chem Mater 8:1236–1244

Behrens EA, Poojary DM, Clearfield A (1998) Syntheses, X-ray powder structures, and preliminary ion-exchange properties of germanium-substituted titanosilicate pharmacosiderites: $HM_3(AO)_4(BO_4)_3 \cdot 4(H_2O)$ (M = K, Rb, Cs; A = Ti, Ge; B = Si, Ge). Chem Mater 10:959–967

Chapman DM, Roe AL (1990) Synthesis, characterization and crystal chemistry of microporous titanium–silicate materials. Zeolites 10:730–737

Dadachov MS, Harrison WTA (1997) Synthesis and crystal structure of $Na_4[(TiO)_4\ (SiO_4)_3] \cdot 6H_2O$, a rhombohedrally distorted sodium titanium silicate pharmacosiderite analogue. J Solid State Chem 134:409–415

Harrison WTA, Gier TE, Stucky GD (1995) Single-crystal structure of $Cs_3HTi_4O_4(SiO_4)_3 \cdot 4(H_2O)$, a titanosilicate pharmacosiderite analog. Zeolites 5:408–412

Tobermorite 11 Å and Its Synthetic Counterparts: Structural Relationships and Thermal Behaviour

Stefano Merlino, Elena Bonaccorsi, Marco Merlini, Fabio Marchetti and Walter Garra

Introduction

Tobermorite is a hydrated calcium silicate, structurally related to the C–S–H compounds, the main binding product of Portland cement.

The story of tobermorite 11 Å and tobermorite group started in 1880 when Heddle described a hydrate calcium silicate found in three localities of Scotland, two near Tobermory, in Mull island, and one at Dunvegan, in Skye island (Heddle, 1880). Afterwards tobermorite has been discovered in two other Scottish localities and subsequently in various localities all over the world.

The minerals of the tobermorite group (tobermorite 11 Å, sometimes together with the 14 Å phase, plombierite, and in a couple of cases with the 9 Å phase, riversideite) form through the action of hydrothermal fluids mainly at late stages of the evolution of different geological environments.

One of the two most recurrent occurrences is in vugs, fissures or veins in basalts, frequently in association with zeolites and gyrolite. The other frequent genesis is in

Stefano Merlino
Dipartimento di Scienze della Terra, Università di Pisa, Via S. Maria 53, 56126 Pisa, Italy, e-mail: Merlino@dst.unipi.it

Elena Bonaccorsi
Dipartimento di Scienze della Terra, Università di Pisa, Via S. Maria 53, 56126 Pisa, Italy

Marco Merlini
Dipartimento di Scienze della Terra "A. Desio", Università di Milano, Via Botticelli 23, 20133 Milano, Italy

Fabio Marchetti
Dipartimento di Chimica e Chimica Industriale, Università di Pisa, Via Risorgimento 35, 56126 Pisa, Italy

Walter Garra
Dipartimento di Chimica e Chimica Industriale, Università di Pisa, Via Risorgimento 35, 56126 Pisa, Italy

connection with the occurrence of hydrothermal conditions at the contact between limestone and dolerites or granodiorites, or more generally through the action of hydrothermal fluids on calcium silicate minerals. For a recent complete list of the tobermorite occurrences, see Bonaccorsi and Merlino (2005).

As regards clinotobermorite, the last member of the group, it was firstly described as a new mineral from Fuka (Japan) in skarns occurring at the contact between quartz monzonite dykes and limestones (Henmi and Kusachi, 1989, 1992). Later it was found in fissures of the Wessels mine, associated with xonotlite and datolite (Hoffmann and Armbruster, 1997).

Although synthetic tobermorite 11 Å has been prepared from a variety of starting materials, the synthesis procedures most widely used are either hydrothermal reactions of mixtures of CaO or $Ca(OH)_2$ and finely ground quartz or autoclaving amorphous C–S–H preparations of appropriate $CaO:SiO_2$ ratio (more details may be found in Bonaccorsi and Merlino, 2005). More recently, tobermorite-like samples have been obtained through hydrothermal syntheses, for compositions including sodium and lanthanides atoms (Ferreira et al., 2003) as well as sodium and bismuth atoms (Zanardi et al., 2006).

OD Character of Tobermorite Group

The first crystallographic study on tobermorite has been carried by McConnell (1954) on specimens from Ballycraigy, North Ireland. His study indicated pseudo-orthorhombic symmetry, with cell parameters $a = 11.3$, $b = 7.33$, $c = 22.6$ Å. Megaw and Kelsey (1956) sketched a model for the average structure, characterized by layers parallel to (001) built up by a central sheet with CaO_2 stoichiometry, connected on both sides with silicate chains of wollastonite-type. This model has been confirmed by Hamid (1981) who refined it with X-ray diffraction data collected on samples from Zeilberg, Germany. The definition of the real structure (Merlino et al., 1999, 2001) has been made possible on the basis of the following considerations. The various compounds in the tobermorite group present OD character, clearly manifested by their diffraction patterns displaying streaks, diffuse reflections and unusual systematic absences rules. It depends on their peculiar crystal chemistry, in particular on the metrical relationships between the calcium polyhedral module (Fig. 1) with the repeat of 3.65 Å, and the tetrahedral chains with the typical repeat of 7.3 Å. The tetrahedral chain may be connected to the calcium ribbons in two distinct but equivalent positions shifted by 3.65 Å in the **b** direction. Consequently the various compounds in the tobermorite group may be described in terms of OD layers, fully ordered in two dimensions, with **a** and **b** translation vectors ($a = 11.3$, $b = 7.4$ Å, $\gamma = 90°$ in all the tobermorite phases), which – thanks to the ambiguity of the connection between the silicon tetrahedral and calcium polyhedral modules – may stack according to two distinct ways along the **c*** direction, giving rise to a whole family of disordered or ordered sequences (polytypes): in all the possible sequences pairs of adjacent layers are geometrically equivalent, no matter

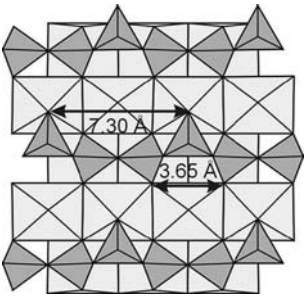

Fig. 1 Connection of wollastonite-like silicate chains and Ca polyhedral layer

whether taken in one member or in different members of the family (principle of OD structures).

The possible members of each family present diffraction patterns characterized by a set of common reflections (those with $k = 2n$ in all the tobermorite compounds), which are always sharp and have the same position in the reciprocal space and the same intensity in all the members of the family: these reflections define the "family cell", subcell in short, and consent to determine the so called "average structure". On the other hand, the various members of each family may be distinguished on the basis of the characteristic reflections, namely those with $k = 2n + 1$, more or less diffuse (sometimes continuous streaks) along **c***; they present different positions and intensities in the different members of the family. Two main polytypes exist in each tobermorite family and OD theory indicates how to single them out. In fact they correspond to the MDO (Maximum Degree of Order) structures, in which not only pairs but also triples (quadruples, ... n-tuples) of OD layers are geometrically equivalent (principle of MDO structures). A detailed treatment of the OD features for the various compounds in the tobermorite group, including the derivation of the MDO polytypes, may be found in the papers devoted to their structure determinations (Merlino et al., 1999, 2000, 2001; Bonaccorsi et al., 2004). Two MDO polytypes occur in natural samples, often intergrown with disordered sequences of layers. The cell parameters and space group symmetry of the various MDO structures are collected in Table 1 of Bonaccorsi and Merlino (2005).

The phases of the tobermorite family are all characterised by the constant presence of the complex module drawn in Fig. 2, built up by calcium polyhedral layers with wollastonite chains grasped to it on both the sides. In few words, the differences

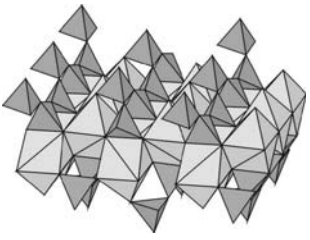

Fig. 2 Calcium polyhedral layer (*light grey*) and wollastonite-like chains (*dark grey*)

among the various phases of the tobermorite group depend on the way in which these complex layers are stacked along **c**, and on the amounts of water molecules and additional "zeolitic" calcium cations, which are located between these layers.

Thermal Behaviour

Tobermorite 14 Å, in which the complex layers are separated by water-rich sheets, looses part of its water molecule if heated to about $80 \div 100$°C. The distance between the complex layers decreases from 14 Å to nearly 11.3 Å.

A further heating up to 300°C induces a further shrinking of the structure, which finally shows an interlayer distance of only 9.3 Å. Not all the samples of tobermorite 11Å show this thermal behaviour, which was called "normal". On the contrary, the heating up to 300°C of some samples results in a dehydrated tobermorite without shrinking of the unit cell. It was initially suggested that the normal tobermorites should show single chains and that the anomalous behaviour should depend on the many linkages between the chains (double chains). Actually, the structural determination of several samples of tobermorite and clinotobermorite (Merlino et al., 1999, 2000, 2001) clearly showed that it was not true: both normal and anomalous samples, in fact, showed double silicate chains. We hypothesize that the different behaviour upon heating can be related to the occurrence of a significant amount of calcium cations within the structural cavities of the normal tobermorite. These cations cannot reduce their coordination from 6 to 2, and hence induce the rearrangement and the shrinking of the structure, until they newly reach a satisfactorily coordination.

In order to understand the dehydration mechanism in tobermorite-like phases, the thermal behaviour of several samples, both natural and synthetic, were investigated through XRPD.

Experimental

In-situ high temperature powder diffraction was used to obtained time-resolved structural data for different samples of natural and synthetic tobermorites. The data were collected at the Beamline Gilda, at the synchrotron ESRF (Grenoble, France). Samples were loaded in thin capillaries (diameter 0.5 mm) and heated by an air blower up to 900°C. In front of the IP a slit selects a vertical slice of the diffracted pattern; the IP can translate horizontally so permitting the collection of time resolved data for studying phase transitions.

The samples we examined were: (1) a natural tobermorite 11 Å from S. Vito di Leguzzano (Vicenza, Italy); (2) a natural tobermorite 11 Å, mixed with ettringite, from Montalto di Castro (Italy); (3) a natural tobermorite 11 Å from Wessels mine (South Africa); (4) a synthetic (Na+Eu)-tobermorite, described in Ferreira et al. (2003) and kindly given us by Prof. Rocha (Aveiro, Portugal). The sample we

studied had chemical formula $Ca_{0.5}Na_2Eu_2[Si_6O_{16}(OH)]\cdot 3H_2O$, and was obtained from the original phase by cation-exchange, namely substituting 1 K^+ by 0.5 Ca^{2+} cations; (5) a Tb–tobermorite, synthesised by one of us (Garra, 2007).

The cell parameters were refined using the GSAS crystallographic suite of programs (Larson and Von Dreele, 1994) with the EXPGUI graphical user interface (Toby, 2001).

Preliminary Results

(1) The sample has chemical formula $Ca_{4.0}(Si_{5.5}Al_{0.5})O_{14.5}(OH)_{2.5}.5H_2O$. Its unit cell parameters were measured from room temperature up to 900°C. In Fig. 3 the ratios between the *a*, *b* and *c* parameters and the corresponding values at room temperature are displayed in function of T.
The changes are obviously anisotropic; however, no sharp discontinuity was observed, and its *c* parameter increased quite smoothly during all the heating run. This sample can be classified as "anomalous" tobermorite.

(2) In the sample from Montalto di Castro, a Ca- and Al-rich tobermorite 11 Å, with chemical composition $Ca_{5.0}Si_{5.0}Al_{1.0}O_{16}(OH)\cdot 5H_2O$, is mixed with ettringite. At nearly 150°C the ettringite peaks disappears from the powder pattern (it becomes amorphous), whereas at nearly 270°C all the tobermorite 11 Å transforms into tobermorite 9 Å (Fig. 4). This behaviour can be classified as "normal".

(3) A more complex pattern is shown by the tobermorite 11 Å from Wessels mine (Fig. 5). At 300°C it does not shrink its interlayer spacing to 9.3 Å, as normal tobermorites do. On the contrary, it preserves its *c* parameter until, at nearly 450°C, it partially transforms into a new phase with interlayer spacing of about

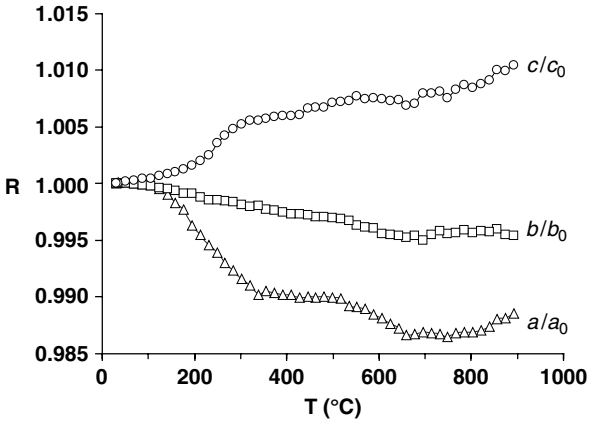

Fig. 3 Changes with temperature of the ratios a/a_0, b/b_0, c/c_0 for an anomalous tobermorite

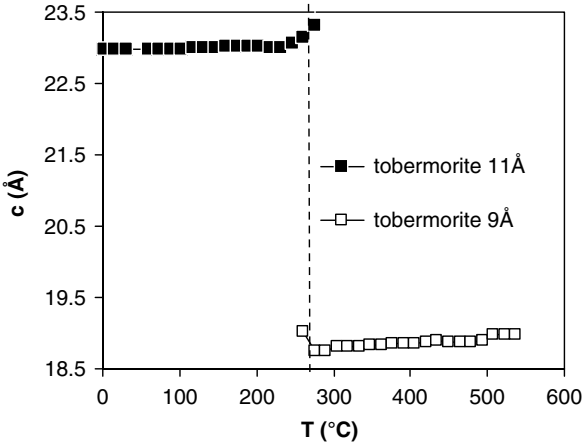

Fig. 4 Normal behaviour of tobermorite 11 Å from Montalto di Castro (Italy): before 300°C it completely transforms into tobermorite 9 Å

10.4 Å. The structure of the high-temperature phase is unknown; however, a structural model has been built taking into account also NMR data and single-crystal X-ray diffraction data.

(4) The synthetic Eu–tobermorite follows a substantially anomalous behaviour. However, a discontinuity in its *c* parameter is observed at nearly 400°C (Fig. 6). Before and after the discontinuity, its *c* parameter changes from 22.49 Å to 22.08 Å.

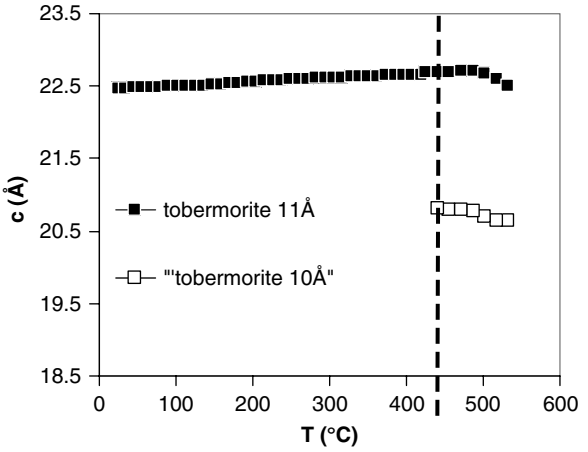

Fig. 5 Coexistence of tobermorite 11 Å and of a new phase with a shorter *c* parameter after heating up to 450°C

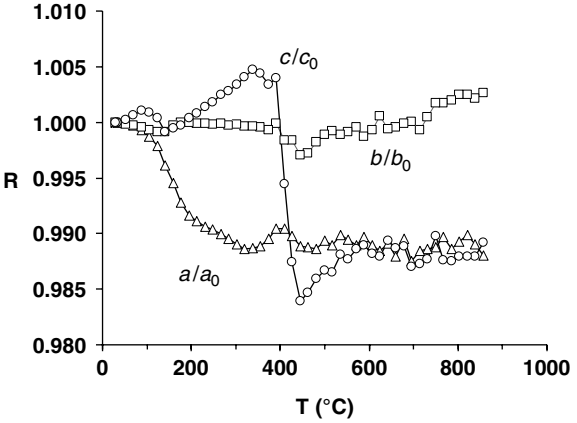

Fig. 6 Changes with temperature of the ratios a/a_0, b/b_0, c/c_0 for the Eu-tobermorite

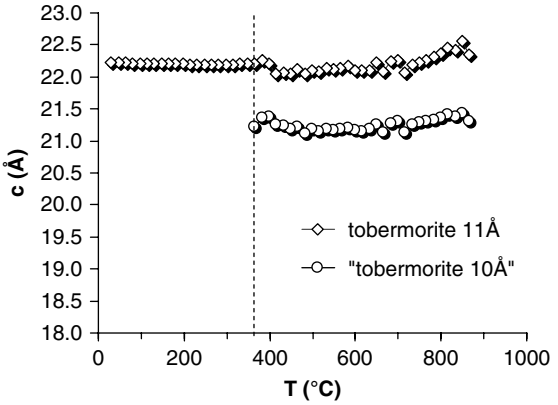

Fig. 7 Coexistence of tobermorite 11 Å and of a new phase with a shorter *c* parameter after heating up to 370°C

(5) The synthetic Tb–tobermorite, $Na_{2.8}Tb_2Si_6O_{15.8}(OH)_{1.2}\cdot 3H_2O]$ (Fig. 7), may be compared with the tobermorite from Wessels mine (Fig. 5). Also the Tb-tobermorite, in fact, does not shrink its *c* parameter before 300°C, but partially transforms into a different phase at higher temperature, with an interlayer spacing of nearly 10.8 Å.

Finally, the heating above 880°C results in a fully dehydrated phases, which corresponds to an apatite-like structure with composition $NaTb_9(SiO_4)_6O_2$.

References

Bonaccorsi E, Merlino S, Kampf AR (2004) The crystal structure of tobermorite 14 Å (plombierite), a C–S–H phase. J Am Ceram Soc 88:505–512

Bonaccorsi E, Merlino S (2005) Modular microporous minerals: cancrinite-davyne group and C–S–H phases. Rev Mineral Geochem 57:241–290

Ferreira A, Ananias D, Carlos LD, Morais CM, Rocha J (2003) Novel microporous lanthanide silicates with tobermorite-like structure. J Am Ceram Soc 125:14573–14579

Garra W (2007) Silicati microporosi di terre rare, con struttura tipo "tobermorite": preparazione e studio strutturale. Dissertation (in Italian), University of Pisa

Hamid SA (1981) The crystal structure of the 11 Å natural tobermorite $Ca_{2.25}[Si_3O_{7.5}(OH)_{1.5}]\cdot 2H_2O$. Z Kristallogr 154:189–198

Heddle MF (1880) Preliminary notice of substances which may prove to be new minerals. Mineral Mag 4:117–123

Henmi C, Kusachi I (1989) Monoclinic tobermorite from Fuka, Bitchu-cho, Okayama prefecture, Japan (in Japanese). J Min Pet Econ Geol 84:374–379 (in Japanese)

Henmi C, Kusachi I (1992) Clinotobermorite $Ca_5Si_6(O,OH)_{18}.5H_2O$, a new mineral from Fuka, Okayama prefecture, Japan. Mineral Mag 56:353–358

Hoffmann C, Armbruster T (1997) Clinotobermorite, $Ca_5[Si_3O_8(OH)]_2.4H_2O$ – $Ca_5[Si_6O_{17}].5H_2O$, a natural C–S–H(I) type cement mineral: determination of the substructure. Z Kristallogr 212:864–873

Larson AC, Von Dreele RB (1994) General structure analysis system (GSAS). Los Alamos National Laboratory Report LAUR 86–748

McConnell JDC (1954) The hydrated calcium silicates riversideite, tobermorite, and plombierite. Mineral Mag 30:293–305

Megaw HD, Kelsey CH (1956) Crystal structure of tobermorite. Nature 177:390–391

Merlino S, Bonaccorsi E, Armbruster T (1999) Tobermorites: their real structure and order-disorder (OD) character. Am Mineral 84:1613–1621

Merlino S, Bonaccorsi E, Armbruster T (2000) The real structures of clinotobermorite and tobermorite 9 Å: OD character, polytypes, and structural relationships. Eur J Mineral 12:411–429

Merlino S, Bonaccorsi E, Armbruster T (2001) The real structure of tobermorite 11 Å: normal and anomalous forms, OD character and polytypic modifications. Eur J Mineral 13:577–590

Toby BH (2001) EXPGUI, a graphical user interface for GSAS. J Appl Crystallogr 34:210–213

Zanardi S, Carati A, Cruciani G, Bellussi G, Millini R, Rizzo C (2006) Synthesis, characterization and crystal structure of new microporous bismuth silicates. Micropor Mesopor Mat 97:34–41

Mixed-Framework Microporous Natural Zirconosilicates

Natalia V. Zubkova and Dmitrii Yu. Pushcharovsky

Among the rare elements in the Earth Crust, Zr is the most abundant one. Zr-minerals mainly occur in alkaline rocks, except zircon $ZrSiO_4$ which was described in various types of rocks. Zirconium silicates revealed widely in nature and their formation is mainly connected with hydrothermal conditions (200–500°C). The most recent statistics of the IMA Commission of New Minerals, Nomenclature and Classification (CNMNC) shows that among Zr containing minerals Zr silicates form the largest class (73 from the total number of 94 mineral species). The crystal structures of Zr-silicates and Ti-silicates in the beginning of 70th contributed the theory of mixed frameworks formed by TO_4 tetrahedra (T=P,Si) and MO_6 octahedra (M=Zr,Ti). Zirconosilicates which mixed frameworks are characterized by general formula $[Zr_mSi_nO_{3m+2n}]^{-2m}$ form the largest group within the family of Zr-silicates (53 min. sp.). Most of these compounds exhibit technologically important alkali-ion mobility and ion exchange properties. The mixed frameworks in the structures of these compounds are characterized by the formation of the almost equivalent bonds Si–O–Si or Si–O–Zr, which determine the stability of such polyhedral configurations. ZrO_6-octahedra in the structures of zirconosilicates with mixed frameworks do not show the tendency to condensation (unlike TiO_6- and NbO_6-octahedra in the structures of titano- and niobosilicates) (Pyatenko et al., 1999). That's why there are no natural zirconosilicates with the ratio Si:Zr$<$1. The lowest Si:Zr ratio occurs in keldyshite, parakeldyshite and khibinskite (Si:Zr = 2) and some other related zirconosilicates in which structures isolated ZrO_6-octahedra are connected with Si_2O_7 pyrogroups (Pekov and Chukanov, 2005). The configuration of silicate complexes in the structures of zirconosilicates with mixed frameworks may be different. Silicate pyrogroups, 3-, 4- and 6-membered tetrahedral rings, spiral chains, bands and corrugated sheets were identified as the elements of the mixed frameworks in the

Natalia V. Zubkova
Geology Department, Moscow State University, 119992 Moscow, Russia, e-mail: Nata_Zubkova@rambler.ru

Dmitrii Yu. Pushcharovsky
Geology Department, Moscow State University, 119992 Moscow, Russia

structures of natural zirconosilicates. All known so far natural zirconosilicates with different types of silicate complexes are listed in the Table 1.

It is worthy to note that in some mineral species, namely zircon, $ZrSiO_4$, gittinsite, $CaZrSi_2O_7$, garnet-like kimzeyite, $Ca_3Zr_2(Al_2Si)O_{12}$, etc. Zr-polyhedra belong to the cationic component of the structure.

New data on crystal structures of some of natural zirconosilicates with mixed frameworks characterized by general formula $[Zr_mSi_nO_{3m+2n}]^{-2m}$ are listed here. These data give the new insight on the crystal chemistry and structure/properties relationship of such compounds.

Table 1 Natural zirconosilicates with mixed frameworks

Mineral name	Chemical formula	Reference	Silicate complex
Khibinskite	$K_2ZrSi_2O_7$	Khomyakov et al. (1974)	$[Si_2O_7]$-pyrogroups
Parakeldyshite	$Na_2ZrSi_2O_7$	Pekov et al. (2007)	
Keldyshite	$(Na,H)_2ZrSi_2O_7 \cdot nH_2O$	Khalilov et al. (1978)	
Catapleiite	$Na_2ZrSi_3O_9 \cdot 2H_2O$	Ilyushin et al. (1981b); Brunowsky (1936)	3-membered Si-rings
Calcium catapleiite	$CaZrSi_3O_9 \cdot 2H_2O$	Merlino et al. (2004)	
Wadeite	$K_2ZrSi_3O_9$	Blinov et al. (1977)	3-membered Si-rings
Bazirite	$BaZrSi_3O_9$	Hawthorne (1987)	
IMA 2003-019*	$Na_6\ Sr_{12}\ Ba_2\ Zr_{13}\ Si_{39}\ B_4\ O_{123}\ (OH)_6 \cdot 20H_2O$	Burke and Ferraris (2004)	Presumably related to the benitoite group
Bobtraillite	$Na_{15}\ Sr_{12}\ Zr_{14}\ Si_{42}\ B_6O_{138}\ (OH)_6 \cdot 12H_2O$	McDonald and Chao (2005)	Two types of 3-membered (Si_3O_9) rings and additional 3-membered $[Si_2BO_7(OH)_2]$ ring comprise a two-dimensional, giant pinwheel motif along [001].
Kostylevite	$K_4Zr_2Si_6O_{18} \cdot 2H_2O$	Ilyushin et al. (1981a)	6-membered Si-rings
Petarasite	$Na_5\ Zr_2\ Si_6O_{18}\ (Cl,OH) \cdot 2H_2O$	Ghose et al. (1980)	6-membered elliptical Si-rings
Lovozerite group			
Kapustinite	$Na_{5.5}\ Mn_{0.25}\ ZrSi_6\ O_{16}\ (OH)_2$	Yamnova et al. (2004)	
Litvinskite	$Na_{3-x}\ (\square,Na,Mn)ZrSi_6\ O_{12}\ (OH,O)_6\ nH_2O$	Yamnova et al. (2001)	Pseudotetragonal 6-membered rings
Zirsinalite	$Na_6\ (Ca,Mn,Fe^{2+})\ ZrSi_6O_{18}$	Pudovkina et al. (1980)	
Lovozerite	$Na_{2-x}Ca(Zr,Ti)\ Si_6(O,OH)_{18}$	Yamnova et al. (2001)	

Table 1 (continued)

Mineral name	Chemical formula	Reference	Silicate complex
Eudialyte group (20 mineral species)	$(Na,H_2O)_{12}N_3$ Ca_3 MI_3MII_{3-x} $(Zr,Ti)_3MIIISi_{25}$ O_{73} O_3X_2, $N = Na, Ca, Sr, REE, H_2O$, K; *MI* = Ca,Mn,Fe; *MII* = Fe,Mn,Na; *MIII* = Si,Nb,W; *X*= Cl,OH,F,CO_3	Johnsen and Grice (1999); Johnsen et al. (2003) (review for the whole group)	3- and 9-membered Si-rings; additional Si-tetrahedron can occupy center of one 9-membered ring (center of the second 9-membered ring is occupied by M^{III}-octahedron)
Sazykinaite (Y)	$Na_5YZrSi_6O_{18}{\cdot}6H_2O$	Rastsvetaeva and Khomyakov (1992)	Helical chains $[Si_3O_9]$ with 3 tetrahedra in period
Hilairite	$Na_2ZrSi_3O_9{\cdot}3H_2O$	Ilyushin et al. (1981c)	
Calciohilairite	$CaZrSi_3O_9{\cdot}3H_2O$	Pushcharovsky et al. (2002)	
Komkovite	$BaZrSi_3O_9{\cdot}3H_2O$	Sokolova et al. (1991)	
Umbite	$K_2ZrSi_3O_9{\cdot}H_2O$	Ilyushin (1993)	Wollastonite-type chains $[Si_3O_9]$
Paraumbite*	$K_3HZr_2Si_6O_{18}{\cdot}nH_2O$ (n$\sim$7)	Khomyakov et al. (1983)	
Vlasovite	$Na_2ZrSi_4O_{11}$	Gobechiya et al. (2003)	Infinite bands with 4-membered silicate rings in section
Elpidite	$Na_2ZrSi_6O_{15}{\cdot}3H_2O$	Cannillo et al. (1973)	Silicate double chains formed by two wollastonite-like chains
Georgechaoite	$NaKZrSi_3O_9{\cdot}2H_2O$	Ghose and Thakur (1985)	Zigzag silicate chains with 6 tetrahedra in period
Gaidonnayite	$Na_2ZrSi_3O_9{\cdot}2H_2O$	Chao (1985)	
Terskite	$Na_4ZrSi_6O_{16}{\cdot}2H_2O$	Pudovkina and Chernitsova (1991)	Branched $[H_4Si_6O_{18}]_\infty$-chains with 4 tetrahedra in period
Natrolemoynite	$Na_4Zr_2Si_{10}O_{26}{\cdot}9H_2O$	McDonald and Chao (2001)	3-layered silicate sheets formed by altered 6- and 10-membered Si-rings
Lemoynite	$(Na,K)_2CaZr_2Si_{10}O_{26}{\cdot}$ $5\text{-}6H_2O$	Le Page and Perrault (1976)	
Tumchaite	$Na_2(Zr,Sn)Si_4O_{11}{\cdot}2H_2O$	Subbotin et al. (2000)	$[Si_4O_{11}]$-sheets
Armstrongite	$CaZrSi_6O_{15}{\cdot}2.5H_2O$	Kabalov et al. (2000)	Corrugated silicate sheets $[Si_6O_{15}]$
Dalyite	$K_2ZrSi_6O_{15}$	Fleet (1965)	Corrugated silicate sheets $[Si_6O_{15}]$ formed by 4-, 6- and 8-membered rings.
Zeravshanite	$Cs_4Na_2Zr_3Si_{18}O_{45}{\cdot}2H_2O$	Uvarova et al. (2004)	$[Si_{18}O_{45}]^{18-}$ sheets with five- and eight-membered silicate rings
Loudounite*	$NaCa_5$ Zr_4 $Si_{16}O_{40}$ $(OH)_{11}{\cdot}$ $8H_2O$	Dunn and Newbury (1983)	

*Structure unknown

Mixed Framework in the Structure of Parakeldyshite – Zirconosilicate with $[Si_2O_7]$ Pyrogroups

Parakeldyshite, $Na_2Zr(Si_2O_7)$, was discovered in Lovozero and Khibiny alkaline complexes (Kola Peninsula, Russia) (Khomyakov, 1977) as Na-analogue of keldyshite $(Na,H)_2ZrSi_2O_7$ (Gerasimovsky, 1962). Crystal structure of parakeldyshite was first carried out in 1970 and refined up to $R = 0.145$ (Voronkov et al., 1970). It is very close to the structures of triclinic keldyshite (Khalilov et al., 1978) and monoclinic khibinskite $K_2ZrSi_2O_7$ (Khomyakov et al., 1974). In 2007 crystal structure of parakeldyshite was re-refined up to $R = 0.0153$ (Pekov et al., 2007) and its structural model offered in 1970 was confirmed. Crystal structure of parakeldyshite is based on a framework formed by $[Si_2O_7]$ diorthogroups and isolated Zr-octahedra. Large cavities of the framework are occupied by Na-cations which are localized in two crystallographically nonequivalent positions. One of these positions is fully occupied by Na, the second Na atom is characterized by partial occupancy factor and two additional Na atoms with small occupancies were localized near Na(2)-position.

Heteropolyhedral framework in parakeldyshite and keldyshite is characterized by a high degree of deformation. This is mainly connected with the different size of the cavities of framework and the cations localized inside them (Sizova et al., 1974). Sizova et al. (1974) described ideal trigonal framework of this type and assume that the value of framework deformation should be decreased when larger cations occupy the cavities. This assumption is confirmed by the structure of monoclinic khibinskite (sp. gr. $C2/m$) (Khomyakov et al., 1974).

Calciohilairite and Calcium Catapleiite: Zirconosilicates with $[Si_3O_9]$ Tetrahedral Complexes

Two zirconosilicates described here contain in there structures $[Si_3O_9]$ tetrahedral complexes which can be considered as main structural units. These minerals are calciohilairite, $CaZrSi_3O_9 \cdot 3H_2O$, and calcium catapleiite, $CaZrSi_3O_9 \cdot 2H_2O$. The only difference in chemical composition of these minerals is connected with one additional water molecule in calciohilairite but their structures differ significantly.

Calciohilairite is a member of hilairite, $NaZrSi_3O_9 \cdot 3H_2O$, group which includes sazykinaite-(Y), $Na_5YZrSi_6O_{18} \cdot 6H_2O$, pyatenkoite-(Y), $Na_5YTiSi_6O_{18} \cdot 6H_2O$, komkovite, $BaZrSi_3O_9 \cdot 3H_2O$. This mineral was discovered in hydrothermalites of alkaline granites from the Golden Horn batholith (Washington, USA) (Boggs, 1988) and in the derivatives of the Mont-Saint-Hilaire and Saint-Amable agpaitic massifs (Quebec, Canada) (Horvath et al., 1998). In 2000 a new occurrence of calciohilairite was found in the endocontact zone of the Lovozero alkaline massive (Kola Peninsula) (Pekov, 2000). Crystal structure analysis of calciohilairite (sp. gr. $R32$, a = 10.498(2), c = 7.975(2) Å; Z = 3; $R = 0.037$) confirmed the formula of this cation-deficient mineral – $(Ca,Na)_{0.67}ZrSi_3O_9[H_3O,H_2O]_3$. The structure of calciohilairite

is characterized by a twice decrease in the size of the unit cell compared with the cells of other representatives of hilairite group with the space group *R*32 being retained. In addition the structure of this mineral has a position (occupied by H_3O^+ cations and water molecules) which was not found in other representatives of hilairite group. At the same time the configuration of the zirconium–silicon–oxygen mixed framework remains unchanged: it consists of helical chains $[Si_3O_9]^{\infty}$ linked by Zr-octahedra. The cavities of the framework are occupied by (Ca,Na)-cations, oxonium and water molecules. The constitution and possible mechanism of the formation of cation-deficient calciohilairite can help to elucidate the nature of partially decationized varieties of many zeolite-like minerals which are widespread in hydrothermally altered alkaline rocks and their derivatives. The general scheme of isomorphism which leads from hilairite to cation-deficient calciohilairite can be presented by the following way: $2Na^+ + H_2O \rightarrow 0.5Ca^{2+} + 1.5\square + (H_3O)^+$(Pushcharovskii et al., 2002). This scheme can explain one of the mechanisms of "gentle" leaching of sodium from zeolite-like compounds.

Calcium catapleiite – calcium counterpart of catapleiite, $Na_2ZrSi_3O_9{\cdot}2H_2O$, is a rare mineral found in hydrothermal assemblages associated with alkaline complexes. The crystal structure of catapleiite was described by Brunowsky (1936) in the space group $P6_3/mmc$, $a = 7.40$, $c = 10.05$ Å. Later the structure of catapleiite has been determined and refined in monoclinic symmetry by Chao et al. (1973) (sp.gr. *I*2/*c*) and by Ilyushin et al. (1981b) (sp.gr. *B*2/*b*). Monoclinic structure and the hexagonal one are essentially the same: they contain a mixed framework built up of $[ZrO_6]$ octahedra and $[Si_3O_9]$ rings of tetrahedra; however the sites occupied by Na atoms and H_2O molecules are exchanged in the monoclinic model with respect to the hexagonal one. Calcium catapleiite, $CaZrSi_3O_9{\cdot}2H_2O$ is considered as an end-member of a solid-solution series with catapleiite, $Na_2ZrSi_3O_9{\cdot}2H_2O$, and was originally described as presenting "the crystal lattice of catapleiite" (Portnov, 1964) with hexagonal space group $P6_3/mmc$. However structural investigations carried out for catapleiite later (Chao et al., 1973; Ilyushin et al., 1981) did not confirm that indication and suggest that the claimed hexagonal symmetry of catapleiite could be not correct (Pyatenko et al., 1999). In 2004 structural determination of calcium catapleiite from the type locality (Burpala massif, northern Baikal Region, Siberia, Russia) (Merlino et al., 2004) showed that this mineral is actually orthorhombic, space group *Pbnn*, $a = 7.378(1)$, $b = 12.779(1)$, $c = 10.096(1)$ Å ($R = 0.0528$). The crystals display three-fold twinning ("Drilling") about the *c* axis, with the three individuals rotated by 120° one from the other. In common with catapleiite, the most specific feature of calcium catapleiite is a mixed framework formed by $[ZrO_6]$ octahedra and 3-membered $[Si_3O_9]$ silicate rings. The Ca cations and H_2O molecules are located in tunnels of the framework. The complex of tetrahedra which has the form of a 3-membered ring is quite rare in minerals. The relatively low stability of 3-membered silicate rings is dependent on the large deviations of the Si–O–Si angles ($\approx 130°$) from 147°, which is typical of a ring of tetrahedra with low energy (Chakoumakos et al., 1981).

Vlasovite – Zirconosilicate with Silicate Bands

Vlasovite, $Na_2ZrSi_4O_{11}$, is a typical zirconium concentrator in a number of alkaline complexes. It was described as a new mineral from albitized eudialyte-microcline fenites and pegmatoid nepheline syenites of the exocontact zone of the Lovozero massif on the Kola Peninsula in 1961 (Tikhonenkova and Kazakova, 1961). The crystal structure of vlasovite was determined by the photographic method (sp.gr. *C*2/*c*) in 1961 for a single crystal from the Lovozero massif (Voronkov and Pyatenko, 1961) and later was refined for the same specimen in the same space group (Voronkov et al., 1974) up to relatively high values of R = 10.1%. In 2003 the structure of vlasovite for a specimen from the Kipawa alkaline complex in Quebec was refined by Gobechiya et al. in the frames of monoclinic symmetry (sp. gr. *C*2/*c*; a = 11.063(1), b = 10.15(1), c = 8.60(1) Å, $\beta = 100.3(1)^\circ$) to R = 0.053. Structural elements of vlasovite are infinite chains of Si tetrahedra oriented along the [101] direction. The tetrahedra form 4-membered centrosymmetric rings, which are linked through isolated Zr-octahedra. Each Zr octahedron is connected with four chains. The cavities of the mixed zeolite-like framework accommodate Na atoms in 2 nonequivalent positions. Both Na-positions are sodium-deficient (only 1.72 Na atoms pfu instead of 2). This is inconsistent with electron microprobe analysis which showed that the composition of the mineral agrees well with the ideal formula. This phenomenon was already predicted in earlier works. The inconsistency of these data suggests that, in the course of the X-ray diffraction experiment, the mineral underwent some changes in composition and structure. Analysis of the IR spectra of vlasovite recorded before and after the experiment when the sample was exposed to X-ray radiation demonstrates that substantial changes take place in the vlasovite structure under irradiation.

These changes indicate the appearance of numerous defects in the framework and the hydration of structurally distorted vlasovite by absorption of atmospheric water and water molecules are located in zeolite-like channels that accommodate Na. Na deficit in both Na-positions can be explained within alternative models. First, Na atoms migrate inside the channels, which results in a decrease in the Na(1) and Na(2) site occupancies. Second, a portion of Na atoms leaves the crystal – the deficit of positive charge can be compensated either by a minor substitution of OH groups for O atoms or due to the appearance of anionic vacancies in the framework. (Gobechiya et al., 2003) consider no more than possible displacements of Na atoms in the channels or even partial removal of Na from the crystal, as is the case, for example, in the minerals of lovozerite group, which undergo decationization and hydration in air (Yamnova et al., 2001).

Taking into account possible radiation damage of the crystal in the course of the X-ray diffraction allows a more critical treatment of the results of structural determinations of some unstable compounds, for example, high-alkaline zeolite-like silicates.

Cation-Exchanged Properties of Zirconosilicates with Mixed Frameworks

All described above minerals and other representatives of their mineralogical groups can be considered as microporous heterosilicate minerals with pronounced zeolite properties (Chukanov and Pekov, 2004) as well as almost all zirconosilicates with heteropolyhedral frameworks. Pekov et al. (2005), tested ion-exchange properties under room conditions of nine natural zirconosilicates from pegmatites of five agpaitic complexes. The studied material includes catapleiite, lovozerite, hilairite and sazykinaite-(Y) from Khibiny (Kola Peninsula, Russia), parakeldyshite and litvinskite from Lovozero (Kola Peninsula), elpidite from Lovozero and Khan-Bogdo (Mongolia), petarasite from Mont Saint-Hilaire (Quebec) and vlasovite from Kipawa (Quebec). Their grains (0.3–0.8 mm size) were placed into 1*M* aqueous solutions of NaCl, KCl, RbCl, CsCl, $CaCl_2$, $SrCl_2$, $BaCl_2$ and $Pb(NO_3)_2$ for 4 months. Crystals after the experiments were examined by electron microprobe on polish sections. Elpidite from Lovozero, catapleiite, lovozerite, petarasite, parakeldyshite and vlasovite show no changes in the chemical composition. Litvinskite slightly absorbs Cs (0.3–0.6 wt.% Cs_2O) and elpidite from Khan-Bogdo, hilairite and sazykinaite-(Y) accumulate K displacing Na. In hilairite, K is distributed evenly in all space of a crystal (K_2O content increases from 0.7–1.1 wt.% to 7.4–8.4% when Na_2O content decreases from 8–9 wt.% to 4.9– 4.1%). In sazykinaite-(Y), K is concentrated in boarder parts of a crystal and in space along margins between concentric growing zones (up to 8.4 wt.% K_2O when its initial content was 3.2–3.4%): thus, secondary concentric chemical zoning appears. In elpidite from Khan-Bogdo, K is concentrated in thin zones along micro-cracks (up to 3.4 wt.% K_2O when its initial content was 0.1%) in all space of a grain.

Recently the ion exchanged properties of hilairite and catapleiite were carefully analyzed at elevated temperatures. Experiments on cation exchange were performed for catapleiite and hilairite found in hydrothermally altered agpaitic pegmatites from the Khibiny alkaline massif (the Kola Peninsula, Russia) (Zubkova et al., 2007). Most interesting results were obtained in ion-exchange experiments in KCl solutions. Mineral grains with sizes of 0.3–0.8 mm were soaked in a 1 N solution of this salt at 90°C under atmospheric pressure for 12 h. K content in catapleiite increased throughout the bulk of the grains from 0.02 to 5.5–7.0 wt% of K_2O, the Na content decreased, and the Ca content remained unchanged. In hilairite the K content increased to from 0.66 to 15.4–18.0 wt% of K_2O, and Na virtually completely disappeared.

Crystal structure determination of the potassium-exchanged forms of catapleiite and hilairite (Zubkova et al., 2007) prepared under the above-described conditions showed that parameters of the hexagonal unit-cell determined for the K-exchanged form of catapleiite (a = 7.344(4), c = 9.984(5) Å) are very similar to those reported by Brunowsky (1936) for catapleiite. The systematic absences in the X-ray diffraction data set indicated sp. gr. $P6_3/mmc$, which has been also revealed for catapleiite in the first study (Brunowsky, 1936). The trigonal unit-cell parameters of

the K-exchanged form of hilairite (a = 10.678(4), c = 7.944(2) Å; sp. gr. $R32$) are very similar to those of calciohilairite. The refinement gave the structural formulas: $(K_{0.49}Ca_{0.42}Na_{0.26})ZrSi_3O_9{\cdot}2[(H_2O)_{0.80}(H_3O)_{0.20}]$ and $K_{0.51}ZrSi_3O_9{\cdot}3[(H_2O)_{0.50}K_{0.27}(H_3O)_{0.23}]$ for K-exchanged forms of catapleiite and hilairite, respectively. Both crystal structures retain the mixed framework of "parent" minerals. At the same time K-cations occupy different positions in these minerals. In the structure of the K-exchanged form of catapleiite, the arrangement of the extraframework cations (K,Ca and Na) randomly replacing each other in the same position and H_2O molecules is similar to the arrangement of the cations and H_2O molecules in the monoclinic modification of catapleiite (Ilyushin et al., 1981) and orthorhombic calcium catapleiite (Merlino et al., 2004). In the structure of the K-exchanged form of hilairite K-cations partially occupy (by ~50%) the $A(1)$ position (in calciohilairite $A(1)$ position occupied by Ca and Na cations). The $A(2)$ position, which has been found for the first time in the calciohilairite structure (Pushcharovskii et al., 2002), where it is occupied by H_3O^+ cations and water molecules, is present in the structure of the K-exchanged form of hilairite: this position is randomly occupied by K and H_3O^+ cations and water molecules in a ratio of 1:1:2.

Armstrongite and Tumchaite: Zr-Silicates with Silicate Corrugated Sheets

The mixed frameworks formed by corrugated silicate sheets connected by Zr-octahedra were found in the crystal structures of microporous armstrongite, $CaZr[Si_6O_{15}]x2.5H_2O$, and tumchaite, $Na_2(Zr_{0.8}Sn_{0.2})[Si_4O_{11}]{\cdot}2H_2O$.

Armstrongite was discovered in a granite pegmatite and alkaline granites in Mongolia. Crystals of armstrongite are characterized by microtwinning parallel to (001). Kashaev and Sapozhnikov (1978) refined the crystal structure to $R = 0.13$ from a twinned crystal. In 2000 the structure of armstrongite was refined with the use of Rietveld method (sp. gr. $C2$, $a = 14.0184(2)$, $b = 14.1326(2)$, $c = 7.8400(1)$ Å, $\beta = 109.396(1)^o$, Z = 4, $R_{wp} = 2.75\%$) (Kabalov et al., 2000): this work confirmed the first model but revealed two new sites for H_2O molecules on the 2-fold axis in the voids of the zeolite like framework. The most specific feature of armstrongite structure is heterogeneous octahedra-tetrahedral framework $(ZrSi_6O_{15})$ built by corrugated silicate sheets (001) connected by ZrO_6 octahedra. Topologically unbranched single layers of armstrongite have a close relationship with those of dalyite, synthetic $K_3\{Nd[Si_6O_{15}]\}$, $NaH_2\{Nd[Si_6O_{15}]\}xnH_2O$ and sazhinite, $HNa_2Ce[Si_6O_{15}]xnH_2O$ which can be described as an alteration of the xonotlite-like bands formed by 8-membered rings with the bands formed by 6- and 4-membered rings. All these structures comprise the silicate sheets which can be considered as a result of condensation of wollastonite-like chains. Due to the different symmetry the REE silicates are characterized by the different mode of stacking between silicate sheets and REE octahedra as compared with armstrongite. Mixed framework in armstrongite also exhibits the similarity with that in elpidite. Their difference is

attributed with different topology of heterogeneous sheets (010) in both structures. Ca polyhedra and water molecules are found in the voids of zeolite-like framework of armstrongite.

Zr-silicate tumchaite $Na_2(Zr,Sn)Si_4O_{11}\cdot 2H_2O$ (space group $P2_1/c$, $a = 9.144(4)$, $b = 8.818(3)$, $c = 7.537(3)$ Å, $\beta = 113.22(3)^\circ$, $Z = 2$) was discovered in carbonatites of the Vuoriyarvi alkali-ultrabasic massif, Murmansk Region. Tumchaite is isotypic with penkvilksite-1*M*, $Na_4Ti_2(Si_8O_{22})\cdot(H_2O)_4$, and is chemically related to vlasovite. Similarly to both polytypes 1*M* and 2*O* of penkvilksite, $Na_2TiSi_4O_{11}\cdot 2H_2O$ (Merlino et al., 1994; Liu et al., 1999), the most specific structural feature of tumchaite is the silicate sheet $[Si_4O_{11}]$ parallel (100), which can be considered as a result of condensation of the tetrahedral spiral chains running along [010] with six tetrahedra in the repeat unit. Adjacent spirals are oriented in alternate clockwise and counterclockwise way. The silicate sheets revealed in penkvilksite and in tumchaite extend the ideas about polymorphism of tetrahedral complexes $[Si_4O_{11}]$, which were reported before as bands (amphiboles, vlasovite) or as framework (neptunite). The tetrahedral silicate sheets are connected by cationic octahedra with a disordered distribution of Zr and Sn (Zr/Sn ratio = 4). Water molecules and Na^+ cations are localized in the wide cavities and tunnels of the mixed heteropolyhedral framework.

Structural similarity between tumchaite and penkvilksite attracts the attention because of a very limited isostructurality among Zr- and Ti-containing mineralogical analogues due to the different chemical nature of Zr and Ti. Other examples of Zr- and Ti-containing isostructural minerals are: wadeite – natural Ti-wadeite; bazirite – benitoite; dalyite – davanite; eudialyte – alluaivite; zircophyllite – astrophyllite.

Most of zirconosilicates described here belong to microporous mineral phases with diameter of their pores and tunnels 0.25–2 nm. Almost all of them can be considered as prototypes of new materials with very important ion-exchange, sorption and catalytic properties. Heteropolyhedral compounds like zirconsilicates have been reported in a wide number of distinct structural types and their detailed mineralogical, structural, chemical and crystal-chemical studies obviously open the new perspectives in physics and chemistry of minerals.

Acknowledgements This study was supported by Russian Foundation for Basic Research (project no. 06-05-64024-a); a joint grant from the Russian Foundation for Basic Research and the Austrian Exchange Service, Agency for International Cooperation in Education and Research (grant no. 06-05-90626-BNTS_a); the Federal Program for the Support of Prominent Scientists and Leading Scientific Schools (project nos. MK-4479.2006.5, and NSh-4964.2006.5).

References

Blinov VA, Shumyatskaya NG, Voronkov AA, Ilyukhin VV, Belov NV (1977) Refinement of the crystal structure of wadeite $K_2Zr(Si_3O_9)$ and its relationship to kindred structural types. Sov Phys Crystallogr 22:31–35

Boggs RC (1988) Calciohilairite: $CaZrSi_3O_9{\cdot}3H_2O$, the calcium analogue of hilairite from the golden horn batholith, northern Cascades, Washington. Am Mineral 73:1191–1194

Brunowsky B (1936) Die Struktur des Katapleits ($Na_2ZrSi_3O_9{\cdot}2H_2O$). Acta phys chim URSS 5:863–892

Burke EAJ, Ferraris G (2004) New minerals approved in 2003 and nomenclature modifications approved in 2003 by the commission on new minerals and mineral names, international mineralogical association. Can Mineral 42:905–913

Cannillo E, Rossi G, Ungaretti L (1973) The crystal structure of elpidite. Am Mineral 58:106–109

Chakoumakos BC, Hill RJ, Gibbs GV (1981) A molecular orbital study of rings in silicates and siloxanes. Am Mineral 66:1237–1249

Chao GY (1985) The crystal structure of gaidonnayite $Na_2ZrSi_3O_9(H_2O)_2$. Can Mineral 23:11–15

Chao GY, Rowland JR, Chen TT (1973) The crystal structure of catapleiite. Abstracts with Programs – Geol Soc Am 5 (7):572

Chukanov NV, Pekov IV (2004) Heterosilicates with tetrahedral-octahedral frameworks: mineralogical and crystal-chemical aspects. Pre-prints of the international symposium "Micro-and mesoporous mineral phases" 9–13

Dunn PJ, Newbury D (1983) Loudounite, a new zirconium silicate from Virginia. Can Mineral 21:37–40

Fleet SG (1965) The crystal structure of dalyite. Zeitschrift fuer Kristallographie 121:349–368

Gerasimovsky VI (1962) Keldyshite, a new mineral. Dokl Akad Nauk USSR Earth Sci 142:123–125

Ghose S, Thakur P (1985) The crystal structure of georgechaoite $NaKZrSi_3O_9{\cdot}2H_2O$. Can Mineral 23:5–10

Ghose S, Wan C, Chao GY (1980) Petarasite, $Na_5Zr_2Si_6O_{18}(Cl,OH).2H_2O$, a zeolite-type zirconosilicate. Can Mineral 18:503–509

Gobechiya ER, Pekov IV, Pushcharovsky DYu, Ferraris G, Gula A, Zubkova NV, Chukanov NV (2003) New data on vlasovite: refinement of the crystal structure and the radiation damage of the crystal during the X-ray diffraction experiment. Crystallogr Rep 48:750–754

Hawthorne FC (1987) The crystal chemistry of the benitoite group minerals and structural relations in (Si_3O_9) ring structures. Neues Jb Miner Monat 16–30

Horvath L, Pfenninger-Horvath E, Gault RA, Tarasoff P (1998) Mineralogy of the Saint-Amable Sill, Varennes and Saint-Amable, Quebec. Mineral Rec 29:83–118

Ilyushin GD (1993) New data on crystal structure of umbite $K_2ZrSi_3O_9{\cdot}H_2O$. Inorg Mater 27:1128–1133

Ilyushin GD, Khomyakov AP, Shumyatskaya NG, Voronkov AA, Nevsky NN, Ilyukhin VV, Belov NV (1981a) Crystal structure of a new natural zirconium silicate $K_4Zr_2Si_6O_{18}{\cdot}2H_2O$. Sov Phys Dokl 26:118–120

Ilyushin GD, Voronkov AA, Ilyukhin VV, Nevsky NN, Belov NV (1981b) Crystal structure of natural monoclinic catapleiite $Na_2ZrSi_3O_9{\cdot}2H_2O$. Sov Phys Dokl 26:808–810

Ilyushin GD, Voronkov AA, Nevskii NN, Ilyukhin VV, Belov NV (1981c) Crystal structure of hilairite $Na_2ZrSi_3O_9$ $(H_2O)_3$. Sov Phys Dokl 26:916–917

Johnsen O, Ferraris G, Gault RA, Grice JD, Kampf AR, Pekov IV (2003) The nomenclature of eudialyte-group minerals. Can Mineral 41:785–794

Johnsen O, Grice JD (1999) The crystal chemistry of the eudialyte group. Can Mineral 37:865–891

Kabalov YuK, Zubkova NV, Pushcharovsky DYu, Schneider J, Sapozhnikov AN (2000) Powder Rietveld refinement of armstrongite, $CaZr[Si_6O_{15}]x3H_2O$. Z Kristallogr 215:757–761

Kashaev AA, Sapozhnikov AN (1978) Crystal structure of armstrongite. Sov Phys Crystallogr 23:539–542

Khalilov AD, Khomyakov AP, Makhmudov SA (1978) Crystal structure of keldishite $NaZr(Si_2O_6OH)$. Sov Phys Dokl 23:8–10

Khomyakov AP (1977) Parakeldyshite, a new mineral. Dokl Akad Nauk SSSR 237:703–705 (in Russian)

Khomyakov AP, Voronkov AA, Kobyashev YuS, Polezhaeva LI (1983) Umbite and paraumbite, new potassium zirconosilicates from the Khibiny alkalic massif. Zapiski VMO 112:461–469 (in Russian)

Khomyakov AP, Voronkov AA, Lebedeva SI, Bykov VN, Yurkina KV (1974) Khibinskite, a new mineral. Zapiski VMO 103:110–116 (in Russian)

Le Page Y, Perrault G (1976) Structure cristalline de la lemoynite, $(Na,K)_2CaZr_2Si_{10}O_{26}\cdot 5\text{-}6H_2O$. Can Mineral 14:132–138

Liu Yu, Du H, Xu Y, Ding H, Pang W, Yue Y (1999) Synthesis and characterization of a novel microporous titanisilicate with a structure of penkvilksite-1*M*'. Micropor Mesopor Mat 28: 511–517

McDonald AM, Chao GY (2001) Natrolemoynite, a new hydrated sodiium zirconosilicate from Mont Saint-Hilaire, Quebec: Description and structure determination. Can Mineral 39: 1295–1306

McDonald AM, Chao GY (2005) Bobtraillite, $(Na,Ca)_{13}Sr_{11}(Zr,Y,Nb)_{14}Si_{42}B_6O_{132}(OH)_{12}\cdot 12H_2O$, a new mineral species from Mont Saint-Hilaire, Quebec: description, structure determination and relationship to benitoite and wadeite. Can Mineral 43:747–758

Merlino S, Pasero M, Artioli G, Khomyakov AP (1994) Penkvilksite, a new kind of silicate structure: OD character, X-ray single-crystal (1M), and powder Rietveld (2O) refinements of two MDO polytypes. Am Mineral 79:1185–1193

Merlino S, Pasero M, Bellezza M, Pushcharovsky DYu, Gobechia ER, Zubkova NV, Pekov IV (2004) Crystal structure of calcium catapleite. Can Mineral 42:1037–1045

Pekov IV (2000) Lovozero Massif: History, Pegmatites, Minerals, Moscow, OP

Pekov IV, Chukanov NV (2005) Microporous framework silicate minerals with rare and transition elements: minerogenetic aspects. In: Mineralogy and Geochemistry, vol 57. Rev Mineral Geochem, pp 145–171

Pekov IV, Turchkova AG, Chukanov NV (2005) A study of caiton-exchange properties of natural sodium zirconosilicates. I. Experiments in aqueous solutions under room conditions. Abstr V International Symposium "Mineralogical museums", pp 291–292

Pekov IV, Zubkova NV, Pushcharovsky DYu, Kolitsch U, Tillmanns E (2007) Refined crystal structure of parakeldyshite and genetic crystal chemistry of zirconium minerals with $[Si_2O_7]$ diorthogroups. Crystallogr Rep 52:1066–1071

Portnov AM (1964) Calcium catapleiite, a new catapleiite variety. Dokl Acad Nauk USSR Earth Sci 154:98–100

Pudovkina ZV, Chernitsova NM (1991) Crystal structure of terskite $Na_4Zr[H_4Si_6O_{18}]$. Sov Phys Dokl 36:201–203

Pudovkina ZV, Chernitsova NM, Voronkov AA, Pyatenko YuA (1980) Crystal structure of zirsinalite $Na_6CaZr(Si_6O_{18})$. Sov Phys Dokl 25:69–70

Pushcharovskii DYu, Pekov IV, Pasero M, Gobechiya ER, Merlino S, Zubkova NV (2002) Crystal structure of cation-deficient calciohilairite and possible mechanisms of decationization in mixed-framework minerals. Crystallogr Rep 47:748–752

Pyatenko YuA, Kurova TA, Chernitsova NM, Pudovkina ZV, Blinov VA, Maximova NV (1999) Niobium, tantalum and zirconium in minerals. Crystal chemistry guide, Moscow, IMGRE (in Russian)

Rastsvetaeva RK, Khomyakov AP (1992) Crystal structure of a rare earth analog of hilairite. Sov Phys Crystallogr 37:845–847

Sizova RG, Voronkov AA, Khomyakov AP (1974) Refinement of crystal structure of triclinic modification of $Na_2ZrSi_2O_7$. Structura i Svoistva Kristallov Vladimir 2:30–42 (in Russian)

Sokolova EV, Arakcheeva AV, Voloshin AV (1991) Crystal structure of komkovite. Sov Phys Dokl 36:666–668

Subbotin VV, Merlino S, Pushcharovsky DYu, Pakhomovsky YaA, Ferro O, Bogdanova AN, Voloshin AV, Sorokhtina NV, Zubkova NV (2000) Tumchaite $Na_2(Zr,Sn)Si_4O_{11}x2H_2O$ – a new mineral from carbonatites of the Vuoriyarvi alkali-ultrabasic massif, Murmansk Region, Russia. Am Mineral 85:1516–1520

Tikhonenkova RP, Kazakova ME (1961) Vlasovite, a new zirconium silicate from the Lovozero massif'. Dokl Acad Nauk USSR Earth Sci 137:451–452

Uvarova YuA, Sokolova E, Hawthorne FC, Pautov LA, Agakhanov AA (2004) A novel $[Si_8O_{45}]^{18-}$ sheet in the crystal structure of zeravshanite, $Cs_4Na_2Zr_3[Si_{18}O_{45}](H_2O)_2$. Can Mineral 42:125–134

Voronkov AA, Pyatenko YuA (1961) Crystal structure of vlasovite. Sov Phys Crystallogr 6: 755–760

Voronkov AA, Shumyatskaya NG, Pyatenko YuA (1970) Crystal structure of a new natural modification of $Na_2Zr(Si_2O_7)$. Zh Strukt Khim 11:932–933 (in Russian)

Voronkov AA, Zhdanova TA, Pyatenko YuA (1974) Refinement of the structure of vlasovite $Na_2ZrSi_4O_{11}$ and some characteristics of the composition and structure of the zirconosilicates. Sov Phys Crystallogr 19:152–156

Yamnova NA, Egorov-Tismenko YuK, Pekov IV (2001) Refined Crystal Structure of Lovozerite $Na_2CaZr[Si_6O_{12}(OH,O)_6]\cdot H_2O$. Crystallogr Rep 46:937–941

Yamnova NA, Egorov-Tismenko YuK, Pekov IV, Ekimenkova IA (2001) Crystal structure of litvinskite – a new natural member of the lovozerite group. Crystallogr Rep 46:190–193

Yamnova NA, Egorov-Tismenko YuK, Pekov IV, Shchegol'kova LV (2004) The crystal structure of kapustinite $Na_{5.5}Mn_{0.25}Zr(Si_6O_{16}(OH)_2)$: a new mineral of the lovozerite group. Dokl Earth Sci 397:658–662

Zubkova NV, Pekov IV, Turchkova AG, Pushcharovskii DYu, Merlino S, Pasero M, Chukanov NV (2007) Crystal structures of potassium-exchanged forms of Catapleiite and Hilairite. Crystallogr Rep 52:65–70

Chivruaiite, a New Mineral with Ion-Exchange Properties

Viktor N. Yakovenchuk, Sergey V. Krivovichev, Yurii P. Men'shikov, Yakov A. Pakhomovsky, Gregory Yu. Ivanyuk, Thomas Armbruster and Ekaterina A. Selivanova

Introduction

Microporous titano- and niobosilicates are promising materials for a wide range of industrial applications, including gas separation, catalysis, radioactive waste management, etc. (Rocha and Anderson 2000; Ferraris and Merlino 2005). The most famous representatives of the titanosilicate family are Engelhard TitanoSilicates, ETS-4 and ETS-10. Ion-exchanger ETS-4 firstly synthesized by S. M. Kuznicki (1989) is a synthetic analog of zorite, $Na_6[Ti(Ti, Nb)_4(Si_6O_{17})_2(OH)_5](H_2O)_{10.5}$, a rare mineral discovered by Mer'kov et al. (1973) in the aegirine-microcline-natrolite vein "Yubileinaya" within lujavrite at Mt. Karnasurt (the Lovozero alkaline massif).

Chivruaiite is found in three different hydrothermal veins within the Khibiny and Lovozero alkaline massifs (Men'shikov et al., 2006): (1) microcline vein in

Viktor N. Yakovenchuk
Geological Institute, Kola Science Centre of the Russian Academy of Sciences, Apatity, Russia
e-mail: yakovenchuk@geoksc.apatity.ru

Sergey V. Krivovichev
Department of Crystallography, Faculty of Geology, St. Petersburg State University, University Emb. 7/9, St. Petersburg, Russia

Yurii P. Men'shikov
Geological Institute, Kola Science Centre of the Russian Academy of Sciences, Apatity, Russia

Yakov A. Pakhomovsky
Geological Institute, Kola Science Centre of the Russian Academy of Sciences, Apatity, Russia

Gregory Yu. Ivanyuk
Geological Institute, Kola Science Centre of the Russian Academy of Sciences, Apatity, Russia

Thomas Armbruster
Institute of Geological Sciences, Research Group: Mineralogical Crystallography, University of Bern, Freiestr. 3, CH-3012 Bern, Switzerland

Ekaterina A. Selivanova
Geological Institute, Kola Science Centre of the Russian Academy of Sciences, Apatity, Russia

eudialyte-bearing lujavrite of the Chivruai River valley (the Lovozero massif), (2) astrophyllite-aegirine-microcline vein in foyaite at the Eveslogchorr Mt. (the Khibiny massif), and (3) natrolite-microcline vein in foyaite at the Eveslogchorr Mt. (the Khibiny massif). It is associated with microcline, eudialyte, natrolite, astrophyllite, aegirine, analcime, barytolamprophyllite, galena, hemimorphite, hydroxylapatite, loparite-(Ce), lorenzenite, murmanite, pectolite, rhabdophane-(Ce), etc. Chivruaiite occurs as elongate-prismatic crystals (up to 3 mm long) with {100}, {010}, {001}, {101}, and {011} as dominant faces, as well as radiating aggregates (Fig. 1). It is a product of low-temperature hydrothermal alteration of primary titanosilicates: mainly murmanite (veins nos 1 and 2) and astrophyllite (vein no. 3).

Our investigations (Men'shikov et al., 2006) showed that chivruaiite is a Ca-analogue of zorite and ETS-4 and is closely related to haineaultite. Chemical composition of chivruaiite and zorite corresponds the next empirical formulas (Men'shikov et al., 2005):

$$(Ca_{3.00}K_{0.44}Na_{0.05}Sr_{0.04}Mn_{0.01})_{3.54}(Ti_{4.13}Nb_{0.44}Fe^{3+}_{0.04}Al_{0.02})_{4.63}$$
$$[Si_{12}O_{34}|O_{0.49}(OH)_{4.51}]\cdot 13.08H_2O \text{ for chivruaiite,}$$

$$(Na_{6.71}K_{0.28}Ca_{0.07}Mn_{0.03}Sr_{0.05}Ce_{0.02})_{7.16}(Ti_{4.05}Nb_{0.45}Fe^{3+}_{0.11})_{4.61}$$
$$[Si_{12}O_{34}|(OH_{3.79}O_{1.21}]\cdot 13-14H_2O \text{ for zorite.}$$

There is a positive linear correlation ($r^2 = 0.61$) between the K and Ti contents (*apfu*): K = –3.83+1.01Ti (Fig. 2). This correlation can be explained by the next substitution:

$$K^+ + Ti^{4+} \leftrightarrow \square + Nb^{5+}.$$

If potassium really occupies a separate site in the mineral structure, the general formula of chivruaiite must be written as

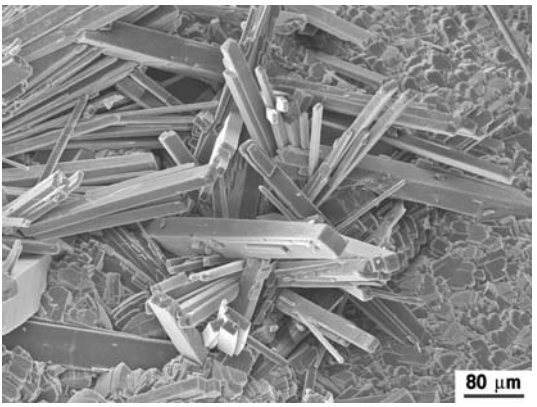

Fig. 1 Radiating aggregates of prismatic chivruaiite crystals from a microcline vein in eudialyte-bearing lujavrite of the Chivruai River valley

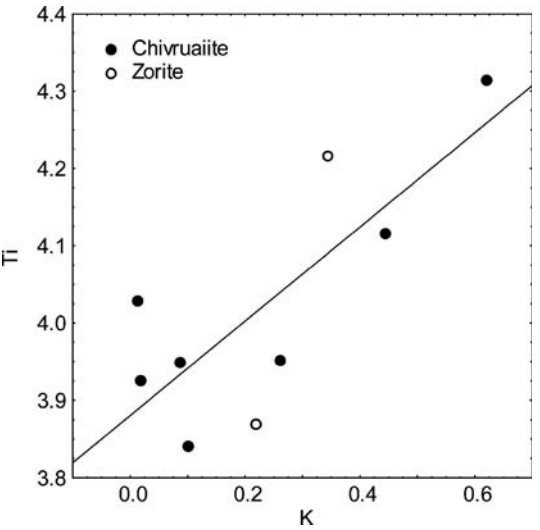

Fig. 2 Plot (in apfu) of K versus Ti for chivruaiite–zorite series minerals

$$Ca_4K_{1-x}(Ti_{5-x}Nb_x)[(Si_6O_{17})_2|(O,OH)_5]\cdot 13-14H_2O, \text{where } x = 0-1.$$

The structure of chivruaiite is based upon open framework of SiO_4 tetrahedra, TiO_6 octahedra, and TiO_5 pyramids, cavities are occupied by Ca^{2+} and K^+ cations, and H_2O molecules (Fig. 3a). Large K^+ cations are located within the large channels of octangular prisms (see Fig. 3b) and is approximately at the center of 8-membered rings of tetrahedra formed as a result of condensation of two single tetrahedral chains (Men'shikov et al., 2006). The Ca^{2+} cations are in the walls of the titanosilicate framework: the Ca1 site blocks the 7 MR formed by four silicate tetrahedra and three Ti polyhedra (see Fig. 3b), whereas the Ca2 site is approximately at the center of the 6 MR formed by four silicate tetrahedra and two Ti

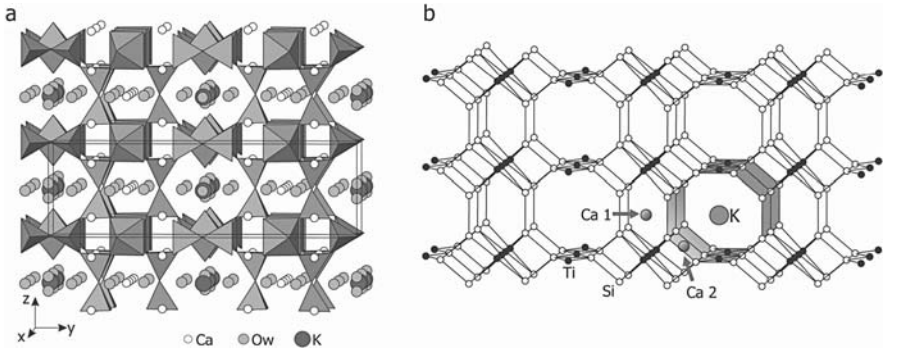

Fig. 3 Crystal structure of chivruaiite (**a**), in which some H_2O molecules are omitted for clarity, and nodal representation of its titanosilicate framework (**b**) with positions of Ca^{2+} and K^+ cations

octahedra. The structural formula for minerals of chivruaiite–zorite series based on single-crystal structure study can be written as:

$$(Na, Ca, Mn, \square)_8(\square, K)(Ti, Nb, \square)_5[(Si_6O_{17})_2|(OH, O)_5] \cdot 13 - 14H_2O,$$

which is in good agreement with the results of our chemical data.

Thus, chivruaiite can accumulate up to 1 *apfu* of large cations such as K^+ and (more importantly) Cs^+ and Rb^+ if they are incorporated into the large channels of the mineral structure. The possibility to use zorite as a material for the removal of both ^{137}Cs and ^{89}Sr from radioactive waste solutions was firstly suggested by Dyer and Pillinger (1999). Taking into account structural similarities between zorite and chivruaiite, we suggest that chivruaiite can also have similar ion-exchange properties.

Experimental

In our experiments, small (up to 0.5 mm long) crystals of chivruaiite from the Lovozero massif (vein no. 1) were loaded in 1*M* solutions of NH_4Cl, CsCl or RbCl at ambient temperature during 12–48 h. No visible changes were found after the treating and crystal structure and unit cell parameters remain without noticeable changes according to powder X-ray diffraction data. Examination of polished sections of treated crystals using Leo-1450 scanning electron microscope with Röntec EDS-analyzer showed homogeneous distributions of Rb and Cs over the whole crystals (Fig. 4).

The chemical composition of original and treated crystals of chivruaiite from the vein no. 1 (Table 1) has been studied by wave-length dispersion spectrometry using Cameca MS-46 electron microprobe (Geological Institute, Kola Science Centre of the Russian Academy of Sciences, Apatity) operating at 20 kV and 20–30 nA. The following standards were used:

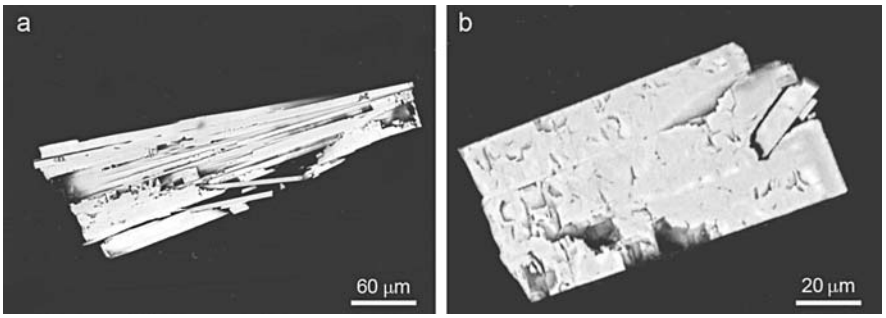

Fig. 4 BSE-images of chivruaiite crystals exchanged by Cs (**a**) and Rb (**b**)

Table 1 Chemical composition (wt.%) and unit formula (*apfu*, Si = 12) of chivruaiite crystals treated with solutions of NH_4Cl, RbCl and CsCl at ambient temperature during 12–48 h

Component	Original	Treated with		
		NH_4Cl	RbCl	CsCl
Na_2O	0.10	–	–	–
MgO	0.01	–	–	–
Al_2O_3	0.07	–	–	–
SiO_2	45.14	45.37	44.30	46.60
K_2O	1.30	0.06	–	0.92
CaO	10.53	10.19	10.23	9.72
TiO_2	20.63	21.51	19.53	20.74
MnO	0.02	–	–	–
FeO	0.16	0.04	0.19	–
RbO	–	–	10.33	–
SrO	0.28	0.48	0.56	0.60
Nb_2O_5	3.63	4.74	5.57	5.27
Cs_2O	–	–	–	5.42
SUM	81.87	82.39	90.71	89.27
H_2O = 100 – SUM	18.13	17.61	9.29	10.73
Ca	3.00	2.89	2.97	2.68
Sr	0.04	0.07	0.09	0.09
Mn	0.01	–	–	–
Na	0.05	–	–	–
K	0.44	0.02		0.30
Rb	–	–	1.80	–
Cs	–	–	–	0.59
Ti	4.13	4.28	3.98	4.28
Nb	0.44	0.57	0.68	0.57
Fe^{3+}	0.04	0.01	0.04	–
Al	0.02	–	–	–
Si	12.00	12.00	12.00	12.00
H	30.68	31.10	16.81	18.42

lorenzenite (Na, Ti), pyrope (Mg, Al), diopside (Si, Ca), wadeite (K), metallic vanadium (V), synthetic $MnCO_3$ (Mn), hematite (Fe), sphalerite (Zn), celestine (Sr), synthetic $ZrSiO_4$ (Zr), metallic niobium (Nb), barite (Ba), synthetic CeS (Ce), lepidolite (Rb) and pollucite (Cs). Water content was calculated as 100 wt.% minus SUM of analysis. It is established that treated crystals have up to 5 wt.% of Cs and up to 10 wt.% of Rb in their compositions, content of K decreases slightly in the CsCl solution and up to zero in the RbCl and NH_4Cl solutions, Ca content decreases after treatment in the CsCl solution only, and content of water decreases twice when Ca and K are exchanged by Rb and Cs:

Original chivruaiite -

$$(Ca_{3.00}Na_{0.05}Sr_{0.04}Mn_{0.01})_{3.10}K_{0.44}$$
$$(Ti_{4.13}Nb_{0.44}Fe_{0.04})_{4.61}[Si_{12}O_{34}|O_{0.49}(OH)_{4.51}] \cdot 13.08H_2O$$

Chivruaiite decationized by NH_4Cl -

$$(Ca_{2.89}Sr_{0.07})_{2.96}K_{0.02}$$
$$(Ti_{4.28}Nb_{0.57}Fe_{0.01})_{4.86}[Si_{12}O_{34}|O_{0.92}(OH)_{4.08}] \cdot 13.51H_2O$$

Rb-exchanged chivruaiite -

$$(Ca_{2.97}Rb_{0.80}Sr_{0.09})_{3.86}Rb_{1.00}$$
$$(Ti_{3.98}Nb_{0.68}Fe_{0.04})_{4.70}[Si_{12}O_{34}|O_{2.37}(OH)_{2.63}] \cdot 7.09H_2O$$

Cs-exchanged chivruaiite -

$$(Ca_{2.68}Sr_{0.09})_{2.77}(Cs_{0.59}K_{0.30})_{0.89}$$
$$(Ti_{4.28}Nb_{0.57})_{4.85}[Si_{12}O_{34}|O_{0.58}(OH)_{4.42}] \cdot 7.00H_2O.$$

Discussion

Therefore, the following substitution mechanisms can be considered for chivruaiite:

1) substitutions within the Ca–Na positions: $2Na^+ \leftrightarrow (Ca, Sr, Mn)^{2+}$, $3Na^+ \leftrightarrow$ REE^{3+} etc;
2) introduction of large cations (K^+, Cs^+, Rb^+, Tl^+ etc.) into the channel position;
3) substitutions within the Ti-Nb positions: $K^+ + Ti^{4+} \leftrightarrow \square + Nb^{5+}$;
4) $O^{2-} \leftrightarrow OH^-$ substitutions for the anion positions bridging between two Ti1 sites.

Medium-large cation of Rb can replace not only cation of K, but also Ca1, whereas large cation of Cs replaces K only. Besides, such substitution "ejects" a half of water molecules from the channels, and in case of Cs – part of Ca2 also (see Fig. 3). It is important that Cs-excanged phase is exclusively stable and can not be re-exchanged under ambient conditions. It means that chivruaiite-based materials really can be exclusively effective for the removal of ^{137}Cs from radioactive waste solutions.

It has been known that ETS-4 molecular sieve (synthetic analogue of zorite) has a strong ion-exchange capacity for Sr^{2+} also (Braunbarth et al. 2000). Analysis of the structural data reported by Braunbarth et al. (2000) shows that Sr^{2+} cations in Sr-exchanged ETS-4 occupy the *Ca*1 site. Taking into account structural similarities between zorite and chivruaiite, we suggest that chivruaiite can also have similar ion-exchange properties as regards as strontium, which requires special investigations.

Because of zorite-chivruaiite series minerals easily change their composition in dependence on environment, chivruaiite origin in Nature can be caused by few reasons. The Lovozero massif is strongly depleted in calcium in contrast with the

Khibiny massif, which explains the presence of chivruaiite in the Khibiny massif and zorite in the Lovozero massif. Chivruaiite occurrence within the Chivruai River valley can be caused by partial assimilation of numerous xenoliths of Devonian basalt by nepheline-syenite melt as well as by cation-exchange of zorite under influence of low-temperature solutions enriched in Ca. Really, Na minerals (aegirine, murmanite, lorenzenite, lamprophyllite, loparite-(Ce) etc.) are earlier in the vein, while Ca minerals (pectolite, hydroxilapatite and whewellite) are the late.

Acknowledgements We thank Swiss National Foundation (SNF) for financial support in the framework of the SCOPES program.

References

Braunbarth C, Hillhouse HW, Nair S, Tsapatis M, Burton A, Lobo RF, Jacubinas RM, Kuznicki SM (2000) Structure of strontium ion-exchanged ETS-4 microporous molecular sieves. Chem Mater 12:1857–1865

Dyer A, Pillinger M (1999) Treatment of radioactive waste using a titanosilicate analog of the mineral zorite. Roy Soc Chem 239:261–269 (Special Publication)

Ferraris G, Merlino S (eds) (2005) Micro- and Mesoporous Mineral Phases. Rev Mineral Geochem, vol 57. Mineralogical Society of America, Washington DC

Kuznicki SM (1989) Large-pored crystalline titanium molecular sieve zeolites. US Patent No 4853202

Men'shikov YuP, Krivovichev SV, Pakhomovsky YaA, Yakovenchuk VN, Ivanyuk GYu, Mikhailova JA, Armbruster T, Selivanova EA (2005) Natural molecular sieves of the zorite-chivruaiite series from hydrothermalites of the Lovozero and Khibiny massif. Appl Geochem 7:43–50 (in Russian)

Men'shikov YuP, Krivovichev SV, Pakhomovsky YaA, Yakovenchuk VN, Ivanyuk GYu, Mikhailova JA, Armbruster T, Selivanova EA (2006) Chivruaiite, $Ca_4(Ti,Nb)_5[(Si_6O_{17})_2(OH,O)_5]\cdot 13\text{-}14H_2O$, a new mineral from hydrothermal veins of Khibiny and Lovozero alkaline massifs. Am Mineral 91:922–928

Mer'kov AN, Bussen IV, Goiko EA, Kul'chitskaya EA, Men'shikov YuP, Nedorezova AP (1973) Raite and zorite – new minerals from the Lovozero Tundra. Zapiski VMO 102:1:54–62

Rocha J, Anderson MW (2000) Microporous titanosilicates and other novel mixed octahedral-tetrahedral framework oxides. Eur J Inorg Chem 2000:801–818

Tl-Exchange in Zorite and ETS-4

Dar'ya V. Spiridonova, Sergey N. Britvin, Sergey V. Krivovichev,
Viktor N. Yakovenchuk and Thomas Armbruster

Introduction

Within recent years, titanosilicates and other octahedral–tetrahedral framework materials have attracted considerable attention due to their applications in catalysis, gas separation, energy storage, optoelectronics, radioactive waste management, etc. (Behrens et al. 1998; Lamberti 1999; Rocha and Anderson 2000; Zecchina et al. 2001). Before being synthesized under laboratory conditions, many of these materials were known as minerals. Engelhard titanosilicate ETS-4, which is now used in gas industry on a multitonn scale (Kuznicki et al. 2001), is a synthetic analogue of zorite, a framework sodium titanosilicate described in 1970s from alkaline complexes of the Kola peninsula, Russia (Mer'kov et al. 1973; Sandomirskii and Belov 1979). This and many other examples show that investigations of minerals are not only of mineralogical interest but may also provide important ideas for synthesis of new materials with important industrial applications.

Dar'ya V. Spiridonova
Department of Crystallography, Faculty of Geology, St. Petersburg State University, University Emb. 7/9, St. Petersburg, Russia, e-mail: dasha@crystalspb.com

Sergey N. Britvin
Department of Crystallography, Faculty of Geology, St. Petersburg State University, University Emb. 7/9, St. Petersburg, Russia

Sergey V. Krivovichev
Department of Crystallography, Faculty of Geology, St. Petersburg State University, University Emb. 7/9, St. Petersburg, Russia

Viktor N. Yakovenchuk
Geological Institute, Kola Science Centre of the Russian Academy of Sciences, Apatity, Russia

Thomas Armbruster
Institute of Geological Sciences, Research Group: Mineralogical Crystallography, University of Bern, Freiestr. 3, CH-3012 Bern, Switzerland

Zorite and its synthetic analogue ETS-4 have been subjects of relatively few ion-exchanged experiments. Braunbarth et al. (2000) and Nair et al. (2001) reported structure of Sr-exchanged ETS-4 (sometimes indicated as Sr-ETS-4), whereas Zubkova et al. (2005, 2006) reported structures of Cs-, K-, and Pb-exchanged forms of zorite. Recently, we have studied Rb- and Ag-exchanged structures of zorite (Spiridonova et al., to be published). It is noteworthy that, in all mentioned ion-exchanged forms of ETS-4 and zorite, ion exchange does not induce any unusual structural transformations. Ion exchange is either complete (Ag-zorite) or incomplete, with one of the two Na sites being exchanged and another replaced completely (K-, Cs-, Pb-zorites, and Sr-ETS-4).

Here we report preliminary data on Tl-exchange in zorite and ETS-4 in aqueous solutions. Quite unexpectedly, X-ray single crystal diffraction studies of Tl-exchanged zorite provided direct evidence of superstructure reflections that are associated with ordering of Tl^+ cations within the titanosilicate porous framework.

Experimental

Crystals of zorite used in this study originated from 'Yubileinaya' vein, the Lovozero massif. Its chemical composition corresponds to the empirical formula $(Na_{6.71}Ca_{0.07}Mn_{0.03}Mg_{0.01}Sr_{0.05}Ce_{0.02}K_{0.28})_{7.17}$ $(Ti_{4.05}Nb_{0.45}Al_{0.02}Fe^{3+}_{0.11})_{4.63}$ $[Si_{12}O_{34}|$ $(OH_{3.79}O_{1.21}]\cdot 13–14H_2O$ as reported by Men'shikov et al. (2006).

The ETS-4 powder was obtained by hydrothermal method from synthesis mixture with molar composition 1Ti:5.7Si:4Na:2K. The synthesis mixture was formed by combining two precursor solutions, one containing titanium(III) chloride and deionized water, and another containing crystal hydrate of sodium silicate, sodium hydroxide, crystal hydrate of potassium fluoride, and deionized water. A total weight of 3.238 g of sodium silicate (18–23 % Na_2O, 19–21 % SiO_2) was mixed with 15 ml of deionized water, 0.320 g of sodium hydroxide (98% NaOH, Vekton), 0.376 g of crystal hydrate of potassium fluoride ($KF\cdot 2H_2O$, Vekton) (Sol. 1). This mixture was stirred thoroughly until a homogeneous white solution was obtained (for 10 min). For the preparation of the other precursor solution (Sol. 2), we have used 1.813 g of titanium chloride(III) (15% $TiCl_3$), and 10 ml of deionized water. This mixture was also stirred for 10 min. The solution 2 was added to the solution 1. The resulting white viscous mixture was transferred to 50 ml Teflon-lined stainless steel autoclave. Crystallization was carried out at 190°C for 14 days. After cooling, the content of the autoclave was filtered and washed by deionized water, followed by overnight drying at room temperature in ambient air.

Ion-exchange experiments were performed as follows: 50 mg of zorite or ETS-4 were immersed into 5 ml of saturated solution of Tl_2SO_4. Exchange reaction was done in 5 days, and each day reaction mixture was slightly stirred. The resulting material washed by deionized water, followed by drying at room temperature in ambient air.

Table 1 Crystallographic data on zorite, ETS-4, and Tl-exchanged zorite determined in this study

Parameters	Zorite	ETS-4	Tl-zorite	
			Powder data	Single crystal data
Space group	*Cmmm*	*Cmmm*		*Immm*
a, Å	23.215(3)	23.161(5)	23.158(4)	23.188(5)
b, Å	7.222(3)	7.159(1)	21.593(4)	21.573(5)
c, Å	6.957(1)	6.916(1)	13.779(2)	13.803(3)
V, Å^3	1166.3(4)	1146.8(3)	6890(1)	6905(3)

Chemical analysis of Tl-exchange zorite was done using electron microprobe that demonstrated a complete absence of Tl and provided the empirical chemical formula $Tl_{3.80}(Ti_{4.14}Nb_{0.45}Fe^{3+}_{0.11}Al_{0.02})_{\Sigma=4.63}[Si_{12}O_{34}|(OH)_{4.00}]\cdot nH_2O$.

The crystal of Tl-exchanged zorite selected for data collection was mounted on a glass fibre. Data were collected by means of a SMART 1K CCD diffractometer using monochromated MoK_α radiation and frame widths of 0.3° in ω up to 27.5°θ. Even initial indexing provided superstructure reflections that can be indexed with triple *b* and double *c* unit-cell parameters compared to the original zorite sample (Table 1). The data were corrected for Lorentz, polarization, absorption, and background effects. The intensity statistics indicated the body-centered centrosymmetric

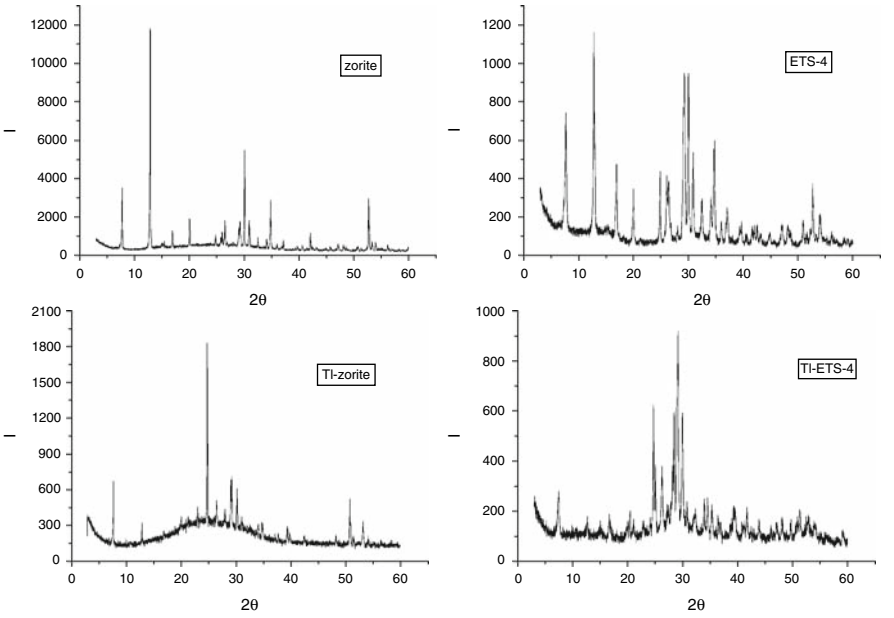

Fig. 1 X-ray powder diffraction patterns of zorite and ETS-4 in comparison to their Tl-exchanged forms

space group *Immm*. The structure was solved and refined by means of the program SHELX-97. The details of structure determination and refinement will be reported elsewhere (Krivovichev et al., in preparation).

X-ray powder diffraction experiments were performed at ambient conditions using automated DRON-2 powder diffractometer with CuK_α radiation. Unit-cell parameters for zorite, ETS-4, and Tl-zorite were refined by least squares method and are listed in Table 1. Unfortunately, no single crystals of ETS-4 could be found in the synthesis products so it is unclear whether Tl-ETS-4 possess the same superstructure as Tl-exchanged zorite. X-ray powder diffraction patterns for Tl-exchanged ETS-4 and zorite are similar but no superstructure reflections could be unambiguously identified (Fig. 1).

Results

The most interesting and important result of this study is the detection of a $1 \times 3 \times 2$ superstructure in Tl-exchanged zorite. The superstructure occurs as a result of ordering of Tl^+ ions in the framework channels.

In comparison to original zorite that has only two extra-framework cation sites (see Men'shikov et al. (2006) for details), Tl-zorite contains a number of disordered Tl sites with different coordination environments.

As it has been known from literature data, zorite and ETS-4 contain two types of octahedral (Ti) sites, Ti(1) and Ti(2). The Ti(1) site is in octahedral coordination and corresponds to the infinite chains of Ti-centered octahedra. Coordination of the Ti(2) site has been debated in the literature since this site is 25%-occupied and related to the adjacent Ti(2) site by a mirror plane. For this reason, it has been unclear whether this site is 6- or 5-coordinated. Sandomirskii and Belov (1979) suggested that a true coordination is a square pyramid with one Ti–O distance being rather short (1.6–1.7 Å). This statement was supported by other studies on ETS-4 and related minerals haineaultite (McDonald and Chao, 2004) and chivruaiite (Men'shikov et al. 2006). However, Cruciani et al. (1998) on the basis of a Rietveld refinement of synchrotron X-ray diffraction data suggested that this site is in fact octahedrally coordinated. In the superstructure observed in Tl-zorite, the mirror plane that relate the Ti(2) site with its symmetry equivalent is absent and two symmetrically independent Ti(2a) and Ti(2b) sites are observed. It is remarkable that both these sites have an octahedral coordination with both octahedral corners occupied by H_2O molecules (as can be deduced from bond-valence analysis). It is unclear whether ion-exchange does change coordination of the Ti(2) site (e.g., through an additional hydration) or the observed effect is due to relaxation of the average structure induced by the formation of the superstructure.

Another interesting result of the ion exchange can be seen in Fig. 1. It is clear that intensities in the X-ray diffraction pattern are drastically different for original and Tl-exchanged samples. These effects are similar for both zorite and ETS-4 that provides an indirect evidence that Tl-ETS-4 might also possess a superstructure. It is

our intention to check this possibility with the help of advanced diffraction methods, e.g. by means of synchrotron radiation sources.

Acknowledgements We thank Swiss National Foundation (SNF) for financial support in the framework of the SCOPES program. D.V.S., S.N.B., and S.V.K. thank Russian federation Ministry of Science and Education for financial support through the RNP grant (2.1.1.3077) and 'Molecular geochemistry and biogeochemistry' project of the program 'Innovative education environment in a classical University'.

References

Behrens EA, Poojary DM, Clearfield A (1998) Syntheses, X-ray powder structures, and preliminary ion-exchange properties of germanium-substituted titanosilicate pharmacosiderites: $HM_3(AO)_4(BO_4)_3 4(H_2O)$ (M = K, Rb, Cs; A = Ti, Ge; B = Si, Ge). Chem Mater 10:959–967

Braunbarth C, Hillhouse HW, Nair S, Tsapatis M, Burton A, Lobo RF, Jacubinas RM, Kuznicki SM (2000) Structure of strontium ion-exchanged ETS-4 microporous molecular sieves .Chem Mater 12:1857–1865

Cruciani G, de Luca P, Nastro A, Pattison P (1998) Rietveld refinement of the zorite structure of ETS-4 molecular sieves. Micropor Mesopor Mat 21:143–153

Kuznicki SM, Bell VA, Nair S, Hillhouse HW, Jacubinas, Braunbarth CM, Toby BH, Tsapatis M (2001) A titanosilicate molecular sieve with adjustable pores for size-selective adsorption of molecules. Nature 412:720–724

Lamberti C (1999) Electron-hole reduced effective mass in monoatomic –O–Ti–O–Ti–O- quantum wires embedded in the siliceous crystalline matrix of ETS-10. Micropor Mesopor Mat 30: 155–163

McDonald AM, Chao GY (2004) Haineaultite, a new hydrated sodium calcium titanosilicate from Mont Saint-Hilaire, Quebec: description, structure determination and genetic implications. Can Mineral 42:769–780

Men'shikov YuP, Krivovichev SV, Pakhomovsky YaA, Yakovenchuk VN, Ivanyuk GYu, Mikhailova YuA, Armbruster T, Selivanova EA (2006) Chivruaiite, $Ca_4Ti_5[(Si_6O_{17})_2|O_4(OH)]\cdot 14H_2O$, a new mineral from hydrothermalites of Khibiny and Lovozero alkaline massifs, and its relations with zorite. Am Mineral 91:922–928

Mer'kov AN, Bussen IV, Goiko EA, Kul'chitskaya EA, Men'shikov YuP, Nedorezova AP (1973) Raite and zorite – new minerals from the Lovozero Tundra. Zapiski VMO 102(1)54–62 (in Russian)

Nair S, Jeong H-K, Chandrasekaran A, Braunbarth C, Tsapatis M, Kuznicki SM (2001) Synthesis and structure determination of ETS-4 single crystals. Chem Mater 13:4247–4254

Rocha J, Anderson MW (2000) Microporous titanosilicates and other novel mixed octahedral–tetrahedral framework oxides. Eur J Inorg Chem 2000:801–818

Sandomirskii PA, Belov NV (1979) The OD structure of zorite. Sov Phys Crystallogr 24:686–693

Zecchina A, Llabres i Xamena FX, Paze C, Turnes Palomino G, Bordiga S, Otero Arean C (2001) Alkyne polymerization on the titanosilicate molecular sieve ETS-10. Phys Chem Chem Phys 3:1228–1231

Zubkova NV, Pushcharovsky DYu, Giester G, Pekov IV, Turchkova AG, Chukanov NV, Tillmanns E (2005) Crystal structures of K- and Cs-exchanged forms of zorite. Crystallogr Rep 50: 367–373

Zubkova NV, Pushcharovsky DYu, Giester G, Pekov IV, Turchkova AG, Tillmanns E, Chukanov NV (2006) Crystal structure of Pb-exchanged form of zorite. Crystallogr Rep 51:379–382

The Largest Source of Minerals with Unique Structure and Properties

Alexander P. Khomyakov

Among the best known mineral localities on our planet, the Khibina–Lovozero agpaitic nepheline syenite complex stands out as truly unique; it far surpasses any other locality both in the total number of mineral species (more than 600) and in the number of those first described from it (about 200), with all important classes of chemical compounds being represented (Khomyakov 2006). Theoretical understanding of this unique repository of minerals of alkaline rocks increased continuously as more and more minerals were discovered, which was reflected in the works of several generations of mineralogists, geochemists, and geologists. As a result, many fundamental theories were formulated and developed, such as A.E. Fersman's idea that Zr, Ti, and Nb occur in agpaitic magmas as complex anions rather than as ordinary highly charged cations. This concept not only explained the main mineralogical and geochemical features of the characteristic elements of agpaitic massifs, but also acquired a wider significance. It was successfully used in particular by N.V. Belov and his school to develop the theoretical foundations of the crystal chemistry of minerals with mixed anionic radicals. It was widely used in the works of L.N. Kogarko and other researchers to justify the most probable models for the genesis of superlarge apatite, loparite, and eudialyte deposits associated with the Khibina–Lovozero complex.

The author's extensive research on the mineralogy of these deposits revealed that their deep unweathered zones contain abundant hyperagpaitic pegmatoid rocks supersaturated with alkali, volatile, and rare elements (Khomyakov 1980b, 1990, 1995). These rocks are characterized by the presence of a whole series of very unusual minerals, such as natrosilite $Na_2Si_2O_5$, natrite Na_2CO_3,olympite $Na_5Li(PO_4)_2$, which are, respectively, the most alkaline water-soluble silicate, carbonate, and phosphate ever found in nature. The existence of such salts as crystalline phases of rocks could not be predicted by traditional theories, so the discovery of their abundant accumulations in the rocks of Khibina and Lovozero actually signified the

Alexander P. Khomyakov
Institute of Mineralogy, Geochemistry, and Crystal Chemistry of Rare Elements, Moscow, Russia,
e-mail: noomineral@noomin.msk.ru

discovery of a previously unknown phenomenon: ***the peralkaline state of natural substance***. In this state, not only Zr, Ti, and Nb, but also all other electropositive elements that are less basic than Na exhibit amphoteric properties, stimulating their passage from the cationic part of the structure of agpaitic magma into the considerably more capacious anionic part. As a result, agpaitic magma turns into a universal solvent, thus accumulating huge amounts of P, Nb, Ta, Ti, Zr, Hf, REE, U, Th, Al, Ga, Sr, Ba, Be, Na, K, F, and other useful components. This factor is responsible both for the supergiant sizes of mineral deposits associated with agpaitic magmatism and for their pronounced multi-element character. It also explains why hyperagpaitic rocks are so abundant in minerals with unique compositions, structures, and properties.

The largest and most diverse group of these minerals are zeolite-like Al-free titanosilicates and their analogues with microporous heteroframework or heterolayer structures, for which the author introduced the term "amphoterosilicates" (Khomyakov 1990, 1995, 2002, 2004a). They can all be schematically described by the general formula $A_xM_ySi_pO_q$, where A denotes Na, K, and other highly alkaline cations; and M stands for Ti, Nb, Zr, and all other electropositive elements that exhibit amphoteric properties in the presence of A cations. Mostly represented by unique structure types, amphoterosilicates are based on mixed frameworks composed of usually discrete M polyhedra (octahedral, tetrahedral, or five-coordinated) and SiO_4 tetrahedra, which are linked to form rings, chains, tubes, etc. Their cavities and channels are filled with extra-framework cations, additional anions, and water molecules. Layered amphoterosilicates mostly form polysomatic series of mica-like titanosilicates and their analogues, which contain mobile cations in their channels and interlayers (Ferraris 1997; Ferraris et al. 1997; Ferraris and Merlino 2005).

Research results on the unique properties of zeolite-like amphoterosilicates are reflected in the author's numerous papers, some of which are listed in the References and are discussed below. Many of these minerals exhibit unusual behavior as they interact with air, water, salts, alkalis, acids, X-rays, etc. In particular, in the zones of epithermal and supergene alteration of hyperagpaitic rocks, many highly alkaline amphoterosilicates are readily replaced by their hydrated analogues by reactions of the following type: highly alkaline mineral + $H_2O \Rightarrow$ low-alkaline mineral + NaOH. For example, as a result of the six reactions described below (their numbers are given in parentheses), zirsinalite $Na_6CaZrSi_6O_{18}$ is replaced by lovozerite $Na_3CaZrSi_6O_{15}(OH)_3$ (1); kazakovite $Na_6MnTiSi_6O_{18}$is replaced by tisinalite $Na_3MnTiSi_6O_{15}(OH)_3$ (2); parakeldyshite $Na_4Zr_2(Si_2O_7)_2$ is replaced by keldyshite $Na_3HZr_2(Si_2O_7)_2$ (3); keldyshite $Na_3HZr_2(Si_2O_7)_2$ is replaced by "hydrokeldyshite" (phase M34) $NaHZrSi_2O_7 \cdot H_2O$ (4); lomonosovite $Na_4Ti_4Si_4O_{18} \cdot 2Na_3PO_4$is replaced by murmanite $Na_4Ti_4Si_4O_{18} \cdot H_2O$ (5); and vuonnemite $Na_5TiNb_2Si_4O_{17}F \cdot 2Na_3PO_4$ is replaced by epistolite $Na_5TiNb_2Si_4O_{17}\ F \cdot 4H_2O$ (6).

These reactions are irreversible and proceed at extremely high rates. The highest rates are typical of reactions 1 and 2, the study of which led to the discovery of a previously unknown phenomenon: ***superfast hydrolysis of peralkaline titano- and zirconosilicates*** (Khomyakov et al. 1978). Under atmospheric conditions, there is

spontaneous replacement of zirsinalite by lovozerite and of kazakovite by tisinalite. When this occurs, the fresh surfaces of highly alkaline minerals rapidly become cloudy as sodium hydroxide of the surface film reacts with atmospheric carbon dioxide according to the scheme: $2NaOH + CO_2 = Na_2CO_3 \cdot H_2O$. This behavior of zirsinalite and kazakovite is caused by their specific mixed-framework structures in which the local charge balance is substantially disturbed on some oxygen atoms of the "lovozerite" ring (Si_6O_{18}). Replacement of these atoms by hydroxyl groups normalizes the local balance, so that lovozerite and tisinalite, in contrast to their highly alkaline analogues, are quite stable under atmospheric conditions. Reactions 3 and 4 follow approximately the same scheme, with the result that parakeldyshite is most commonly found as relics surrounded by its replacement products consisting of keldyshite and/or "hydrokeldyshite" (phase M34).

Somewhat different behavior is exhibited by layered titano-niobosilicates of the lomonosovite family (Khomyakov 1976a). In contrast to the above cases, the highly alkaline members of this family are quite stable under atmospheric conditions, but are readily leached out by reactions 5 and 6 in epithermal and supergene processes. The same result is produced when lomonosovite and vuonnemite are treated with cold water. Note that some other highly alkaline minerals of the lomonosovite family, such as beta-lomonosovite and bornemanite, do not react with water at room temperature, but are decationized with the exchange of sodium phosphate for H_2O molecules when ground samples are treated with boiling water.

The above reactions produce a special class of homoaxial pseudomorphs in which the secondary minerals inherit both the chemical and the structural basis from the primary minerals. This gives rise to evolutionary sequences (kazakovite–tisinalite, zirsinalite–lovozerite, parakeldyshite–keldyshite– "hydrokeldyshite" (phase M34), lomonosovite–murmanite, and vuonnemite–epistolite) in which there is a certain protomineral corresponding to each secondary mineral. Until recently, lovozerite and epistolite were regarded as completely independent primary minerals, while murmanite was assumed to have two modes of origin: primary crystallization and pseudomorphic replacement of lomonosovite. The results of special studies (Khomyakov 1976a, b, c, 1980a, b, 1990, 1995, 1996; Khomyakov et al. 1978) led to the radical revision of traditional assumptions in favor of an exclusively secondary origin for these hydrated minerals and it was proposed that they be categorized as a special genetic group of ***transformation mineral species*** (TMS).

In contrast to the ordinary polygenetic minerals, capable of crystallizing from melts or solutions, TMSs form only by alteration of specific precursor minerals, from which they inherit their essential compositional and structural features. The one-to-one correspondence between the evolutionarily related protomineral–TMS pairs offers wide possibilities for interpreting paleoconditions and paleoprocesses of mineral formation, contributing significantly to the development of the overall concept of ***inheritance in mineral genesis*** (Khomyakov 1980a; Khomyakov and Yushkin 1981; Yushkin et al. 1984). One of the main practical uses of the links between highly alkaline amphoterosilicates and their hydrated analogues is to reliably reconstruct the primary mineral composition of rocks and ores from their secondary products. On this basis, the lovozerite–murmanite lujavrites of

the Lovozero massif have been found to be altered rocks that were originally zirsinalite–lomonosovite lujavrites. Another important application is to use the inferred links to obtain materials with desired structures and properties on the basis of natural minerals through their thermochemical or other treatment (Khomyakov 1990, 1995; Solodov et al. 1977, 1978).

Returning to the above assessment of the Khibina–Lovozero complex as an inexhaustible source of new mineral discoveries, it should be noted that the first significant discoveries of minerals with unusual compositions and properties (lomonosovite–murmanite group, etc.) were made by members of the Finnish expeditions headed by Wilhelm Ramsay (in the 1890s) and later by staff of several Academy of Sciences institutions led by Alexander Fersman, Kuzma Vlasov, and other prominent scientists. It was, in no small part, through the major advances in mineralogical research at these institutions, but most notably through their contribution to the discovery of the giant apatite, loparite, and eudialyte deposits that the Khibina and Lovozero alkaline massifs gained worldwide fame and became a unique national treasure. The achievements of these pioneers were successfully continued and multiplied by their students and followers. This can be seen from the following figures: the first 80 years of mineralogical discoveries in these two massifs (1890–1970) yielded 35 minerals new to science, whereas the much shorter period from 1971 to 2005 yielded about 150 new minerals (Khomyakov 2006), the greater part of which (more than 80 species) were discovered with the author's participation.

The marked acceleration in the rate of new mineral discoveries in the Khibina–Lovozero complex in recent decades, as already mentioned, has been due to detailed studies of the mineral composition of hyperagpaitic rocks. The results of these studies, which were widely publicized in scientific and more popular publications and presentations in various forums, prompted many researchers to further investigate the mineralogy of these rocks. In particular, very impressive progress in this area has been achieved by the young multidisciplinary teams of researchers led by I.V. Pekov and N.V. Chukanov, who have described more than fifty new minerals approved by the IMA (Pekov 2005).

Many of the new minerals originally described from hyperagpaitic rocks of the Kola Peninsula were soon found in similar rocks in other regions, namely in the alkaline massifs of the Gardar (Greenland) and Monteregian (Canada) provinces. At present, numerous discoveries along these lines continue both Russia and elsewhere, deepening our understanding of the structural and chemical diversity of the mineral kingdom and confirming the author's concept of an unlimited number of mineral species (Khomyakov 1997). Simultaneously, hyperagpaitic rocks are yielding increasing numbers of minerals with unusual properties that are of interest to technological mineralogy and materials science, where research on their practical applications is underway.

Synthetic titano- and zirconosilicates have long been of interest to materials engineers as a promising new class of sorbents and ion exchangers that could find applications in various branches of the chemical and petroleum industries (Joung 1967). Minerals of hyperagpaitic rocks can serve as prototypes for creating such materials, as was demonstrated in laboratory tests of titanosilicate penkvilksite, zirconosilicate

"hydrokeldyshite" (phase M34), and beryllosilicate lovdarite. These tests proved that the aforementioned minerals can be used as efficient sorbents; subsequent development work yielded patented techniques for removing sulfur dioxide from waste gas in the production of sulfuric acid and heavy nonferrous metals from sulfide ores and in heat and power engineering (Chelishchev et al. 1984, 1986). Among the recently described natural prototypes for microporous materials, of particular note is Lovozero's titanosilicate seidite-(Ce), $Na_4(Ce,Sr)_2\{Ti(OH)_2(Si_6O_{18})\}(O,OH,Fe)_4 \cdot H_2O$ (Khomyakov et al. 1998; Ferraris et al. 2003). Owing to its mixed-framework structure traversed by wide through channels, this mineral is capable of actively interacting with organic liquids and salts of different metals at room temperature and of exchanging Na for Tl, K, Rb, Cs, and Ba.

In recent years the extensive families of natural amphoterosilicates and other minerals with mixed anionic radicals have received considerable attention from environmental scientists as a class of materials with a large capacity to hold radionuclides and other elements of high-level nuclear waste (Khomyakov 2004a). This is reflected in the rapid growth of research papers on the conditions of synthesis and properties of these minerals, including zorite, keldyshite, kostylevite, lovdarite, nenadkevichite, penkvilksite, seidite, terskite, and umbite, which were first described as new minerals from the hyperagpaitic rocks of the Khibina–Lovozero complex (Lin et al. 1997). Many mineralogists and materials engineers in various countries are now engaged in the search for new types of natural matrices for immobilizing high-level radioactive waste, as indicated by the highly successful international symposium "Micro- and Mesoporous Mineral Phases," which was recently held in Rome (Khomyakov 2004b; Ferraris and Merlino 2005). Another important milestone in this direction will undoubtedly be the present international symposium at Apatity, where more than half of the papers included in the program are based to one degree or another on studies of minerals of hyperagpaitic rocks.

There is no doubt that effective methods for disposing high-level waste components will ultimately certainly be found, in particular based on their immobilization within crystalline matrices of natural origin. The crystalline state is the dominant form of fixation of chemical elements in the Earth's crust, ensuring the high compositional stability of the hydrosphere and atmosphere and thus the evolutionary development of organic life on our planet. Transforming the major portion of high-level waste into the crystalline state would allow humanity to maintain favorable environmental conditions for life on Earth over a period of time comparable to geologic periods.

Acknowledgements This work was supported by the Russian Foundation for Basic Research, project no. 07-05-00084.

References

Chelishchev NF, Berenshtein BG, Khomyakov AP, Smola VI (1986) A method for removing sulfur dioxide from gases. Author's Certificate no. 1241558, Byull. Otkrytiya, Izobreteniya, no 24 (in Russian)

Chelishchev NF, Khomyakov AP, Berenshtein BG, Smola VI, Lukin VD (1984) A method for removing sulfur dioxide from gases. Author's Certificate no 1096794, Byull. Otkrytiya, Izobreteniya, no 21 (in Russian)

Ferraris G (1997) Polysomatism as a tool for correlating properties and structures. In: Merlino S (ed) Modular aspects of minerals, EMU Notes in Mineralogy, vol 1. Eotvos University Press Budapest, pp 275–295

Ferraris G, Belluso E, Gula A, Soboleva SV, Khomyakov AP (2003) The crystal structure of seidite-(Ce), $Na_4(Ce,Sr)_2\{Ti(OH)_2(Si_8O_{18})\}(O,OH,F)_4{\cdot}5H_2O$, a modular microporous titanosilicate of the rhodesite group. Can Mineral 41:1183–1192

Ferraris G, Khomyakov AP, Belluso E, Soboleva SV (1997) Polysomatic relationships in some titanosilicates occurring in the hyperagpaitic alkaline rocks of the Kola Peninsula, Russia. Proc 30th Int Geol Congr 16:17–27

Ferraris G, Merlino S (eds) (2005) Micro- and mesoporous mineral Phases. Rev Mineral Geochem, vol 57

Joung DA (1967) Methods for manufacture of group IV-B metallosilicate zeolites. US Patent Office, no 3.329 (480, 481, 482)

Khomyakov AP (1976a) Constitution and typochemical features of the lomonosovite group minerals. Constitution and Properties of Minerals, Kiev, Naukova Dumka 10:96–104 (in Russian)

Khomyakov AP (1976b) The types of oriented intergrowths of the keldyshite group minerals. Geochemistry, Mineralogy, Petrology 25th Int Geol Congr Papers by Soviet Geologists Moscow Nauka 233–240 (in Russian with English abs)

Khomyakov AP (1976c) Homoaxial pseudomorphs of titano- and zirconosilicates as indicators of the physicochemical conditions of mineral formation in alkaline massifs. Problems of Genetic Information in Mineralogy. All-Union Mineralogical Seminar, Syktyvkar, Komi Branch, USSR Academy of Sciences, p 68 (in Russian)

Khomyakov AP (1980a) Inheritance of crystal structures in minerals owing to pseudomorphism as a factor of speciation. Genetic Information in Minerals Syktyvkar Komi Branch Acad Nauk USSR 31:20–21 (in Russian)

Khomyakov AP (1980b) Typomorphism of minerals in hyperagpaitic pegmatites. Scientific Bases and Utilization of the Typomorphism of Minerals Nauka Moscow 152–157 (in Russian with English abs)

Khomyakov AP (1990) Mineralogy of Hyperagpaitic Alkaline Rocks. Nauka, Moscow (in Russian with English abs)

Khomyakov AP (1995) Mineralogy of Hyperagpaitic Alkaline Rocks (Translated from the Russian edition of 1990: Moscow, Nauka). Clarendon Press, Oxford, UK

Khomyakov AP (1996) Transformation mineral species and their use in palaeomineralogical reconstructions. 30th Int Geol Congr Beijing China 2/3:450

Khomyakov AP (1997) Recent mineral discoveries and the number of mineral species: a reconsideration. Structure and Evolution of the Mineral World Int Mineral Seminar Syktyvkar Geoprint 98–99

Khomyakov AP (2002) Highly ordered amphoterosilicates of the eudialyte group as indicators of maximally alkaline conditions of mineral formation in magmatic processes. Geochemistry of Igneous Rocks. Alkaline Magmatism of the Earth. All-Russia Seminar Involving CIS Countries, Moscow, GEOKHI, pp 96–97 (in Russian)

Khomyakov AP (2004a) Natural aluminium-free micro- and mesoporous amphoterosilicates—a unique class of matrices for immobilizing high-level waste. 32th Int Geol Congr Florence Italy Abstr part 1, p 534

Khomyakov AP (2004b) Zeolite-like amphoterosilicates of hyperagpaitic rocks and their unique properties. Micro- and Mesoporous Mineral Phases, Accademia Nazionale dei Lincei, Rome 231–234

Khomyakov AP (2006) The record contribution of the Kola region to the overall system of mineral species. Proc. III Fersman Scientific Session, Kola Division, Russian Mineral. Soc, Apatity, K & M, pp 96–98 (in Russian)

Khomyakov AP, Ferraris G, Belluso E, Britvin SN, Nechelyustov GN, Soboleva SV (1998) Seidite-(Ce), $Na_4SrCeTiSi_8O_{22}F \cdot 5H_2O$, a new mineral with zeolitic properties. Zapiski VMO 4:94–100 (in Russian with English abs)

Khomyakov AP, Kaptsov VV, Shchepochkina NI, Rudnitskaya ES (1978) Superfast hydrolysis of peralkalic titano- and zirconosilicates: experimental verification (in Russian). Dokl Akad Nauk SSSR 243(4):1028–1031

Khomyakov AP, Yushkin NP (1981) The principle of inheritance in crystallogenesis. Dokl Akad Nauk SSSR 256(5):1229–1233 (in Russian)

Lin Z, Rocha J, Brandao P, Ferreira A, Esculcas AP, Jesus JDP, Philippou A, Anderson W (1997) Synthesis and structural characterization of microporous umbite, penkvilksite and other titanosilicates. J Phys Chem B 101:7114–7120

Pekov IV (2005) Genetic mineralogy and crystal chemistry of rare elements in highly alkaline postmagmatic systems, Author's Abstract of Doctoral (Geol-Mineral) Dissertation, Moscow, Moscow State University (in Russian)

Solodov NA, Chepizhnyi KI, Chelishchev NF, Khomyakov AP, Kapitonova TA, Kremenetsky AA, Nazarova AE (1977) Natural minerals as a basis of new materials. Zapiski VMO 2:193–200 (in Russian)

Solodov NA, Chepizhnyi KI, Chelishchev NF, Kremenetsky AA, Nazarova AE, Khomyakov AP (1978) New directions in industrial use of natural minerals. Express Information on Laboratory and Technological Studies and the Concentration of Mineral Raw Materials Moscow VIEMS 4:1–19 (in Russian)

Yushkin NP, Khomyakov AP, Evzikova NZ (1984) The principle of inheritance in mineral genesis. Preprint no 93, Syktyvkar, Komi Branch, USSR Academy of Sciences, pp 1–32 (in Russian with English abs)

Trigonal Members of the Lovozerite Group: A Re-investigation

Andrey A. Zolotarev, Sergey V. Krivovichev, Viktor N. Yakovenchuk, Thomas Armbruster and Yakov A. Pakhomovsky

Minerals of the lovozerite group are natural microporous titano- and zirconosilicates. Understanding crystal chemistry of these minerals might be useful for understanding specific features of microporous octahedral-tetrahedral materials in general, especially those that are of existing or potential use in chemical industry. Today the lovozerite group includes nine minerals: trigonal (lovozerite, tisinalite, kazakovite, zirsinalite, combeite), orthorhombic (koashvite, imandrite) and monoclinic (kapustinite, litvinskite).

Lovozerite, has been first described by Gerasimovskii (1939) from the Lovozero alkaline massif, Kola peninsula, Russia. The crystal structure of lovozerite was reported by Ilyukhin and Belov (1960a, b) as based upon six-membered rings of silicate tetrahedra in chair configuration. Initially, the structure was solved in the monoclinic space group *C*2, though the crystals were reported to display optically uniaxial properties. Later and Yamnova et al. (2001a) refined the lovozerite structure in the space group *R*3. In 1970–1980s, a number of lovozerite-type minerals were found in the alkaline massifs of the Kola peninsula: koashvite, (Kapustin

Andrey A. Zolotarev
Department of Crystallography, Faculty of Geology, St. Petersburg State University, St. Petersburg, Russia, e-mail: AAZolotarev@gmail.com

Sergey V. Krivovichev
Department of Crystallography, Faculty of Geology, St. Petersburg State University, St. Petersburg, Russia

Viktor N. Yakovenchuk
Geological Institute of the Kola Science Center of the Russian Academy of Sciences, Apatity 184200, Russia

Thomas Armbruster
Institute of Geological Sciences, research group: mineralogical crystallography, University of Bern, Freiestr. 3, CH-3012 Bern, Switzerland

Yakov A. Pakhomovsky
Geological Institute of the Kola Science Center of the Russian Academy of Sciences, Apatity 184200, Russia

et al. 1974a), zirsinalite, (Kapustin et al. 1974b), (Khomyakov et al. 1974), imandrite (Khomyakov et al. 1979), and tisinalite (Kapustin et al. 1980). Zirsinalite, kazakovite, and tisinalite have been described as trigonal, whereas imandrite and koashvite have been determined as orthorhombic. Combeite, is another trigonal lovozerite-group mineral that had initially been described from nephelinites of the Mt. Shaheru, Congo (Zaire) (Sahama and Hytoeonen 1957) and later from nephelinite and ash ejecta of the Oldoinyo Lengai volcano (Tanzania) (Dawson et al., 1989).

There are two varieties of combeite that have been identified as combeite-high and combeite-low which crystallize in the space groups $R\bar{3}m$ and $P3_121$, respectively (Fischer and Tillmanns 1983, 1987; Ohsato et al. 1985; Ohsato and Takeuchi 1986). Recently, two new mineral species of the lovozerite group, litvinskite (Pekov et al. 2000) and kapustinite (Pekov et al. 2003), have been approved by the Commission on New Minerals and Mineral Names of the International Mineralogical Association (CNMMN IMA). Their structures have been determined to be monoclinic (Yamnova et al. 2001b, 2004).

We have studied crystal structures of 13 trigonal samples of the lovozerite-group minerals from various localities within the Khibiny and Lovozero alkaline massifs of the Kola peninsula, Russia (Table 1). All 13 samples were successfully refined in the maximal space group $R\bar{3}m$ and were identified as lovozerite, kazakovite, tisinalite, and zirsinalite (Table 2). No indications of superstructure or symmetry lowering have been observed. Crystals selected for X-ray diffraction experiments were mounted on a Bruker three-circle CCD-based X-ray diffractometer. The unit-cell parameters were refined using least-squares techniques (Table 2). Crystal chemical formulas for the lovozerite-group minerals are given in Table 2. Systematic absences and reflection statistics were consistent with the space group $R\bar{3}m$ for all 13 crystals.

Table 1 Sample localities for the lovozerite-group mineral samples studied by the authors

Sample	Locality
9	Alluaiv Mt., Lovozero massif
12AR	Alluaiv Mt., Lovozero massif
70	Palitra pegmatite (Palette pegmatite), Kedykverpakhk Mt., Lovozero massif
73	Koashva Mt., Khibiny massif
64	Rasvumchorr Mt., Khibiny massif
65	= 'litvinskite'? Shkatulka pegmatite, Umbozero mine, Alluaiv Mt., Lovozero massif
67	Rasvumchorr Mt., Khibiny massif
10	Alluaiv Mt., Lovozero massif
12AU	Alluaiv Mt., Lovozero massif
56	Rasvumchorr Mt., Khibiny massif
51	Palitra pegmatite (Palette pegmatite), Kedykverpakhk Mt., Lovozero massif
52	= 'kapustinite'? Palitra pegmatite (Palette pegmatite), Kedykverpakhk Mt., Lovozero massif
72	Rasvumchorr Mt., Khibiny massif

Table 2 Crystallographic data and chemical composition of minerals of the lovozerite group studied by the authors

Mineral	Sample	Space group	a, Å	c, Å	R_1 (obs. refl.)	Chemical formula $A_3B_3C_2M[Si_6O_{18}]$
Lovozerite	9	$R\bar{3}m$	10.1646(4)	13.061(1)	0.0464 (593)	$Na_{2.19}Mn_{0.23}(Zr_{0.92}Ti_{0.08})$ $[Si_6(O_{12.65}(OH)_{5.35})]$
	12AR	$R\bar{3}m$	10.1663(4)	13.036(1)	0.0408 (565)	$Na_{2.22}Mn_{0.30}(Zr_{0.93}Ti_{0.07})$ $[Si_6(O_{12.82}(OH)_{5.18})]$
	70	$R\bar{3}m$	10.140(3)	13.125(5)	0.0488 (312)	$Na_{2.57}Mn_{0.18}(Zr_{0.84}Ti_{0.16})$ $[Si_6(O_{12.93}(OH)_{5.07})]$
	73	$R\bar{3}m$	10.155(2)	13.139(2)	0.0437 (294)	$Na_{2.61}Mn_{0.20}(Zr_{0.85}Ti_{0.15})$ $[Si_6(O_{13.01}(OH)_{4.99})]$
	64	$R\bar{3}m$	10.184(5)	13.171(9)	0.0449 (302)	$Na_{2.41}Ca_{0.24}Fe_{0.05}$ $(Zr_{0.84}Ti_{0.16})$ $[Si_6(O_{12.99}(OH)_{5.01})]$
	65	$R\bar{3}m$	10.213(2)	13.177(3)	0.0446 (292)	$Na_{2.26}Mn_{0.21}Ca_{0.15}$ $(Zr_{0.99}Ti_{0.01})$ $[Si_6(O_{12.98}(OH)_{5.02})]$
	67	$R\bar{3}m$	10.102(2)	13.044(3)	0.0394 (333)	$Na_{2.37}Ca_{0.15}Fe_{0.09}Mn_{0.05}$ $(Zr_{0.88}Ti_{0.12})$ $[Si_6(O_{12.95}(OH)_{5.05})]$
Tisinalite	10	$R\bar{3}m$	10.033(5)	12.895(8)	0.0515 (430)	$Na_{2.03}Mn_{0.39}Fe_{0.06}$ $(Ti_{0.73}Zr_{0.20}Nb_{0.07})$ $[Si_6(O_{13.00}(OH)_{5.00})]$
	12AU	$R\bar{3}m$	10.057(1)	12.931(1)	0.0456 (482)	$Na_{1.94}Mn_{0.52}(Ti_{0.87}Zr_{0.13})$ $[Si_6(O_{12.98}(OH)_{5.02})]$
	56	$R\bar{3}m$	10.025(2)	13.085(2)	0.0474 (416)	$Na_{2.73}Na_{0.93}Fe_{0.28}Mn_{0.25}$ $(Ti_{0.92}Zr_{0.08})$ $[Si_6(O_{14.98}(OH)_{3.02})]$
Kazakovite	51	$R\bar{3}m$	10.163(1)	13.042(2)	0.0345 (295)	$Na_{2.97}Na_{2.27}Mn_{0.64}Fe_{0.29}$ $(Ti_{0.86}Zr_{0.14})$ $[Si_6(O_{17.13}(OH)_{0.87})]$
Zirsinalite	52	$R\bar{3}m$	10.306(1)	13.128(2)	0.0422 (308)	$Na_{3.00}Na_{2.07}Mn_{0.92}Ca_{0.10}$ $(Zr_{0.90}Ti_{0.10})$ $[Si_6(O_{17.11}(OH)_{0.89})]$
	72	$R\bar{3}m$	10.322(6)	13.158(5)	0.0414 (292)	$Na_{2.91}Na_{2.40}$ $(Ca_{0.80}Na_{0.60}Mn_{0.09})$ $(Zr_{0.82}Fe_{0.13}Ti_{0.05})$ $[Si_6(O_{17.56}(OH)_{0.44})]$

The space-group assignments were confirmed by the structure refinements. The Bruker SHELXTL Version 5.1. system of programs was used for the determination and refinement of the crystal structures. The final models included all atomic positional parameters, anisotropic-displacement parameters for all atoms, and weighting schemes of the structure factors. The final refinement converged to agreement indices (R_1) given in Table 2. The final coordinates and isotropic displacement parameters are given in Table 3.

Minerals of the lovozerite group are cyclosilicates with general formula $A_3B_3C_2M[Si_6O_{18}]$ (A = Na, Ca; B = Na, Ca; C = Mn, Ca, Fe, Na; M = Zr, Ti, Fe^{3+}, Ca.

The framework of crystal structures of minerals of the lovozerite group are based upon six-membered rings of silicate tetrahedra (Si_6O_{18})connected through the common tops with isolated *M*-octahedron (*M* = Ti, Zr, Fe^{3+}) which are connected through the common planes with *C*-octahedron (*C* = Mn, Fe, Ca, Na). Inside framework are located atoms of sodium and a molecule of water - positions *A* and *B*.

The nomenclature of the trigonal lovozerite-group minerals is based upon two chemical principles. First, in terms of the *M* sites, there are Zr-rich (zirsinalite, lovozerite), Ti-rich (tisinalite, kazakovite), and Ca-rich (combeite) members. Second, among the Ti and Zr members, there are Na-rich (zirsinalite, kazakovite) and Na-deficient (lovozerite, tisinalite) members (position *B*). This rather simple classification scheme for Ti and Zr members is presented in the following Scheme:

	B site occupancy	
	Na > 50%	Na < 50%
Ti > Zr	kazakovite	tisinalite
Zr > Ti	zirsinalite	lovozerite

This scheme takes into account the *M* sites (that can be occupied by Ti and Zr), the *A* sites (occupied by Na in all members), and the *B* sites (occupied by Na in Na-rich members). According to the accepted nomenclature, we had been structurally studied (Table 2) seven crystals of lovozerite (samples 9, 12ap, 64, 65, 67, 70, 73), three crystals of tisinalite (samples 10, 12ay, 56), one crystal of kazakovite (the sample 51) and two crystals of zirsinalite (samples 52, 72).

Trigonal members of the lovozerite group include lovozerite, kazakovite, tisinalite, zirsinalite, and combeite (not studied in this work). The structure of *kazakovite* was refined by Voronkov et al. (1979) in space group $R\bar{3}m$ that is the maximal symmetry for the trigonal lovozerite-type structure (Malinovsky et al. 1993). Our sample 51 was identified as kazakovite on the basis of chemical and structural studies and the space group $R\bar{3}m$ was confirmed.

The structure of *zirsinalite* was studied by Pudovkina et al. (1980) and reported in the space group $R\bar{3}c$ and rhombohedral unit cell with parameters $a = 10.593(5)$ ´Å, $\alpha = 58.13(2)^{o}$. This cell is equivalent to the *R* cell in a hexagonal setting with parameters $a = 10.29$, $c = 26.31$ Å, i.e. with doubled *c* parameter as compared to the 'usual' trigonal lovozerite-type structure (Table 2). The R_1 index obtained by Pudovkina et al. (1980) was rather high (0.087). Our samples 52 and 72 were identified as zirsinalite by microprobe analyses (high Na content, Zr-rich member). The structure refinements for both crystals proceeded smoothly in space group $R\bar{3}m$ without any indication of a doubled *c* parameter. The R_1 indices are 0.042 and 0.041 for the samples 52 and 72, respectively. The observed differences between our results and those reported by Pudovkina et al. (1980) may be explained either by twinning effects that were not taken into account by the previous authors, or by a possible superstructure.

Table 3 Atomic coordinates, occupancies, and isotropic displacement parameters of the minerals of the lovozerite group studied by the authors

Site	Sample*	*x*	*y*	*z*	Occupancy	U_{eq}, Å^2
Si	LV-9	0.14968(7)	0.2994(1)	0.06328(9)	Si	0.0399(4)
	LV-12AR	0.14960(6)	0.2992(1)	0.06327(8)	Si	0.0397(3)
	LV-70	0.1492(1)	0.2983(2)	0.0635(1)	Si	0.0385(8)
	LV-73	0.1492(1)	0.2983(2)	0.0634(1)	Si	0.0364(7)
	LV-64	0.14960(9)	0.2992(2)	0.0633(1)	Si	0.0389(6)
	LV-65	0.1495(1)	0.2990(2)	0.0635(1)	Si	0.0469(7)
	LV-67	0.14966(8)	0.2993(2)	0.0639(1)	Si	0.0370(6)
	TS-10	0.15163(7)	0.3033(1)	0.06448(9)	Si	0.0376(4)
	TS-12AU	0.15210(6)	0.3042(1)	0.06487(8)	Si	0.0308(4)
	TS-56	0.15199(7)	0.3040(2)	0.06629(9)	Si	0.0230(4)
	KZ-51	0.15215(7)	0.3043(1)	0.06894(9)	Si	0.0199(4)
	ZS-52	0.15037(9)	0.3008(2)	0.0668(1)	Si	0.0254(7)
	ZS-72	0.1510(1)	0.3020(2)	0.0671(1)	Si	0.0136(8)
M	LV-9	1/3	2/3	1/6	$Zr_{0.92}Ti_{0.08}$	0.0274(3)
	LV-12AR	1/3	2/3	1/6	$Zr_{0.93}Ti_{0.07}$	0.0276(2)
	LV-70	1/3	2/3	1/6	$Zr_{0.84}Ti_{0.16}$	0.0302(6)
	LV-73	1/3	2/3	1/6	$Zr_{0.85}Ti_{0.15}$	0.0286(6)
	LV-64	1/3	2/3	1/6	$Zr_{0.84}Ti_{0.16}$	0.0299(6)
	LV-65	1/3	2/3	1/6	$Zr_{0.99}Ti_{0.01}$	0.0349(5)
	LV-67	1/3	2/3	1/6	$Zr_{0.88}Ti_{0.12}$	0.0275(5)
	TS-10	1/3	2/3	1/6	$Ti_{0.73}Zr_{0.20}Nb_{0.07}$	0.0301(4)
	TS-12AU	1/3	2/3	1/6	$Ti_{0.87}$ $Zr_{0.13}$	0.0228(4)
	TS-56	1/3	2/3	1/6	$Ti_{0.92}Zr_{0.08}$	0.0171(6)
	KZ-51	1/3	2/3	1/6	$Ti_{0.86}Zr_{0.14}$	0.0159(6)
	ZS-52	1/3	2/3	1/6	$Zr_{0.90}Ti_{0.10}$	0.0219(6)
	ZS-72	1/3	2/3	1/6	$Zr_{0.82}Fe_{0.13}Ti_{0.05}$	0.0119(6)
C	LV-9	0	0	0.253(1)	$Mn_{0.11}$	0.060(5)
	LV-12AR	0	0	0.2520(7)	$Mn_{0.15}$	0.058(3)
	LV-70	0	0	0.254(1)	$Mn_{0.09}$	0.048(8)
	LV-73	0	0	0.253(1)	$Mn_{0.10}$	0.049(7)
	LV-64	0	0	0.255(1)	$Ca_{0.12}Fe_{0.03}$	0.072(9)
	LV-65	0	0	0.241(2)	$Mn_{0.10}Ca_{0.08}$	0.095(7)
	LV-67	0	0	0.252(1)	$Ca_{0.08}Fe_{0.04}$ $Mn_{0.02}$	0.067(6)
	TS-10	0	0	0.2549(5)	$Mn_{0.18}Fe_{0.04}$	0.060(2)
	TS-12AU	0	0	0.2552(4)	$Mn_{0.26}$	0.050(1)
C	TS-56	0	0	0.2546(3)	$Fe_{0.14}Mn_{0.12}Ca_{0.06}$	0.026(1)
	KZ-51	0	0	0.2552(2)	$Mn_{0.32}Fe_{0.14}$	0.025(1)
	ZS-52	0	0	0.2507(3)	$Mn_{0.46}Ca_{0.05}$	0.037(1)
	ZS-72	0	0	0.2522(3)	$Ca_{0.40}Na_{0.30}Mn_{0.04}$	0.022(1)
O1	LV-9	0.2390(2)	0.4779(5)	0.0750(4)	O	0.080(1)
	LV-12AR	0.2389(2)	0.4779(4)	0.0752(3)	O	0.078(1)
	LV-70	0.2371(4)	0.4742(7)	0.0747(5)	O	0.077(2)
	LV-73	0.2370(3)	0.4740(6)	0.0746(4)	O	0.075(2)
	LV-64	0.2370(3)	0.4741(6)	0.0752(4)	O	0.078(2)
	LV-65	0.2378(3)	0.4755(6)	0.0774(4)	O	0.079(2)
	LV-67	0.2385(3)	0.4770(5)	0.0763(4)	O	0.074(2)
	TS-10	0.2425(2)	0.4851(4)	0.0761(3)	O	0.072(1)
	TS-12AU	0.2431(2)	0.4862(3)	0.0769(3)	O	0.059(1)

Table 3 (continued)

Site	Sample*	*x*	*y*	*z*	Occupancy	U_{eq}, Å^2
O1	TS-56	0.2433(2)	0.4865(4)	0.0754(3)	O	0.0376(9)
	KZ-51	0.2436(2)	0.4873(4)	0.0727(3)	O	0.0318(9)
	ZS-52	0.2412(2)	0.4824(4)	0.0682(3)	O	0.043(1)
	ZS-72	0.2414(2)	0.4829(5)	0.0656(4)	O	0.029(1)
O2	LV-9	0.1043(3)	0.2086(6)	0.1719(3)	O	0.083(2)
	LV-12AR	0.1045(3)	0.2091(6)	0.1724(2)	O	0.085(2)
	LV-70	0.1053(4)	0.2106(8)	0.1717(4)	O	0.083(2)
	LV-73	0.1051(4)	0.2101(7)	0.1715(4)	O	0.080(2)
	LV-64	0.1050(4)	0.2101(7)	0.1720(4)	O	0.083(2)
	LV-65	0.1038(4)	0.2077(8)	0.1709(4)	O	0.093(2)
	LV-67	0.1042(3)	0.2085(7)	0.1724(3)	O	0.078(2)
	TS-10	0.1070(2)	0.2140(5)	0.1744(3)	O	0.077(1)
	TS-12AU	0.1077(2)	0.2155(4)	0.1748(2)	O	0.068(1)
	TS-56	0.1080(3)	0.2160(6)	0.1732(3)	O	0.066(1)
	KZ-51	0.1100(2)	0.2201(4)	0.1751(2)	O	0.038(1)
	ZS-52	0.1115(3)	0.2229(5)	0.1738(3)	O	0.054(1)
	ZS-72	0.1130(3)	0.2259(5)	0.1735(3)	O	0.038(1)
O3	LV-9	0.2528(7)	0.2528(7)	0	O	0.098(2)
	LV-12AR	0.2532(5)	0.2532(5)	0	O	0.090(1)
	LV-70	0.256(1)	0.256(1)	0	O	0.012(3)
	LV-73	0.2565(8)	0.2565(8)	0	O	0.098(3)
	LV-64	0.2557(8)	0.2557(8)	0	O	0.016(2)
	LV-65	0.2519(6)	0.2519(6)	0	O	0.082(2)
	LV-67	0.2549(8)	0.2549(8)	0	O	0.091(2)
	TS-10	0.2564(5)	0.2564(5)	0	O	0.093(2)
	TS-12AU	0.2584(5)	0.2584(5)	0	O	0.078(1)
	TS-56	0.2584(5)	0.2584(5)	0	O	0.052(1)
	KZ-51	0.2584(3)	0.2584(3)	0	O	0.0312(8)
	ZS-52	0.2539(4)	0.2539(4)	0	O	0.045(1)
	ZS-72	0.2534(4)	0.2534(4)	0	O	0.039(1)
A	LV-9	1/6	1/3	1/3	$Na_{0.73}$	0.041(1)
	LV-12AR	1/6	1/3	1/3	$Na_{0.74}$	0.045(1)
	LV-70	1/6	1/3	1/3	$Na_{0.86}$	0.048(2)
	LV-73	1/6	1/3	1/3	$Na_{0.87}$	0.049(1)
	LV-64	1/6	1/3	1/3	$Na_{0.80}$	0.045(2)
	LV-65	1/6	1/3	1/3	$Na_{0.75}$	0.058(2)
	LV-67	1/6	1/3	1/3	$Na_{0.79}$	0.044(1)
	TS-10	1/6	1/3	1/3	$Na_{0.68}$	0.041(1)
	TS-12AU	1/6	1/3	1/3	$Na_{0.65}$	0.037(1)
	TS-56	1/6	1/3	1/3	$Na_{0.91}$	0.049(2)
	KZ-51	1/6	1/3	1/3	$Na_{0.99}$	0.032(1)
	ZS-52	1/6	1/3	1/3	Na	0.041(1)
	ZS-72	1/6	1/3	1/3	$Na_{0.97}$	0.021(1)
*B***	TS-56	-1/6	1/6	1/6	$Na_{0.31}$	0.012(3)
	KZ-51	-1/6	1/6	1/6	$Na_{0.76}$	0.027(1)
	ZS-52	-1/6	1/6	1/6	$Na_{0.69}$	0.039(2)
	ZS-72	-1/6	1/6	1/6	$Na_{0.78}$	0.025(2)

* LV = lovozerite; TS = tisinalite; KZ = kazakovite; ZS = zirsinalite.

** this position is vacant in samples LV-9, 12AR, 70, 73, 64, 65, 67, TS-10, and 12AU.

The structure of *lovozerite* has been studied by Yamnova et al. (2001a) and refined in the space group $R3$ to the R_1 index of 0.077. Our structure refinements of the samples 9, 12AR, 70, 73, 64, 65, and 67, identified as lovozerite, were successful in the space group $R\bar{3}m$ without observation of additional superstructure reflections. The R_1 indices obtained did not exceed 0.047. At the moment we are unable to explain the differences between our study and the results reported by Yamnova et al. (2001a).

The structure of *tisinalite* was refined by Yamnova et al. (2003) in the space group $P\bar{3}$. These authors observed 'a small number of weak reflections not satisfying the rule of systematic extinction $-h+k+l=3n$' that led them to the conclusion that primitive cell is preferred for tisinalite. We studied three tisinalite crystals (10, 12AU, and 56) and did not obtain any violations of their structures from the $R\bar{3}m$ symmetry. The disagreement with the results of Yamnova et al. (2003) might be explained by the obverse-reverse twinning frequently observed for rhombohedral crystals (Herbstirmer and Sheldrick 2002) and responsible for the reflections that violate the '$-h+k+l=3n$' systematic absences rule.

Acknowledgements We thank Swiss National Foundation (SNF) for financial support of the collaboration between the Russian and Swiss research groups. Russian authors thank Russian federation Ministry of Science and Education for financial support through the RNP grant (2.1.1.3077), 'Molecular geochemistry and biogeochemistry' project of the program 'Innovative education environment in a classical University' and INTAS program for young sciences (05-109-4549).

References

Bruker (1997) SHELXTL, Version 5.1. Bruker AXS Inc, Madison, Wisconsin, USA

Dawson JB, Smith JV, Steele IM (1989) Combeite ($Na_{2.33}Ca_{1.74}others_{0.12}$)$Si_3O_9$ from Oldoinyo Lengai, Tanzania. J Geol 97:365–372

Fischer RX, Tillmanns E (1983) Die Kristallstrukturen von natuerlichem $Na_2Ca_2Si_3O_9$ vom Mt. Shaheru (Zaire) und aus dem Mayener Feld (Eifel). Neues Jb Miner Monat 49–59

Fischer RX, Tillmanns E (1987) Revised data for combeite $Na_2Ca_2Si_3O_9$. Acta Crystallogr C 43:1852–1854

Gerasimovskii VI (1939) Lovozerite – a new mineral. Dokl Akad Nauk SSSR A 25:753–756

Herbst-Irmer R, Sheldrick G (2002) Refinement of obverse/reverse twins. Acta Crystallogr B 58:478–481

Ilyukhin VV, Belov NV (1960a) Determination of the structure of lovozerite from sections of three-dimensional Patterson functions. Kristallografiya 5:200–214 (in Russian)

Ilyukhin VV, Belov NV (1960b) Crystal structure of lovozerite. Dokl Akad Nauk SSSR 131: 176–179 (in Russian)

Kapustin YuL, Pudovkina ZV, Bykova AV, Lyubomilova GV (1974a) Koashvite, a new mineral. Zapiski VMO 103:559–566 (in Russian)

Kapustin YL, Pudovkina ZV, Bykova AV (1974b) Zirsinalite, a new mineral. Zapiski VMO 103:551–558 (in Russian)

Kapustin YuL, Pudovkina ZV, Bykova AV (1980) Tisinalite – $Na_3H_3(Mn,Ca,Fe)TiSi_6(O,OH)_{18}2H_2O$ – a new mineral of the lovozerite group. Zapiski VMO 109:223–229 (in Russian)

Khomyakov AP, Semenov EI, Es'kova EM, Voronkov AA (1974) Kazakovite, a new mineral from the lovozerite group. Zapiski VMO 103:342–345 (in Russian)

Khomyakov AP, Chernitsova NM, Sandomirskaya SM, Vasil'eva GL (1979) Imandrite, a new mineral of the lovozerite family. Mineral Zh 1:89–93 (in Russian)

Malinovsky YuA, Burzlaff H, Rothammel W (1993) Structures of the lovozerite type – a quantitative investigation. Acta Crystallogr B 49:158–164

Ohsato H, Maki I, Takeuchi Y (1985) Structure of $Na_2CaSi_2O_6$. Acta Crystallogr C 41:1575–1577

Ohsato H, Takeuchi Y (1986) Structure of $Na_4Ca_4(Si_6O_{18})$. Acta Crystallogr C 42:924–927

Pekov IV, Ekimenkova IA, Chukanov NV, Zadov AE, Yamnova NA, Egorov-Tismenko YuK (2000) Litvinskite Na_2(,Na,Mn)$Zr[Si_6O_{12}(OH,O)_6]$ – a new mineral of the lovozerite group. Zapiski VMO 129:1:45–53 (in Russian)

Pekov IV, Chukanov NV, Yamnova NA, Egorov-Tismenko YuK, Zadov AE (2003) New mineral kapustinite $Na_{5.5}Mn_{0.25}ZrSi_6O_{16}(OH)_2$ from Lovozero massif (Kola Peninsula) and new data on the genetic crystallochemistry of the lovozerite group. Zapiski VMO 123:6:1–14 (in Russian)

Pudovkina ZV, Chernitsova NM, Voronkov AA, Pyatenko YuA (1980) Crystal structure of zirsinalite $Na_6Ca(Zr(Si_6O_{18})$. Dokl Akad Nauk SSSR 250:865–867 (in Russian)

Sahama TG, Hytoeonen K (1957) Goetzenite and combeite, two new silicates from the Belgian Congo. Mineral Mag 31:503–510

Voronkov AA, Pudovkina ZV, Blinov VA, Ilyukhin VV, Pyatenko YuA (1979) Crystal structure of kazakovite $Na_6Mn(Ti(Si_6O_{18}))$. Dokl Akad Nauk SSSR 245:106–109 (in Russian)

Yamnova NA, Egorov-Tismenko YuK, Pekov IV (2001a) Refined crystal structure of lovozerite $Na_2CaZr[Si_6O_{12}(OH,O)_6]\cdot H_2O$. Kristallografiya 46:1019–1023 (in Russian)

Yamnova NA, Egorov-Tismenko YuK, Pekov IV, Ekimenkova IA (2001b) Crystal structure of litvinskite – a new natural representative of the lovozerite group. Kristallografiya 46:230–233 (in Russian)

Yamnova NA, Egorov-Tismenko YuK, Pekov IV, Shchegol'kova LV (2003) Crystal structure of tisinalite $Na_2(Mn,Ca)_{1-x}(Ti,Zr,Nb,Fe^{3+})[Si_6O_8(O,OH)_{10}]$. Crystallogr Rep 48:551–556

Yamnova NA, Egorov-Tismenko YuK, Pekov IV, Shchegol'kova LV (2004) The crystal structure of kapustinite $Na_{5.5}Mn_{0.25}Zr[Si_6O_{16}(OH)_2]$: a new mineral of the lovozerite group. Dokl Earth Sci 397:658–662

Ion-Exchange Properties of Natural Sodium Zirconosilicate Terskite

Arina A. Grigorieva, Igor V. Pekov and Igor A. Bryzgalov

Terskite $Na_4ZrSi_6O_{16}\cdot 2H_2O$ is a zeolite-like zirconosilicate common in the hyperagpaitic pegmatites of the Lovozero alkaline massif (Kola Peninsula, Russia). The base of its crystal structure is the heteropolyhedral framework formed by branched infinite chains of Si tetrahedra and isolated Zr octahedra (Pudovkina and Chernitsova, 1991). Extra-framework Na atoms and H_2O molecules are located in the zeolite channels. The framework density is 18.0 Si and Zr atoms per 1000 $Å^3$. It allowed to suppose that the mineral is a potential ion-exchanger.

The cation-exchange properties of terskite were studied on a sample from the Shkatulka pegmatite located at Mountain Alluaiv in the north-western part of the Lovozero massif. Its chemical composition is well-corresponding to the formula above, contents of K and Ca impurities are <0.2 wt.%, contents of Rb, Cs, Sr and Ba are below detection limits for routine electron microprobe analysis.

Terskite grains with size of 0.5–2 mm were placed into aqueous solutions of KCl, $RbNO_3$, $CsNO_3$, $CaCl_2$, $SrCl_2$ and $BaCl_2$. Two series of experiments were developed:

(1) In 1N solutions: under room conditions for 2.5 months, at 90°C for 6 hours and at 150°C for 3 hours.
(2) For the examination of the influence of different parameters (salt concentration, temperature, pressure, duration of experiment) on the ion exchange, following experiments were made:

    in 0.01N, 0.1N and 1N KCl and $CsNO_3$ solutions at 20°C for 1 hour and 24 hours;

Arina A. Grigorieva
Faculty of Geology, Moscow State University, 119991 Moscow, Russia, e-mail: arina1984@bk.ru

Igor V. Pekov
Faculty of Geology, Moscow State University, 119991 Moscow, Russia
Institute of Geochemistry and Analytical Chemistry, 119991 Moscow, Russia

Igor A. Bryzgalov
Faculty of Geology, Moscow State University, 119991 Moscow, Russia

in 0.01N and 0.1N solutions of KCl at 90°C for 3 hours;
in 0.01N and 0.1N solutions of KCl at 150°C for 3 hours with autoclave filled for 75 and 25 vol.%.

After the experiments, samples were studied on polished sections using scanning electron microscopy (images in BSE) and quantitative electron microprobe analysis.

As a result of *the first series of experiments,* we have established that terskite shows ion exchange properties towards all cations used in the experiments. They displace Na both under room conditions and in "hot" experiments (90°C and 150°C). The maximum contents of exchanged cations were observed in cracked and porous areas. Temperature increase slightly influences on Na to K exchange whereas direct relation between exchange degree and temperature for Cs, Ca, Sr and Ba is found: the higher temperature the more contents of exchanged cations (Table 1).

The second series of experiments. In the experiments with KCl solutions at 20°C, the increase of exchange degree with the salt concentration raising occurs. The areas with the highest content of exchanged K are located along cracks and in porous zones. The ion exchange becomes more intensive with temperature and concentration increase in the experiments at 90 and 150°C, 3 hours (Table 2). The pressure (controlled by different amount of the solution in an autoclave) also influence to the ion exchange (Table 2). Duration of the experiment stronger influence on the degree of exchange in 0.01N and 0.1N solutions than 1N solution (Table 3).

The experiments with $CsNO_3$ solution at 20°C show no direct dependence of ion-exchange intensity on the salt concentration: more likely it depends on abundance of microcracks and porosity of the grains. It is the most obvious in the experiments with 1N $CsNO_3$ solution: in porous grain Na replacement by Cs in all space occurs for 1 hour whereas in solid grain the exchange occurs only in the areas along cracks even for 24 hours. The correlation between concentration of exchanged Cs and the experiment duration was found for 0.01N and 0.1N solutions unlike 1N solution (Table 3).

Table 1 Ranges of contents of exchanged cations in terskite

	K_2O	Rb_2O	Cs_2O	CaO	SrO	BaO
wt.% 20°C	5.7–10.2	0.3–23.9	1.2–21.5	0.5–7.7	2.7–12.6	0.2–19.0
apfu	(0.73–1.38)	(0.02–2.13)	(0.05–0.96)	(0.05–0.86)	(0.15–0.83)	(0.01–0.85)
wt.% 90°C	6.1–8.3	7.1–10.5	0–25.2	1.9–12.7	2.2–16.4	0.2–30.4
apfu	(0.70–1.08)	(0.34–0.68)	(1.14)	(0.20–1.53)	(0.11–1.10)	(0.01–1.57)
wt.% 150°C	10.7–13.7	1.3–8.6	5.7–32.9	*	2.3–20.8	2.8–33.5
apfu	(1.34–1.93)	(0.08–0.57)	(0.22–1.43)		(0.13–1.46)	(0.10–1.77)

Note: * – experiment did not work out due to some technical problems. Formulae were calculated on the basis of 6 Si atoms.

Table 2 Ranges of contents of exchanged K in terskite

	3 hours 90°C 0.1N	3 hours 90°C 0.01N	3 hours 150°C 0.1N, 3/4V	3 hours 150°C 0.01N, 3/4V	3 hours 150°C 0.1N, 1/4V	3 hours 150°C 0.01N, 1/4V
K_2O, wt.%	6.9–12.3	3.7–8.2	7.4–20.8	5.8–10.8	9.8–15.8	0.5–7.1
K, *apfu*	(0.86–1.66)	(0.46–1.09)	(0.96–2.75)	(0.78–1.62)	(1.21–2.23)	(0.06–0.97)

Note: formulae were calculated on the basis of 6 Si atoms. 1/4V and 3/4V means that an autoclave was filled for 25 and 75 vol.% respectively.

Table 3 Ranges of contents of exchanged K and Cs in terskite at 20°C

	1 hour 0.1N	24 hours 0.1N	1 hour 0.01N	24 hours 0.01N	1 hour 1N	24 hours 1N
K_2O wt.%	1.0–3.7	3.9–10.0	1.5–1.3	2.6–3.9	2.0–7.9	0.7–9.4
K, *apfu*	(0.11–0.51)	(0.47–1.39)	(0.23–0.17)	(0.36–0.54)	(0.26–1.11)	(0.09–1.32)
Cs_2O wt.%	0.6–7.6	1.4–21.9	1.5–6.5	2.5–28.3	0.8–23.2	0.4–23.8
Cs, *apfu*	(0.25–0.40)	(0.06–1.03)	(0.06–0.32)	(0.10–1.32)	(0.04–1.12)	(0.02–1.19)

Note: formulae were calculated on the basis of 6 Si atoms.

Thus, the temperature and the duration are more important for the cation exchange in terskite in dilute solutions than concentrated ones. The maximum contents of exchanged cations are in cracked and porous areas in all cases.

From the experimental data, we consider that ion-exchange processes can occur in terskite in nature, under hydrothermal and supergene (taking into account the result of the experiments at 20°C) conditions.

Terskite, as it was found, is a strong cationite for K, Cs and Ba not only at 90 and 150°C but also under room conditions. This property of the mineral may favor the use of its synthetic analogue in chemical technologies *e.g.* for the extraction of alkaline and earth-alkaline elements (Cs, Ba) from dilute solutions.

Acknowledgements We are grateful to E.V. Guseva for help in SEM study of our samples. This work was supported by grants of President of Russian Federation MD-7230.2006.5, NSh-4964.2006.5 and NSh-4818.2006.5, grant RFBR 06-05-90626-BNTS_a and grant of Russian Science Support Foundation (for IVP).

References

Pudovkina ZV, Chernitsova NM (1991) Crystal structure of terskite, $Na_4Zr[H_4Si_6O_{18}]$. Sov Phys Dokl 36:201–203

Chemistry of Cancrinite-Group Minerals from the Khibiny–Lovozero Alkaline Complex, Kola Peninsula, Russia

Lyudmila V. Olysych, Igor V. Pekov and Atali A. Agakhanov

Natural and synthetic microporous compounds of hexagonal symmetry with the general formula $A_{6-8}[T^{I}T^{II}O_4]_6X_{1-4} \cdot nH_2O$ (A = **Na**$^{+}$, **K**$^{+}$, **Ca**$^{2+}$; T^{I}= **Al**$^{3+}$; T^{II}= **Si**$^{4+}$, Ge^{4+}; X= **Cl**$^{-}$, **(OH)**$^{-}$, $(NO_3)^{-}$, **(CO$_3$)**$^{2-}$, **(SO$_4$)**$^{2-}$, **S**$^{2-}$, $(MoO_4)^{2-}$, $(WO_4)^{2-}$, $(PO_4)^{3-}$, $(VO_4)^{3-}$; species-forming constituents of minerals are marked boldtype) form the cancrinite family. The cancrinite-type structures are characterized by a framework of $T^{I}T^{II}O_4$ tetrahedra. The alternating AlO_4 and SiO_4 tetrahedra form six-membered rings. Within a framework, wide continuous channels parallel to the 6_3 axis and chains of small cages (cancrinite cages) along the three-fold axes occur. This structural cavities host alkaline and alkaline-earth cations (A), and a wide variety of extra-framework anions, as well as H_2O molecules (Bonaccorsi and Merlino, 2005).

Five members of the cancrinite group are known in the Khibiny–Lovozero alkaline complex (Kola Peninsula, Russia), namely cancrinite *ss*, vishnevite, cancrisilite, hydroxycancrinite and sacrofanite. The ideal formula of representatives of the cancrinite subgroup, the most common minerals in the Khibiny–Lovozero complex, have been presented as:

cancrinite – $[Al_6Si_6O_{24}][(Na,Ca)_6(CO_3)_{1-2}][Na_2(H_2O)_2]$,
vishnevite – $[Al_6Si_6O_{24}][Na_6(SO_4)][Na_2(H_2O)_2]$,
cancrisilite – $[Al_5Si_7O_{24}][Na_5(CO_3)(H_2O)][Na_2(H_2O)_2]$,
hydroxycancrinite – $[Al_6Si_6O_{24}][Na_6(OH)_2][Na_2(H_2O)_2]$,

where the framework composition, contents of the wide channel and contents of the cancrinite cages are given in brackets consequently.

Lyudmila V. Olysych
Faculty of Geology, Moscow State University, Moscow, Russia, e-mail: Olyssych@mail.ru

Igor V. Pekov
Faculty of Geology, Moscow State University, Moscow, Russia
Institute of Geochemistry and Analytical Chemistry, Moscow, Russia

Atali A. Agakhanov
Fersman Mineralogical Museum, Moscow, Russia

Thirty eight samples of cancrinite-subgroup minerals from different localities within the Khibiny–Lovozero complex were analysed using an electron microprobe instrument. These and all earlier published analyses of cancrinite-group minerals from Khibiny and Lovozero were calculated on the basis of (Si+Al+Fe)=12 *apfu*. The CO_3 and H_2O contents were determined for some samples using the selective sorption method and the Alimarin method respectively. All samples were also checked by means of the IR spectroscopy for qualitative determination of the type of extra-framework anions.

The general features of the chemistry of cancrinite-subgroup minerals from Khibiny and Lovozero are as follows.

The main extra-framework cation is sodium. All studied samples are represented by Ca-poor minerals: the calcium content varies in the range of 2.4–3.5 wt.% CaO (0.5–0.6 *apfu*); some samples from Khibiny contain up to 6.3 wt.% CaO (up to 1.29 *apfu* Ca). The potassium content in most samples never exceed 1.9 wt.% K_2O (0.43 *apfu* K), only exception is K-rich vishnevite from the Kirovskii mine (Khibiny). The Al/Si atom ratio varies very significantly: from 0.57 to 1.01. Some samples contain phosphorus: up to 3.5 wt.% P_2O_5 (up to 0.53 *apfu* P). In some samples strontium is present as an admixture cation (up to 2.2 wt.% SrO that corresponds 0.22 *apfu* Sr). Maximum concentrations of fluorine and chlorine never exceed 0.4 wt.% (0.13 *apfu*) and 0.4 wt.% (0.10 *apfu*) respectively. $(CO_3)^{2-}$ is a prevailing anion in most samples, especially in Khibiny. Vishnevite, the sulfate member of the subgroup, is rare in the Lovozero massif and almost absent in the Khibiny massif.

The detailed study shows very significant differences between minerals of the cancrinite subgroup from Khibiny and Lovozero.

In the Lovozero massif the cancrinite group minerals are the most Na-rich samples, with minor Ca impurity (less than 0.20 *apfu*) and the widest variation of the Al/Si ratio: from 0.5 to 1.0 (Fig. 1). The most Si-rich samples correspond to cancrisilite, the most Al-rich minerals are non-carbonate members of the cancrinite subgroup, namely vishnevite and hydroxycancrinite. The intermediate group is represented by samples containing uncommon C-bearing groups as an extra-framework anion: the IR-spectra of these samples display an unusual situations and combination of absorption bands in the range of C–O stretching vibrations.

The chemical composition of cancrinite-subgroup minerals from the Khibiny massif is quite different (Fig. 2). The main difference is distinct positive correlation between the Al/Si ratio and Ca(+Sr) content in Khibiny samples.

The majority of samples from hyperagpaitic pegmatites are Ca-poor and the most Si-rich (Al/Si ratio is 0.72–0.85). They correspond to cancrisilite. The samples with the highest Ca concentration (0.5–1.3 *apfu*) and the Al/Si ratio close to 1.0 are considered as cancrinite *ss*. As well as the common concentration of Ca in these samples is about 0.6–0.8, the crystal chemical formula of typical cancrinite from the Khibiny massif can be presented as $Na_6Ca[Al_6Si_6O_{24}](CO_3)\cdot nH_2O$. Thus, even the Ca-richest samples of cancrinite from the Khibiny–Lovozero complex contain less than half of bivalent cations (firstly Ca) compare to the value considered for so-called "ideal cancrinite", $Na_6Ca_2[Al_6Si_6O_{24}](CO_3)_2 \cdot nH_2O$.

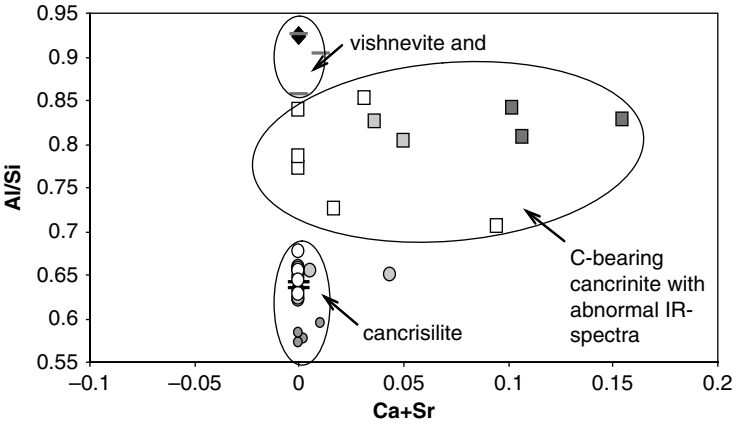

Fig. 1 Correlation between the Al/Si ratio and contents of bivalent cations (Ca with minor Sr, *apfu*) in cancrinite-subgroup minerals from the Lovozero massif

On the basis of the data obtained, we can consider two main schemes of isomorphous substitutions involving framework constituents and extra-framework cations and anions (located in a wide channel; contents of cancrinite cages is probably not involved) for cancrinite-subgroup minerals from the Kibiny–Lovozero alkaline complex.

The cancrinite–cancrisilite continuous isomorphous series (Khibiny):

$$\mathbf{Ca^{2+} + Al^{3+}\left[+(CO_3)^{2-}\right] \rightarrow Na^{+} + Si^{4+}\left[+(CO_3)^{2-}\right].}$$

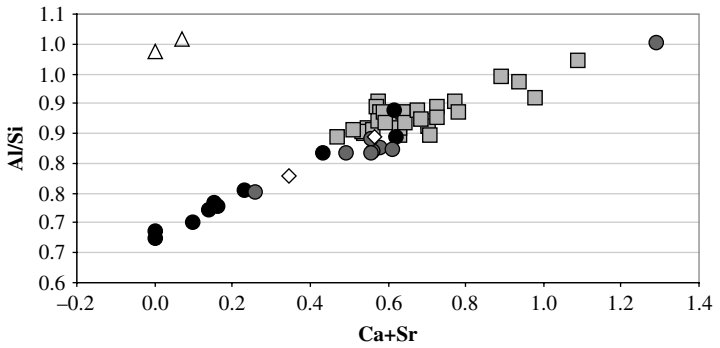

Fig. 2 Correlation between the Al/Si ratio and contents of bivalent cations (Ca with minor Sr, *apfu*) in cancrinite-subgroup minerals from the Khibiny massif

The cancrisilite-hydroxycancrinite solid-solution system (Lovozero):

$$\square + Si^{4+} + \left[(CO_3)^{2-} + H_2O\right] \rightarrow Na^{+} + Al^{3+} + 2(OH)^{-}.$$

Acknowledgements We are grateful to M.F. Vigasina for help in the IR study the samples and N.V. Chukanov for discussion. This work was supported by grants of President of Russian Federation MD-7230.2006.5, NSh-4964.2006.5 and NSh-4818.2006.5, grant RFBR 06-05-90626-BNTS_a and grant of Russian Science Support Foundation (for IVP).

References

Bonaccorsi E, Merlino S (2005) Modular microporous minerals: cancrinite–davyne group and C–S–H phases. Rev Mineral Geochem 57:241–290

On the Inhomogeneities in the Structures of Labuntsovite-Group Minerals

Natalia I. Organova, Sergey V. Krivovichev, Andrey A. Zolotarev and Zoya V. Shlyukova

Labuntsovite was discovered as a mineral species by the Russian geologist A.N. Labuntsov from alkaline massifs of Kola Peninsula in 1925. However, Labuntsov described it as a variety of elpidite, not as a separate mineral species. In 1955, Semenov and Burova (1955) analysed the mineral chemically and named it "labuntsovite". The first crystallographic study was done by Milton et al. (1958) who determined for the mineral monoclinic symmetry with the following unit-cell parameters: $a = 14.24$, $b = 13.74$, $c = 15.57$ Å, b = 116.55^0.

The crystal structure of labuntsovite was solved by N.I. Golovastikov in 1973 using crystals from Kola Peninsula provided by E.I. Semenov. According to the current nomenclature, its composition corresponds to the composition intermediate between labuntsovite and lemmleinite (in 1:1 ratio) with the space group determined as $C2/m$. According Golovastikov, labuntsovite has a zeolite-like structure (Fig. 1). It is a porous titanium and niobium silicate based upon chains of corner-sharing (Ti, Nb)- octahedra extending along the a axis. The chains are cross-linked by four-membered rings of silicate tetrahedra. The resulting frameworks contains channels with different dimensions (Fig. 1). Channels are occupied by a number of different interstitial sites that were denoted later as A, B, C, and D (Chukanov et al. 2003), and occupied by Ca, Na, K, Ba, Sr, Fe, Mg, Mn and H_2O. Golovastikov was perplexed

Natalia I. Organova
Institute of Geology of Ore Deposits, Petrology, Mineralogy, Russian Academy of Scienses, Staromonetny per. 35, 109017 Moscow, Russia, e-mail: Natalia@igem.ru

Sergey V. Krivovichev
Department of Crystallography, St. Peterburg State University, State University Emb. 7/9, 199034 St. Peterburg, Russia

Andrey A. Zolotarev
Department of Crystallography, St. Peterburg State University, State University Emb. 7/9, 199034 St. Peterburg, Russia

Zoya V. Shlyukova
Institute of Geology of Ore Deposits, Petrology, Mineralogy, Russian Academy of Scienses, Staromonetny per. 35, 109017 Moscow, Russia

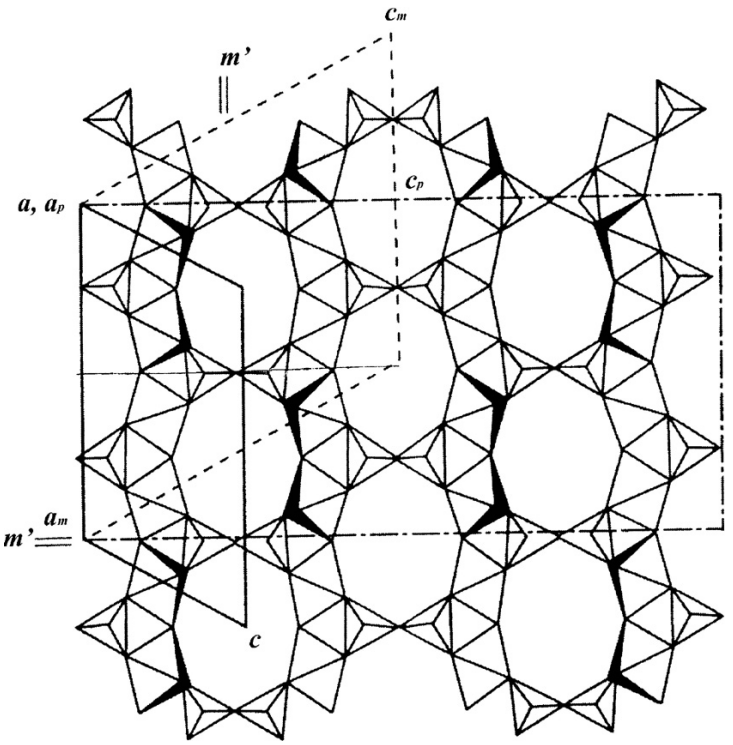

Fig. 1 Octahedral-tetrahedral framework in the structures of labuntsovite-group minerals

by the short (*ca*. 2.1 Å) distance between D and C sites. In addition, Golovastikov identified diffuse streaks at halved $\boldsymbol{c}^*$ recorded on long-exposure oscillation X-ray photographs. He concluded his structure study with the statement: "Refinement of these errors in the structure awaits following research". Along this line, Organova et al. (1976, 1980, 1981) investigated several "labuntsovites" (Fig. 2a, b).

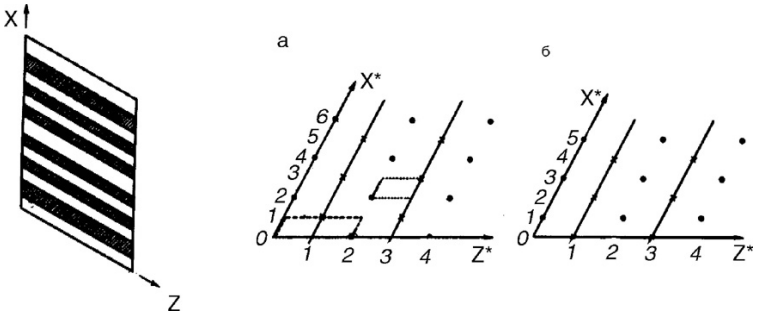

Fig. 2 Labuntsovite in real (*left*) and reciprocal space (*right*)

Organova et al. (1980) considered problems of order and disorder in labuntsovite-group minerals and classified diffraction patterns obtained from them into:

(1) patterns that have only sharp "superstructure" reflections corresponding to space group $I2/m$ and a "doubled" c parameter equal to about 15.5 Å;
(2) patterns that have only sharp reflections with a unit cell of c 7.75 Å in the space group $C2/m$;
(3) patterns that have sharp reflections indexable in a unit cell with $c \sim 7.75$ Å but with additional diffuse reflections streaked along **a*** that indicates the presence of thin layered domains parallel to (100); ordered domains of the labuntsovite structure have shifted to each other by $\pm c/2$ and can be indexed in the $I2/m$ unit cell; the thinner the domains, the more diffuse the respective reflections.

There is also another description of this phenomenon based upon the results obtained using modern techniques (Armbruster et al. 2004). The latter reference contains interesting results about structures of two labuntsovites (Fig. 3) with

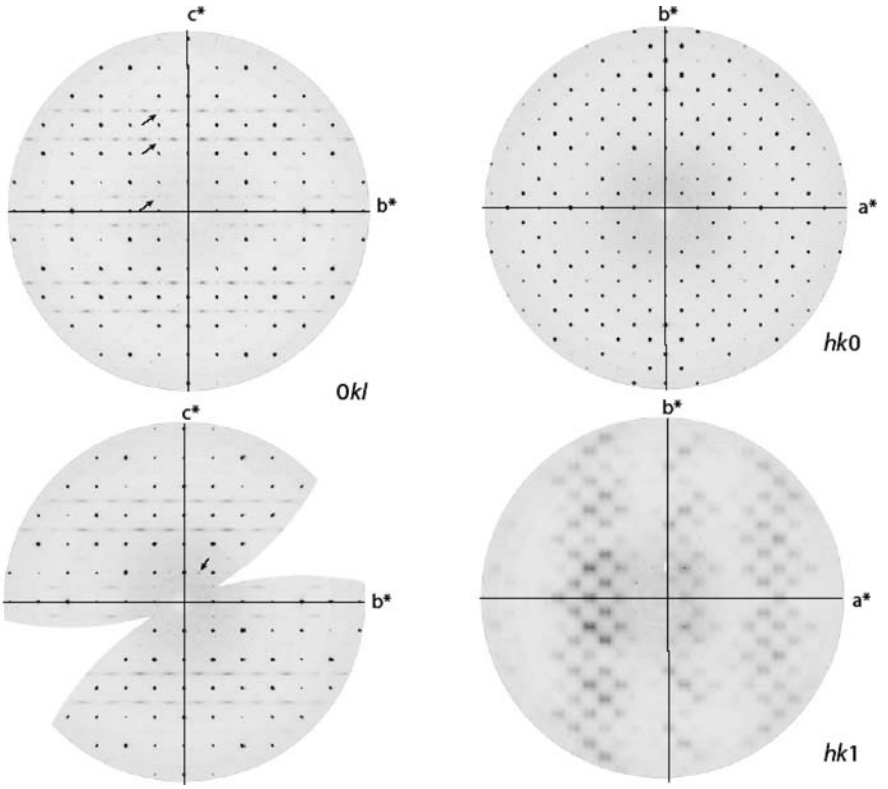

Fig. 3 *Left*: Reconstructed 0*kl* reciprocal space plots for labuntsovite crystals displaying sharp X-ray refections indicating a *C*2/*m* average structure with c = 7.75 Å and diffuse layers at $\boldsymbol{c}^*/2$ intervals fulfilling conditions of an *I*-centered superlattice. *Right*: reconstructed *hk*0 and *hk*1 reciprocal space plots for labuntsovite crystal. Reproduced from Armbruster et al. (2004)

reconstructed 0*kl*, 1*kl, hk*0*, hk*1 reciprocal space plots. From the 0*kl* plots, one can derive for labuntsovites the monoclinic space group $I2/m$. Diffusion reflections are probably related to the thickness of ordered domains that can be determined by comparison of reflection length with distance between neighbouring sharp coordinate reflections along axis. In this case we have domains with approximate thickness of about 2 nm.

In the $hk2n+1$ plot (Fig. 3, right), the same crystals of labuntsovite have only doubled and diffuse reflections along X^*. According to Guinier (1961), such pictures are generated by a smooth change of electron density along the X axis. According to Fig. 4, such a change has a period of about 20 nm and might be correlated with the conditions of crystal growth from hydrothermal solutions. The smooth and periodic

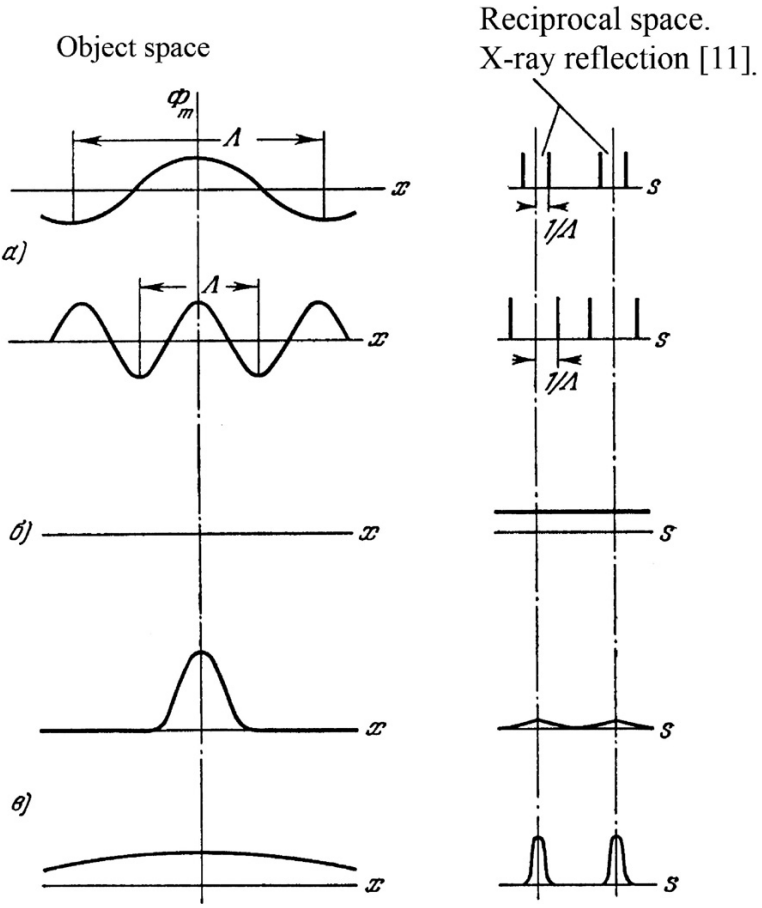

Fig. 4 Connection between real and reciprocal space by smoothing one dimensional change of density (Guinier 1961)

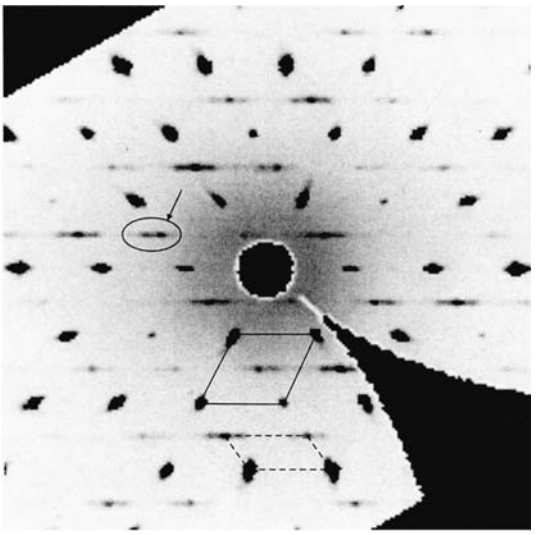

Fig. 5 Section of reciprocal space *h*0*l* for highly ordered labuntsovite mineral

change in the chemical composition is due to the different occupances of the A, B, C, and D sites.

Similar phenomena are recognized for alloys for a long time (Organova et al. 1976; Semenov and Burova 1955) and correspond to diffraction patterns obtained from materials being at the first stage of phase decomposition of solid solutions. It is likely that, in the case of labuntsovite, we have the same situation with decomposition of solid solutions between D-filled and D-vacant labuntsovites. After decomposition, there are two new phases, D-filled and D-vacant ones. In alloys, a new phase with thin layers has been called a "Guinier-Preston zone" (Guinier, 1961). It is possible to measure thickness of these zones from the fine features of diffraction patterns. Usually, properties of alloys after decomposition of solid solutions change dramatically. As a rule, after high-temperature treatment, a

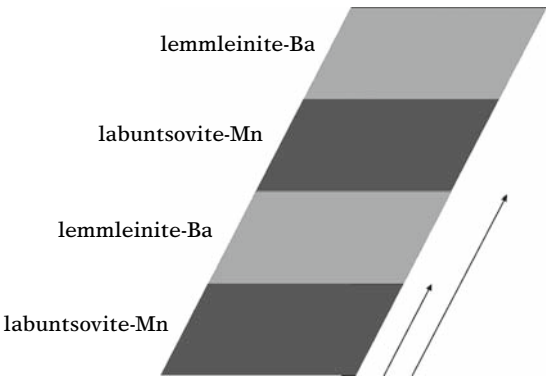

Fig. 6 Successive alternation of lemmleinite–Ba and labuntsovite–Mn in the structure of ordered labuntsovite-group mineral. Reproduced from Zolotarev (2007)

hardness of material grows. It is of interest to probe and to measure such properties for labuntsovites as well.

Recently, Zolotarev et al. (2006) reported the (h0l) section of reciprocal space from another labuntsovite sample with very intensive diffusion reflections (Fig. 5). Other interesting results are contained in Ph.D. dissertation of A.A. Zolotarev (2007). Figure 6 represents a scheme of disposition of layers of lemmleinite–Ba and labuntsovite–Mn with their ordered successive alternation.

It is clear that the problem of labuntsovite inhomogeneities needs additional studies not only by X-ray diffraction techniques but by other methods as well, in particular, by a high-resolution transmission electron microscopy.

Acknowledgements This work was supported by the Russian Foundation for Basic Research, grant 05-05-64959.

References

Armbruster T, Krivovichev SV, Weber T, Gnos E, Organova NI, Yakovenchuk VN, Shlyukova ZV (2004) Origin of diffuse superstructure reflections in labuntsovite-group minerals. Am Mineral 89:1655–1667

Chukanov NV, Pekov IV, Zadov AT, Voloshin AV, Subbotin VV, Rastsvetaeva RK, Sorochtina NV, Krivovichev SV (2003) Minerals of the Labunstovite group. Nauka, Moscow, p 323 (in Russian)

Golovastikov NI (1973) Crystal structure of of the alkali titanosilicate labuntsovite. Kristalografiya 18:950–955 (in Russian)

Guinier A (1961) Theorie et Techigue de la Radiocristallographie. Gos Izdatelstvo Fiz-Mat Lit Russian translation, Moscow

Milton C, Mrose ME, Fahey JI (1958) Labuntsovite from the trona mine, Seawater Counntry, Wioming. Bull Geol Soc Am 64:1614–1615

Organova NI, Archipenko DR, Dikov JuP, Karpinsky OG, Shlyukova ZV (1981) Structure particularities of new K-variety of labuntsovite and its place in the labuntsovite-nenadkevichite family. Mineral Zh 2:49–63

Organova NI, Shlyukova ZV, Tsepin A (1980) Crystal chemistry of disorder in labuntsovites. In: Shadlun TN (ed) Uporjadochenie I Raspad Tverdjuch Rastvorov v Mineralach. Nauka, Moscow, pp 39–57 (in Russian)

Organova NI, Shlyukova ZV, Zabavnikova NI (1976) On crystal chemistry of labuntsovite and nenadkevichite. Izv Acad Nauk SSSR Geol 2:98–116 (in Russian)

Semenov EI, Burova TA (1955) On a new mineral labuntsovite and so-called titanium elpidite. Dokl Akad Nauk SSSR 101:1113–1116 (in Russian)

Zolotarev AA (2007) Crystal Chemistry of Minerals of the Lovozerite and Labuntsovite Groups. Candidate of Sciences Dissertation, Resumé, St. Petersburg State University

Zolotarev AA, Krivovichev SV, Yakovenchuk VN, Pakhomovsky YaA, Organova NI, Armbruster T (2006) High degree of cation ordering in structure of a new member of labuntsovite group. Dokl Ross Akad Nauk 410:86–90

Phosphates with Amphoteric Oxocomplexes: Crystal Chemical Features and Expected Physical Properties

Olga V. Yakubovich

For the most part, the rocks are formed by oxosalts – minerals containing complex acid anionic radicals, first of all silicate, but also phosphate, carbonate, borate, sulfate, etc. Statistical data on chemical compositions of minerals show that amphoteric elements (first row of transition metals, aluminum, beryllium, zinc, zirconium, niobium and some others) are typical for most cases. Depending on the conditions of crystal genesis the amphoteric complexes can act as the cationic part of the crystal structure or as another species of anions besides the usual acid tetrahedral groups. In other words, in combination with acid complex anions like $[SiO_4]^{4-}$, $[PO_4]^{3-}$, $[SO_4]^{2-}$, $[BO_4]^{5-}$ amphoteric metal complexes can form mixed anionic networks with alkali or organic cations inside the channels or pores. The chemical composition and P/T conditions of system during crystallization are the most important criteria defining the way of amphoteric metal behavior in a specific physicochemical situation.

The multivalued crystal chemical function of cations – i.e., to behave amphoterically – is well known in chemistry. The ability of some cations "to be converted" into complex anions under conditions of high alkalinity of agpaite pegmatites has even been noticed by Fersman in his fundamental monograph "Pegmatites" (Fersman 1940) and other papers published in connection with his famous "Kolskii" expeditions. Just with alkaline rocks, mineral deposits with active role of beryllo- titano- zircono-silicates, alumino- ferri- ferro- and mangano-phosphates are related. A detailed mineralogo-geochemical analysis of alkaline rocks was presented in studies of E.I. Semenov (1972), A.P. Khomyakov (1990), A.V. Voloshin and Ya.A. Pakhomovskii (1986) and I.V. Pekov (2005). A crystal chemical assignment of minerals from the alkaline complexes based on the extraction of mixed radicals of octahedra and tetrahedra was made in works (Pyatenko et al. 1976, Voronkov et al. 1978), where the main types of mixed anionic titanosilicate and zirconosilicate constructions from one dimensional to 3D frameworks were demonstrated.

Olga V. Yakubovich
Moscow State Lomonosov University, Moscow, Russia, e-mail: yakubol@geol.msu.ru

The overview of the concept of "mixed anionic radicals" – condensed groups of acid and amphoteric oxocomplexes that play the anionic function in mineral crystal structures – was published by Sandomirskii and Belov (1984). The authors showed that the anionic function of this kind of radicals is caused by crystal chemical laws. The features of interaction between the cationic matrix of crystal structure and the mixed anionic radicals were analyzed and a general scheme of arrangement of these compounds was proposed. It was indicated that the topology of crystal structures characterizes the peculiarities of its energy: the type of coordination geometry and the way of the polyhedra' interaction attest the crystal structure stability.

We used this approach during the description of phosphates, on the basis of our experimental results of hydrothermal synthesis in the systems containing amphoteric metals and volatile components (F, Cl), and/or alkaline cations (Yakubovich and Urusov 1996). Under controlled conditions of temperature, pressure and concentrations we got many analogues of pegmatite phosphates and fluorides, namely triphylite, sarcopside, maricite, lithiophosphate, triplite, zweiselite, alluaudite, wyillieite, arrojadite, lipscombite, tavorite, leucophosphite, tinsleite, niahite, cryolite, elpasolite, cryolithionite. We also synthesized many new phases and established about 30 novel structure types in the phosphate class.

The chemical formulae analysis of more than 200 phosphate minerals showed that the most frequent cations in phosphates are Fe^{2+} and Fe^{3+} (95 compounds), Al^{3+} (60), Ca^{2+} (56), Mn^{2+} and Mn^{3+} (45) (Fisher 1973). The phosphates of Cu, Zn, Be and Zr are also quite widespread. Being mostly amphoteric (naturally, excluding Ca), the complexes of these elements in phosphates often play, not only the cationic function, but also assume the role of anion-formers, creating anion radicals of mixed crystal chemical nature together with acid tetrahedral units $[PO_4]^{3-}$. It was suggested to pick out the anionic component in the crystal, which is composed of crystal chemically different complexes (phosphorus tetrahedra and polyhedra around Fe, Mn, Al, Zn, etc.). So, it appeared to be possible to divide phosphate minerals into three large groups: **(1)** with only acid phosphate tetrahedra; **(2)** with mixed anion radicals, which are associations of amphoteric and acid oxo complexes differing in chemical nature and geometry; **(3)** with amphoteric oxo complexes playing both the cationic and anion-former function (Yakubovich and Urusov 1996; Karimova et al. 1997). The chemical bond type in crystals manifesting itself in the way of polyhedra' assembling in the crystal structures is the basis of these groups recognition, which correlates with the process of phosphates' division in geochemically different rocks. We showed that "the cationic" function of amphoteric complexes is typical for the minerals from granite pegmatites, where the conditions of phosphates' crystallization were mostly neutral or slightly acidic, while "the anionic" role of these complexes is characteristic for postmagmatic derivatives formed under the conditions of increased alkalinity. In these conditions the alkaline elements (usually K and Na) were incorporated into the cationic part of the crystal structure and amphoteric oxocomplexes together with orthophosphate tetrahedra form the anionic radicals in the presence of a large number of electropositive ions. Such situation can occur in agpaitic pegmatites, where this kind of minerals crystallize from the "late fluid" enriched by the alkali cations, or on the stage

of hydrothermal or late metasomatic recrystallization of earlier formed minerals, if this process runs with the inclusion of the alkaline elements. Thus, the phosphates of this type are mainly of secondary origin; they are also usual for surface process where they often develop as biogenic minerals.

The crystal structures and physical properties of phosphates from these three groups are absolutely different. Very dense cationic architecture built by polyhedra around amphoteric metals or together with another kind of metals is typical for the phosphates of **the first group**. Thus, the highest-temperature primary minerals that crystallize in the core of pegmatite (triplite-zwieselite, amblygonite-montebrasite, triphylite-lithiophyllite series, sarcopside, etc.) have more complicated three-dimensional cationic frameworks formed by octahedra or/and five vertex polyhedra. According to Moore (1984), 75% of high temperature phosphates possess dense-packed or "denser-than-dense-packed" structures. Their cationic frameworks incorporate "clusters" of octahedra sharing edges and faces; and PO_4 tetrahedra in these structures have edge contacts with cationic polyhedra.

Highly polymerized associations of octahedra are also the basis of crystal structures of early metasomatic phosphates that crystallize on the boundary of the pegmatite core and the intermediate zone. They are forming as a result of the alteration of the earlier phosphates under the influence of the later fluid; usually they are represented by smaller crystals (Fransolet et al. 1984; Kampf 1982; Mücke 1981; Shigley and Brown 1986). It is worth mentioning after P. Keller and O. Knorring (1989) that the earliest metasomatic replacements in phosphates mark a very important stage of pegmatite evolution: they occur simultaneously with economic core-margin silicates (tourmaline, beryl, spodumen etc.). A distinctive typomorphic feature of these phosphate minerals containing mixed valence transition metals is the brown-black or green-black color due to a charge transfer of the type $M^{2+} \leftrightarrow M^{3+}$. These earliest phosphates of the metasomatic origin have also a structural typomorphic feature: their 3D cationic frameworks built by amphoteric complexes contain hole defects (arrojadite, lipscombite, wyllieite), or their cationic constructions present 2D layers (alluaudite, kryzhanovskite) of edge sharing octahedra.

A good example of the phosphate from this group is lipscombite – the mineral of variable composition generally described by the formula $(Fe^{2+}_{x}\ Fe^{3+}_{n-x})(PO_4)_4O_y(OH)_{4-y}$, where n is the number of iron atoms, x is the number of Fe^{2+} ions, and y is the number of oxygen atoms that are not involved in the coordination of phosphorus (Yakubovich et al. 2006). In the lipscombite crystal structure, four types of octahedra around the Fe(1), Fe(2), Fe(3), and Fe(4) atoms are alternated in a column. These columns cross the unit cell in two orthogonal directions. Neighboring columns share oxygen vertices of octahedra; as a result, an octahedral 3D framework forms with PO_4 tetrahedra located between columns (Fig. 1). All octahedra have close sizes with average Fe–O distances from 2.057 Å in the Fe(1) and Fe(2) polyhedra to 2.060 Å in the Fe(3) polyhedron. The shared faces of octahedra are the main specific feature of the lipscombite structure and suggest unusual physical properties of this mineral. The distances between iron atoms in columns are 2.769(1) Å (Fe(2)–Fe(3)), 2.623(1) Å (Fe(3)–Fe(4)), 2.673(1) Å (Fe(4)–Fe(1)), and 2.514(1) Å (Fe(1)–Fe(2)). It is likely that such small values of the Fe–Fe distances

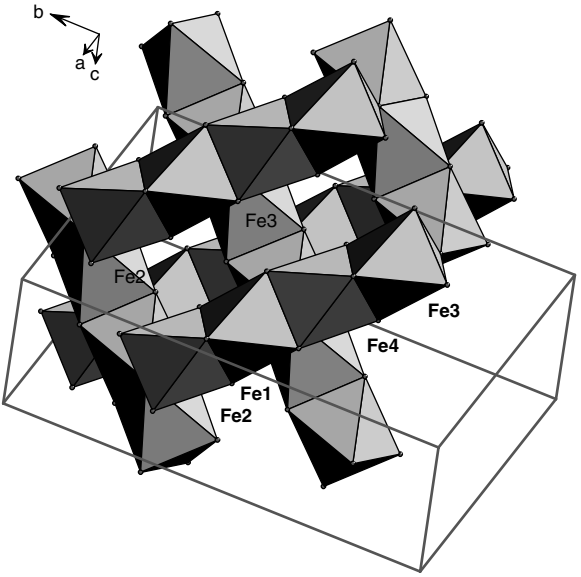

Fig. 1 Cationic framework in the crystal structure of lipscombite

are responsible for the electronic transitions of the $Fe^{2+} + Fe^{3+} \Leftrightarrow Fe^{3+} + Fe^{2+}$ type, strong absorption, black color of the crystals (Moore 1970) and expected magnetic properties. This nearness of iron atoms to each other and their tendency to avoid direct contact explain the void defects in the octahedral columns (where three of four octahedra are statistically occupied by iron atoms) and the impossibility of the existence of the ordered Fe^{2+}-containing end member $Fe^{2+}{}_8(PO_4)_4(OH)_4$ with completely occupied octahedral positions (Gheith 1953).

Hydrothermally reworked phosphates from granite pegmatites that have been carefully discussed by Moore (1973), are built by less coherent structures. On the initial stage of the process amphotheric complexes still can act as cations only (whitmoreite, augelite). More often, however, amphoteric metals here perform both the cationic and the anion-former functions, if the primary minerals' transformation occurs without the activity of Na or K (or ammonium playing the crystal chemical role of alkaline metals in hypergene conditions). Minerals of this **third group** are: strunzite, laueite, paravauxite, sigloite, pseudolaueite, stewartite, to name a few.

Usually, the process of a transition metal oxidation proceeds stepwise; therefore, at a lower degree of oxidation the transition metal plays the cationic role, while the higher oxidized ion forms the mixed anionic radical together with PO_4 tetrahedra. Laueite $[Mn^{2+}(H_2O)_4]\{Fe_2^{3+}(OH)_2(H_2O)_2(PO_4)_2\}(H_2O)_2$, isotypic with minerals gordonite $[Mg(H_2O)_4]\{Al_2(OH)_2(H_2O)_2(PO_4)_2\}(H_2O)_2$, and paravauxite $[Fe^{2+}(H_2O)_4]\{Al_2(OH)_2(H_2O)_2(PO_4)_2\}(H_2O)_2$, is formed likewise: 2D anionic constructions formed by chains of vertice-sharing Fe^{3+} octahedra, and P tetrahedra that link the octahedral chains in the layers, alternate with layers of isolated (i.e., without direct contents with other octahedra) Mn^{2+} octahedra. As one can see from the

crystal chemical formulae of the discussed minerals, the cationic function of Mg^{2+} in gordonite is played by Mn and Fe at the lowest oxidation state in laueite and paravauxite respectively. During the progressive process of oxidation the paravauxite can be converted to sigloite $[Fe^{3+}(H_2O, OH)_4]\{Al_2(OH)_2(H_2O)_2(PO_4)_2\}(H_2O)_2$ (Hawthorne 1988) without fundamental structural transformation. It means that in certain geochemical situations the transition metal even at the highest state of oxidation might form the cationic part of the crystal structure.

One more case is common for secondary pegmatite phosphates. If different amphotheric metals occur in one mineral, then the less electronegative ion forms the cationic part of the crystal structure. This case may be illustrated by the crystal structure of phosphophyllite $[Fe(H_2O)_4]\{Zn_2(PO_4)_2\}$ (Thomas and Weller 1992), where the mixed anionic layers of vertice-sharing ZnO_4 and PO_4 tetrahedra alternate with layers of isolated Fe^{2+} octahedra. For Zn phosphates the crystal structures of the third type are representative enough (hopeite, parahopeite, kipushite, veszelyite, etc.). They consist of two types of layers, differing in geometry and chemistry. The first "cationic" layer is built of Zn (or Zn and Cu) octahedra; the second "anionic" layer is formed by vertice-sharing Zn and P tetrahedra.

The phosphates containing significant amounts of alkaline cations (the **second group**) have zeolite-like microporous architecture. In the alkaline conditions of mineral genesis (agpaitic pegmatites, hydrothermalites, etc.) the alkaline metals quantitatively dominate in the system of crystallization. One of the most effective ways of their deposition as a solid phase in peralkaline aluminosilicate systems where Al turns out in a relative deficit, is the formation of titano(niobo)- and zirconosilicates, as shown by Yu. A. Pyatenko (1987). According to our experimental results (Yakubovich and Urusov 1996), in a high alkalinity of the phosphate system Fe^{3+}, Fe^{2+}, Mn^{2+}, Zn^{2+} cations help P^{5+} in the crystallization of alkaline phases with mixed anionic radicals. These anionic radicals can be formed as by octahedra around amphotheric metal sharing vertices with acid PO_4 tetrahedra, or by different kinds of tetrahedral oxo-complexes as well. In the alkaline systems of our experiments we received many new phosphates of this type that often represent structural varieties of known minerals (leucophosphite, tinsleite, minyulite, pharmacosiderite, natisite, cancrinite, ect.).

For example, a synthetic phase $\{[Rb_{1.94}(H_2O,OH)_{3.84}](H_2O)_{0.1}\}\{Al_4(OH)_4[PO_4]_3\}$ (Yakubovich et al., 2008) belongs to the pharmacosiderite structure type $K\{Fe_4(OH)_4[AsO_4]_3 6H_2O$ and represents the first aluminophosphate in the group of minerals and synthetic analogues in question. (Fig. 2). This structure type proved to be stable enough to form of many phases different in chemical composition on its basis: ferri- and aluminoarsenates, germinates, titanosilicates, molybdenophosphates and some others (Table 1). The main difference between these compounds consists in "chemical filling" of the mixed anionic 3D framework of octahedra (occupied by larger cations) and tetrahedra (occupied by smaller cations). All alkaline cations from Li^+ to Cs^+ and also Tl^+, H^+ and $(NH_4)^+$ are now in the voids of these frameworks; and their absorption characteristics permit the allocation of four cations per formula unit besides water molecules also incorporated by open channel of these crystal structures.

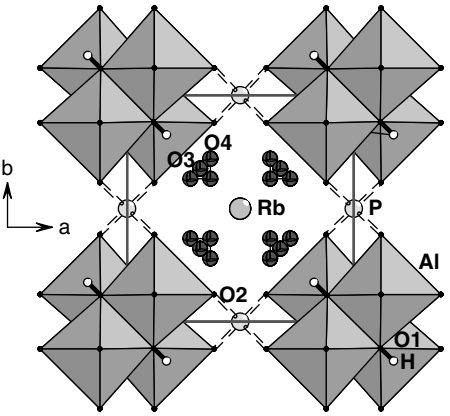

Fig. 2 The crystal structure of the aluminophosphate variety of pharmacosiderite

The analysis of Table 1 data allowed us to define the main crystal chemical factor that determines the stability of this structure type despite the noticed diversity of chemical compositions. This factor is the ratio of charges of the cations in octahedral and tetrahedral surroundings that provides a local bond valence on oxygen atoms of the framework. Thus, for Fe^{3+}/As^{5+}, Al^{3+}/As^{5+} и Al^{3+}/P^{5+} cation pairs, the local bond valence is maintained when hydroxyl groups at the vertices of the framework octahedra that are not shared with tetrahedral, form. This situation is described by general formula of the anionic framework $\{M^{3+}{}_4(OH)_4[T^{5+}O_4]_3\}^-{}_{\infty\infty\infty}$ (M – octahedral cations, T– tetrahedral cations). In the case when the octahedral positions are populated by transition metals in 4+ oxidation state, the local bond valence on the framework oxygen atoms is observed if the tetrahedral cations have the same 4+ charge (Ti^{4+}/Si^{4+}, Ge^{4+}/Ge^{4+}), and the framework formula transforms into $\{M^{4+}{}_4O_4[T^{4+}O_4]_3\}^{4-}{}_{\infty\infty\infty}$. For the pair $Mo^{3.5+}/P^{5+}$ according to [2, 18] this formula looks like: $\{M^{3.5+}{}_4O_4[T^{5+}O_4]_3\}^{3-}{}_{\infty\infty\infty}$.

As can be seen from the shown formulae (Table 1), the change of framework charge – one of the key parameters that regulate absorption and selective properties of this type of compounds – is a direct consequence of variations of the framework composition. The second key parameter is the effective diameter of framework windows, and it is defined by the octahedra and tetrahedra sizes (edge lengths) (Fig. 2), which in their turn depend on the radius values of cations occupying these polyhedra. Such crystal structure topology when the cubic unit cell parameter is approximately equal to the sum of three M–O distances and one O–O distance (corresponds to the edge lengh of the tetrahedron) characterizes the size of the framework windows. In other words, the larger the cubic unit cell parameter of the compound crystallizing in the pharmacosiderite structure type, the large the effective diameter of the micropores.

Therefore, the absorption ability of this kind of compounds should grow with the increase of the framework's negative charge and with the augmentation of the sizes of the cations forming this framework. It seems that it is possible to move in the direction of the enlargement of both of these parameters until a certain limit (for same

Table 1 Crystal chemical data for pharmacosiderite type compounds (sp. gr. $P\bar{4}3m$, $Z = 1$)

No	Anionic framework formula	Cations and water in framework cavities	Unit cell parameters, a (min – max), Å	References
1	$\{Al_4(OH)_4[PO_4]_3\}^-$	Rb^+, OH^-, H_2O	7.4931(6)	Yakubovich et al. (in press)
2	$\{Al_4(OH)_4[AsO_4]_3\}^-$	K^+, H_2O	7.72 – 7.745(1)	NIST/FIZ (2007)
3	$\{Fe_4(OH)_4[AsO_4]_3\}^-$	H^+, K^+, Na^+, Ba^{2+}, H_2O	7.93 – 7.9816(5)	NIST/FIZ (2007)
4	$\{Ge_4O_4[GeO_4]_3\}^{4-}$	H^+, Li^+, K^+, Tl^+, NH_4^+, Rb^+, Cs^+, H_2O	7.6699(1) – 7.74	NIST/FIZ (2007)
5	$\{Mo_4O_4[PO_4]_3\}^{3-}$	Cs^+, NH_4^+	7.728(4) – 7.736(2)	NIST/FIZ (2007)
6	$\{Ti_4O_4[SiO_4]_3\}^{4-}$	H^+, K^+, Cs^+, H_2O	7.7644(3) – 7.8214(6)	NIST/FIZ (2007)
7	$\{(Ti,Ge)_4O_4[(Ge,Si)O_4]_3\}^{4-}$	H^+, Cs^+, H_2O	7.8577(2) – 8.0237(2)	NIST/FIZ (2007)
8	$\{(Ti,Nb)_4O_4[SiO_4]_3\}^{3-}$	H^+, Cs^+, H_2O	7.7937(2) – 7.8622(12)	NIST/FIZ (2007)

structure type). This fact is illustrated on Fig. 3, where real and hypothetic compositions of the pharmacosiderite type frameworks without isomorphous defects are shown. Thus, the unit cell parameter and the negative charge of the framework grow simultaneously on the way from point 1 to point 6 (Table 1). Further increase of both

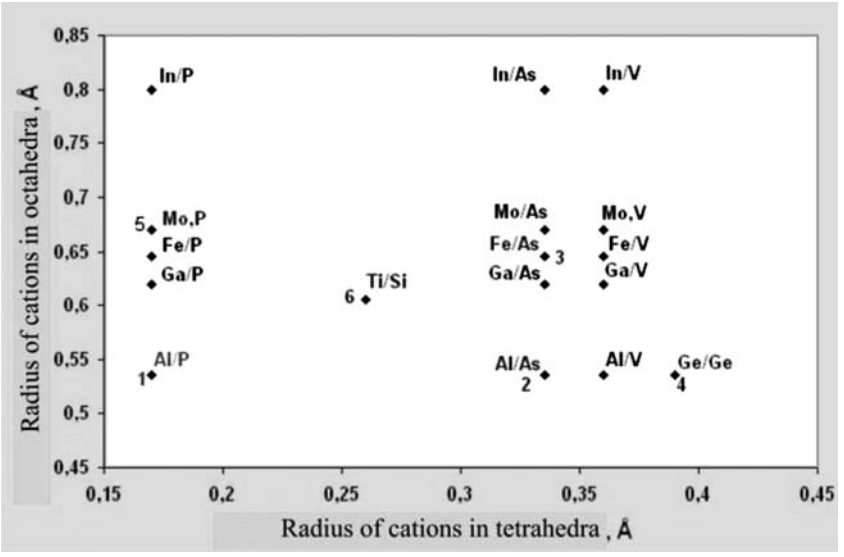

Fig. 3 Distribution of pharmacosiderite-type compounds

octahedral and tetrahedral cation sizes leads to the composition of mineral pharmacosiderite (point 3) having smaller framework charge equal to -1. The compositions of the hypothetic phases on Fig. 3 have been chosen on the basis of the crystal chemical factors and the probable radiation stability of the microporous frameworks. The largest pore size should be expected in the compound with mixed anionic framework built by In^{3+}octahedra and V^{5+} tetrahedra; the charge of this framework should be equal to -1. By varying the pore sizes and the value of the framework negative charge in the course of "a chemical design" it is possible, in principle, to get the compounds with high selectivity to one or another cation. Absorption characteristics of their pharmacosiderite type frameworks with low negative charge could be augmented in case if the pores absorb the cations and coordinating anions together. This effect was observed in the crystal structure of the new pharmacosiderite type aluminophosphate $\{[Rb_{1.94}(H_2O,OH)_{3.84}](H_2O)_{0.1}\}\{Al_4(OH)_4[PO_4]_3\}$, where the microporous -1 charged framework is able to absorb about two Rb^{2+} cations together with the coordinating OH^- groups.

References

Fisher DG (1973) Geochemistry of phosphorus containing minerals. In: Griffith E, Beeton A, Spenser J (eds) Environmental phosphorus handbook. Wiley, New York

Fransolet A-M, Antenucci D, Speetjeus J-M, Tarte P (1984) An X-ray determinative method for the divalent cation ratio in the triphylite-lithiophilit series. Mineral Mag 40:373–378

Gheith MA (1953) Lipscombite, a new synthetic "iron lazulite". Am Mineral 38:612–628

Hawthorne FC (1988) Sigloite: the oxidation mechanism in $(M_2(III)(PO_4)_2(OH)_2(H_2O)_2)^{2-}$ structures. Miner Petrol 38:201–211

Kampf AR (1982) The phosphate mineralogy of the Palermo pegmatite. In: Brown GE (ed) The mineralogy of pegmatites, vol 67:1–2. Am Mineral, pp 180–189

Karimova OV, Yakubovich OV, Urusov VS (1997) Crystal chemical function of zinc in the structures of phosphates. Moscow University Geology Bulletin 52:6:35–45

Keller P, Von Knorring O (1989) Pegmatites at the Okatjimukuju farm, Karibib, Namibia. Part. 1: Phosphate mineral associations of the Clementine II pegmatit. Eur J Mineral 1:4:567–593

Khomjakov AP (1990) Mineralogy of ultraagpaite alkaline rocks. Nauka, Moscow (in Russian)

Moore PB (1970) Crystal chemistry of the basic iron phosphates. Am Mineral 55:135–169

Moore PB (1973) Pegmatite phosphates: descriptive mineralogy and crystal chemistry. Mineral Rec 4:103–130

Moore PB (1984) Crystallochemical aspects of the phosphate minerals. In: Nriagu JO, Moore PB (eds) Phosphate Minerals. Springer, Berlin Heidelberg New York Tokyo, pp 155–170

Mücke A (1981) The paragenesis of the phosphate minerals of the Hagendorf pegmatite – a general view. Chem Erde 40:3:217–237

NIST/FIZ, Inorganic Crystal Structure Database (2007) part 1

Pekov IV (2005) Genetic mineralogy and crystal chemistry of rare elements in high-alkaline postmagmatic systhems (thesis). Moscow

Pyatenko YuA (1987) About specific group of water containing aluminosilicates, stable in natural ultrabasic conditions (crystal chemical aspect). Geokhimiya 8:1208–213

Pyatenko YuA, Voronkov AA, Pudovkina ZV (1976) Mineralogical crystal chemistry of titanium. Nauka, Moscow (in Russian)

Sandomirskii PA, Belov NV (1984) Crystal chemistry of mixed anionic radicals (in Russian)

Semenov EI (1972) Mineralogy of Lovozero alkaline massif. Nauka, Moscow (in Russian)

Shigley JE, Brown GE (1986) Lithiophilite formation in granitic pegmatites: a reconnaissance experimental study of phosphate crystallization from hydrous aluminosilicate melts. Am Mineral 71:356–366

Thomas IM, Weller MT (1992) Synthesis, structure and thermal properties of phosphophyllite, $Zn_2Fe(PO_4)_24(H_2O)$. J Mater Chem 2:1123–1126

Voloshin AV, Pakhomovskii YaA (1986) Minerals and mineral evolution in amazonite pegmatites of Kolskii peninsula. Nauka, Leningrad (in Russian)

Voronkov AA, Shumjatskaja NG, Pyatenko YuA (1978) Crystal chemistry of zirconium minerals and their synthetic analogues. Nauka, Moscow (in Russian)

Yakubovich OV, Urusov VS (1996) The genetic crystal chemistry of pegmatite phosphates. Moscow University Geology Bulletin 51:2:18–40

Yakubovich OV, Massa W, Dimitrova OV (2008) A novel representative in the pharmacosiderite structure type. Crystallogr Rep 53:3

Yakubovich OV, Steele IM, Rusakov VS, Urusov VS (2006) Hole defects in the crystal structure of synthetic lipscombite $(Fe^{2+}_{2.3}Fe^{3+}_{4.7})[PO_4]_4O_{2.7}(OH)_{1.3}$, and genetic crystal chemistry of minerals of the lipscombite-barbosalite series. Crystallogr Rep 51:401–411

Structural Mineralogy of Borates as Perspective Materials for Technological Applications

Stanislav K. Filatov and Rimma S. Bubnova

Unique character of crystal structures of borates determines their excellent nonlinear optical, piezoelectric, luminescent etc. properties, enhanced UV transparency, and relatively high resistance against laser-induced damage.

Crystal Chemistry of Borates

Up to now, crystal structures of about 1000 borates have been determined, including those of 210 mineral species. The 70-year period of borate crystal structure determinations (Becker, 2001; Bokij and Kravchenko, 1966; Christ, 1960; Christ and Clark, 1977; Filatov and Bubnova, 2000; Hawthorne et al., 1996; Krogh-Moe, 1965; Tennyson, 1963; Zachariasen, 1938; Zachariasen and Ziegler, 1932) has come up with a unique borate crystal chemistry at ambient conditions characterized by the following principles:

(1) Boron atoms can occur in both triangular and tetrahedral coordination to oxygen and hydroxyl groups.
(2) Under ambient conditions, BO_3 triangles and BO_4 tetrahedra can link to each other via common corners (oxygen atoms) only and not via edges or faces to form rigid boron-oxygen groups consisting of 3–6 boron-oxygen polyhedra. These groups are considered as rigid structure fragments when they occur in the structures of various borate crystals and glasses without significant changes.

Stanislav K. Filatov
Department of Crystallography, St. Petersburg State University, St. Petersburg, Russia, e-mail: filatov@crystalspb.com

Rimma S. Bubnova
Institute of Silicate Chemistry of Russian Academy of Sciences, St. Petersburg, Russia, e-mail: Rimma-Bubnova@mail.ru

(3) Triangles, tetrahedra, and rigid groups polymerize with each other to form finite boron-oxygen complex anions and infinite chain, layer and framework anions. Existence of two types of B coordination polyhedra is the determining factor for a formation of a unique variety of anion groups characteristic exclusively for borates and not present in silicates built up from TO_4 tetrahedra solely or carbonates built up from TO_3 triangles etc.

Application of borate-based materials at elevated temperatures and their crystal growth require knowledge of their crystal structures and their correlation with physical properties, in particular, with anisotropy of their thermal expansion.

High-Temperature Crystal Chemistry of Borates

Thermal behavior of more than 40 borates of mono-, bi- and trivalent cations has been investigated, in addition to 10 borates studied earlier, by means of high-temperature X-ray powder diffraction, dilatometry, and differential thermal analysis. Dimensionality of the borate structural units in these structures varied from 0D to 3D, including interpenetrating frameworks. In addition, single crystal X-ray diffraction studies at high temperatures of 5 borate structures have been carried out. As far as we know, this is the first structural studies of borates at high temperatures using both harmonic and anharmonic approximations (Shepelev et al., 2005; Sennova et al., 2007) etc.

To summarize, more than two thirds out of 50 borates studied demonstrate highly anisotropic thermal expansion ($\alpha_{max}/\alpha_{min} \geq 5$). Moreover, about half of them show negative linear thermal expansion. The average linear coefficient of thermal expansion is about $25 \cdot 10^{-6}\ ^{\circ}C^{-1}$. The following regularities of high-temperature crystal chemistry of borates can be formulated on the basis of our experimental results (Filatov and Bubnova, 2000):

(1) BO_3 and BO_4 polyhedra practically do not change upon heating, similarly to tetrahedra in silicates (Filatov and Bubnova, 2000; Shepelev et al., 2005; Sennova et al., 2007) and other oxygen compounds.
(2) Within the rigid groups formed by these polyhedra through shared oxygen atoms, bond lengths and angles practically do not change on heating, whereas bond angles in silicates (Hazen and Finger, 1982) can change considerably, for example in borosilicates (B,Si)–O–(B,Si) angles between tetrahedra within the rings of four tetrahedra might change more than on 10 degrees, this brings together borosilicates and silicates.
(3) The rigid groups linked into polyanions through common oxygen atoms, might rotate relatively to each other like hinges.
(4) Breaking strength of bonds inside the rigid boron-oxygen groups and the ability of these groups to rotate relatively to each other around shared oxygen atoms dictate plasticity of thermal behavior of crystalline and glass borates. As a result, most borates viewed as one-, two- and three-dimensional hinges demonstrate

greatly anisotropic thermal expansion, including linear negative thermal expansion, unusual first-order phase transitions without change of a space-group type, sometimes singular points on temperature dependence of unit cell parameters close to the glass transition temperature, etc.

(5) Thermal expansion of borates decreases with increase of metal-oxygen chemical bonds, i.e. with increase of a valence of charge-compensating cations and the decrease of their size.

(6) It can be expected that a number of triangularly coordinated boron atoms in borates increases on heating. This is testified by investigations of borate melts, i.e., it is known that a number of triangularly coordinated boron atoms increases on heating.

(7) Thermal expansion of borate crystals is more intensive than thermal expansion of borate glasses of the same chemical composition.

So, unusual thermal behaviour of borates is considered herein as the result of formation of borate crystal structures from rigid B-O groups. The reason of a considerable anisotropy of borate thermal deformations is due to thermal invariability of rigid boron-oxygen groups and their mutual rotation around common oxygen atoms, by a shear mechanism (monoclinic and triclinic crystals) and hinge mechanism (crystals of any symmetry). Simultaneous expansion of crystal lattice along certain directions and compression along others can be explained as a result of shears and hinges.

Elements of High-Pressure Crystal Chemistry of Borates

Starting from the first papers summarizing crystal chemistry of borates (Bokij and Kravchenko, 1966; Christ, 1960; Christ and Clark, 1977; Krogh-Moe, 1962; 1965; Tennyson, 1963) and until quite recently (Christ and Clark, 1977; Hawthorne, Burns, Grice, 1996; Filator and Bubnova, 2000), polymerization in borates was thought to be exclusively by corner-sharing. This was one of the first postulates in the "four rules" formulated by (Christ, 1960). By now the first examples of borate crystal structures are known where BO_4 polyhedra polymerize via common O···O edges. These unique compounds, namely $Dy_4B_6O_{15}$ (Huppertz and Eltz, 2002), $Ho_4B_6O_{15}$ (Huppertz, 2003) isostructural to $Dy_4B_6O_{15}$ and a series of α-$Ln_2B_4O_9$ compounds (Ln = Eu, Gd, Tb, Dy) (Emme and Huppertz, 2003) were synthesized under extreme conditions, i.e. high pressure (8–10 GPa) and high temperature ($\sim 1000^{\circ}$C).

In general, it can be said that borates become denser under pressure due to the following reasons:

interatomic distances decreasing;

coordination number of atoms increasing; in the case of borates, that is an increase in a number of tetrahedra in the borate crystal structures;

a possibility of BO_4 polyhedra polymerization via common OO edges instead of polymerization via corners only at atmospheric pressure.

Technological Applications of Borates and Borosilicates

Borates have many technological applications. While traditionally during at least two thousand years they are used for glass production, many of crystalline borates, for example CsB_3O_5, LiB_3O_5, β-BaB_2O_4, and $KB_5O_6(OH)_4{\cdot}2H_2O$, demonstrate important physical properties. So the study of borates contributes not only to the development of the borate structural mineralogy, structural chemistry and physical chemistry but to materials science as well.

Elements exhibiting almost any possible for inorganic compounds coefficient of linear thermal expansion can be cut from a single crystal of a nonlinear-optical LiB_3O_5 borate showing extreme anisotropy of thermal expansion, i.e., $\alpha_{\text{min.}} = -71$, $\alpha_{\text{avg.}} = 31$, $\alpha_{\text{max.}} = 101 \cdot 10^{-6}\ ^{\circ}\text{C}^{-1}$.

Correlation between an anharmonicity of cationic thermal vibrations and a second harmonic generation were found (Shepelev et al., 2005; Sennova et al., 2007). Thus, we can get closer to the understanding of the nature of nonlinear-optical effects and materials. Nonlinear optical effects might be caused by anharmonicity of atomic thermal displacement factors that can be seen in thermal expansion tensor and in deviations from ellipsoidal form of the probability function of atomic thermal displacement factors.

In comparison to the silicate glass, the boron addition improves considerably the chemical durability and the thermal shock resistance that provide for borosilicate glasses a wide variety of applications. Advanced products based on borosilicate glasses include flat panel display substrates, chemical and heat-resistive lab ware, optical glasses, nuclear waste containment materials, sealing, electrodes, and fiber glasses and so on.

The database of thermal expansion coefficients for boroleucite-based materials has been collected that are characterized by a wide range of thermal expansion coefficients ($0–30 \cdot 10^{-6}\ ^{\circ}\text{C}^{-1}$). Materials with zero, low, as well as any other required value can now be found in this database. Taking into account chemical and thermo shock stability of boroleucites, these compounds can be used in the fields of glass-ceramic coatings, house and chemical glassware production, radioactive wastes disposal, etc.

Acknowledgements The work was supported by RFBR (08-03-00232-a) and the Program of Russian Ministry of Science and Education (RNP-2.1.1.3077).

References

Becker P (2001) A contribution to borate crystal chemistry: rules for the occurrence of polyborate anion types. Z Kristallogr 216:523–533

Bokij GB, Kravchenko VB (1966) Crystal chemical classification of borates (in Russian). Zh Strukt khim 7:920–937

Christ CL (1960) Crystal chemistry and systematic classification of hydrated borate minerals. Am Mineral 45:334–340

Christ CL, Clark JR (1977) A crystal-chemical classification of borate structures with emphasis on hydrated borates. Phys Chem Miner 2:59–87

Emme H, Huppertz H (2003) High-pressure preparation, crystal structure, and properties of α-$(RE)_2B_4O_9$(RE = Eu, Gd, Tb, Dy): oxoborates displaying a new type of structure with edge-sharing BO_4 tetrahedra. Chem Eur J 9:3623–3633

Filatov SK, Bubnova RS (2000) Borate crystal chemistry. Phys Chem Glasses 41:216–224

Hawthorne FC, Burns PC, Grice JD (1996) The crystal chemistry of Boron. Rev Miner 33:41–116

Hazen RM, Finger LW (1982) Comparative crystal chemistry: temperature, pressure, compositic and variation of the crystal structure. John Wiley & Sons, London

Huppertz H (2003) High-Pressure Preparation, Crystal Structure, and Properties of RE_4B_6O15 (RE = Dy, Ho) with an Extension of the "Fundamental Building Block"-Descriptors. Z Naturforsch B 58:278–290

Huppertz H, Eltz B (2002) Multianvil high-pressure synthesis of $Dy_4B_6O_{15}$: the first oxoborate with edge-sharing BO_4 tetrahedra. J Am Chem Soc 124:9376

Krogh-Moe J (1962) Structural interpretation of melting point depression in the sodium borate system. J Phys Chem Glasses 3:101–110

Krogh-Moe J (1965) Interpretation of the infra-red spectra of boron oxide and alkali borate glasses Phys Chem Glasses 6:46–54

Sennova NA, Bubnova RS, Shepelev JuF, Filatov SK, Yakovleva OI (2007) $Li_2B_4O_7$ Crystal structure in anharmonic approximation at 20, 200, 400 and 500°C. J Alloy Compd 428:290–296

Shepelev YuF, Bubnova RS, Filatov SK, Sennova NA, Pilneva NA (2005) LiB_3O_5 crystal structure at 20, 227 and 377°C. J Solid State Chem 178:2987–2997

Tennyson C (1963) Eine Systematik der Borate auf kristallchemischer Grundlage. Fortschr Mineral 41:64–91

Zachariasen WH (1938) The crystal structure of Potassium Acid Dihydronium Pentaborate $KH_2(H_3O)_2B_5O_{10.}$ Z Kristallogr 98:266–274

Zachariasen WH, Ziegler GE (1932) The crystal structure of calcium metaborate, CaB_2O_4. Z Kristallogr 83:354–361

Zeolite-Like Borosilicates from the Si-Rich Part of the R_2O–B_2O_3–SiO_2 (R = K, Rb, Cs) Systems

Maria G. Krzhizhanovskaya, Rimma S. Bubnova and Stanislav K. Filatov

Traditionally, alkali borosilicate systems are used as a source for borosilicate glass production (Cable 2005). Borosilicate glasses are far stronger than "soft" silicate glass and have been used for everything from cookware to nuclear waste containment. A mixed alkali borosilicate glass is currently used as a wasteform for the vitrification of high level nuclear waste (Ewing et al. 1995; Plodinec 2000). In this connection there are numerous investigations of borosilicate glass structure and properties. On the other side borosilicate crystalline materials are studied poorly. Since most known crystalline borosilicates are structurally similar to aluminosilicates (leucite family, feldspars, zeolites and others) well known for their properties, the preparation and investigation of new borosilicate materials is of technological interest.

Comparing to the similar aluminosilicate the number of the compounds in ternary alkali borosilicate systems R_2O–B_2O_3–SiO_2 with large alkali cation R = K, Rb, Cs is very limited. Except boroleucite compounds $RBSi_2O_6$ (R = K (Ihara and Kamei, 1980), Rb (Voldan 1981), Cs (Richerson and Hummel 1972)) in the ternary R_2O–B_2O_3–SiO_2 (R = K, Rb, Cs) there are the structural data on hydrotermally prepared compound $KBSi_3O_8$ (Kimata 1993) isostructural to danburite and natural mineral lisitsynite, $KBSi_2O_6$, reported in (Sokolova et al. 2001) as boroleucite polymorph. Additionally there are XRD data for some low temperature potassium borosilicates (Polyakova 2000 and references therein) and presumably metastable low temperature polymorph of $CsBSi_2O_6$ (Huebner et al. 2000) but their structures have not been solved. Last years the boroleucite $RBSi_2O_6$ (R = K, Rb, Cs)

Maria G. Krzhizhanovskaya
Department of Crystallography, St. Petersburg State University, St. Petersburg, Russia, e-mail: Krzhizhanovskaya@mail.ru

Rimma S. Bubnova
Institute of Silicate Chemistry of Russian Academy of Science, St. Petersburg, St. Petersburg Russia

Stanislav K. Filatov
Department of Crystallography, St. Petersburg State University, St. Petersburg, Russia

stoichimetry has been studied widely by us. $RbBSi_2O_6$ structure, isostructural with $KBSi_2O_6$ (Ihara and Kamei, 1980), was refined in the *I*-43*d* space group using XRD powder data (Bubnova et al. 2000; Krzhizhanovskaya et al. 2003). According to single crystal data Cs-deficient boropollucite, $CsBSi_2O_6$, crystallizes in the *Ia3d* space group (Bubnova 2004).

All of the compounds $RBSi_2O_6$ (R = K, Rb, Cs) are structurally similar to the high-temperature cubic leucites. The *I*-43*d* boroleucite framework composed of statistically distributed boron- and silica-oxygen tetrahedra linked into 4-, 6- and 8-fold rings is presented in Fig. 1a. Both *I*-43*d* and *Ia3d* frameworks are practically identical: the difference in the number of crystallographically non-equivalent oxygens in the structure (two for *I*-43*d* and one for *Ia3d* structure) leads to realizing of slightly different types of (B,Si)O-rings (Fig. 1b) although the structural topology does not change. In the K, Rb, Cs-boroleucite structures the alkali cation columns fill the infinite channels formed by 6-fold rings along the [111] direction (see Fig. 3a). The structure transformations of mixed K–Cs and Rb–Cs boroleucites are presented as a function of chemical composition and temperature in Bubnova et al. (2002) Krzhizhanovskaya et al. (2006), respectively. The Rietveld refinement of solid solutions demonstrates that the phases with a high content of smaller alkali atoms (K, Rb) crystallize in the cubic *I*-43*d* space group, wherever the boroleucites with a considerable Cs content have *Ia3d* symmetry. K and Rb can substitute Cs in a wide range of compositions although a narrow range of immiscibility was revealed near the middles if the rows.

Under the substitution of a smaller alkali atom by a larger Cs the cubic lattice parameter (Fig. 2a), the R–O distances, and the angles between tetrahedra of the *I*-43*d* phase change clearly, while those of the *Ia3d* phase change slightly.

Thermal behavior of boroleucite structures has been studied using high-temperature X-ray diffraction (HTXRD), dilatometry and DTA (DSC) methods.

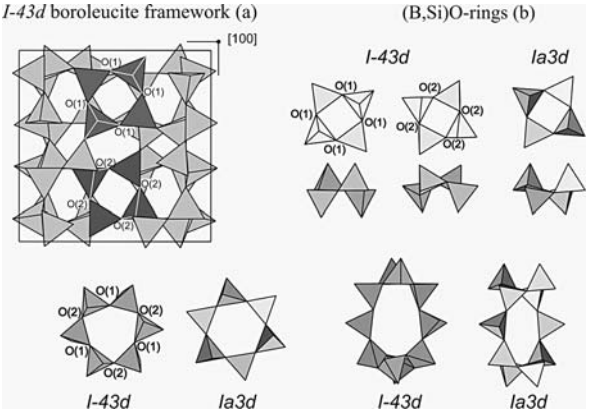

Fig. 1 The structure of $RBSi_2O_6$ (R=K, Rb, Cs) boroleucite. The example of complete framework is shown for *I*-43*d* structure realized in $RBSi_2O_6$, R=K, Rb, (the marked 4-fold rings are crystallographically independent). For *Ia3d* $CsBSi_2O_6$ structure the tetrahedral rings are presented only

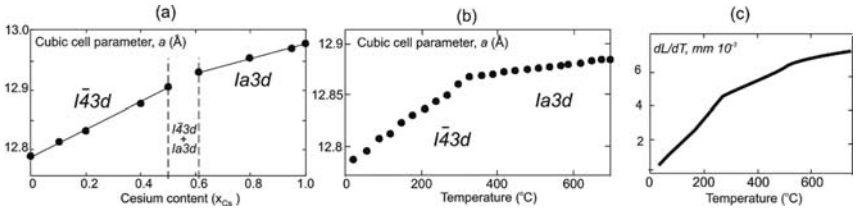

Fig. 2 $RbBSi_2O_6$ boroleucite cell parameter as a function of chemical composition (**a**) and temperature from HTXRD (**b**) or dilatometry (**c**) data

Comparing to the natural leucite and pollucite boron-exchanged compounds represent lower melting points and lower thermal expansion coefficients. For example the thermal expansion coefficient calculated using the data from Palmer et al. (1997) for high-temperature cubic $RAlSi_2O_6$ (R = K, Rb, Cs) are 14, 7 and 4×10^{-6} °C^{-1} correspondingly, wherever those of the same B-exchanged phases are 10, 6 and 2×10^{-6} °C^{-1}. Similar to aluminosilicate systems it is shown that Cs-rich boroleucites belonged to the highest known for leucite symmetry *Ia3d* represent the lowest thermal expansion in the studied K–Cs and Rb–Cs rows (Bubnova et al. 2002; Krzhizhanovskaya et al. 2006). The cell parameter dependence on chemical composition looks similar to that on heating (Fig. 2). Thus the substitution of a smaller atom by a larger Cs one and the heating gives rise to the same change of the cell parameter and presumably to the same structure transformations.

Varying the chemical composition we obtained about a dozen of mixed boroleucites with a diversity of thermal expansion coefficients from near the zero up to 25×10^{-6} °C^{-1}. The determination of the linear thermal expansion coefficients using two different approaches, HTXRD and dilatometry, for micro- (a crystal structure) and macro- (a pressed tablet) objects shows that the results are comparable to each other (Fig. 2b and c) (Krzhizhanovskaya et al. 2007b). Thus for studied

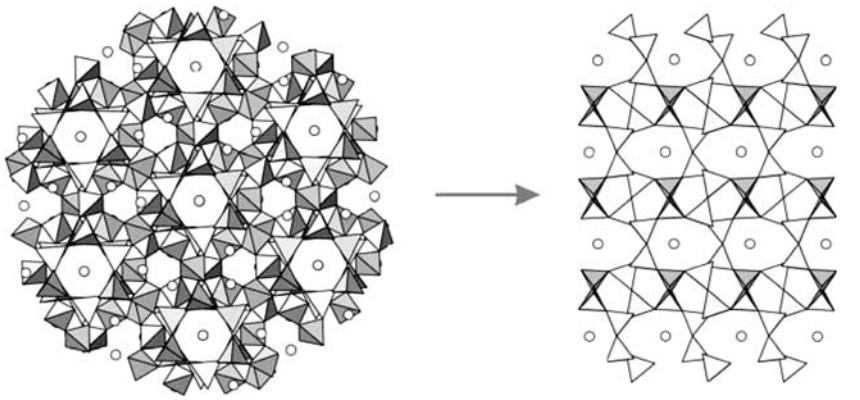

Fig. 3 High-temperature decomposition of boropollucite $CsBSi_2O_6$ (**a**) into $CsBSi_5O_{12}$ borosilicate of CAS zeolite type (**b**)

boroleucites the thermal expansion of atomic structure (HTXRD method) reflects the expansion of real material or product prepared on its basis.

All boroleucites mentioned above can be prepared by solid-state reactions or glass crystallization over 900°C. Up to now the stoichiometry $RBSi_2O_6$ was known as unique stable in the R_2O–B_2O_3–SiO_2 (R= K, Rb, Cs) systems under ambient conditions. Similar K, Rb-, Cs-phases prepared under mild hydrothermal conditions by hydrogel technique have been reported without structural characteristics in Renzo et al. 1996.

Recently, the borosilicate of $CsBSi_5O_{12}$ stoichiometry has been prepared by us from the boropollucite $CsBSi_2O_6$ using a long high-temperature annealing over 1000°C (Bubnova et al. 2007). Crystal structure of a new borosilicate $CsBSi_5O_{12}$ has been refined using X-ray powder diffraction data on powders prepared by solid-state reaction as well as glass crystallization Krzhizhanovskaya et al. 2007a. It is isostructural to $CsAlSi_5O_{12}$ (Araki 1980) with the zeolite framework type CAS (Zeolite structure database...). This compound as well as noted before boroleucites has an open zeolite-like structure composed of (B,Si)O tetrahedral rings (5-, 6- and 8-fold). Along [001] 8-fold rings build infinite channels filled by Cs atoms. The diameter of the channels in $CsBSi_5O_{12}$ structure is slightly larger than that of the channels constructed by 6-fold rings in boroleucite structures (Fig. 3). Non-random distribution of Si and B atoms over tetrahedral position has been revealed. Ordered or partially ordered distribution for Si and B in tetraherda is typical for borosilicates with small alkali cation Li and Na and have also been reported for lisitsynite, $KBSi_2O_6$, in Sokolova et al. (2001) and $KBSi_3O_8$ in Kimata (1993). According to HTXRD data thermal deformation of $CsBSi_5O_{12}$ has anisotropic character with the maximum expansion along the infinite channels, where the columns of Cs atoms are located.

The experiments done in the Si-rich part of R_2O–B_2O_3–SiO_2 (R = K, Rb, Cs) systems show that these regions of compositions demonstrate a potentiality for preparation of new borosilicate crystalline materials with porous structures and/or low thermal expansion which could be considered for different applications particularly for radioactive Cs and Sr immobilization. The data on synthetic boroleucite–boropollucite raws expand the crystal chemistry of natural zeolite like minerals from the leucite–analcime group. According our results on solid-state or glass crystallization synthesis in R_2O–B_2O_3–SiO_2 (R= K, Rb, Cs) systems for the range of compositions $RBSiO_4$–$RBSi_5O_{12}$ and synthesis temperature from 600 up to 1000°C it could be confirmed that the $RBSi_2O_6$ ($R_2O \times B_2O_3 \times 4SiO_2$) stoichiometry is most stable in the systems. New Si-rich phases with another oxide ratio could be probably obtained using the other synthesis approaches only. The fact that boroleucite–boropollucite compounds decompose at high temperature should be taking into account in connection to their potential applications.

Acknowledgements This research has been supported by the grant of the President of Russia for young scientists (MK-3661.2007.5) and the Ministry of Science and Education through the grant 2.1.1.3077.

References

Araki T (1980) Crystal structure of a cesium alumosilicate, $CsAlSi_5O_{12}$. Z Kristallogr 152: 207–209

Bubnova RS, Krzhizhanovskaya MG, Filatov SK, Ugolkov VL, Paufler P (2007) XRD and DSC study of the formation and the melting of a new zeolite like borosilicate $CsBSi_5O_{12}$ and $(Cs,Rb)BSi_5O_{12}$ solid solutions. Z Kristallogr 222:83–86

Bubnova RS, Levin AA, Stepanov NK, Belger A, Meyer DC, Polyakova IG, Filatov SK, Paufler P (2002) Crystal structure of $K_{1-x}Cs_xBSi_2O_6$ (x=0.12, 0.50) boroleucite solid solutions and thermal behaviour of $KBSi_2O_6$ and $K_{0.5}Cs_{0.5}BSi_2O_6$. Z Kristallogr 217:55–62

Bubnova RS, Polyakova IG, Krzhizhanovskaya MG, Filatov SK, Paufler P, Meyer DC (2000) Structure-density relationship for crystals and glasses in the Rb_2O–B_2O_3–SiO_2 system. Phys Chem Glasses 41(6):389–391

Bubnova RS, Stepanov NK, Levin AA, Filatov SK, Paufler, Meyer DC (2004) Crystal structure and thermal behaviour of boropollucite $CsBSi_2O_6$. Solid State Sci 6:629–637

Cable M. (2005) Classical glass technology. In: Zarzyeki J (ed) Material science and technology, vol 9, Glasses and Amorphous Materials. Wiley-VCH Verlag GmbH & Co, Weinheim, Germany, pp 3–85

Ewing RC, Webert WJ, Clinard FWJr (1995) Radiation effects in nuclear waste forms for high-level radioactive waste. Prog Nucl Energ 29(2):63–121

Huebner R, Belger A, Meyer DC, Paufler P, Polyakova IG (2002) Crystallisation of caesium borosilicate glasses with approximate boroleucite composition. Z Kristallogr 217:223–232

Ihara M, Kamei F (1980) Crystal structure of potassium borosilicate, K_2O B_2O_3 $4SiO_2$. Nippon Seram Kyo Gak 88:32–34

Kimata M (1993) Crystal structure of $KBSi_30_8$ isostructural with danburite. Mineral Mag 57: 157–164

Krzhizhanovskaya MG, Bubnova RS, Depmeier W, Filatov SK (2007a) Crystal structure and thermal behavior of a new borosilicate of CAS zeolite type. Book of Abstr XVI Intern Conf On Crystal Chemistry and Diffraction Studies of Minerals. Miass, Russia:223–224

Krzhizhanovskaya MG, Bubnova RS, Filatov SK, Meyer DC, Paufler P (2003) Crystal structure transformation in Rb-boroleucite solid solutions from powder diffraction data. Glass Phys Chem 29:827–838 (in Russian)

Krzhizhanovskaya MG, Bubnova RS, Filatov SK, Meyer DC, Paufler P (2006) Crystal structure and thermal behaviour of $(Rb,Cs)BSi_2O_6$ solid solutions. Cryst Res Technol 41:285–292

Krzhizhanovskaya MG, Bubnova RS, Ugolkov VL, Filatov SK (2007b) Thermal behaviour and polymorphism of Rb–Cs boroleucites from powder X-ray diffraction and dilatometry data. Glass Phys Chem 33:341–350 (in Russian)

Palmer DC, Dove MT, Ibberson RM, Powell AM (1997) Structural behavior, crystal chemistry, and phase transitions in substituted leucite: high-resolution neutron powder diffraction studies. Am Mineral 82:16–29

Plodinec MJ (2000) Borosilicate glasses for nuclear waste immobilization. Glass Technol 41: 186–193

Polyakova IG (2000) Alkali borosilicate systems: phase diagrams and properties of glasses. Phys Chem Glasses 41:247–258

Renzo FD, Derewinski M, Chiari G, P1evert J, Driole M-F, Fajula F, Schulz Ph (1996) Insertion of boron in tectosilicate frameworks in the presence of large alkali cations. Micropor Mater 6:151–157

Richerson DW, Hummel FA (1972) Synthesis and thermal expansion of polycrystalline cesium minerals. J Am Ceram Soc 55:269–273

Sokolova EV, Hawthorne FC, Khomyakov AP (2001) The crystal chemistry of malinkoite, $NaBSiO_4$, and lisitsynite, $KBSi_2O_6$, from the Khibina–Lovozero complex, Kola peninsula, Russia. Can Mineral 39:159–169

Voldan J (1981) Crystallization of $Rb_2O{\cdot}B_2O_3{\cdot}4SiO_2$. Silikaty 25:165–167

Zeolite structures database (www.iza-structure.org/databases/)

Structural Diversity of Layered Double Hydroxides

Sergey N. Britvin

Layered double hydroxides (LDH) – a wide family of compounds involving representatives of closely related mineral groups, including hydrotalcite–manasseite, quintinite, woodwardite, meixnerite and hydrocalumite-kuzelite groups, as well as their numerous synthetic analogues (Strunz and Nickel 2001, Rives 2001, Khan and O'Hare 2002). In the past decades, LDH attracted considerable attention due to their chemical and structural features applicable in different fields of industry. These compounds are easily synthesized in water solutions under ambient conditions. LDH adopt huge variety of cations inside hydroxide slabs, making possible easy preparation of oxide catalysts by simple heat treatment. But the most striking and useful peculiarity is their anion-exchange properties. Contrary to large number of cation-exchangers related to different classes of compounds, number of known anion-exchange frameworks is rather limited. Among them, LDH (also known as "anionic clays") are quite unique because they may adopt and exchange tenths of different anions (Miyata and Kimura 1973, Miyata 1975, Miyata and Okada 1977, Rives 2001, Khan and O'Hare 2002, Kloprogge et al. 2002 and the references cited herein). As a consequence, they are widely used for selective extraction of anions, purification of solutions and preparation of different types of combined catalysts.

Structural topology of LDH is governed by presence of positively charged hydroxide slabs (sheets) $[(M^{2+}_{1-x}M^{3+}_{x})(OH)_2]^{x+}$ or $[(Li_{1/3}M^{3+}_{2/3})(OH)_2]^{1/3+}$, – derivatives of $[M^{2+}(OH)_2]$ slabs of brucite structure type. The slabs inherit hexagonal symmetry of corresponding brucite units and like that are composed of edge-sharing $[M(OH)_6]$ octahedra parallel to (0001). In brucite, $Mg(OH)_2$, and its analogues, hydroxide slabs are charge balanced, and interlayer interactions are maintained by hydrogen bonds. In LDH, part of divalent cations in slabs is substituted by M^{3+} or by combination of $(Li_{1/3}M^{3+}_{2/3})$. As a consequence, the slabs

Sergey N. Britvin
Department of Crystallography, Faculty of Geology, St. Petersburg State University, University Emb. 7/9, St. Petersburg, Russia, e-mail: SBritvin@gmail.com

become positively charged. Charge balance is then achieved by intercalation of anions (CO_3^{2-}, SO_4^{2-}, NO_3^-, Cl^-, OH^-, etc.) in the interlayer. Besides that, water, polar organic molecules and large solvated cations ($[Na(H_2O)_6]^+$, $[Ca(H_2O)_6]^{2+}$) may intercalate in the interlayer space.

Several different factors are responsible for formation of complex hybrid structures of LDH.

1. Ordering of octahedral cations within the slabs results in superstructures based on multiplication of simplest "in-slab" brucite translation (a_b) equal to edge of [M(OH)$_6$] octahedron. Typical examples are structures with M^{2+}/M^{3+} = 2/1, minerals related to motukoreaite ($a = 3a_b$) and quintinite ($a = 2a_b\sqrt{3}$) series (Rius and Plana 1986, Cooper and Hawthorne 1996, Huminicki and Hawthorne 2003, Arakcheeva et al. 1996, Chao and Gault 1997). Wermlandite, $[Mg_7(Al,Fe)_2(OH)_{18}]^{2+}[(Ca,Mg)(SO_4)_2(H_2O)_{12}]^{2-}$ (M^{2+}/M^{3+} = 7/2) also possess $3a_b$ superstructure (Rius and Allmann 1978, 1984) (Fig. 1). Insertion of large-radii cations (i.e. Ca^{2+}) in hydroxide slabs may lead to further distortion of lattice yielding pseudo-hexagonal superstructures like hydrocalumite, $[Ca_4Al_2(OH)_{12}]^{2+}[Cl_2(H_2O)_4]^{2-}$ (Sacerdoti and Passaglia 1988).
2. Anions and solvated cations in the interlayer may be packed in a different ways. Composition of intercalants and their ordering affects the thickness of interlayer space and consequently, of packet thickness (= hydroxide slab + interlayer). Typical examples of interlayer packing are shown on Fig. 2.
3. Different stacking sequences of packet units (hydroxide slab + interlayer) along *c*-axis result in formation of a variety of polytypes. In addition, brucite-like layers may be double-stacked along hexagonal *c*-axis resulting in unique structure of coalingite, $[Mg_{10}Fe_2^{3+}(OH)_{24}]^{2+}[(CO_3)(H_2O)_2]^{2-}$ (Pastor-Rodriguez and Taylor 1971).
4. In case of intercalation of large polar organic molecules (carboxylate- and hydroxyl-anions), a strong interaction between hydroxide slabs and anions

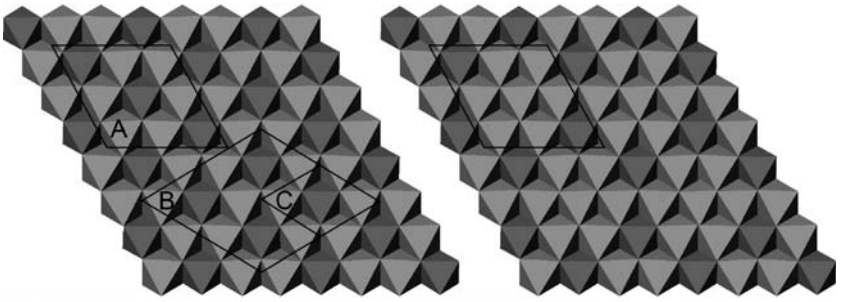

Fig. 1 Schemes of ordering of octahedral cations within brucite-like slabs of LDH, projection on (0001). *Left* picture – 2/1 compounds: motukoreaite, $[Mg_6Al_3(OH)_{18}]^{3+}$ $[Na(SO_4,CO_3)_2(H_2O)_{12}]^{3-}$(cell **A**, $a = 3a_b$), and quintinite, $[Mg_4Al_2(OH)_{12}]^{2+}[(CO_3)(H_2O)_3]^{2-}$ (cell **B**: $a = 2a_b\sqrt{3}$ by Chao and Gault 1997, cell **C**: $a = a_b\sqrt{3}$ by Arakcheeva et al. 1996). *Right* picture – 7/2 compound, wermlandite ($[Mg_7(Al,Fe)_2(OH)_{18}]^{2+}$ $[(Ca,Mg)(SO_4)_2(H_2O)_{12}]^{2-}$, $a = 3a_b$). Light octahedra – M^{2+}, dark ones – M^{3+}

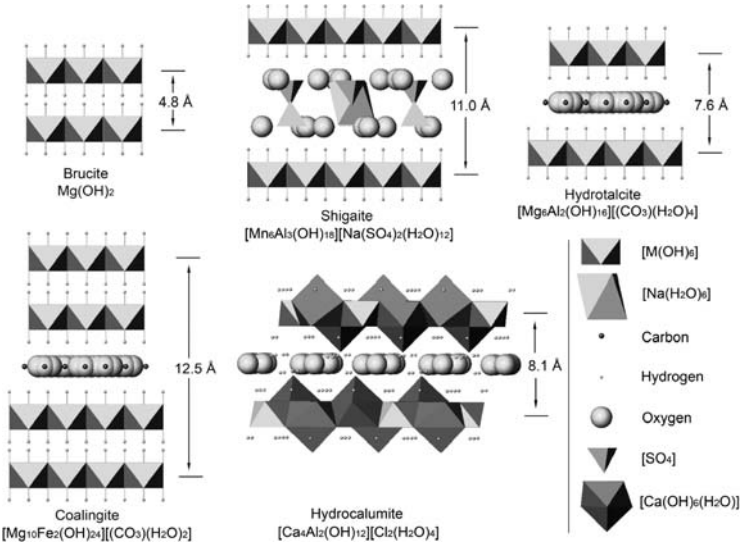

Fig. 2 Typical kinds of interlayer stacking observed in layered double hydroxides. Structural data are taken from the references cited in the text

results in stable frameworks known as *pillared layered structures*, with interlayer spacings considerably exceeding those typical of inorganic LDH (Mitchell 1990, Gago et al. 2004).

Note that crystal structure of many LDH is not yet studied in detail, due to poor crystallinity of the substances, nanometer-scale size of their particles (especially for synthetic compounds) and intimate intergrowths of closely related phases. Karchevskyite, a new mineral recently described from carbonatites of Kovdor massif, Kola Peninsula, Russia (Britvin et al. 2007), is an example of such "difficult" compound. Despite quite good natural appearance (Fig. 3) and well-developed crystal morphology, the mineral still resists single-crystal study. Data obtained by electron diffraction, X-ray powder diffraction, IR-spectroscopy, TGA and electron microprobe unambiguously indicate its relationship to LDH. Chemical formula of karchevskyite may be represented by the different ways, either as $[Mg_{18}Al_9(OH)_{54}][Sr_2(CO_3,PO_4)_9(H_2O,H_3O)_{11}]$ or $[Mg_{18}Al_9(OH)_{54}]$ $[Sr_2(CO_3, HCO_3,PO_4)_9(H_2O)_{11}]$. The mineral possess well developed superstructure along a-axis (SAED data) and basal spacing d = 8.5 Å. The latter value is much higher than d = 7.6 Å characteristic of all known carbonate-dominant LDH (Table 1). There are two basic chemical differences between karchevskyite and typical CO_3^{2-}-LDHs (hydrotalcite, quintinite, etc.). Karchevskyite is the first known carbonate-dominant LDH intercalated both with CO_3^{2-} and cation (Sr^{2+}), and this is the first Sr-bearing LDH. It is obvious that Sr^{2+} is responsible for interlayer expansion observed in karchevskyite, but structural position of this cation remains enigmatic.

It is well known that Sr^{2+} is much larger than Mg^{2+} (ionic radii of Sr^{2+} is 1.18 Å against 0.75 Å of Mg^{2+}) thus its insertion in $[Mg(OH)_6]$ octahedra of brucite-like

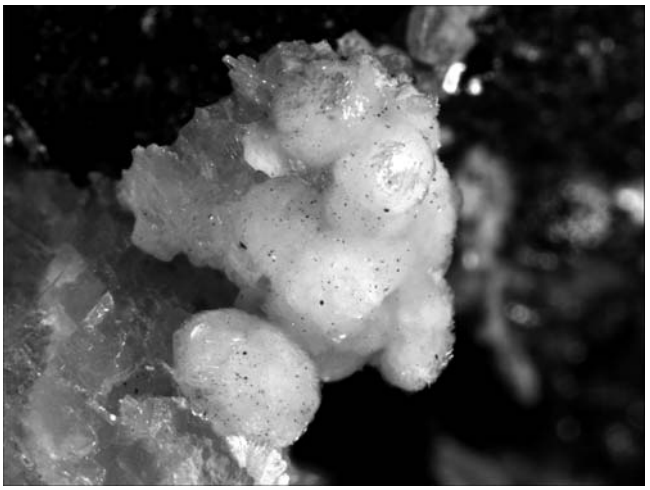

Fig. 3 White spherulites composed of karchevskyite and quintinite-*3T* on pink dolomite. Field of view = 3 mm

slabs is quite unlikely. On the other part, free solvated Sr^{2+} expected in the interlayer would adopt eight-fold coordination typical of that observed in aqua solutions of Sr^{2+} salts or in $Sr(OH)_2 \cdot 8H_2O$ (Smith 1953, Moreau et al. 2002, Ricci et al. 2005). In particular, $Sr(OH)_2 \cdot 8H_2O$ possess two-layer structure composed of $[Sr(OH)_8]$ square antiprisms and water molecules; the thickness of single $[Sr(OH)_2]$ layer is 5.8 Å. This value is by 2 Å large than thickness of free interlayer space of 3.75 Å calculated for karchevskyite. Consequently, Sr^{2+} can not intercalate into karchevskyite interlayer as solvated ion. The only way of such intercalation is to form polyhedra which are linked with adjacent brucite-like slabs. A calculation based on published data (Desgranges et al. 1996, Ricci et al. 2005) leads to a speculation that $[SrO_8]$ polyhedra may be linked with $[(Mg,Al)(OH)_6]$ octahedra via hydrogen bridges like Sr−O−H−O−(Mg, Al). In such a case, karchevskyite might be the first representative of layered double hydroxide pillared by inorganic ion.

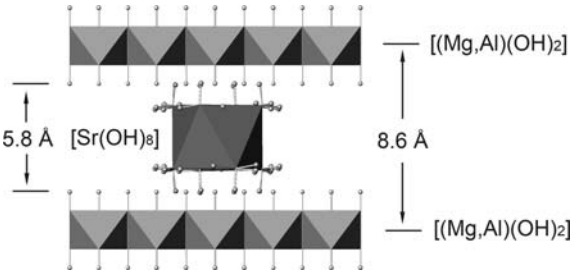

Fig. 4 Possible way of Sr^{2+} intercalation into karchevskyite interlayer. Polyhedra dimensions and lengths of hydrogen bonds are adjusted to the ordinal scale

Table 1 Comparative characteristics of Mg–Al layered double hydroxides

	Hydrotalcite	Quintinite-3*T*	Karchevskyite	Motukoreaite	Wermlandite
Brucite-like slab	$[Mg_{1-x}Al_x(OH)_2]^{x+}$	$[Mg_4Al_2(OH)_{12}]^{2+}$	$[Mg_{18}Al_9(OH)_{54}]^{9+}$	$[Mg_6Al_3(OH)_{18}]^{3+}$	$[Mg_7(Al,Fe)_2(OH)_{18}]^{2+}$
Interlayer	$[(CO_3)_x(H_2O)_2]^{x-}$	$[(CO_3)(H_2O)_3]^{2-}$	$[Sr_2(CO_3,PO_4)_9(H_2O, H_3O)_{11}]^{9-}$	$[Na(SO_4,CO_3)_2(H_2O)_{12}]^{3-}$	$[(Ca,Mg)(SO_4)_2\ (H_2O)_{12}]^{2-}$
Reference	Bellotto et al. (1996)	Chao and Gault (1997)	Britvin et al. (2007)	Rius and Plana (1986)	Rius and Allmann (1984)
Space group	*R*-3*m*	*P*321, *P*312	*P*3*	*R*-3m	*P*-3*c*1
a, Å	3.05	10.56	16.06	9.17	9.30
c, Å	22.77	22.71	25.66	33.51	22.57
Z	3	6	3	3	2
Basal *d*, Å	7.59	7.57	8.55	11.17	11.29
a relative to a_b (of brucite)	a_b	$2a_b\sqrt{3}$	$3a_b\sqrt{3}$	$3a_b$	$3a_b$

References

Arakcheeva AV, Pushcharovskii DYu, Rastsvetaeva RK, Atencio D, Lubman GU (1996) Crystal structure and comparative crystal chemistry of $Al_2Mg_4(OH)_{12}(CO_3)\cdot 3H_2O$, a new mineral from the hydrotalcite- manasseite group. Kristallografiya 41:1024–1034 (in Russian)

Bellotto M, Rebours B, Clause O, Lynch J, Bazin D, Elkaim E (1996) A reexamination of hydrotalcite crystal chemistry. J Phys Chem 100:8527–8534

Britvin, SN, Chukanov NV, Bekenova GK, Yagovkina MA, Antonov AV, Bogdanova AN, Krasnova NI (2007) Karchevskyite $[Mg_{18}A_{19}(OH)_{54}][Sr_2(CO_3,PO_4)_9(H_2O,H_3O)_{11}]$, a new mineral related to layered double hydroxides. Proceedings of the Russian Mineralogical Society 36(5):52–64 (in Russian)

Chao G, Gault RA (1997) Quintinite-2H, quintinite-3T, charmarite-2H, charmarite-3T and caresite-3T, a new group of carbonate minerals related to the hydrotalcite-manasseite group. Can Mineral 35:1541–1549

Cooper MA, Hawthorne FC (1996) The crystal structure of shigaite, $[Mn_2^{2+}(OH)_6]_3(SO_4)_2 Na(H_2O)_6\{H_2O\}_6$, a hydrotalcite-group mineral. Can Mineral 34:91–97

Desgranges L, Calvarin G, Chevrier G (1996) Interlayer interactions in $M(OH)_2$: a neutron diffraction study of $Mg(OH)_2$. Acta Crystallogr B 52:82–86

Gago S, Pillinger M, Santos TM, Gonçalves IS (2004) Zn–Al layered double hydroxide pillared by different dicarboxylate anions. Ceram–Silikaty 48(4):155–158

Huminicki DMC, Hawthorne FC (2003) The crystal structure of nikischerite, $NaFe^{2+}{}_6Al_3(SO_4)_2 (OH)_{18}(H_2O)_{12}$, a mineral of the shigaite group. Can Mineral 41:79–82

Khan AI, O'Hare D (2002) Intercalation chemistry of layered double hydrohides: recent developments and applications. J Mater Chem 12:3191–3198

Kloprogge JT, Wharton D, Hickey L, Frost RL (2002) Infrared and Raman study of interlayer anions CO_3^{2-}, NO_3^-, SO_4^{2-} and ClO_4^- in Mg/Al hydrotalcite. Am Mineral 87:623–629

Mitchell IV (ed) (1990) Pillared layered structures: current trends and applications. Elsevier Applied Science, London

Miyata S (1975) The synthesis of hydrotalcite-like compounds and their structures and physico-chemical properties – I: the systems Mg^{2+}-Al^{3+}-NO_3^-, Mg^{2+}-Al^{3+}-Cl^-, Mg^{2+}-Al^{3+}-ClO_4^-, Ni^{2+}-Al^{3+}-Cl^- and Zn^{2+}-Al^{3+}-Cl^-. Clay Clay Miner 23:369–375

Miyata S, Kimura T (1973) Synthesis of new hydrotalcite-like compounds and their physico-chemical properties. Chem Lett 843–848

Miyata S, Okada A (1977) Synthesis of hydrotalcite-like compounds and their physico-chemical properties – the system Mg^{2+}-Al^{3+}-SO_4^{2-} and Mg^{2+}-Al^{3+}-CrO_4^{2-}. Clay Clay Miner 25:14–18

Moreau G, Helm L, Purans J, Merbach AE (2002) Structural investigation of the aqueous Eu^{2+} Ion: comparison with Sr^{2+} using the XAFS technique. J Phys Chem A 106:3034–3043

Pastor-Rodriguez J, Taylor HFW (1971) Crystal structure of coalingite. Mineral Mag 38:286–294

Ricci JS, Stevens RC, McMullan RK, Klooster WT (2005) Structure of strontium hydroxide octahydrate, $Sr(OH)_2\cdot 8H_2O$, at 20, 100 and 200 K from neutron diffraction. Acta Crystallogr B 61:381–386

Rius J, Allmann R (1978) Structure des wermlandites, $[Mg_7(Al,Fe)_2(OH)_{18}]^{2+}[Ca(H_2O)_6 (SO_4)]^{2-}$. Fortschr Mineral B 56:113–114

Rius J, Allmann R (1984) The superstructure of the double layer mineral wermlandite $[Mg_7(Al_{0.57},Fe_{0.433})(OH)_{18}]^{2+}[(Ca_{0.6},Mg_{0.4})(SO_4)_2(H_2O)_{12}]^{2-}$. Z Kristallogr B 168:133–144

Rius J, Plana F (1986) Contribution to the superstructure resolution of the double layer mineral motukoreaite. Neues Jb Miner Monat 6:263–272

Rives V (ed) (2001) Layered double hydroxides: present and future. Nova Scientific Publishing Inc, New York

Sacerdoti M, Passaglia E (1988) Hydrocalumite from Latium, Italy: its crystal structure and relationship with related synthetic phases. Neues Jb Miner Monat 462–475

Smith HG (1953) The crystal structure of strontium hydroxide octahydrate, $Sr(OH)_2(H_2O)_8$. Acta Crystallogr 6:604–609

Strunz H, Nickel EH (2001) Strunz mineralogical tables. Schweizerbart'sche Verlagsbuchhandlung, Stuttgart

Crystal Chemistry of Oxocentered Chain Lead Oxyhalides and their Importance as Perspective Materials

Oleg I. Siidra and Sergey V. Krivovichev

Introduction

Lead oxy- and hydroxychlorides are common in alteration zones of Pb mineral deposits (Table 1), where they form as a result of hydrolysis of Pb^{2+} ions in aqueous chloride media during oxidation of primary sulfide minerals (e.g. PbS). Formation and precipitation of lead oxide and hydroxide chlorides play an important role in the transport of Pb from mines and mill tailings to the biosphere. These phases are also well-known as corrosion products of lead artefacts (Edwards et al., 1992) and as precipitates in natural gas production installations. Pb oxide chlorides were detected in dust particles emitted from a lead smelter. Pb halides (chloride-bromides) and oxy- and hydroxyhalides were observed in automobile exhaust gases (Post and Buseck, 1985) and roadside soils (Smith, 1976). Pb oxyhalides have not only environmental importance, but are also interesting from the viewpoint of material science. Materials with anisotropic crystal structure exhibit a variety of physical properties that depend strongly on crystallographic direction, such as a refractive index (i.e., birefringent materials), the permanent dipole moment in ferroelectrics, the magnetocrystalline anisotropy in ferromagnets, and carrier mobilities in ionic conductors. Glasses based on lead oxyhalides are widely used in the conversion of infrared light into visible light. $PbO{\pm}PbBr_2$ based materials, the dehydroxylation products of Pb(OH)Br, are used in the preparation of low melting glasses useful as glass scintillators in high energy physics.

Oleg I. Siidra
Department of Crystallography, St. Petersburg State University, University Emb. 7/9, 199034 St. Petersburg, Russia, e-mail: siidra@mail.ru

Sergey V. Krivovichev
Department of Crystallography, St. Petersburg State University, University Emb. 7/9, 199034 St. Petersburg, Russia

Table 1 Crystallographic data of Pb(II) oxychloride minerals containing OPb_4 oxocentered tetrahedra

O:Pb	Chemical formula and mineral name	Space group	a, Å / α,°	b, Å / β,°	c, Å /γ,°	V, Å^3	Reference
2:3	$Cu[Pb_3O_2](OH)_2Cl_2$ chloroxiphite	$P2/m$	10.46	5.76 / 97.79	6.70	399.4	Finney et al. (1977)
2:3	$[Pb_3O_2]Cl_2$ mendipite	$Pnma$	11.88	5.81	9.51	655.8	Krivovichev and Burns (2001)
2:3	$[Pb_3O_2](OH)Cl$ damaraite	$Pmc2_1$	5.81	6.90	15.14	606.7	Krivovichev and Burns (2001)
3:8	$[Pb_8O_3]Cu(AsO_3)_2Cl_5$ freedite	$C2/m$	13.58	20.10 105.73	7.46	1961.0	Pertlik (1987)
1:1	$[(Pb,Mo,\square)O]_8Cl_2$ parkinsonite	$I4/mmm$	3.99	3.99	22.51	358.8	Symes et al. (1994)
1:1	$[Pb_3Sb_{0.6}As_{0.4})O_3]$ $(OH)Cl_2$ thorikosite	$I4/mmm$	3.92	3.92	12.85	197.4	Rouse and Dunn (1985)
1:1	$[Pb_{12}(SiO_4)O_8]Cl_4$ asisite	$I4/mmm$	3.89	3.89	22.80	345.6	Welch (2004)
5:8	$[Pb_8O_5](OH)_2Cl_4$ blixite	$C2/c$	26.07	5.84 / 102.61	22.74	3375.3	Krivovichev and Burns (2006)
9:14	$[Pb_{14}O_9](VO_4)_2Cl_4$ kombatite	$C2/c$	12.68	22.57 / 118.11	11.28	2847.1	Cooper and Hawthorne (1994)
9:14	$[Pb_{14}O_9](AsO_4)_2Cl_4$ sahlinite	$C2/c$	12.70	22.58 / 118.37	11.29	2848.4	Bonaccorsi and Pasero (2003)
7:10	$[Pb_{10}O_7](SO_4)$ $Cl_4(H_2O)$ symesite	$B\bar{1}$	19.73 / 82.21	8.80 / 78.08	13.63 / 100.04	2242.4	Welch et al. (2000)
2:1:1	$[PbSbO_2]Cl$ nadorite	$Cmcm$	5.60	12.25	5.45	373.8	Giuseppetti and Tadini (1973)
2:1:1	$[PbBiO_2]Cl$ perite	$Bmmb$	5.63	5.58	12.43	389.8	Gillberg (1961)

Crystal Chemistry of Lead and Oxygen in Pb Oxyhalides

An outstanding feature of all lead oxyhalides described in this short review is the presence in their structure of OPb_4 oxocentered tetrahedra.

Traditional inorganic crystal chemistry and structural mineralogy are based upon the concept of cation-centered polyhedra. However, there is a number of inorganic salts (sulfates, phosphates, silicates, chlorides, sulphides, etc.) that can be considered as consisting of strongly bonded structural units formed by anion-centered coordination polyhedra. This is the group of compounds that contain additional anions, i.e. anions that are not parts of strong anionic complexes ("acid residues"). Additional oxygen anions, O^{2-}, are the most widespread examples of such anions. In most cases, in Pb compounds, additional O^{2-} anions are coordinated by four Pb^{2+} cations, thus forming oxocentered $[OPb_4]$ tetrahedra.

As shown by bond-valence theory, anion-centered tetrahedra represent units with high bond-valences (Krivovichev and Filatov, 2001). The bond-length and bond-valence analysis of minerals and inorganic compounds containing O atoms belonging to oxyanions (TO_q) (T = Se, S, Cr, V, As; q = 3, 4) and additional O atoms (O_T and O_a, respectively) shows that the strength of O_a–A bonds is higher than that of the O_T–A bonds. This effect is particularly pronounced for the Pb compounds: the Pb–O_a bond lengths are in the range of 2.10–2.40 Å, whereas the Pb–O_T bond lengths are usually higher than 2.5 Å. For instance, in the structure of lanarkite, $Pb_2O(SO_4)$, the Pb-O_a bond lengths are in the range of 2.27–2.33 Å, whereas all Pb-O_T bonds are longer than 2.45 Å.

The basic feature of Pb(II) is the presence of the $6s^2$ lone electron pair that might or might not be stereochemically active (Mudring, 2006). In the latter case, cation coordination is symmetrical with more or less equal bonds to anions. In the former case, coordination is distorted with several short bonds in one hemisphere and additional long bonds in another hemisphere. In spatial terms, stereochemically active lone electron pair plays a role of additional ligand and occupies a volume approximately equal to the volume of O^{2-} anion. The lone electron pair is active, when the structure contains strong Lewis bases. Brown and Faggiani (1980) demonstrated that lone electron pair on Tl^+ cations is active when Lewis base strength is higher than 0.22 valence units (v.u.). It is very likely that there are similar limits for the Pb^{2+} cations as well. Additional oxygen atoms act as strong Lewis bases with the Lewis strength of 0.5 v.u. (calculated as a formal charge divided by four). Therefore, in Pb(II) compounds with additional O atoms, lone electron pairs on the Pb^{2+} cations are usually stereochemically active. This implies concentration of short Pb^{2+}–O_a bonds in one cation coordination hemisphere and, consequently, high strength of the Pb–O_a structural motifs.

Taking into account short bonds only, the most usual coordination of Pb^{2+} cations in oxysalts is either trigonal pyramidal or tetragonal pyramidal with Pb situated in a pyramid apex. Other types of coordination are also possible but are relatively rare. For instance, in mendipite, $Pb_3O_2Cl_2$ (Krivovichev and Burns, 2001), and synthetic $Pb_3O_2Br_2$ and $Pb_3O_2I_2$, Pb^{2+} cations form only two short Pb–O bonds and a couple of long and weak bonds with halogen anions. It is remarkable that the PbO_2 complex is not linear but has an angular structure with the O–Pb–O angle of ~80–90°. Short and strong Pb–O bonds in the Pb^{2+} coordination hemisphere

opposite to the $6s^2$ electron pair are in the range 2.20–2.40 Å, which is equal to 0.60–0.40 v.u.

The interesting feature of Pb(II) compounds is a possible presence of weak Pb···Pb attractive interactions with energy close to that of a hydrogen bond (Pyykö, 1997). The role of these close shell interactions seems to be very important in stabilization of some structure types. The crystal structure of litharge (tetragonal PbO) is based upon the [OPb] sheets formed by edge sharing of OPb_4 tetrahedra. However, despite its layered character, the mineral does not have a good cleavage parallel to the plane of the sheets. On the basis of nuclear magnetic resonance (NMR) investigations, Gabuda et al. (1999) suggested presence of attractive Pb···Pb interactions that provide interlayer bonding and three-dimensional integrity of the structure.

Due to the low charge of the central O^{2-} anion, OPb_4 tetrahedra may link through edges as well as through corners. Therefore, structural complexity of the oxocentered tetrahedral units is higher than that of other tetrahedral units known in chemistry, i.e. of silicate anions. Topological complexity induced by the possibility of edge and corner sharing tetrahedra results in the fact that the Pb:O ratio in oxocentered complexes might be more than one, which is in stark contrast to silicates, where the Si:O ratio is in the range of 0.250–0.500.

Below we provide description of some practically-significant chain lead oxyhalides based upon OPb_4tetrahedra in the order of increasing complexity, i.e. starting from single OPb_4 chains, double chains and complex chains with mixed OPb_nA_{4-n} tetrahedra in final.

Quasi-One-Dimensional (Chain) Pb Oxyhalides

The $[OPb_2]^{2+}$ chains of *trans*-edge-sharing OPb_4 tetrahedra (Fig. 1) are common in minerals and inorganic compounds (Krivovichev and Filatov, 2001). They were first described by Sahl (1970) in the structure of lanarkite, $Pb_2O(SO_4)$. The identity periods of these $[OPb_2]^{2+}$ chains are in the range of 5.68–5.80 Å since their periodicity is usually equal to 2. The known examples of such chains with a periodicity of 4 have been observed in the structures of elyite, $[Pb_2O]Cu(SO_4)(OH)_4{\cdot}H_2O$ (Kolitsch and Giester, 2000), and $Pb_4O(VO_4)_2$ (Krivovichev and Burns, 2003), where the identity periods of the chains are 11.532 and 11.540 Å, respectively. In the structure of philolithite, $[Pb_2O]_6Mn(Mg_{0.54}Mn_{0.46})_2(Mn_{0.68}Mg_{0.32})_4(SO_4)(CO_3)_4Cl_4(OH)_{12}$ (Moore et al., 2000), the $[OPb_2]^{2+}$chains have a periodicity of 6 and the identity period of 17.857 Å. In all cases, the identity periods are multiples of 2.73–2.98 Å, which is a distance between the imaginary middle points of the two opposite edges of a OPb_4 tetrahedron. Similar chains have also been found in the structure of $\mathbf{Pb_{2+x}OCl_{2+2x}}$ (Siidra et al., 2007c).

The ionic conductivity of the PbO–$PbCl_2$ system was studied in detail in Matsumoto et al., 2001, where the $3PbCl_2{\cdot}2PbO$ phase (identified by X-ray powder diffraction as $Pb_5O_2Cl_6$) was found to have the highest conductivity ($(2–4){\cdot}10^{-2}$ S/cm at 350°C and $1{\cdot}10^{-4}$S/cm at 25°C). However, the structure of this phase and,

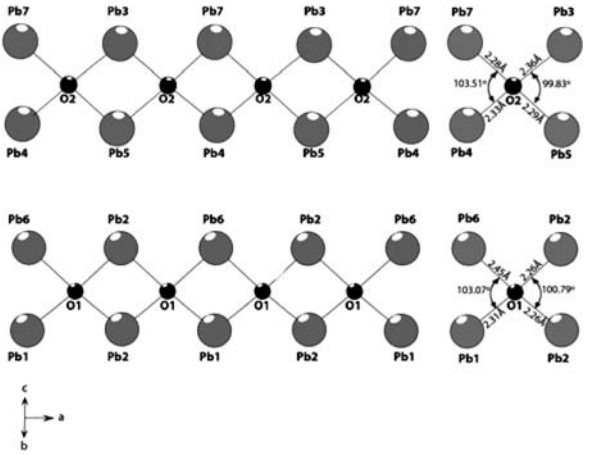

Fig. 1 Chains of edge-sharing oxocentered OPb_4 tetrahedra in the structure of $Pb_{2+x}OCl_{2+2x}$ (*left*) and geometrical parameters of OPb_4 tetrahedra (*right*). Note the deviation of the Pb–O–Pb angles corresponding to the Pb··Pb shared edge from the ideal tetrahedral value of 109.5°

consequently, the mechanism of the ionic conductivity remained unknown until recently. The structure contains seven completely occupied Pb positions; each of them is coordinated by two O^{2-}anions (Pb^{2+}–O^{2-}= 2.26–2.45 Å) and by several (from 4 to 7) Cl^-anions (Pb^{2+}–Cl^-= 2.75–3.60 Å). The lead sites with low occupancy are coordinated only by Cl^-ions. The $Pb_{2+x}OCl_{2+2x}$ structure as a whole can be represented as consisting of two structurally different two-dimensional (2D) blocks L' and L'' (Fig. 2). The L' block consists of completely ordered $[O_2Pb_4]^{4+}$ chains (Fig. 2) and Cl^- anions, whereas the L'' unit contains a system of Pb and Cl positions with low occupancy. The determined crystal structure of $Pb_{2+x}OCl_{2+2x}$ allows one to understand the mechanism of the high ionic conductivity of this compound described for the first time by Matsumoto et al. The presence in the structure of columns of cation and anion vacancies is indicative of a high mobility of ions located in these channels and shows possible directions of ion transfer in the structure. Matsumoto et al. identified the chloride ion as the major charge carrier in this system, which is in agreement with the results of the present work.

In as much as the structure can be divided into alternating nonconducting (with completely occupied positions) and conducting (with low-occupancy sites) 2D layers, $Pb_{2+x}OCl_{2+2x}$ can be considered to be a two-dimensional ionic conductor (Fig. 3). The thickness of the nonconducting layer is about 1.5 nm, which allows us to preliminarily describe $Pb_{2+x}OCl_{2+2x}$ as a nanocondenser. At the same time, additional studies are required to measure conductivity anisotropy in single crystals of the compound.

Note that lead oxyhalides are also of considerable interest for fabrication of new nanomaterials. Sigman and Korgel (2005) recently described synthesis and properties of highly birefringent $Pb_3O_2Cl_2$ nanostructures, with composition of a natural mineral mendipite. Bulk $Pb_3O_2Cl_2$ (mendipite) shows relatively strong

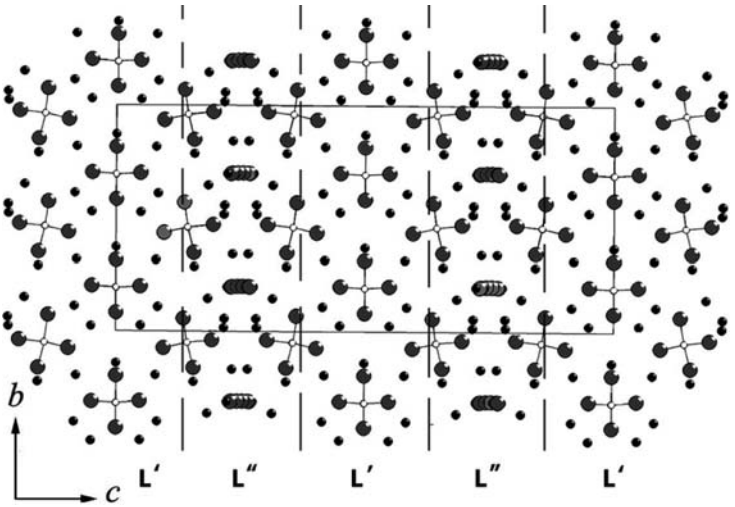

Fig. 2 The crystal structure of $Pb_{2+x}OCl_{2+2x}$ projected along the *a* axis. Large grey spheres are Pb^{2+} cations, small black and white spheres are Cl^{-} and O^{2-} anions, respectively. Only the Pb–O bonds are shown

birefringence with direction-dependent refractive indices of 2.27 A (*a* axis), 2.31A (*b* axis), and 2.24 A (*c* axis) with a maximum birefringence of 0.07 (Sigman and Korgel, 2005). $Pb_3O_2Cl_2$ nanobelts synthesized using a solventless approach exhibit greatly enhanced birefringence relative to the bulk material. The birefringence of nanobelt bundles has been determined as 1.1. The largest reported birefringence is 0.43 for a polymer (polyethylene 2,6-naphthalene-dicarboxylate) (PEN). Two of the most birefringent natural minerals are calcite and rutile that have values of 0.154 and 0.287. The largest reported birefringence of any inorganic material is 0.3 for

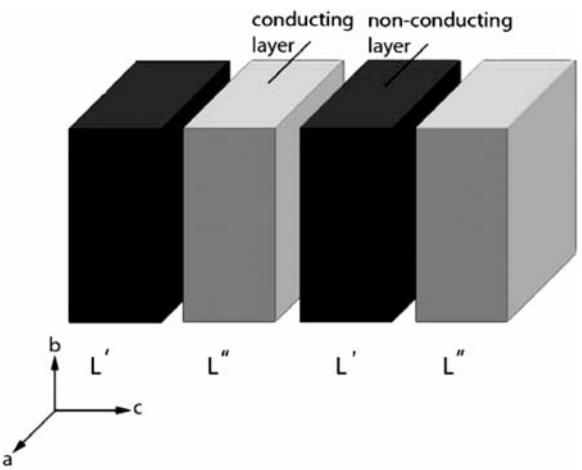

Fig. 3 Schematic representation of the structure of $Pb_{2+x}OCl_{2+2x}$ as based upon 2D blocks

Table 2 Crystallographic data and chemical composition of mendipite-related compounds

Cl:Br*	Formula**	*a*, Å	*b*, Å	*c*, Å	R_1
0:1	$Pb_3O_2Br_2$	12.244(5)	5.872(2)	9.799(4)	0.056
1:9	$Pb_3O_2Cl_{0.19}Br_{1.81}$	12.1949(7)	5.8705(5)	9.7968(9)	0.065
2:8	$Pb_3O_2Cl_{0.46}Br_{1.54}$	12.100(9)	5.855(5)	9.755(2)	0.081
3:7	$Pb_3O_2Cl_{0.52}Br_{1.48}$	12.0518(11)	5.8556(5)	9.7526(9)	0.025
4:6	$Pb_3O_2Cl_{0.81}Br_{1.19}$	11.9818(19)	5.8485(9)	9.7273(15)	0.047
5:5	$Pb_3O_2Cl_{1.03}Br_{0.97}$	11.922(5)	5.835(2)	9.701(4)	0.083
6:4	$Pb_3O_2Cl_{1.09}Br_{0.91}$	11.917(9)	5.819(5)	9.663(8)	0.053
7:3	$Pb_3O_2Cl_{1.41}Br_{0.59}$	11.8957(28)	5.8244(14)	9.6441(23)	0.038
8:2	$Pb_3O_2Cl_{1.61}Br_{0.39}$	11.9077(17)	5.8264(8)	9.6117(13)	0.051
9:1	$Pb_3O_2Cl_{1.84}Br_{0.16}$	11.8928(17)	5.8163(9)	9.5653(14)	0.053
1:0	$Pb_3O_2I_2$	11.808(8)	5.7790(41)	9.4784(68)	0.040

*–Cl:Br ratio used in the synthesis.
**–obtained by microprobe chemical analysis.

porous Si. Thus, the birefrigent of the $Pb_3O_2Cl_2$ nanobelts is strongly enhanced in comparison to a bulk material.

Practical importance of mendipite-related phases prompted us to take a closer look at the crystal chemistry of the series $\mathbf{Pb_3O_2Cl_2}-\mathbf{Pb_3O_2Br_2}$. Crystal structure studies of these phases also provide important information pertinent to an understanding of the transport of lead and the crystallization of lead compounds in natural systems.

Single crystals of mendipite phases were synthesized by the solid-state reactions method with the step of 10% Cl:Br ratio (Table 2). Elongated yellowish transparent crystals were used for a single-crystal X-ray diffraction analysis. Chemical composition of all samples was confirmed by a microprobe chemical analysis.

In crystal structures of the mendipite series $Pb_3O_2Cl_2-Pb_3O_2Br_2$, the $[O_2Pb_3]$ chains extend along the *b* axis (Figs. 4, 5) (Siidra et al., 2007b). They have two mutually perpendicular orientations and are linked through weak Pb–X (X = Cl, Br) bonds only.

The double $[O_2Pb_3]$ chains of OPb_4 tetrahedra are shown in Fig. 4. These chains are quite common in minerals and inorganic compounds (Krivovichev et al., 2004). The identity periods of the $[O_2Pb_3]$ chains are in the range from 5.71 to 5.95 Å.

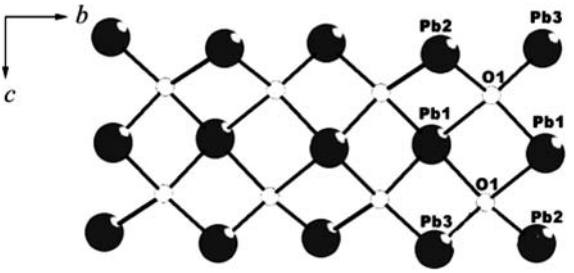

Fig. 4 The $[O_2Pb_3]$ chains in the crystal structures of the mendipite series $Pb_3O_2Cl_2$–$Pb_3O_2Br_2$

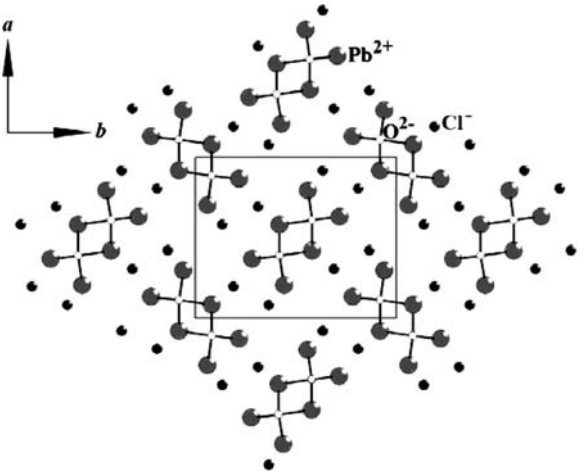

Fig. 5 The crystal structure of mendipite projected along the *c* axis. Only the Pb–O bonds are shown

In closely related structure of damaraite, the $[O_2Pb_3]$ chains are linked through OH groups to form a $[Pb_3O_2](OH)$ sheet. As is common in structures containing Pb–O/OH clusters, in damaraite, OH groups form two short (OH)–Pb bonds that result in $(OH)Pb_2$ dimers. In the structures of $Pb_7O_4(OH)_4Cl_2$ (Krivovichev and Burns, 2002) and $Pb_7O_4(OH)_4Br_2$ (Siidra et al., 2007d) the $[O_2Pb_3]$ chains extend along *a* and are linked by the $(OH)Pb_2$ dimers into a three-dimensional framework. This Pb–O/OH framework has channels parallel to *a* that contain Cl^- anions.

Determination of lattice parameters by single crystal studies showed strong deviation from Vegard's rule, which can be seen on Fig. 6. Note that the cell volume changes linearly (Fig. 7).

Nonlinearity of lattice parameters drawn on Fig. 6 is caused by the ordering of halide anions over two crystallographically nonequivalent sites, X1 and X2 (Table 3; Fig. 8). Br atoms prefer the X2 position (Table 3), whereas Cl prefers the X1 site.

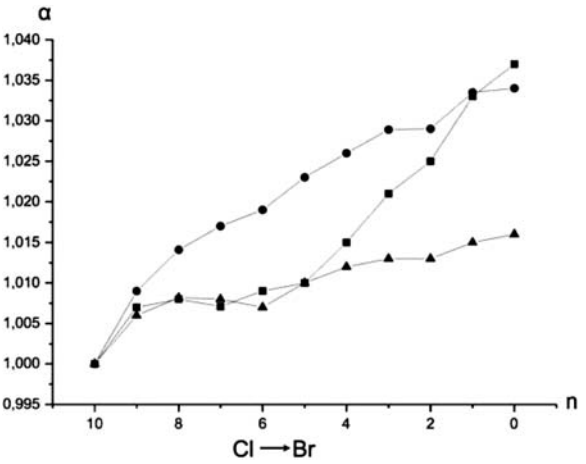

Fig. 6 Normalized lattice parameters (α = a/a_{Cl} - ■, b/b_{Cl} - ▲, c/c_{Cl} - ●) versus the Cl:Br ratio for the $Pb_3O_2Cl_2$–$Pb_3O_2Br_2$ system

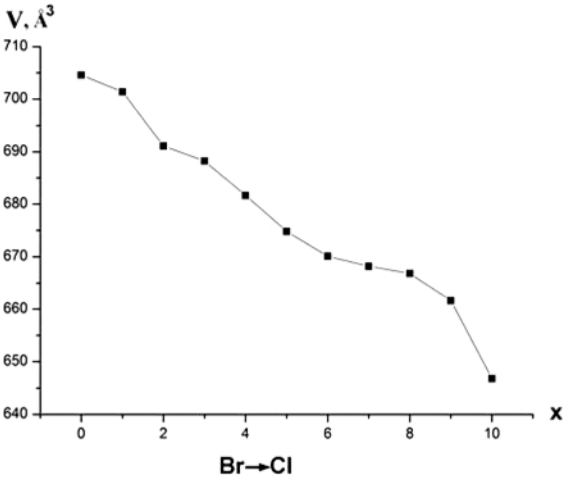

Fig. 7 Cell volume V, Å^3 versus the Cl:Br ratio for mendipite-related $Pb_3O_2Cl_2$–$Pb_3O_2Br_2$ compounds

Pb1–X2 and Pb2–X2 bond lengths are most sensitive to the occupancy of the X sites, which is in agreement with the non-linear behaviour of the *a* and *c* parameters (Fig. 6). Bond lengths oriented along the *b* axis are changing only slightly.

Recently we have reported (Siidra et al., 2007a) synthesis and crystal structures of $\mathbf{Pb_6LaO_7X}(\mathbf{X = Cl}, \mathbf{Br})$ (Fig. 9) based upon the $[O_7Pb_6La]^+$ chains of mixed-metal OPb_nLa_{4-n} tetrahedra (Fig. 10). The topology of the chains can be described as being based upon an arrangement of eight tetrahedra that all share the same central La atom.

This complex has the $[O_8Pb_{10}La_3]$ composition and represents a fragment of the fluorite (CaF_2) structure, where each Ca atom is shared between eight FCa_4 tetrahedra.

It is important to note that the La-free OPb_4 tetrahedra do not participate in the $[O_8Pb_{10}La_3]$ clusters but are attached to them, providing their linkage into an one

Table 3 Occupancy of X1 and X2 positions by halogen atoms in the $Pb_3O_2Cl_2$–$Pb_3O_2Br_2$ system

Cl:Br ratio	X1	X2
0:1	Cl	Cl
1:9	$Br_{0.815(18)}Cl_{0.185(18)}$	Cl
2:8	$Br_{0.54(4)}Cl_{0.46(4)}$	Cl
3:7	$Br_{0.450(9)}Cl_{0.550(9)}$	$Br_{0.934(9)}Cl_{0.066(9)}$
4:6	$Br_{0.289(14)}Cl_{0.711(14)}$	$Br_{0.907(13)}Cl_{0.093(13)}$
5:5	$Br_{0.15(3)}Cl_{0.85(3)}$	$Br_{0.81(3)}Cl_{0.19(3)}$
6:4	$Br_{0.14(2)}Cl_{0.86(2)}$	$Br_{0.77(2)}Cl_{0.23(2)}$
7:3	$Br_{0.043(12)}Cl_{0.957(12)}$	$Br_{0.553(13)}Cl_{0.447(13)}$
8:2	$Br_{0.020(16)}Cl_{0.980(16)}$	$Br_{0.369(16)}Cl_{0.631(16)}$
9:1	Br	$Br_{0.186(19)}Cl_{0.814(19)}$
1:0	Br	Br

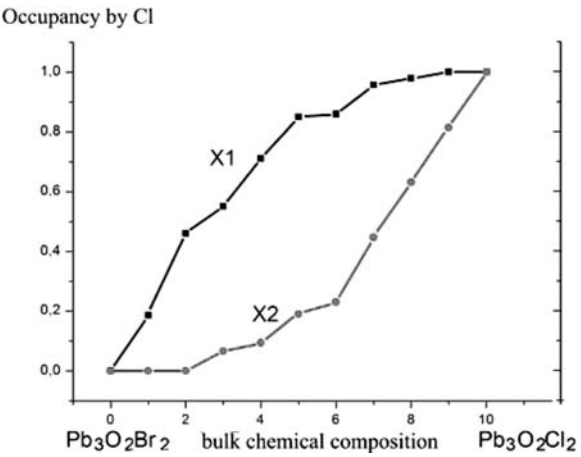

Fig. 8 X1 (■) and X2 (●) occupancy by Cl atoms versus the Cl:Br ratio for the $Pb_3O_2Cl_2$–$Pb_3O_2Br_2$ compounds

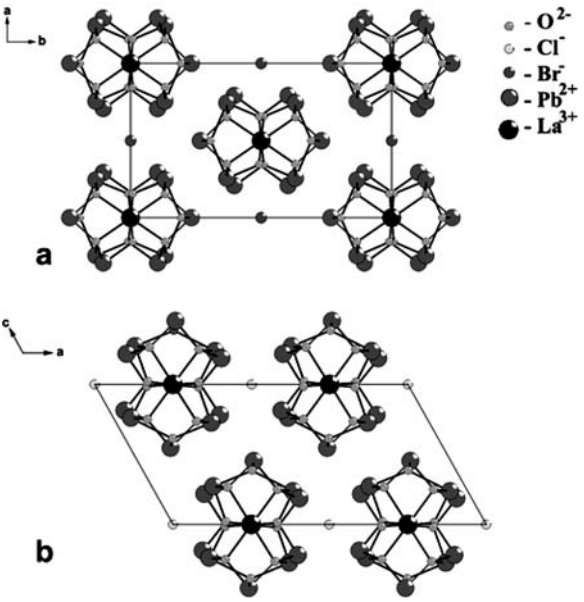

Fig. 9 Projections of the crystal structures of Pb_6LaO_7Br (**a**) and Pb_6LaO_7Cl (**b**) along the *c* and *b* axes, respectively

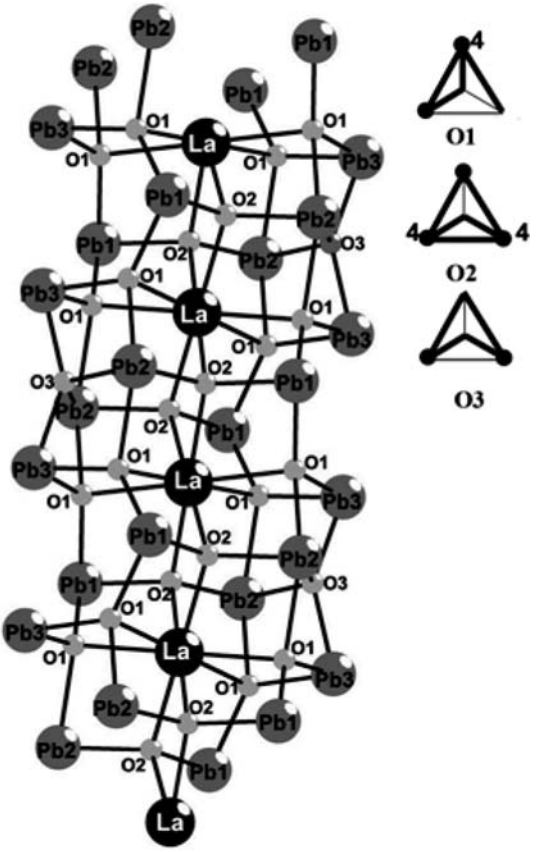

Fig. 10 The $[O_7Pb_6La]^+$ chain in the structure of Pb_6LaO_7Br and connectivity diagrams of its oxocentered tetrahedra

dimensional chain. This makes the structure of compounds Pb_6LaO_7X (X = Cl, Br) even more complex. Despite the number of symmetrically independent atoms, the metal oxide chains in these compounds are topologically and geometrically identical. The halogen ions connect the chains through the weak Pb-X bonds. It is of interest that incorporation of Cl atoms instead of Br atoms into the structure causes a lowering of the symmetry from *Cmcm* to *C*2/*m*. For all known lead oxyhalides that have chlorine and bromine analogues, this effect has never been reported.

As fas as we know, this is the first example of a Pb oxyhalide with such a dramatic influence of halogen atoms on the symmetry of the structure.

Studied mixed lead-lanthanum oxybromides are known as a good luminescent material (U.S. Patent 4029851) which is stimulable or excitable through the intermediary of X-rays for the emission of photographically effective light. Such luminescent material excitable by X-rays consisting essentially of activated lanthanum-lead oxybromide crystals wherein the lead content is in the range of 0.01–10 mole percen. This compound include terbium as an activator and this luminescent material have the general formula: (La,Pb)OBr:Tb.

Fluorescent or luminescent materials of this type are utilized in order to convert X-rays into light, the latter of which is transmitted to an observation or

photographic system responsive to this light, and which is more sensitive with respect to this light as compared to X-rays themselves. Hereby, sensitive exposure or photographic systems are such as the photofilms or photocathodes of a luminescent material-photocathode sandwich arrangement, as would be utilized in X-ray image intensifiers and X-ray television camera tubes.

However, encountered in this luminescent material is the disadvantage that, upon stimulation with X-rays light is emitted primarily in the green spectral range. Usual X-ray films, however, have their maximum responsiveness in the blue spectral range. Insofar as it desired to obtain an optimum conversion, it is necessary to employ a special film which is sensitized particularly to this green light. Moreover, the mentioned luminescent or fluorescent materials are more or less hygroscopic so as to lose their luminescent power with time through moisture absorption. This is predicated on that most organic binding agents absorb water from the air during the course of time, so that the luminescent material changes under the formation of lanthanum hydroxide. Under this influence of the moisture, the luminescent capacity thus constantly reduces. In accordance with an earlier proposal there is provided a luminescent material in which the above-mentioned advantages are avoided and which is thereby durable also in moist air and optimally converts X-rays into light within a spectral band (blue light) which has a good effect on commercially available photographic material.

The mentioned above data on some natural and synthetic chain lead oxyhalides demonstrate that studies of this class of compounds are of fundamental importance and are promising from the viewpoint of their applications in creation materials with new and unusual properties.

Acknowledgements This work was financially supported by the Alexander von Humboldt Stiftung, RFBR-DFG (06-05-04000), and the Swiss Science Foundation, the Ministry of Science and Education (Grant RNP 2113077) and the Federal Agency on Education (SPbSU innovation project "Innovation educational environment in the classic University") for financial and instrumental support.

References

Bonaccorsi E, Pasero M (2003) Crystal structure refinement of sahlinite, $Pb_{14}(AsO_4)_2O_9Cl_4$. Mineral Mag 67:15–21

Brown ID, Faggiani R (1980) The structure of thallium(I) tetraacetatothallate(III) when is the lone pair of electrons on Tl^I stereoactive?. Acta Crystallogr B 36:1802–1806

Cooper MA, Hawthorne FC (1994) The crystal structure of kombatite, $Pb_{14}(VO_4)_2O_9Cl_4$, a complex heteropolyhedral sheet mineral. Am Mineral 79:550–554

Edwards R, Gillard RD, Williams PA, Pollard AM (1992) Studies of secondary mineral formation in the PbO–H_2–HCl system. Mineral Mag 56:53–65

Finney JJ, Graeber EJ, Rosenzweig A (1977) The structure of chloroxiphite, $Pb_3CuO_2(OH)_2Cl_2$. Mineral Mag 41:357–361

Gabuda SP, Kozlova SG, Terskikh VV, Dybowski C, Neue G, Perry DL (1999) ^{207}Pb NMR study of novel Pb-Pb chemical bonding in lead monoxides, □-PbO and □-PbO. Chem Phys Lett 305:353–358

Gillberg M (1961) Perite, a new oxyhalide mineral from Långban, Sweden. Ark Mineral Och Geol 2:565–570

Giuseppetti G, Tadini C (1973) Riesame della struttura cristallina della nadorite $PbSbO_2Cl$. Per Mineral 42:335–345

Kolitsch U, Giester G (2000) Elyite $Pb_4Cu(SO_4)O_2(OH)_4^{\prime}H_2O$ crystal structure and new data. Am Mineral 85:1816–1821

Krivovichev SV, Burns PC (2001) Crystal chemistry of lead oxide chlorides. I. Crystal structures of synthetic mendipite, $Pb_3O_2Cl_2$, and synthetic damaraite, $Pb_3O_2(OH)Cl$. Eur J Mineral 13: 801–809

Krivovichev SV, Filatov SK (2001) Crystal chemistry of minerals and inorganic compounds based on complexes of anion-centered tetrahedra. St. Petersburg University Press, St. Petersburg

Krivovichev SV, Burns PC (2002) Crystal chemistry of lead oxide chlorides. II. Crystal structure of $Pb_7O_4(OH)_4Cl_2$. Eur J Miner 14:135–139

Krivovichev SV, Burns PC (2003) Chains of edge-sharing tetrahedra in the structure of $Pb_4O(VO_4)_2$ and in related minerals and inorganic compounds. Can Mineral 41:951–958

Krivovichev SV, Avdontseva EYu, Burns PC (2004) Synthesis and crystal structure of $Pb_3O_2(Se_2O_3)$. Z Anorg Allg Chem 630:558–562

Krivovichev SV, Burns PC (2006) The crystal structure of $Pb_8O_5(OH)_2Cl_4$, a synthetic analogue of blixite?. Can Mineral 44:515–522

Matsumoto H, Miyake T, Iwahara H (2001) Chloride ion conduction in $PbCl_2$-PbO system. Mater Res Bull 36:1177–1184

Moore PB, Kampf AR, Sen Gupta PK (2000) The crystal structure of philolithite, a trellis-like open framework based on cubic closest-packing of anions. Am Mineral 85:810–816

Mudring A (2006) Stereochemical activity of lone pairs in heavier main-group element compounds. In: Meyer G, Naumann D, Wesemann L (eds) Inorganic chemistry in focus III. Wiley-VCH, Weinheim pp 15–28

Pertlik F (1987) The structure of freedite, $Pb_8Cu(AsO_3)_2O_3Cl_5$. Miner Petrol 36:85–92

Post JE, Buseck PR (1985) Quantitative energy-dispersive analysis of lead halide particles from the Phoenix urban aerosol. Environ Sci Technol 19:682–685

Pyykö P (1997) Strong closed-shell interactions in inorganic chemistry. Chem Rev 97:597–636

Rouse RC, Dunn PJ (1985) The structure of thorisokite, a naturally occurring member of the bismuth oxyhalide group. J Solid State Chem 57:389–395

Sahl K (1970) Zur Kristallstruktur von Lanarkit, $Pb_2O(SO_4)$. Z Kristallogr 132:99–117

Sigman MB Jr, Korgel BA (2005) Strongly birefringent $Pb_3O_2Cl_2$ nanobelts. J Am Chem Soc 127:10089–10095

Siidra OI, Krivovichev SV, Armbruster T, Depmeier W (2007a) Lead-rare-earth oxyhalides syntheses and characterization of Pb_6LaO_7X (X = Cl, Br). Inorg Chem 46:1523–1525

Siidra OI, Krivovichev SV, Depmeier W (2007b) Crystal chemistry of natural and synthetic lead oxyhalide. I. Crystal structure of $Pb_{13}O_{10}Cl_6$. Zapiski RMO 136(2):79–89 (in Russian)

Siidra OI, Krivovichev SV, Depmeier W (2007c) Structure and mechanism of the ionic conductivity of the nonstoichiometric compound $Pb_{2+x}OCl_{2+2x}$. Dokl Phys Chem 414: 128–131

Siidra OI, Krivovichev SV, Depmeier W (2007) Crystal chemistry of natural and synthetic lead oxohalogenides. II. Crystal structure of $Pb_7O_4(OH)_4Br_2$. Zapiski RMO 136(6):85–91 (in Russian)

Smith WH (1976) Lead contamination of the roadside ecosystem. J Air Pollution Control Assessment 26:753–766

Symes RF, Cressey G, Criddle AJ, Stanley CJ, Francis JG, Jones GC (1994) Parkinsonite, $(Pb, Mo, \square)_8O_8Cl_2$, a new mineral from Merehead Quarry, Somerset. Mineral Mag 58:59–68

Welch MD, Cooper MA, Hawthorne FC, Criddle AJ Symesite (2000) $Pb_{10}(SO_4)O_7Cl_4(H_2O)$, a new PbO-related sheet mineral description and crystal structure. Am Mineral 85:1526–1533

Welch MD (2004) Pb-Si ordering in sheet-oxychloride minerals the super-structure of asisite, nominally $Pb_7SiO_8Cl_2$. Mineral Mag 68:247–254

Features of Low-Temperature Alteration of Ti- and Nb-Phyllosilicates Under Laboratory Conditions

Ekaterina A. Selivanova, Viktor N. Yakovenchuk, Yakov A. Pakhomovsky and Gregory Yu. Ivanyuk

Introduction

Titano- and niobo-phyllosilicates such as lomonosovite $Na_4Ti_4[(Si_2O_7)_2|O_4]\cdot 2Na_3PO_4$, β-lomonosovite $Na_4Ti_4[(Si_2O_7)_2|(OH, F)_4]\cdot NaPO_2(OH)_2$, murmanite $Na_4Ti_4[(Si_2O_7)_2|O_4]\cdot 5H_2O$, vuonnemite $Na_5TiNb_2[(Si_2O_7)_2|(F, O)_4]\cdot 2Na_3PO_4$, and epistolite $Na_5TiNb_2[(Si_2O_7)_2|(F, O)_4]\cdot 5H_2O$ – are widespread in alkaline massifs worldwide. All the species are typical medium-late minerals of alkaline pegmatites, and lomonosovite and murmanite are also rock-forming minerals of nepheline and sodalite syenites (up to 20 vol. % in poikilitic sodalite-nepheline syenite of the Lovozero massif).

Crystal structures of lomonosovite and vuonnemite are based upon parallel to (001) trilaminar packets with their cores consisting of close packed TiO_6 and NaO_6 octachedra and marginal sheets consisting of TiO_6 (in lomonosovite and β-lomonosovite) or NbO_6 (in-vuonnemite) octachedra and corner-sharing Si_2O_7 dimers reinforced with $Na(O, OH)_8$ polyhedra (Fig. 1). Between the packets, there are two-laminar layers of $2Na_3PO_4$. So far, there are six sodium positions in the structures under considerations (Belov et al., 1977; Ercit et al., 1998).

There is a widespread opinion that lomonosovite and vuonnemite easily alter in Nature, loose Na_3PO_4, absorb water and transform into murmanite and epistolite,

Ekaterina A. Selivanova
Geological Institute, Kola Science Centre of the Russian Academy of Sciences, Apatity, Russia

Viktor N. Yakovenchuk
Geological Institute, Kola Science Centre of the Russian Academy of Sciences, Apatity, Russia

Yakov A. Pakhomovsky
Geological Institute, Kola Science Centre of the Russian Academy of Sciences, Apatity, Russia

Gregory Yu. Ivanyuk
Geological Institute, Kola Science Centre of the Russian Academy of Sciences, Apatity, Russia, e-mail: ivanyuk@geoksc.apatity.ru

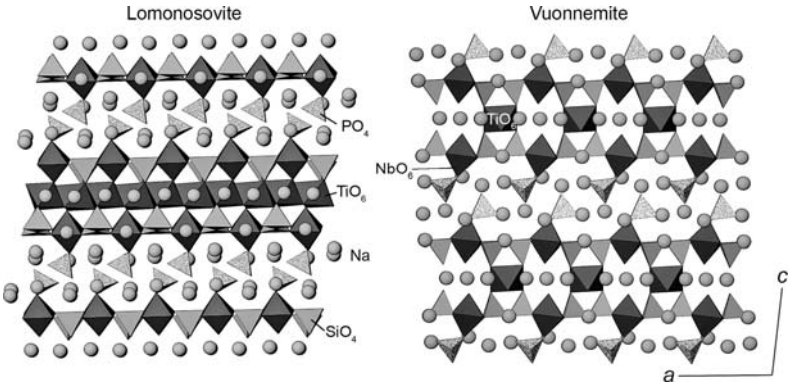

Fig. 1 Crystal strucrures of lomonosovite after Belov et al. (1977) and vuonnemite after Ercit et al. (1998)

respectively (Kostyleva-Labuntsova et al., 1978; Khomyakov, 1995; 2004; Azarova et al., 2002):

$Na_4Ti_4[(Si_2O_7)_2|O_4]\cdot 2Na_3PO_4 + 5H_2O = Na_4Ti_4[(Si_2O_7)_2|O_4]\cdot 5H_2O + 2Na_3PO_4$;

$Na_5TiNb_2[Si_2O_7)_2|(F, O)_4]\cdot 2Na_3PO_4 + 5H_2O = Na_5TiNb_2[Si_2O_7)_2|(F, O)_4]\cdot 5H_2O + 2Na_3PO_4$.

According to Borneman-Starynkevich (1946), murmanite can be obtained from lomonosovite treated with cold water. Khomyakov (2004) noted that murmanite and epistolite can be obtained from lomonosovite and vuonnemite, respectively, treated with boiling water. The next alteration of murmanite and epistolite into komarovite, belyankinite and Nb–Ti oxides are considered usually as later stages of lomonosovite and vuonnemite alteration, which is not absolutely correct, of course.

Really, our experience in mineralogical studies in alkaline massifs shows that clear pseudomorphs of murmanite after lomonosovite as well as of epistolite after vuonnemite are absent in Nature. Moreover, all these minerals do not coexist in one rock or vein (Pekov, 2000; Pekov & Podlesny, 2004; Yakovenchuk et al., 2005)! Optical evidence on lomonosovite replacement by murmanite (Sokolova et al., 1971) is probably doubtful, because of our electron microscopic investigation of similar specimens shows lomonosovite and beta-lomonosovite presence only. No phases structurally intermediate between lomonosovite and murmanite have been established by structural investigations too. To solve these contradictions, we carried out a special laboratory study of alteration of lomonosovite, vuonnemite, and murmanite under "soft" hydrothermal conditions.

Experimental

To simulate the low-temperature hydrothermal alteration of lomonosovite, vuonnemite and murmanite at the background of the media alkalinity decreasing, small lamellae of these minerals were loaded in 1M solution of $CaCl_2$ and NH_4Cl at 80°C

during 100 h. The lamellae were obtained by crushing of large homogeneous crystals (Table 1) from the polymineral "Palitra" vein in foyaite of Mt. Kedykvyrpakhk (lomonosovite and vuonnemite) and from an ussingite-nepheline-microcline vein in nepheline syenite of Mt. Alluaiv (murmanite). After the treating, murmanite had no any visible changes, bright-yellow vuonnemite becames colourless with a pearl lustre, and brown lomonosovite showed an interchange of brown and white layers.

The powder X-ray-diffraction patterns of treated lomonosovite, vuonnemite and murmanite were obtained by means of the URS–1 instrument operated at 40 kV and 30 mA with a 114.7 mm Debye–Scherrer camera and FeKα radiation (Fig. 2). Lomonosovite transforms into β-lomonosovite but nor in murmanite during the treating. At the powder X-ray diffraction pattern of treated vuonnemite, reflections became more diffuse and really look like those belonging to epistolite. However, all the reflections do not change their position and, so far, the pattern quite differs from epistolite one (compare positions of (002) reflection at ∼7Å of original and treated vuonnemite and at 5.9 Å in epistolite). Treated murmanite gives diffuse powder X-ray diffraction patterns up to continuous spectrum of amorphous substance with some perovskite reflections. The examination of these lamellae using Leo-1450 scanning electron microscope with Röntec EDS-analyzer shows a weak linear gradient of composition from rim to core (Fig. 3). No layers with different composition have been observed. The chemical composition of original and treated phases has been studied by wave-length dispersion spectrometry using Cameca MS-46 electron microprobe (Geological Institute, Kola Science Centre of the Russian Academy of Sciences, Apatity) operating at 20 kV and 20–30 nA. Analyses were performed by electron probe defocused up to 30 microns and by continuous movement of the sample in order to minimize mineral damage and water loss during 10-second counting time. The following standards were used: lorenzenite (Na, Ti), pyrope (Mg, Al), diopside (Si, Ca), wadeite (K), synthetic $MnCO_3$ (Mn), hematite (Fe), celestine (Sr), synthetic $ZrSiO_4$ (Zr), metallic niobium (Nb), fluorapatite (P), synthetic CeS (Ce) and atacamite (Cl).

Water content was calculated as 100 wt. % minus SUM of oxides of analyzed elements.

It is established that lomonosovite and vuonnemite loose more than a 2/3 of Na, insignificant part of which has been exchanged by Ca, whereas all phosphorus remains in the structure (see Table 1). Murmanite transforms into fine-powder mix of opal and Ti-oxides with insignificant changes in total chemical composition. So far, the intermediate product of lomonosovite alteration is β-lomonosovite (core of treated lamellae: point 1 at Fig. 3) and final product is Na-deficient phase of the same structure with H_2O or H_3O^+ in mica-like packets and H_3PO_4 molecules between them (rims of treated lamellae: point 3 at Fig. 3):

Table 1 Chemical composition (wt.%) and unit formula (*apfu*, Si+Al=4) of lomonosovite, vuonnemite and murmanite lamellae treated with solution of $CaCl_2$ and NH_4Cl at 80°C during 48 h and boiled in distilled water during 24 h

Component	Lomonosovite				Vuonnemite				Murmanite	
	Original	Treated		Boiled	Original	Treated		Boiled	Original	Treated
		Core	Rim			Core	Rim			
1	2	3	4	5	6	7	8	9	10	11
Na_2O	30.24	27.31	9.3	28.31	28.91	7.99	2.03	29.68	9.20	7.80
MgO	–	0.44	0.48	–	–	–	–	–	0.54	0.55
Al_2O_3	–	–	–	–	0.08	0.15	0.21	0.09	–	–
SiO_2	23.16	24.08	25.68	22.44	22.41	26.58	24.81	22.28	28.76	31.53
P_2O_5	13.78	13.83	14.85	12.90	12.67	14.69	14.3	12.53	0.17	0.19
Cl	–	–	–	–	–	0.09	0.26	–	–	–
K_2O	–	–	–	–	–	0.1	0.09	–	0.43	0.58
CaO	2.47	2.29	3.02	0.59	0.57	–	–	0.50	3.41	3.84
TiO_2	21.86	23.6	26.04	23.51	9.82	9.88	10.81	9.39	26.07	25.08
MnO	1.63	1.31	1.29	1.38	0.96	0.72	0.72	1.08	3.88	2.93
FeO	2.37	1.89	2.21	1.40	0.14	0.23	0.36	0.20	1.33	1.42
SrO	–	–	–	–	–	–	–	–	0.49	0.80
ZrO_2	–	–	–	–	–	–	–	–	2.87	3.49
Nb_2O_5	4.96	4.34	4.74	4.18	18.83	21.38	23.93	19.35	6.61	7.51
SUM	100.50	99.08	87.68	94.71	94.39	83.96	80.06	95.10	83.76	85.72
$H_2O = 100 - SUM$	0.00	0.92	12.32	5.29	5.61	16.04	19.94	4.90	16.24	14.28

Table 1 (Continued)

Component	Lomonosovite				Vuonnemite				Murmanite	
	Original	Treated		Boiled	Original	Treated		Boiled	Original	Treated
		Core	Rim			Core	Rim			
1	2	3	4	5	6	7	8	9	10	11
Na	10.13	8.80	2.81	9.78	9.96	2.32	0.63	10.28	2.48	1.92
K	–	–	–	–	–	0.02	0.02	–	0.08	0.09
Ca	0.46	0.41	0.50	0.11	0.11	–	–	0.10	0.51	0.52
Sr	–	–	–	–	–	–	–	–	0.04	0.06
Mn	0.24	0.18	0.17	0.21	0.15	0.09	0.10	0.16	0.46	0.32
Mg	–	0.11	0.11	–	–	–	–	–	0.10	0.10
Ti	2.84	2.95	3.05	3.15	1.31	1.11	1.30	1.26	2.73	2.39
Nb	0.39	0.33	0.33	0.34	1.51	1.45	1.73	1.56	0.42	0.43
Zr	–	–	–	–	–	–	–	–	0.20	0.22
Fe^{3+}	0.34	0.26	0.29	0.21	0.02	0.03	0.05	0.03	0.16	0.15
Si	4.00	4.00	4.00	4.00	3.98	3.97	3.96	3.98	4.00	4.00
Al	–	–	–	–	0.02	0.03	0.04	0.02	–	–
P	2.02	1.95	1.96	1.95	1.91	1.86	1.93	1.90	0.02	0.02
H	–	1.01	12.87	6.28	6.65	18.14	23.94	5.87	15.08	12.08
Cl	–	–	–	–	–	0.02	0.07	–	–	–

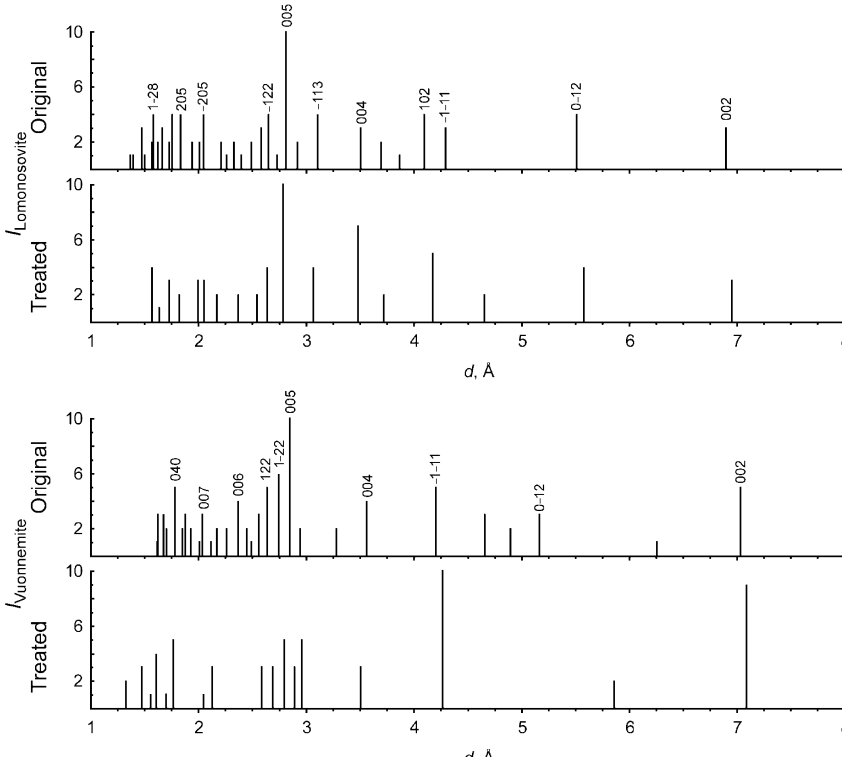

Fig. 2 Powder X-ray diffraction patterns of lomonosovite, vuonnemite and products of their alteration in 1M solution of $CaCl_2$ and NH_4Cl at 80°C during 100 h

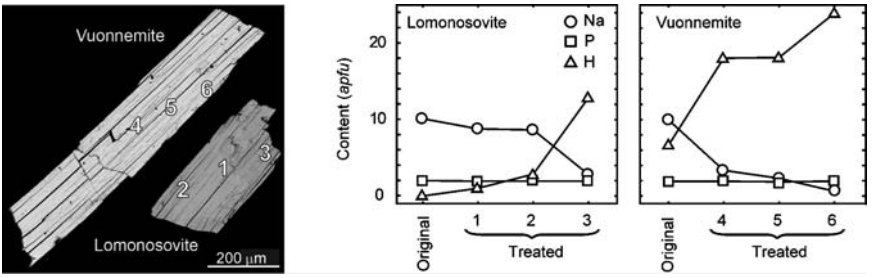

Fig. 3 BSE image of lomonosovite and vuonnemite lamellae treated in solution of $CaCl_2$ and NH_4Cl and content of Na, P and H in the numbered points

Original lomonosovite:

$$(Na_{10.13}Ca_{0.46}Mn_{0.24})_{\Sigma=10.83}(Ti_{2.84}Nb_{0.39}Fe^{3+}{}_{0.34})_{\Sigma=3.57}[Si_4O_{17.90}](PO_4)_{2.02}$$

$$\downarrow$$

Point 1 :

$$(Na_{8.80}Ca_{0.41}Mn_{0.18}Mg_{0.11})_{\Sigma=9.50}(Ti_{2.95}Nb_{0.33}Fe^{3+}{}_{0.26})_{\Sigma=3.54}[Si_4O_{16.56}(OH)_{1.44}](PO_4)_{1.95}$$

$$\downarrow$$

Point 3 :

$$(Na_{2.81}Ca_{0.50}Mn_{0.17}Mg_{0.11})_{\Sigma=3.59}(Ti_{3.05}Nb_{0.33}Fe^{3+}{}_{0.29})_{\Sigma=3.67}[Si_4O_{14.23}(OH)_{3.77}](PO_4)_{1.96}\cdot 4.55H_2O$$

Decationization of vuonnemite produces similar Nb-phases (points 4 and 6 at Fig. 3):

Original vuonnemite:

$$(Na_{9.96}Mn_{0.15}Ca_{0.11})_{\Sigma=10.22}(Nb_{1.51}Ti_{1.31}Fe^{3+}{}_{0.02})_{\Sigma=2.84}[(Si_{3.98}Al_{0.02})_{\Sigma=4}O_{15.56}(OH)_{2.44}]$$
$$(PO_4)_{1.91}\cdot 2.11H_2O$$

$$\downarrow$$

Point 4 :

$$(Na_{2.32}Mn_{0.09}K_{0.02})_{\Sigma=2.43}(Nb_{1.45}Ti_{1.11}Fe^{3+}{}_{0.03})_{\Sigma=2.59}[(Si_{3.97}Al_{0.03})_{\Sigma=4}O_{6.69}(OH)_{11.31}]$$
$$(PO_4)_{1.86}\cdot 3.22H_2O$$

$$\downarrow$$

Point 6 : $(Na_{0.63}Mn_{0.10}K_{0.02})_{\Sigma=0.75}(Nb_{1.73}Ti_{1.30}Fe^{3+}{}_{0.05})_{\Sigma=3.08}[(Si_{3.96}Al_{0.04})_{\Sigma=4}O_{7.02}(OH)_{10.98}](PO_4)_{1.93}\cdot 6.48H_2O.$

It is evident that there is another mechanism of vuonnemite alteration by Na removing (probably from octahedral sheets of 3-layer mica-like packets), but there are no PO_4 removing. It seems it is process that forms optically inhomogeneous lomonosovite–beta-lomonosovite intergrowth in Nature. May the process to be different principally with the "tradition" way of the phyllosilicate alteration?

To answer the question, we repeat the experiment of A.P. Khomyakov (2004) with alteration of lomonosovite and vuonnemite in boiling water. Lamellae of both the minerals from the same original crystals were boiled in distilled water during 24 h. After the boiling, lamellae of both minerals remain without noticeable changes in colour and composition (see Table 1):

Original lomonosovite:

$$(Na_{10.13}Ca_{0.46}Mn_{0.24})_{\Sigma=10.83}(Ti_{2.84}Nb_{0.39}Fe^{3+}{}_{0.34})_{\Sigma=3.57}[Si_4O_{17.90}](PO_4)_{2.02}$$

$$\downarrow$$

Boiled lomonosovite:

$$(Na_{9.78}Mn_{0.21}Ca_{0.11})_{\Sigma=10.10}(Ti_{3.15}Nb_{0.34}Fe^{3+}{}_{0.21})_{\Sigma=3.70}$$
$$[Si_4O_{17.50}(OH)_{0.50}](PO_4)_{1.95}\cdot 2.89H_2O.$$

and

Original vuonnemite: $(Na_{9.96}Mn_{0.15}Ca_{0.11})_{\Sigma=10.22}(Nb_{1.51}Ti_{1.31}Fe^{3+}{}_{0.02})_{\Sigma=2.84}[(Si_{3.98}Al_{0.02})_{\Sigma=4}O_{15.56}(OH)_{2.44}](PO_4)_{1.91} \cdot 2.11H_2O$

↓

Boiled vuonnemite:

$(Na_{10.28}Mn_{0.16}Ca_{0.10})_{\Sigma=10.54}(Nb_{1.56}Ti_{1.26}Fe^{3+}{}_{0.03})_{\Sigma=2.85}[(Si_{3.98}Al_{0.02})_{\Sigma=4}O_{16.01}(OH)_{1.99}](PO_4)_{1.90} \cdot 1.94H_2O.$

Boiled material has powder X-ray diffraction patterns identical with ones of original crystals. So far, traditional schema of lomonosovite and vuonnemite transition into murmanite and epistolite by means of Na_3PO_4 removing and hydration is doubtful, that is in agreement with our observations of mineral associations.

Discussion

Lomonosovite and vuonnemite heating in solution of $CaCl_2$ and NH_4Cl produce similar sodium-deficient phases without a cardinal reorganization of the mineral structures. Sodium is leached from vuonnemite more easily than from lomonosovite. It is in accordance with natural evidences that lomonosovite is more stable than vuonnemite during hydrothermal alteration. Such lomonosovite stability is obviously caused by titanium presence instead of niobium within marginal sheets of the trilaminar packets.

It seems obvious that atoms of Na within the core of trilaminar packets are mostly stable than ones in others positions, especially between the packets (Khomyakov, 1976). Consequently, β-lomonosovite can be considered as a result of $H_3O^+ \leftrightarrow Na^+$ substitution within Na_3PO_4 layers. In vuonnemite, however, such schema of Na substitution can not explain conservation of *c* parameter of the mineral structure, even if 6 sodium atoms will be exchanged into 6 water molecules. We assume that in our experiments there is removing of Na cations from core of trilaminar packets that swell, so far, “ab intra”.

Alteration of murmanite produces slowly-acid microporous ion-exchangers with TiOH-groups. Really, partial pseudomorphs of labuntsovite and zorite group minerals after murmanite are frequently observed in Nature (Yakovenchuk et al., 2005; Men’shikov et al., 2006). Contrariwise, lomonosovite and vuonnemite are usually very fresh, and no pseudomorphs after them have been fixed. Impossibility of phosphorus redistribution from lomonosovite can be a reason of fluorapatite rarity within lomonosovite-bearing foidolites of the Lovozero massif, whereas adjacent Khibiny massif includes the world largest apatite deposits but nor lomonosovite-bearing ijolite-urtite.

Acknowledgements We thank Swiss National Foundation (SNF) for financial support in the framework of the SCOPES program. Also we are grateful to A.V. Bazai and Yu. P. Men’shikov for help in the investigations and Prof. S. V. Krivovichev who edited our manuscript.

References

Azarova YuV, Pekov IV, Chukanov NV, Zadov AE (2002) Products and processes of vuonnemite alteration under low-temperature transformation of hyperagpaitic pegmatites. Zapiski VMO (Proceedings of the Russian Mineralogical Society) 131:5:112–121 (in Russian)

Belov NV, Gavrilova GS, Solov'eva LP, Khalilov AD (1977) Refined structure of lomonosovite. Sov Phys Dokl 22:422–424 (in Russian)

Borneman-Starynkevich ID (1946) On chemical nature of murmanite. Problems of mineralogy, geochemistry and petrography, AN SSSR Press, Moscow–Leningrad, pp 66–74 (in Russian)

Ercit TS, Cooper MA, Hawthorne FC (1998) The crystal structure of vuonnemite, $Na_{11}Ti^{4+}Nb_2(Si_2O_7)_2(PO_4)_2O_3(F,OH)$, a phosphate-bearing sorosilicate of the lomonosovite group. Can Mineral 36:1311–1320

Khomyakov AP (1976) Constitution and typochemical features of lomonosovite group minerals. Constitution and properties of minerals. Naukova Dumka Kiev 10:96–104 (in Russian)

Khomyakov AP (1995) Mineralogy of hyperagpaitic alkaline rocks. Clarendon Press, Oxford, p 223

Khomyakov AP (2004) Zeolite-like amphoterosilicates of hyperagpaitic rocks and their unique properties. Rev Mineral Geochem Accad Lincei Roma 231–234

Kostyleva-Labuntsova EE, Borutsky BE, Sokolova MN, Shlyukova ZV, Dorfman MD, Dudkin OB, Kozyreva LV, Ikorsky SV (1978) Mineralogiya Khibinskogo massiva (Mineralogy of the Khibiny massif). Minerals Nauka Moscow 2:585 (in Russian)

Men'shikov YuP, Krivovichev SV, Pakhomovsky YaA, Yakovenchuk VN, Ivanyuk GYu, Mikhailova JA, Armbruster T, Selivanova EA (2006) Chivruaiite, $Ca_4(Ti,Nb)_5[(Si_6O_{17})_2(OH,O)_5]\cdot 13\text{-}14H_2O$, a new mineral from hydrothermal veins of Khibiny and Lovozero alkaline massifs. Am Mineral 91:922–928

Pekov IV (2000) Lovozero massif: history, pegmatites, minerals. Ocean Pictures Ltd, Moscow, Russia, p 480

Pekov IV, Podlesny AS (2004) Kukisvumchorr deposit: mineralogy of alkaline pegmatites and hydrothermalites. Mineral Almanac 7:168

Sokolova MN, Zabavnikova NI, Rudnitskaya ES, Organova NI (1971) On composition and homogeneity of lomonosovite group minerals from the Khibiny massif. Problems of homogeneity and non-homogeneity of minerals (in Russian). Nauka Moscow 174–187

Yakovenchuk VN, Ivanyuk GYu, Pakhomovsky YaA, Men'shikov YuP (ed F.Wall) (2005) Khibiny. Laplandia Minerals, Apatity, p 467

Silicate Tubes in the Crystal Structure of Manaksite

Oxana Karimova and Peter C. Burns

Unique tubular ribbons silicate radicals with composition $[Si_8O_{20}]_\infty$ have been found in the crystal structure of manaksite. Group of minerals with tubular silicate radicals is not large. Miserite (Scott 1976), canasite (Rozdestvenskaya et al. 1988), frankamenite (Rozdestvenskaya et al. 1996), narsarsukite (Peacor and Buerger 1962), and manaksite are minerals that contain different types of silicate tubes. Among them, manaksite is the only structure containing tubes with a hexagonal cross-section.

A rare mineral manaksite, ideally $NaKMnSi_4O_{10}$, was discovered in 1992 in Lovozero alkali massif, Kola Peninsula, Russia (Khomyakov et al. 1992). Manaksite is a Mn analog of fenaksite, $NaKFeSi_4O_{10}$, which was found only in Khibiny alkaline massif, Russia (Dorfman et al. 1959; Sokolova et al. 1993). Recently, intermediate compositions between these minerals were described and an isomorphous series fenaksite-manaksite was established (Ageeva 2000). Crystal structure of fenaksite was studied twice (Golovachev et al. 1970, Prencipe et al. 1998). In current study, a CCD-based detector mounted on an automated single-crystal diffractometer has been used to collect X-ray diffraction data, resulting in successful elucidation of the structure. Crystals with different Fe content were chosen from the mineralogical collection of Dr. Maya Sokolova and Dr. Olga Ageeva (IGEM RAS, Moscow, Russia).

Crystals were mounted on a Bruker three-circle diffractometer equipped with a SMART APEX CCD detector, using monochromated MoK_α X-radiation. The unit cell dimensions were refined using least-squares techniques (Table 1). The three-dimensional data were reduced and corrected for Lorentz, polarization, and background effects using the Bruker program SAINT. An empirical absorption correction was done for crystal by modeling it as an ellipsoid.

Oxana Karimova
Department of Mineralogy, Institute of Geology of Ore Deposits Russian Academy of Science, 35 Staromonetny, Moscow 119017, Russia, e-mail: oksa@igem.ru

Peter C. Burns
Department of Civil Engineering and Geological Sciences, University of Notre Dame, 156 Fitzpatrick Hall, Notre Dame, IN 46556-0767, USA

Table 1 Crystallographic data and refinement parameters for manaksite

Sample	1	2
a (Å)	6.9774(5)	6.9752(6)
b (Å)	8.1778(6)	8.1505(7)
c (Å)	9.9664(8)	9.9464(8)
$\alpha(^\circ)$	105.782(2)	105.803(2)
$\beta(^\circ)$	99.743(2)	99.990(2)
$\gamma(^\circ)$	114.440(1)	114.332(2)
V (Å^3)	471.74(6)	468.71(4)
Space group	P-1	P-1
Z	2	2
Total Ref.	9520	9514
Unique Ref.	3798	3793
Unique $\lvert F_0\rvert \geq 4\sigma_F$	2622	3673
R_1	0.029	0.034
wR_2	0.055	0.084
S	0.835	1.023

The Bruker SHELXTL Version 5 system of programs was used for the determination and refinement of crystal structure. Structure was solved by direct methods and refined to R = 0.029 (**1**) and 0.034 (**2**) (Table 1).

After collecting the X-ray-diffraction data, the crystal **1** was polished and analyzed with an electron microprobe. As expected K, Na, Si, Fe and Mn were major elements. Quantitative analysis gave the following: SiO_2 63.6, Na_2O 7.76, MgO 0.41, K_2O 12.4, CaO 0.3, FeO 6.17, MnO 10.3, total 100.94 wt.%. The empirical formula is $(Na_{0.94}K_1Ca_{0.02})(Fe_{0.32}Mn_{0.55}Mg_{0.04})Si_4O_{10}$, assuming Si = 4 and O = 10.

The crystal structure of manaksite contains four symmetrically independent Si-tetrahedra. Inter-atomic Si–O distances lie in the range 1.569–1.635 Å (**1**) and 1.587–1.648 Å (**2**). The M site is occupied by Mn and Fe, and is coordinated by five oxygen atoms. In the fenaksite structure, FeO_5 polyhedron was defined as a tetragonal pyramid (Golovachev et al. 1970). But present study has shown that MO_5 polyhedron may be described as a distorted trigonal bipyramid. Interatomic M–O distances to the apical oxygen atoms are relatively longer (2.14–2.30 Å (**1**) and 2.14–2.29 Å (**2**)) than to the equatorial ones (2.05–2.14 Å (**1**) and 2.00–2.12 Å (**2**)). Na polyhedron is a tetragonal pyramid. It has one long apical Na–O bond (2.83 Å (**1**) and 2.79 Å (**2**)). Terminal Na–O bonds are shorter: 2.38–2.49 Å (**1**) and 2.28–2.49 Å (**2**). K atom is coordinated by nine oxygen atoms, the K–O bonds are spread over an interval of 2.74–3.36 Å (**1**) and 2.72–3.37 Å (**2**).

Si-tetrahedra are joined together via common vertices forming tubes with hexagonal cross-sections (Fig. 1).

The tubes are extended parallel to the a axis. Walls of the silicate tubes are formed by 4-membered rings of silicate tetrahedra. Therefore, manaksite silicate radicals can be considered as lace constructions. Two MnO_5 trigonal bipyramids are connected together via a common edge. Two adjacent NaO_5 tetragonal pyramids share a common edge as well. The dimers of Mn- and Na-polyhedra are linked together via

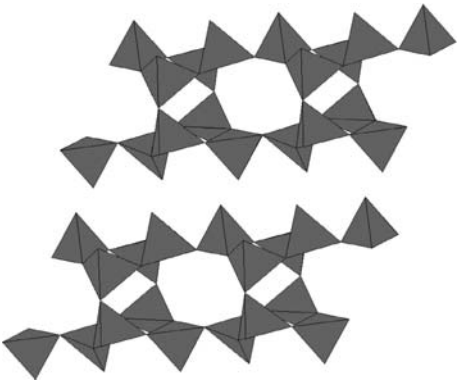

Fig. 1 Silicate tubes in the structure of manaksite

common edges, to form columns parallel to the a axis. The Mn- and Na-polyhedral columns link silicate chains via common vertices into a three-dimensional network (Fig. 2). It is very interesting that Na plays in the structure an anionic role and Na-polyhedra participate in the formation of a mixed framework. K-centered polyhedra are situated inside the silicate tubes.

Mixed framework of in the structure manaksite, formed by SiO_4-tetrahedra, Mn- and Na-polyhedra, has hollow channels with dimensions of 2×3 Å.

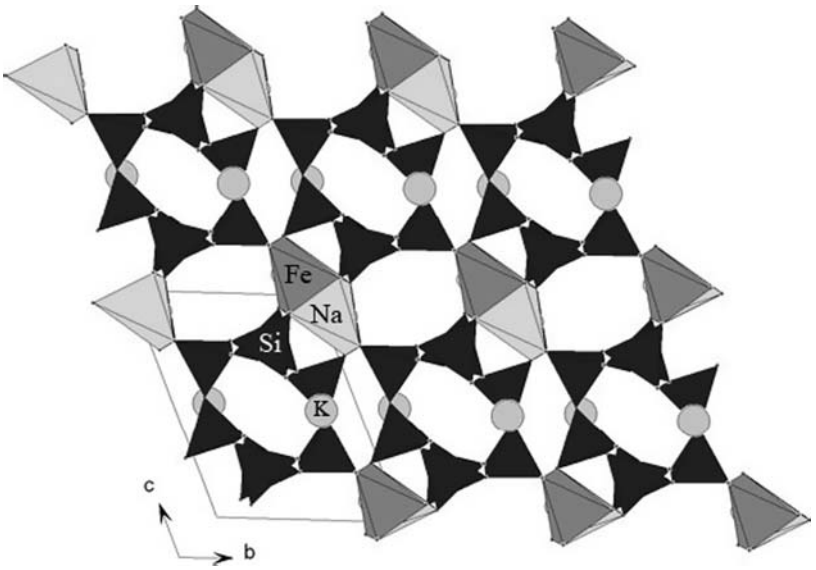

Fig. 2 Projection of the structure of manaksite along the *a* axis

Acknowledgements Authors are grateful to Dr. Maya Sokolova and Dr. Olga Ageeva for providing crystals used in this study and Dr. Ian Steele for quantitative chemical analysis of the manaksite crystal.

References

Ageeva OA (2000) New fenaksite-manaksite isomorphous series. Dokl Akad Nauk Earth Sci A 373:927–929

Dorfman MD, Rogachev DL, Goroshchenko ZI, Morketsova AV (1959) Fenaksite – a new mineral. Tr Mineral Muz Akad Nauk SSSR 9:152–157 (in Russian)

Golovachev VP, Drozdov YuN, Kuz'min EA, Belov NV (1970) The crystal structure of fenaksite, $NaKFeSi_4O_{10}$. Dokl Akad Nauk SSSR 194:818–820

Khomyakov AP, Kurova TA, Nechelyustov GN (1992) Manaksite, $NaKMnSi_4O_{10}$ – a new mineral. Zapiski VMO 121:112–115 (in Russian)

Peacor DR, Buerger MJ (1962) The determination and refinement of the structure of narsarsukite, $Na_2TiOSi_4O_{10}$. Am Mineral 47:539–556

Prencipe M, Gorchakova EA, Ferraris G, Khomyakov AP (1998) Manaksite ($NaKMnSi_4O_{10}$) and fenaksite ($NaKFeSi_4O_{10}$): two silicate from the hyperagpaitic rocks of Lovozero and Khibina (Kola Peninsula, Russia) with a peculiar $[Si_4O_{10}]^{-4}$ channel-like anion. Eighteenth Eur. Cryst. Meeting. Praha. Materials Structure in Chemistry Biology Physics Technology. Bull Czech Slovak Cryst Ass 5B:ECM-18 posters-abstracts:229–230

Rozdestvenskaya IV, Nikishova LV, Bannova II, Labeznik KA (1988) Canasite: refinement and characteristics of the structure, structural typomorphism. Mineral Zh 10:31–44 (in Russian)

Rozdestvenskaya IV, Nikishova LV, Labeznik KA (1996) The crystal structure of frankamenite. Mineral Mag 60:897–905

Scott JD (1976) Crystal strusture of miserite a Zoltal type 5-structure. Can Mineral 14:515–528

Sokolova MN, Suchkova EM, Vlasova EV, Golovanova TI, Kartashov PM, Kovalenko VS (1993) New data on nature and synthetic fenaksite. Dokl Akad Nauk 329:212–215

Heterophyllosilicates, a Potential Source of Nanolayers for Materials Science

Giovanni Ferraris

Introduction

Layer silicates (phyllosilicates) are a well known source of nanolayers for technological applications (Auerbach et al. 2004). In particular, low-charge tetrahedral-octahedral-tetrahedral (*TOT*) layers of clay minerals, e.g. smectites, are used to prepare organoclay complexes, nanocomposites and pillared materials. This contribution aims to attract the attention on the possibility of using *TOT*-like layers of heterophyllosilicates (Ferraris et al. 1996) to prepare organoclay-like hybrids and pillared structures. The presence of five and six co-ordinated titanium in the layers of the heterophyllosilicates looks particularly appealing owing to the well known catalytic properties of this chemical element.

According to the IUPAC nomenclature (Schoonheydt et al. 1999) "pillaring is the process by which a layered compound is transformed into a thermally stable micro- and/or mesoporous material with retention of the layer structure. A pillared derivative is distinguished from an ordinary intercalate by virtue of intracrystalline porosity made possible by the lateral separation of the intercalated guest." A pillared material differs from an ordered porous material by having disordered channels. In fact, whereas the layers of pillared materials are periodically stacked, let say along [001], and their diffraction patterns show sharp 00*l* maxima, the interlayer content is not stacked coherently.

The process of pillaring layered materials includes the following steps: (i) swelling in a polar solvent (usually water); (ii) substitution of the original interlayer cations by bulky (inorganic/organic) cations (pillaring agent); (iii) washing (further chemical reactions occur at this step); (iv) calcination (pillars are formed) (Fig. 1).

Giovanni Ferraris
Dipartimento di Scienze Mineralogiche e Petrologiche, Università di Torino – Istituto di Geoscienze e Georisorse, CNR – Via Valperga Caluso 35, I-10125 Torino, Italy, e-mail: giovanni.ferraris@unito.it

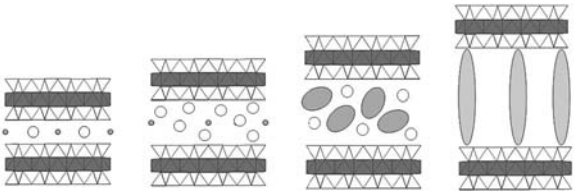

Fig. 1 Schematic representation of the process of pillaring. From left to right side: a phyllosilicate is swelled in water (*large blank circles*); the original interlayer cations (*small grey circles*) are replaced by a pillaring agent (*short ellipses*) that, after further chemical treatment, forms pillars (*elongated ellipses*)

Pillared materials show the following basic characteristics: e.g., in pillared clays the interlayer spacing increases from about 5 Å, in the starting material, to at least 15 Å; the layers do not collapse under calcination; the pillaring agent (inorganic/organic) is laterally spaced; the interlayer space is porous (i.e., at least N_2 molecules can go through); not necessarily, pores and pillars are ordered.

The replacement of the natural interlayer inorganic cations in *TOT* layer silicates by organic cations, through ion exchange, is known since long time. Organic molecules can also be incorporated via the formation of organic complexes with the natural interlayer cations; some of these complexes are stable only in the interlayer ambient. These properties have been exploited to identify expandable clay minerals and, more recently to prepare advanced materials: (i) organoclays which are able either to selectively adsorb neutral or ionic species (e.g., inorganic and organic pollutants) or to act as catalysts; (ii) nanocomposite materials where the organic interlayer consists of a polymeric compound.

Heterophyllosilicates

The polysomatic series of heterophyllosilicates consists of layered minerals where a row of Ti polyhedra (or replacing cations) periodically substitutes a row of disilicate tetrahedra in the *T* tetrahedral sheet of a *TOT* layer; the octahedral *O* sheet is instead maintained (Fig. 2). *HOH* layers are thus obtained where *H* stands for *hetero* to indicate the presence of rows of 5- or 6-coordinated Ti in the *T* sheet. The series has general formula $I_{2+n}Y_{4+3n}[Ti_2(O')_{2+p}Si_{4+4n}O_{14+10n}](O'')_{2+2n}$.

Depending on the periodicity of the Ti substitution and ignoring some minor topological features, three types of *HOH* layers (Fig. 2) are known: bafertisite- (n = 0), astrophyllite- (n = 1) and nafertisite-type (n = 2) layer. In the general formula the value of p (0, 1, 2) depends on the configuration around Ti; *I* and *Y* are interlayer and *O*-sheet cations, respectively.

The so called bafertisite-type layer (cf. Sokolova 2006) is the most versatile of the three known heterophyllosilicate layers, being able to sandwich complex interlayer contents (Table 1). The variety of crystal structures containing this layer is

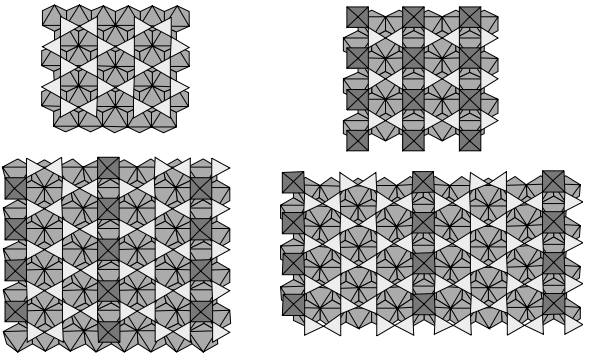

Fig. 2 From left to right and top to bottom: by substitution of rows of Si-tetrahedra (*light grey*) in a TOT phyllosilicate layer by Ti–octahedra (*dark grey*), bafertisite-like, astrophyllite-like, and nafertisite-like HOH heterophyllosilicate layers are obtained. Octahedra of the O sheet are intermediate grey

by far larger than that known for structures containing the *TOT* phyllosilicate layer. However, whereas the latter appears in important rock-forming minerals, like micas and clay minerals, the titanosilicates we are dealing with occur only in rare hyperalkaline rocks (Khomyakov 1995; Pekov 2000; Yakovenchuk et al. 2005).

The swelling capacity of the layer silicates, normally via sorption of H_2O molecules, depends mainly on the negative charge of the *TOT* layer. If the charge is zero (talc, pyrophyllite) or higher than about 0.6 (vermiculites, micas), swelling is not possible or can be obtained only by special procedures; smectites (e.g., montmorillonite, saponite), which bear a low (0.25–0.60) charge, typically swell.

There are consistent evidences of solid-state transformation from one to another member of Table 1 via leaching/substitution of the interlayer composition. In some cases, swelling processes become evident by comparing the structures of the parent and daughter phases. As summarized by Khomyakov (1995) an active interaction with water is a characteristic of many highly alkaline titanosilicates like the heterophyllosilicates of Table 1. Several stage-by-stage replacements of anhydrous titanosilicates by their hydrated and decationated analogues are described in the literature. In particular, the two reactions (lomonosovite + $H_2O \rightarrow$ murmanite + Na_3PO_4) and [vuonnemite + $H_2O \rightarrow$ epistolite + Na_3PO_4; for this transformation see also Azarova et al. (2002)] represent typical transformations observed in nature from primary (lomonosovite and vuonnemite) to secondary (murmanite and epistolite) mineral phases via leaching of interlayer content and hydration that lead to swelling. Modular (Ferraris et al. 2004) structure models (Nèmeth 2004) of bykovaite and M73 [labelling according to Khomyakov (1995)] support the derivation of these phases from bornemanite-like primary phases. The secondary phases that are formed via these transformations seem to be suitable candidates to investigate swelling properties in view of using *HOH* layers to prepare organic–inorganic hybrids and pillared materials.

Table 1 Members of the bafertisite series for which information on the crystal structure is known; they are listed in increasing order of the t (either c or a) cell parameter across the layers

Name	Chemical formula	t[1]	Ref[2]
1	2	3	4
Murmanite	$(Na,\square)_2\{(Na,Ti)_4[Ti_2(O,H_2O)_4Si_4O_{14}](OH,F)_2\}\cdot 2H_2O$	11.70	Khalilov (1989) and Nèmeth et al. (2005)
Bafertisite	$Ba_2\{(Fe,Mn)_4[Ti_2O_2(O,OH)_2Si_4O_{14}](O,OH)_2\}$	11.73	Guan et al. (1963) and Yang et al. (1999)
Hejtmanite	$Ba_2\{(Mn,Fe)_4[Ti_2(O,OH)_4Si_4O_{14}](OH,F)_2\}$	11.77	Rastsvetaeva et al. (1991)
Epistolite	$(Na,\square)_2\{(Na,Ti)_4[Nb_2(O,H_2O)_4Si_4O_{14}](OH,F)_2\}\cdot 2H_2O$	12.14	Sokolova and Hawthorne (2005) and Nèmeth et al. (2005)
Vuonnemite	$Na_8\{(Na,Ti)_4[Nb_2O_2Si_4O_{14}](O,OH,F)_2\}(PO_4)_2$	14.45	Ercit et al. (1998)
Lomonosovite	$Na_8\{(Na,Ti)_4[Ti_2O_2Si_4O_{14}](O,OH)_2\}(PO_4)_2$	14.50	Belov et al. (1978)
Yoshimuraite	$Ba_4\{Mn_4[Ti_2O_2Si_4O_{14}](OH)_2\}(PO_4)_2$	14.75	McDonald et al. (2000)
Innelite	$(Ba,K)_2Ba_2\{(Na,Ca,Ti)_4[Ti_2O_2Si_4O_{14}]O_2\}(SO_4)_2$	14.76	Chernov et al. (1971)
Phosphoinnelite	$(Ba,Sr)_4\{(Na,Ti)_4[Ti_2O_2Si_4O_{14}](O,F)_2\}(PO_4,SO_4)_2$	14.76	Pekov et al. (2006)
Bussenite	$Ba_4Na_2\{(Na,Fe,Mn)_2[Ti_2O_2Si_4O_{14}](OH)_2\}(CO_3)_2F_2\cdot 2H_2O$	16.25	Zhou et al. (2002)
Seidozerite	$Na_2\{(Na,Mn,Ti)_4[(Zr,Ti)_2O_2Si_4O_{14}]F_2\}$	18.20	Pushcharovsky et al. (2002)
Lamprophyllite	$(Sr,Ba)_2\{(Na,Ti)_4[Ti_2O_2Si_4O_{14}](OH,F)_2\}$	19.22	Krivovichev et al. (2003)
Nabalamprophyllite	$Ba(Na,Ba)\{(Na,Ti,)_4[Ti_2O_2Si_4O_{14}](OH,F)_2\}$	19.74	Rastsvetaeva and Chukanov (1999)
Barytolamprophyllite	$(Ba,Na)_2\{(Na,Ti)_4[Ti_2O_2Si_4O_{14}](OH,F)_2\}$	19.83	Pen et al. (1984)
Orthoericssonite	$Ba_2\{Mn_4[Fe_2O_2Si_4O_{14}](OH)_2\}$	20.23	Matsubara (1980)
Quadruphite	$Na_{13}Ca\{(Ti,Na,Mg)_4[Ti_2O_2Si_4O_{14}]O_2\}(PO_4)_4F_2$	20.36	Sokolova and Hawthorne (2001)
Surkhobite	$(Ca,Na,Ba,K)_2\{(Fe,Mn)_4[Ti_2O_2Si_4O_{14}](F,O,OH)_3\}$	20.79	Rozenberg et al. (2003)
Perraultite	$(Na,Ca)(Ba,K)\{(Mn,Fe)_4[(Ti,Nb)_2\ O_3Si_4O_{14}]\ (OH,F)_2\}$	20.84	Yamnova et al. (1998)

Table 1 (continued)

Name	Chemical formula	t^1	Ref[2]
1	2	3	4
Delindeite	$Ba_2\{(Na,Ti,\square)_4$ $[Ti_2(O,OH)_4Si_4O_{14}](H_2O,OH)_2\}$	21.51	Ferraris et al. (2001b)
Polyphite	$Na_{14}(Ca,Mn,Mg)_5\{(Ti,Mn,Mg)_4$ $[Ti_2O_2Si_4O_{14}]\ F_2\}(PO_4)_6F_4$	26.45	Sokolova (2005)
Sobolevite	$Na_{12}CaMg\{(Ti,Na,Mg)_4$ $[Ti_2O_2Si_4O_{14}]\ O_2\}(PO_4)_4F_2$	40.62	Sokolova (2005)
Bornemanite	$BaNa_3\{(Na,Ti,Mn)_4$ $[(Ti,Nb)_2O_2Si_4O_{14}]$ $(F,OH)_2\}PO_4$	47.95	Ferraris et al. (2001a)
M73	$(Ba,Na)_2\{(Na,Ti,Mn)_4$ $[(Ti,Nb)_2(OH)_3Si_4O_{14}]$ $(OH,O,F)_2\}_3H_2O$	48.02	Nèmeth (2004)
Bykovaite	$BaNa\{(Na,Ti)_4$ $[(Ti,Nb)_2(OH,O)_3Si_4O_{14}]$ $(OH,F)_2\}\cdot 3H_2O$	50.94	Nèmeth (2004)

[1]The unit cells given by the quoted authors have been converted to reduced unit cells, if the case.
[2]Reference to the most recent chapter on the structure.

Towards *HOH* nanolayers?

So far, there is no record in the literature of the use of heterophyllosilicates to obtain hybrid materials. Reasons of the limited experimental investigation can be a scarce knowledge of the heterophyllosilicates among materials scientists (but see Ferraris and Merlino 2005; Ferraris 2006; Ferraris et al. 2007). Other reasons are connected with the difficulties in synthesizing these compounds, a step which for sure is needed because the minerals listed in Table 1 are generally rare and show a complex chemical composition. According to Khomyakov (1995), the secondary hydrated phases of heterophyllosilicates are likely to be obtained only (or mainly) via solid-state transformation, an obstacle towards synthesis. Results of direct synthesis are so far limited to two compounds: $Na_8\{(Na,Ti)_4[Ti_2O_2Si_4O_{14}]O_2\}(VO_4)_2$, that corresponds to the phosphate lomonosovite and has been prepared from a melt (Massa et al. 2000), and $BaFe_2TiSi_2O_9$, that has the stoichiometry of bafertisite and has been obtained as minor phase under hydrothermal conditions (Ferraris et al. 2007). Khomyakov (2004) obtained murmanite and epistolite from, in the order, lomonosovite and vuonnemite treated with boiling water.

Acknowledgements Research supported by grants of the Italian Ministry for University and Research (MIUR).

References

Auerbach SM, Carrado KA, Dutta PK (eds) (2004) Handbook of layered materials. Marcel Dekker, New York

Azarova YuV, Pekov IV Chukanov NV, Zadov AE (2002) Products and processes of the vuonnemite transformations at the low-temperature alteration of ultraagpaitic pegmatites (in Russian). Zapiski VMO 131(5):112–121

Belov NV, Gavrilova GS, Solov'eva LP, Khalilov AD (1978) The refined structure of lomonosovite. Sov Phys Dokl 22:422–424

Chernov AN, Ilyukhin VV, Maksimov BA, Belov NV (1971) Crystal structure of innelite, $Na_2Ba_3(Ba,K,Mn)(Ca,Na)Ti(TiO_2)_2[Si_2O_7]_2(SO_4)_2$. Sov Phys Crystallogr 16:87–92

Ercit TS, Cooper MA, Hawthorne FC (1998) The crystal structure of vuonnemite, $Na_{11}Nb_2(Si_2O_7)(PO_4)_2O_3(F,OH)$, a phosphate-bearing sorosilicate of the lomonosovite group. Can Mineral 36:1311–1320

Ferraris G (2006) Pillared materials from layer titanosilicates?. Sol St Phen 111:47–50

Ferraris G, Merlino S (eds) (2005) Micro and mesoporous mineral phases, vol 57. Rev Mineral Geochem, Mineralogical Soc, Washington, DC, America

Ferraris G, Belluso E, Gula A, Soboleva SV, Ageeva OA, Borutskii BE (2001a) A structural model of the layer titanosilicate bornemanite based on seidozerite and lomonosovite modules. Can Mineral 39:1667–1675

Ferraris G, Bloise A, Cadoni M (2007) Layered titanosilicates – a review and some results on the hydrothermal synthesis of bafertisite. Micropor Mesopor Mat doi: 10.1016/j.micromeso.2007.02.036

Ferraris G, Ivaldi G, Khomyakov AP, Soboleva SV, Belluso E, Pavese A (1996) Nafertisite, a layer titanosilicate member of a polysomatic series including mica. Eur J Mineral 8:241–249

Ferraris G, Ivaldi G, Pushcharovsky DYu, Zubkova NV, Pekov IV (2001b) The crystal structure of delindeite, $Ba_2\{(Na,K,\square)_3(Ti,Fe)[Ti_2(O,OH)_4Si_4O_{14}](H_2O,OH)_2\}$, a member of the meroplesiotype bafertisite series. Can Mineral 39:1306–1316

Ferraris G, Makovicky E, Merlino S (2004) Crystallography of modular materials. IUCr Monographs in Crystallography, Oxford University Press, Oxford

Guan YaS, Simonov VI, Belov NV (1963) Crystal structure of bafertisite, $BaFe_2TiO[Si_2O_7](OH)_2$. Dokl Akad Sci 149:123–126

Khalilov AP (1989) Refinement of the crystal structure of murmanite and new data on its crystal chemistry. Mineral Zh 11(5):19–27 (in Russian)

Khomyakov AP (1995) Mineralogy of hyperagpaitic alkaline rocks. Clarendon Press, Oxford

Khomyakov AP (2004) Zeolite-like amphoterosilicates of hyperagpaitic rocks and their unique properties. Rev Mineral Geochem Accad Lincei Roma 231–234

Krivovichev SV, Armbruster T, Yakovenchuk VN, Pakhomovsky YA, Men'shikov YP (2003) Crystal structures of lamprophyllite-2M and lamprophyllite-2O from the Lovozero alkaline massif, Kola Peninsula, Russia. Eur J Mineral 15:711–718

Massa W, Yakubovich OV, Kireev VV, Mel'nikov OK (2000) Crystal structure of a new vanadate variety in the lomonosovite group: $Na_5Ti_2O_2[Si_2O_7](VO_4)$. Solid State Sci 2:615–623

Matsubara S (1980) The crystal structure of orthoericssonite. Mineral J 10:107–121

McDonald AM, Grice JD, Chao GY (2000) The crystal structure of yoshimuraite, a layered Ba–Mn–Ti silicophosphate, with comments of five-coordinated Ti^{4+}. Can Mineral 38:649–656

Nèmeth P (2004) Characterization of new mineral phases belonging to the heterophyllosilicate series. Ph D dissertation Università di Torino Torino Italy

Nèmeth P, Ferraris G, Radnóczi G, Ageeva OA (2005) TEM and X-ray study of syntactic intergrowths of epistolite with murmanite and shkatulkalite. Can Mineral 45:973–987

Pekov IV (2000) Lovozero massif: history, pegmatites, minerals. Ocean Pictures Ltd, Moscow

Pekov IV, Chukanov NV, Kulikova IM, Belakovsky DI (2006) Phosphoinnelite $Ba_4Na_3Ti_3Si_4O_{14}(PO_4,SO_4)_2(O,F)_2$, a new mineral from agpaitic pegmatites of Kovdor massif, Kola Peninsula. Zapiski VMO 135(3):52–60 (in Russian)

Pen ZZ, Zhang J, Shu J (1984) The crystal structure of barytolamprophyllite. Kexue Tongbao 29:237–241

Pushcharovsky DYu, Pasero M, Merlino S, Vladykin NV, Zubkova NV, Gobechiya ER (2002) Crystal structure of zirconium-rich seidozerite. Crystallogr Rep 47:196–200

Rastsvetaeva RK, Chukanov NV (1999) Crystal structure of a new high-barium analogue of lamprophyllite with a primitive unit cell. Dokl Chem 368(4–6):228–231

Rastsvetaeva RK, Tamazyan RA, Sokolova EV, Belakovskii DI (1991) Crystal structures of two modifications of natural Ba,Mn-titanosilicate. Sov Phys Crystallogr 36:186–189

Rozenberg KA, Rastsvetaeva RK, Verin IA (2003) Crystal structure of surkhobite: new mineral from the family of titanosilicate micas. Crystallogr Rep 48:384–389

Schoonheydt RA, Pinnavaia T, Lagaly G, Gangas N (1999) Pillared clays and pillared layered solids. Pure Appl Chem 71:2367–2371

Sokolova E (2006) From structure topology to chemical composition. I. Structural hierarchy and stereochemistry in titanium disilicate minerals. Can Mineral 44:1273–1333

Sokolova E, Hawthorne FC (2001) The crystal chemistry of the $[M_3\Phi_{11-14}]$ trimeric structures from hyperagpaitic complexes to saline lakes. Can Mineral 39:1275–1294

Sokolova E, Hawthorne FC (2005) The crystal chemistry of epistolite. Can Mineral 42:797–806

Sokolova E, Hawthorne FC, Khomyakov AP (2005) Polyphite and sobolevite: revision of their structures. Can Mineral 43:1527–1544

Yakovenchuk VN, Ivanyuk GYu, Pakhomovsky YaA, Men'shikov YuP (2005) Khibiny minerals. Laplandia Minerals, Apatity

Yamnova NA, Egorov-Tismenko YuK, Pekov IV (1998) Crystal structure of perraultite from the Coastal Region of the Sea of Azov. Crystallogr Rep 43:401–410

Yang Z, Cressey G, Welch M (1999) Reappraisal of the space group of bafertisite. Powder Diffr 14:22–24

Zhou K, Rastsvetaeva RK, Khomyakov AP, Ma Z, Shi N (2002) Crystal structure of new micalike titanosilicate – bussenite, $Na_2Ba_2Fe^{2+}[TiSi_2O_7][CO_3]O(OH)(H_2O)F$. Crystallogr Rep 47:50–53

Fullerene-Like Carbon in Nature and Perspectives of its use in Science-Based Technologies

Vladimir V. Kovalevski

Carbon plays an all-important role in nature. Carbon atoms can to form complicated organic networks some of those are base for existence of known forms of life. Elemental carbon also shows very complicated behavior forming a number of different structures. Recent years have been marked by an accented interest of scientists in fullerenes, nanotubes and many nano-sized shapes (Kroto et al., 1985; Iijima, 1991). Non-crystalline fullerene-like carbon forms were additionally obtained using an arc discharge, flame, laser pyrolysis (Chhowalla et al., 1997; Mordkovich, 2000; Grieco et al., 2000), and were even found in petrol soot (Lee et al., 2002). The term "fullerene-like" has been used for roughly spherical carbon structures such as carbon "onions" and hollow nanoparticles consisting of concentric curled carbon layers. Some authors have specified additional characteristics such as a diameter between ca. 5 and 20 nm (Chhowalla et al., 1997) and a lattice spacing of approximately 0.35 nm (Grieco et al., 2000). They infer the curling of graphene layers results from the presence of pentagonal rings as in fullerenes (Grieco et al., 2000). Other authors assume that four- and eight-membered carbon rings can occur in fullerene structures (Slanina et al., 1999). In addition, it has been hypothesized that the graphene layers contain defects in the form of pentagonal, heptagonal, or other kind of rings, singly or in combination, that affect the graphene-layer curvature and create different fullerene-like structures (Cataldo, 2002).

Fullerenes and fullerites have been found in the natural environment (Buseck et al., 1992; Becker et al., 1994; Novgorodova, 1999). Even more intriguingly, the symmetry and shapes of icosahedral viruses, Murine leukemia virus, for instance, are directly related to symmetries of "giant" fullerenes (Nermut and Mulloy, 2007). Much natural free carbon occurs in the amorphous state in varieties that have long been of interest because of their intriguing range in structures, properties, and industrial applications. An interesting type of non-crystalline carbon occurs in the shungite rocks of Karelia (Russia) (Shungites of Karelia, 1975; Buseck et al., 1997), from

Vladimir V. Kovalevski
Institute of Geology, Karelian Research Center, Russian Academy of Sciences, Pushkinskaya St. 11, Petrozavodsk 185610, Russia, e-mail: kovalevs@krc.karelia.ru

which the first natural occurrence of fullerenes was reported (Buseck et al., 1992) and hollow nanospheres and fibers were described (Kovalevski et al., 1996). Shungite rocks have simple mineral composition, which may contain shungite, quartz, mica, carbonates and traces of other minerals. Shungite has chemical composition consisting of C with traces of N, O, H and S. All types of these rocks have very variable physico-chemical properties depending on the shungite structure, C content, the composition and characteristics of minerals and distribution of carbon and minerals in these shungite rocks. For example, type I rocks have a relatively low specific gravity (1.8–2.0 g/cm^3), high electric conductivity (about 100 S/cm), and some types have unusually high specific surface areas (up to 500 m^2/g) as measured by the (BET) adsorption of gaseous nitrogen. Carbon from shungite rocks demonstrates fullerene-like signs on different structural and physical levels.

All high-resolution transmission electron microscopy (HRTEM) images of the samples contain well-defined fringes**,** and these occur in packets of 5–14 sheets. Many of these sheets are curved, and in places they appear as if they might close upon themselves, although the tangle of intervening sheets makes such an interpretation uncertain. The centers of the curved sheets may represent pores, consistent with the high surface areas inferred from BET measurements. The STEM images of shungites suggest 3-dimensional shells or, more commonly, fractions of such shells or regions of graphene structure, that are highly disordered in bent stacks. The 3-dimensional structures that might be surmised from the HRTEM images are confirmed by the sets of nanodiffraction patterns. The strengths and directions of the 00l lines of spots correspond to sets of 0.34 nm fringes in the images. The ellipticity of the rings suggests tilts of the sheets, which are apparently bent into 3-dimensional shapes approximating closed or partly closed shells of rather irregular cross section. In that sense it may be described on the permolecular level as a fullerene-like carbon (Kovalevski et al., 2001).

There are two types of imperfections on the molecular level connected with irregularities of 100 fringes that suggest a disorder of the graphene layers from HRTEM images. The former are connected with essential disorder of fringes that can resulted from the presence of impurity atoms or clusters in the stack of graphene layers. Other imperfections connected with insignificant disorder in the direction of fringes and the distance between them, and can result from point defects or the four-, five-, eight-membered or other carbon rings that are signs of fullerene-like structures (Cataldo, 2002).

The electron energy loss spectroscopy (EELS) of shungites provides information on the electronic structure that is very sensitive to the valency, coordination, and site symmetry of carbon atoms and is right dealing with structure-property relationships. In the low-energy-loss region, two characteristic plasmon peaks occur: one is the π-plasmon corresponding to transitions between the π and π^* states located at approximately 6eV, and the other is σ-plasmon located at 24.5–26.5 eV depending on the structure of different shungite carbons. The σ plasmon peak of those is shifted to a lower energy with respect to the peak of graphite and is similar to the peak of fullerene-like carbon spheres (Kovalevski and Moshnikov, 2001).

The magnetic susceptibility (χ) is one of the more sensitive physical properties of the band and atomic structure. For disordered carbon χ is sensitive to the degree of graphitization, crystallite size, and the degree of folding of the graphene layers. The magnetic susceptibilities of shungites from several localities are different at temperatures ranging from 90 to 150 K. The effect is likely sensitive to the structure of the graphene layers and the presence of trace elements. A distinctive feature is a considerable increase of diamagnetism at liquid-nitrogen temperatures with a temperature range and amount of change similar to that of CuC_{60}. The effect has not been reported for amorphous natural carbon and graphite but has been observed for doped fullerites. The hypothesis that the carbon of shungites is natural fullerene-like carbon can account for the observed structure and magnetic properties (Kovalevski et al., 2005).

The features of fullerene-like natural carbon offer the challenge of its use in science-based technologies. Furthermore, natural fullerene-like carbon from shungite rocks contains trace elements and characterized by a metastable state. The peculiarities can lead to forming at processing of new fullerene-like structures such as hollow particles and fibers and those partially filled by metals or carbide that can be also used.

Acknowledgements This study was supported by grant 05-05-97520C from RFBR and Republic of Karelia.

References

Becker L, Bada JL, Winans RE, Hunt JE, Bunch TE, French BM (1994) Fullerenes in the 1.85-billion-year-old Sudbury impact structure. Science 265:642–644

Buseck PR, Tsipursky SJ, Hettich R (1992) Fullerenes from the geological environment. Science 257:215–217

Buseck PR, Galdobina LP, Kovalevski VV, Rozhkova NN, Valley JW, Zaidenberg AZ (1997) Shungites: the carbon-rich rocks of Karelia. Can Mineral 35(6):1363–1378

Cataldo F (2002) The impact of a fullerene-like concept in carbon black science. Carbon 40(2):157–162

Chhowalla M, Aharonov RA, Kiely CJ, Alexandrov I, Amaratunga (1997) Generation and deposition of fullerene- and nanotube-rich carbon thin films. Phil Mag Lett 75(5):329–335

Grieco WJ, Howard JB, Rainey LC, Vander Sande JB (2000) Fullerenic carbon in combustion-generated soot. Carbon 38(4):597–614

Iijima S (1991) Helical microtubules of graphitic carbon. Nature 354(6349):56–58

Kovalevski VV, Safronov AN, Markovski JuA (1996) Hollow carbon microspheres and fibres produced by catalytic pyrolysis and observed in shungite rocks. Mol Mater 8:21–24

Kovalevski VV, Buseck PR, Cowley JM (2001) Comparison of carbon in shungite rocks to other natural carbons: An X-ray and TEM study. Carbon 39(2):243–256

Kovalevski VV, Moshnikov IA (2001) Electron Energy-Loss Spectra of Carbon from Shungite Rocks' Abstr. of 5th Intern. Workshop in Russia. Fullerenes and Atomic Clusters (IWFAC'01) July 2–6 St Petersb, p 92

Kovalevski VV, Prikhodko AV, Buseck PR (2005) Diamagnetism of natural fullerene-like carbon. Carbon 43(2):401–405

Kroto HW, Heath JR, O'Brien SC, Curl RF, Smalley RE (1985) C60 buckminsterfullerene. Nature 318(6042):162–163

Lee TN, Yao N, Chen TJ, Hsu WK (2002) Fullerene-like carbon particles in petrol soot. Carbon 40(12):2275–2279

Mordkovich VZ (2000) The observation of large concentric shell fullerenes and fullerene-like nanoparticles in laser pyrolysis carbon blacks. Chem Mater 12:2813–2818

Nermut MV, Mulloy B (2007) Consideration of the three-dimensional structure of core shells (capsids) in spherical retroviruses. Micron 38(5):462–470

Novgorodova MI (1999) What are fullerenes and fullerites in mineral world. Geochem 9:1000–1008 (in Russsian)

Slanina Z, Zhao X, Osawa E (1999) Relative stabilities of isomeric fullerenes. Adv Strain Interesting Org Mol 7:185–235

Sokolov VA, Kalinin YuK (eds) (1975) Shungites of Karelia and ways of their all-purpose utilization. Karelia, Petrozavodsk (in Russian)

Fullerenes as Possible Collectors of Noble, Rare, and Disseminated Elements

Yurii L. Voytekhovsky

Introduction

There is no doubt that the laboratory synthesis (Curl & Smalley, 1988) and subsequent findings of stable C_{60} clusters in rocks (Zeidenberg et al., 1996) are the most impressive events in carbon crystallography and mineralogy for the last 20 years. The fullerenes of less than 60 atoms are known to be unstable and registered in physical experiments in a minor amount, with those of 20–36 atoms forming a "restricted zone" (Helden et al., 1993). But just these types of fullerene-like crystalline pores were identified in many clathrate compounds over the last 50 years (Ripmeester & Ratcliffe, 1998). Hence, our idea is to systematically generate the series of fullerenes up to the well known C_{60} shape.

Characterization of Fullerenes

We define fullerenes as simple (three edges meet at each vertex) polyhedra, with only pentagonal and hexagonal facets allowed. Let f_5 and f_6 be the numbers of pentagonal and hexagonal facets and f, e and v be the numbers of facets, edges and vertices of any fullerene. Then

$f_5 + f_6 = f, 5f_5 + 6f_6 = 2e$ *and* $f_5 = 6f - 2e$.

At the same time, $f - e + v = 2$, $2e = 3v$ and $6f - 2e = 12$.

Hence, $f_5 = 12$, $f = 12 + f_6$ with $f_6 \geq 0$.

It follows from the above that $v = 2f - 4 \geq 20$ and

$f_6 = f - 12 = v/2 - 10$.

Yurii L. Voytekhovsky
Geological Institute, Kola Scientific Centre, Russian Academy of Sciences, Apatity, Russia, e-mail: voyt@geoksc.apatity.ru

Thus, any fullerene may be characterized by the vertex C_v and facet $5_{12}6_{v/2-10}$ notations. We use the latter in the generating algorithm. Most of the above equations are due to Euler. They are provided here for the readers' convenience.

Generating Algorithm

We construct a fullerene in the Shlegel projection in the following way. A general idea is to take the first facet and surround it by other facets numbered clockwise. Then, the same procedure should be repeated with the facets numbered as 2, 3 *etc*. As the fullerenes are simple polyhedra, only three facets meet at each vertex. The last facet should be the basal one of the Shlegel projection.

In the simplest case of fullerene 5_{12}, we begin with a pentagonal facet and build the only possible projection (Fig. 1, No. 1). For fullerene $5_{12}6_1$, we begin with the hexagonal facet and try to build the projection. This procedure does not lead to a fullerene. For fullerenes $5_{12}6_n$ with $n > 1$, we also begin with a hexagonal facet. But, in this case, to check all the variants, we previously enumerate the (6, ...) sequences with any permutations of $n-1$ sixes in $n+11$ dotted positions. Then we generate the facets in the above procedure in accord with them. For example, the (6, 5, ..., 5, 6) sequence leads to the only fullerene $5_{12}6_2$ (No. 2). The generating procedure is stopped in three cases: (a) a fullerene is built in accord with a given sequence, (b) a fullerene is not built if the given facets are already exhausted, (c) at some step, the next facet would not be pentagonal or hexagonal.

The duplicated fullerenes of the same combinatorial type for a given $5_{12}6_n$ formula should be eliminated. To do this, we use their adjacency matrices for arbitrary initial numbering of the vertices. Two fullerenes belong to the same combinatorial type if and only if their adjacency matrices are reducible to each other by the symmetrical permutations of rows and columns. Afterwards, we calculate the automorphism group order of a given fullerene as the number of different vertex reindexings that save its adjacency matrix.

The series of C_{20}–C_{60} fullerenes was found to consist of 5770 representatives. They are characterized by the automorphism group orders and point groups in Table 1. As in a general case (Voytekhovsky, 2001), they mostly belong to 1, 2 and m classes. For given ν, the variety of C_v fullerenes slightly drops as an automorphism group order increases. Simultaneously, their physical stability is known to increase (Curl & Smalley, 1988, Helden et al., 1993). The fullerenes of 6–120 automorphism group orders are in Fig. 1.

C_{20}: 1 (−3−5m), C_{24}: 2 (−12m2), C_{26}: 3 (−6m2), C_{28}: 4 (−43m), C_{30}: 5 (−10m2), C_{32}: 6 (32), 7 (−3m), 8 (−6m2), C_{34}: 9 (3m), C_{36}: 10, 11 (−42m), 12 (−6m2), 13 (6/mmm), C_{38}: 14 (32), 15 (3m), 16 (−6m2), C_{40}: 17 (3m), 18 (mmm), 19, 20 (−5m), 21 (−43m), C_{42}: 22 (32), C_{44}: 23, 24 (32), 25 (23), 26–28 (−3m), 29, 30 (−6m2), C_{48}: 31 (32), 32, 33 (mmm), 34, 35 (−12m2), C_{50}: 36, 37 (32), 38 (3m), 39 (−6m2), 40, 41 (−10m2), C_{52}: 42, 43 (3m), 44, 45 (mmm), 46–50 (–42m), 51 (23), C_{54}: 52 (32), 53 (−6m2), C_{56}: 54–59 (32), 60 (mmm), 61 (−42m), 62, 63

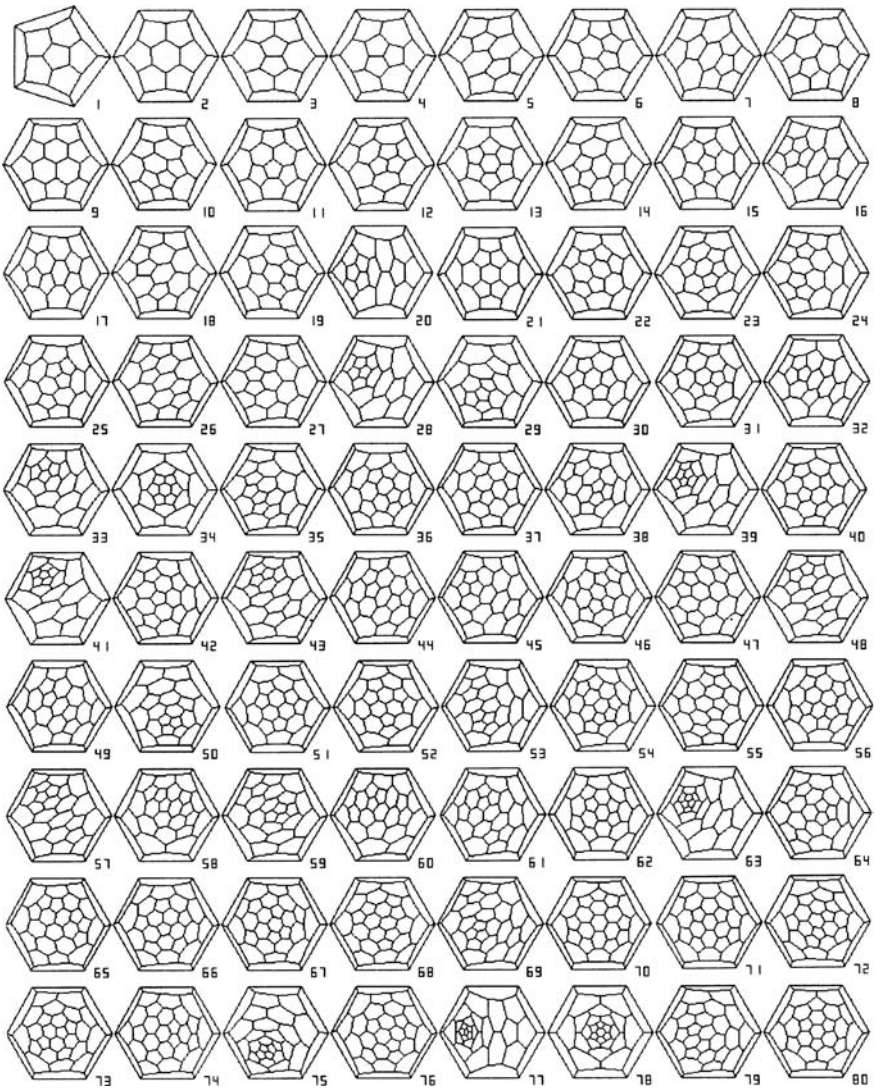

Fig. 1 C_{20}–C_{60} fullerenes of 6–120 automorphism group orders in the Shlegel projections. See text for the point groups

(–3m), 64 (−43m), C_{58}: 65, 66 (3m), C_{60}: 67–69 (32), 70 (3m), 71 (mmm), 72–75 (−42m), 76 (52), 77 (−5m), 78, 79 (6/mmm), 80 (−3−5m).

Except for the famous No. 80 shape, Nos. 34, 35, 40, 41, 64 and 77–79 appear to be the most probable fullerenes in physical experiments. They are far from the "restricted zone" and can be realized as the shapes of rather high symmetry. Except for Nos. 1, 2, 5, 19, 20, 34, 35, 40, 41, 76, 77 and 80, most of the C_{20}–C_{60} fullerenes

Table 1 Point group statistics for C_{20}–C_{60} fullerenes

a.g.o.	s.p.g.	20	24	26	28	30	32	34	36	38	40	42	44
1	1								2	7	8	23	42
2	–1												
	2						2	3	4	5	14	11	22
	m							2	2		7	6	7
3	3										1		
4	–4												1
	222				1		1		2		3		6
	2/m												
	mm2					2			1	2	2	4	3
6	32						1			1		1	2
	3m							1		1	1		
8	mmm										1		
	–42m								2				
10	52												
12	23												1
	–3m						1						3
	–6m2			1			1		1	1			2
20	–5m										2		
	–10m2					1							
24	6/mmm								1				
	–43m				1						1		
	–12m2		1										
120	–3–5m	1											
∑		1	1	1	2	3	6	6	15	17	40	45	89

a.g.o.	s.p.g.	46	48	50	52	54	56	58	60	∑
1	1	69	117	195	307	470	700	1037	1508	4485
2	–1						1			1
	2	22	52	37	78	62	135	98	189	734
	m	19	16	25	26	38	49	58	67	322
3	3	2		2	3		3	4		15
4	–4								2	3
	222		5		9		10		19	56
	2/m		1		1		2		4	8
	mm2	4	3	6	3	8	13	6	9	66
6	32		1	2		1	6		3	18
	3m			1	2			2	1	9
8	mmm		2		2		1		1	7
	–42m				5		1		4	12
10	52								1	1
12	23				1					2
	–3m						2			6
	–6m2			1		1				8
20	–5m								1	3
	–10m2			2						3
a.g.o.	s.p.g.	46	48	50	52	54	56	58	60	∑
24	6/mmm								2	3
	–43m						1			3
	–12m2		2							3
120	–3–5m								1	2
∑		116	199	271	437	580	924	1205	1812	5770

Notes: a.g.o. – automorphism group orders, s.p.g. – symmetry point groups.

are of crystalline symmetry. Hence, they may be considered as probable structural units of various crystalline (*e.g.* clathrate) compounds.

Potentially Stable Fullerenes

As stated by Curl & Smalley (1988), the fullerenes with rather high symmetry and no adjacent pentagons only can be stable because of physical reasons. Hence, the above computer calculations were continued for C_{72}–C_{100} fullerenes to find those with automorphism group order not less than 20 as for the stable C_{70} fullerene. The symmetry point group statistics is given in Table 2. The fullerenes which are to be stable are shown in Fig. 2.

Volume of the Fullerenes

The inner volumes for all the generated C_{60}–C_{100} fullerenes were calculated provided the C atoms with an effective radius 1.7 Å are located in the vertices. It was found that the volume of C_n fullerene depends mostly from the number of atoms than from the symmetry (Fig. 3). The volumes of all potentially stable C_{60}–C_{100} fullerenes (Fig. 2) are given in Table 3. Here, n means the number of atoms in a fullerene, V and R are the volume and radius of its inner sphere, respectively.

Table 2 Point group statistics for C_{72}–C_{100} fullerenes

a.g.o.	s.p.g.	72	74	76	78	80	82	84	86	88	90	92	94	96	98	100	Σ
1	1							1	6	11	16	38	89	108	169	336	774
2	2						3	5	6	7	16	26	26	43	49	62	243
	m						3	5	3	11	6	8	13	14	30	31	124
3	3								1			1	3		3	3	11
4	222			1		1		4		2		4		8		9	29
	mm2				2	2	1	4	2	3	7	2	2	3	5	5	38
6	32				1	1			1			5		3	3		14
	3m						2						1	1			4
8	mmm											1		1			2
	–42m							2						1		1	4
10	52															1	1
	5m															1	1
12	–3m							1						1			2
	–6m2		1		2									1			4
	23									1		1				1	3
20	–10m2					1					1						2
	–5m					1											1
24	–43m			1				1									2
	–12m2	1												2			3
	6/mmm							1						1			2
120	–3–5m					1											1
Σ		1	1	2	5	7	9	24	19	35	46	86	134	187	259	450	1265

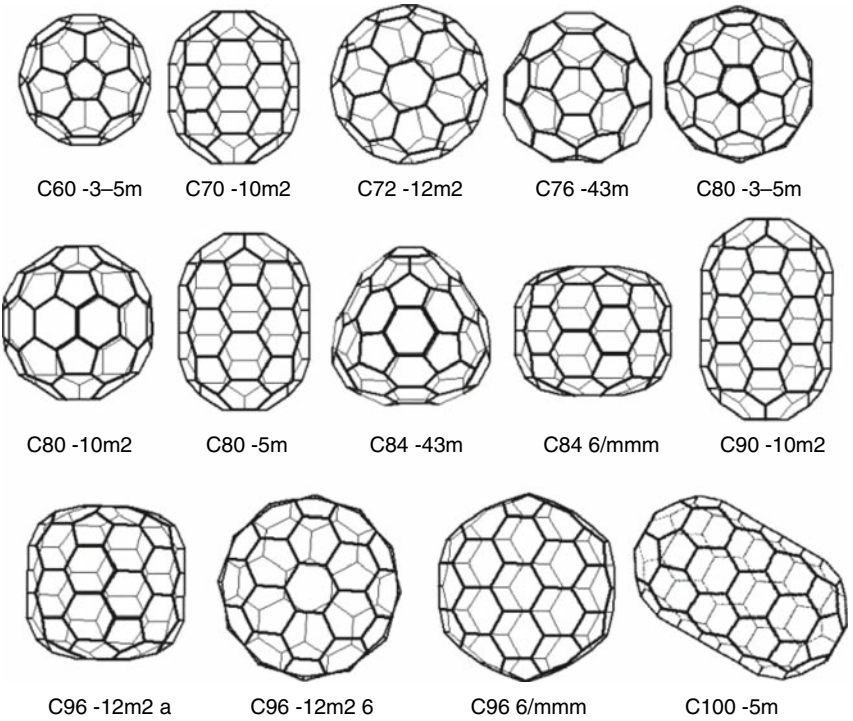

Fig. 2 The C_{60}–C_{100} fullerenes with high automorphism group order not less than 20 and no adjacent pentagons. They appear to be stable in physical experiments and natural conditions

Table 3 Parameters of potentially stable C_{60}–C_{100} fullerenes

n	s.p.g.	V, Å^3	R, Å
60	−3−5m	21.3	1.80
70	−10m2	32.9	1.65
72	−12m2	35.0	1.31
76	−43m	41.8	1.88
80	−3−5m	48.1	2.24
80	−10m2	48.0	2.09
80	−5m	47.1	1.75
84	−43m	53.7	1.83
84	6/mmm	54.1	1.93
90	−10m2	63.3	1.59
96	−12m2 a	76.1	2.39
96	−12m2 b	74.9	1.72
96	6/mmm	75.3	1.75
100	−5m	81.4	1.72

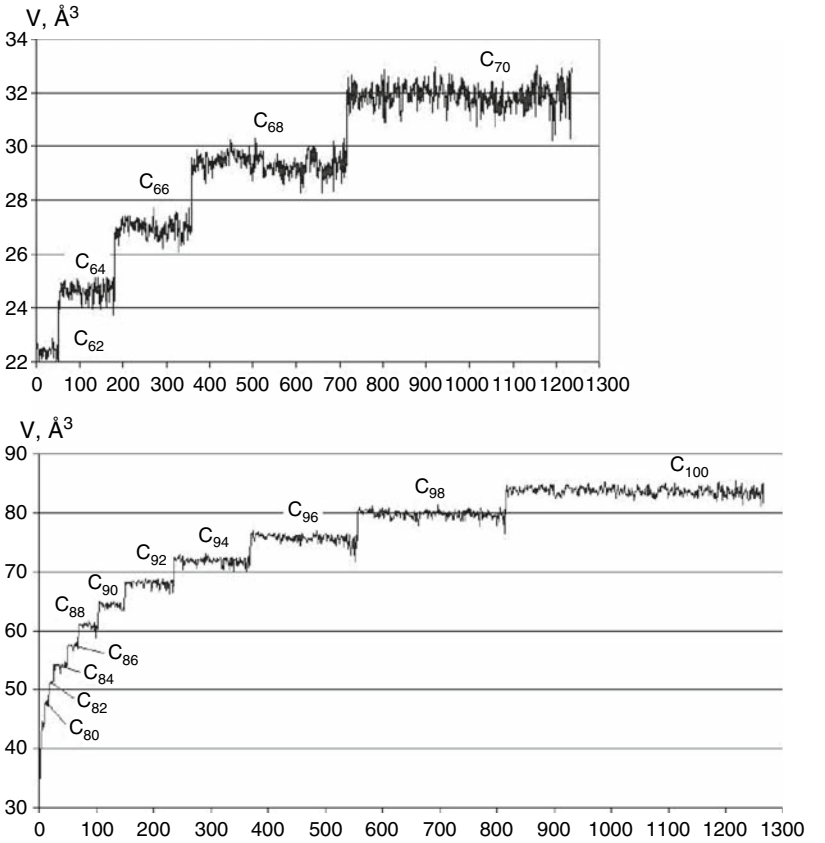

Fig. 3 The volume of fullerenes C_{60}–C_{70} (above) and C_{72}–C_{100} (below). Horizontal axes – the order numbers of fullerenes in the catalogues (Voytekhovsky & Stepenshchikov, 2002, 2003). They increase with the numbers of atoms in the fullerenes

Fullerenes as Possible Collectors of Various Elements

The above computer calculations show that the volumes of the potentially stable C_{60}–C_{100} fullerenes are enough to include some atoms, for example, noble, rare and disseminated elements which are known to be spread in the carbon-bearing geological formations of the Kola Peninsula and other localities.

Taking in mind that the volume of a fullerene depends also from its morphology (symmetry), the appropriate computer calculations for the above 14 fullerenes were made. The results are given in Table 4 for different radii of the inner atoms. They are illustrated in Fig. 4.

Table 4 The maximum number of inner atoms in the potentially stable C_{60}–C_{100} fullerenes

n	s.p.g.	R_a, Å																				
		1.30	1.31	1.32	1.33	1.34	1.35	1.36	1.37	1.38	1.39	1.40	1.41	1.42	1.43	1.44	1.45	1.46	1.47	1.48	1.49	1.50
60	−3−5m	1	1	1	1	1	1	1	1	1	1	1	1	1	1	1	1	1	1	1	1	1
70	−10m2	1	1	1	1	1	1	1	1	1	1	1	1	1	1	1	1	1	1	1	1	1
72	−12m2	1	1	1	1	1	1	1	0	0	0	0	0	0	0	0	0	0	0	0	0	0
76	−43m	1	1	1	1	1	1	1	1	1	1	1	1	1	1	1	1	1	1	1	1	1
80	−3−5m	1	1	1	1	1	1	1	1	1	1	1	1	1	1	1	1	1	1	1	1	1
80	−10m2	1	1	1	1	1	1	1	1	1	1	1	1	1	1	1	1	1	1	1	1	1
80	−5m	2	2	2	2	2	2	2	2	2	2	2	2	2	2	2	2	2	2	2	2	2
84	−43m	1	1	1	1	1	1	1	1	1	1	1	1	1	1	1	1	1	1	1	1	1
84	6/mmm	1	1	1	1	1	1	1	1	1	1	1	1	1	1	1	1	1	1	1	1	1
90	−10m2	2	2	2	2	2	2	2	2	2	2	2	2	2	2	2	2	2	2	2	2	2
96	−12m2 a	2	2	2	2	2	2	2	2	2	2	2	1	1	1	1	1	1	1	1	1	1
96	−12m2 b	3	3	3	3	3	3	3	3	3	3	3	3	3	3	2	2	2	2	2	1	1
96	6/mmm	3	3	3	3	3	3	3	3	3	3	3	3	3	3	3	3	3	3	3	2	2
100	−5m	3	3	3	3	3	3	3	3	3	3	3	3	3	3	3	2	2	2	2	2	2

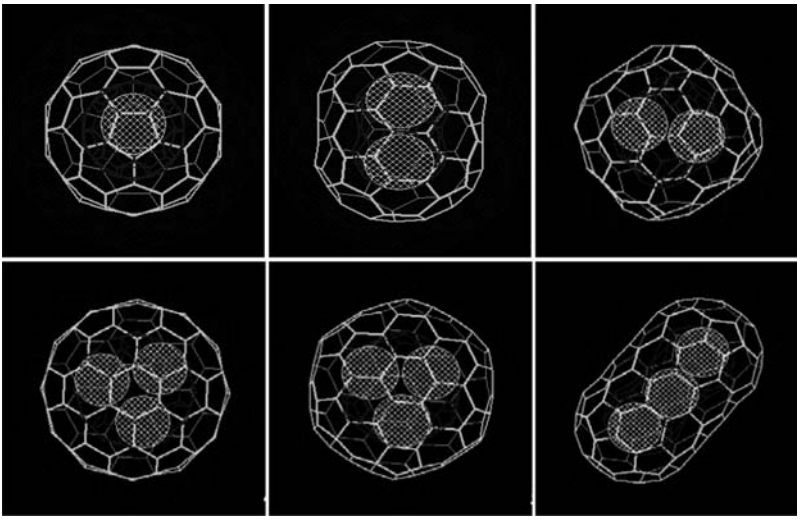

Fig. 4 The fullerenes: 1 – C_{80} (–3–5m), 2 – C_{80} (–5m), 3 – C_{96} (–12m2, a), 4 – C_{96} (-12m2, b), 5 – C_{96} (6/mmm), 6 – C_{100} (-5m) with inner atoms of Au (R_a = 1.44 Å) for the cases 1, 2, 5 and 6, and Pt (R_a = 1.38 Å) for the cases 3 $\mathbf{и}$ 4

Conclusions

The true carbone fullerenes and fullerene-like structures were found in the nature: shungites of the North Karelia (Russia), fulgurites of the Colorado (USA), carbon-bearing rocks of the Pechenga (Russia). As for the carbon-bearing geological formations, the geochemical anomalies of noble, rare and disseminated elements are known there with no distinguished mineral phases. The above calculations give us the arguments to consider the fullerenes and fullerene-like structures as their possible collectors.

Acknowledgements I thank Ph.D. Dmitry G. Stepenshchikov for his highly skilled assistance.

References

Curl RF, Smalley RE (1988) Probing C_{60}. Sci 242:1017–1022

Helden G, Hsu M-T, Gotts N, Bowers MT (1993) Carbon cluster cations with up to 84 atoms: structures, formation mechanism, and reactivity. J Phys Chem 97:8182–8192

Ripmeester JA, Ratcliffe CI (1998) The diverse nature of dodecahedral cages in clathrate hydrates as revealed by ^{129}Xe and ^{13}C NMR spectroscopy: CO_2 as a small-cage guest. Energ Fuel 12:197–202

Voytekhovsky YL (2001) On the symmetry of 4- to 11-hedra. Acta Crystallographica A57: 112–113

Voytekhovsky YL, Stepenshchikov DG (2002) C_{20} to C_{60} fullerenes: a catalogue of combinatorial types and symmetry point groups. K & M Publishing Co, Apatity (in Russian)
Voytekhovsky YL, Stepenshchikov DG (2003) C_{62} to C_{100} fullerenes: a catalogue of combinatorial types and symmetry point groups. K & M Publishing Co, Apatity (in Russian)
Zeidenberg AZ, Kovalevsky VV, Rozhkova NN, Tupolev AG (1996) Fullerene-like structures in shungite carbon. Russ J Phys Chem 70:99–102

Nanotubes in Minerals and Mineral-Related Systems

Sergey V. Krivovichev

Introduction

One of the most important and exciting directions in modern science and technology is the effort to achieve systematic control of matter at the nanoscale (1 nm = 10^{-9} m = 10 Å). This is now seen as a milestone toward a new industrial revolution as nanomanufacturing will allow significantly smaller consumption of energy, water, and resources than is associated with current industries. Nanotechnology involves creation of devices at the nanoscale based upon such materials as nanocrystals and clusters (quantum dots), nanowires, nanotubes, thin films, nanocomposites, and superlattices. The role of the nanoscale in mineralogy and geochemistry has recently received considerable attention because of its importance for a number of processes ranging from biomineralization to the formation of atmospheric nanoparticles (Banfield and Navrotsky 2002; Hochella 2002a,b). In this review, we will focus on naturally occurring nanotubes, i.e. hollow tubular structures with diameters in the range from about 1 to 1000 nm.

The current interest in nanotubes results from the discovery of carbon nanotubular structures by Iijima in 1991. Considerable research effort has subsequently been directed toward the creation of inorganic nanotubes of various chemical composition and structure. Thus, in 1992, Tenne et al. succeeded in synthesis of nanotubes and fullerene-like particles of metal disulfides MS_2 (M = Mo, W), although MoS_2 tubules had been studied earlier by Chianelli et al. (1979) for catalysis applications. To date, nanotubes have been fabricated for many chemical families, including transition metal chalcogenides (e.g., MoS_2, CdS), transition metal oxides, transition metal halides, mixed-phase systems (e.g. $Mo_{1-x}W_xS_2$), boron- and silicon-based systems, pure metals, and so forth. The synthesis, structure, morphology, and properties of inorganic nanotubes have been the subject of several

Sergey V. Krivovichev
Department of Crystallography, Faculty of Geology, St. Petersburg State University, University Emb. 7/9, St. Petersburg, Russia, e-mail: SKrivovi@mail.ru

comprehensive reviews in the recent chemistry literature (Tenne et al. 1998; Tremel 1999; Rakov 1999; Ivanovskii 2002; Patzke et al. 2002; Tenne 2002, 2003; Rao and Nath 2003; Remškar 2004; Rao and Tenne 2004). However, it has been rarely recognized that nanotubes were known to mineralogists and geoscientists for more than 40 years prior to the discovery of carbon nanotubes. The present review is intended to fill this gap and to provide an overview of nanotubes and tubular-shaped materials in mineral (sulfide-based, oxide-based and mixed sulfide–oxide-based) systems. For comparison, we shall also consider data on nanotubes prepared in mineral-related systems, which can be considered as model systems for nanotubes in nature.

Sulfide-Based Micro- and Nanotubes

The tubular morphologies in sulfide minerals have been described by many authors. Frequently, they were observed using scanning electron microscopy (SEM) and identified even on a microscale. In a popular and illustrative account, Bideaux (1970) discussed many interesting SEM observations of microcylindrical and ring-like morphologies in a number of natural sulfides, including cylindrite – $(Pb,Sn^{2+})_8Sb_4Fe_2Sn_5^{4+}S_{27}$ (see below), jamesonite – $Pb_4FeSb_6S_{14}$ (see also Ghiurca and Motiu 1986), boulangerite – $Pb_5Sb_4S_{11}$ and dadsonite – $Pb_{23}Sb_{25}S_{60}Cl$. Tubular microcrystals of acanthite (Ag_2S) were described by Dvurechenskaya et al. (1993).

Cylindrite

Cylindrite is a complex sulphosalt mineral with chemical composition $(Pb,Sn^{2+})_8Sb_4Fe_2Sn_5^{4+}S_{27}$. The mineral was first discovered by Frenzel (1893) from the Santa Cruz mine, Poopó, Bolivia, and was named for the cylindrical morphology of its crystals (Fig. 1, left). Microstructures of cylindrite were investigated in detail by Makovicky (1971, 1974) and Wang and Buseck (1992). According to Makovicky (1971, 1974) and Wang and Kuo (1991), the structure of cylindrite consists of two sulfide modules, one pseudohexagonal (H) and one pseudotetragonal (T), with chemical formulas MS_2 and MS, respectively. The T module has composition $(Pb,Sb,Sn^{2+})S$ and represents two layers of the galena (PbS) structure. The H module is an octahedral brucite-like sheet $(Sn^{4+},Fe)S_2$ similar to that observed in berndtite (SnS_2). The H and T modules are stacked along the [100] axis in the sequence ...HTHT... (Fig. 1, right). The T module has a pseudotetragonal *A*-centered subcell with $a_T = 11.73$, $b_T = 5.79$, $c_T = 5.81$ Å, $\alpha_T = 90.0$, $\beta_T = 92.38$, $\gamma_T = 93.87^\circ$.

Note that the *b* and *c* parameters are just slightly smaller than the 5.93 Å *a* parameter of the face-centered cubic unit cell of galena, due to the Sb→Pb and Sn^{2+} →Pb substitutions. The H module has a pseudohexagonal subcell which, in orthogonal *A*-centered description has dimensions: $a_H = 11.71$, $b_H = 3.67$, $c_H = 6.32$ Å, $\alpha_T = 90.0$, $\beta_T = 92.58$, $\gamma_T = 90.85^\circ$ (Makovicky 1974). The b_H parameter of

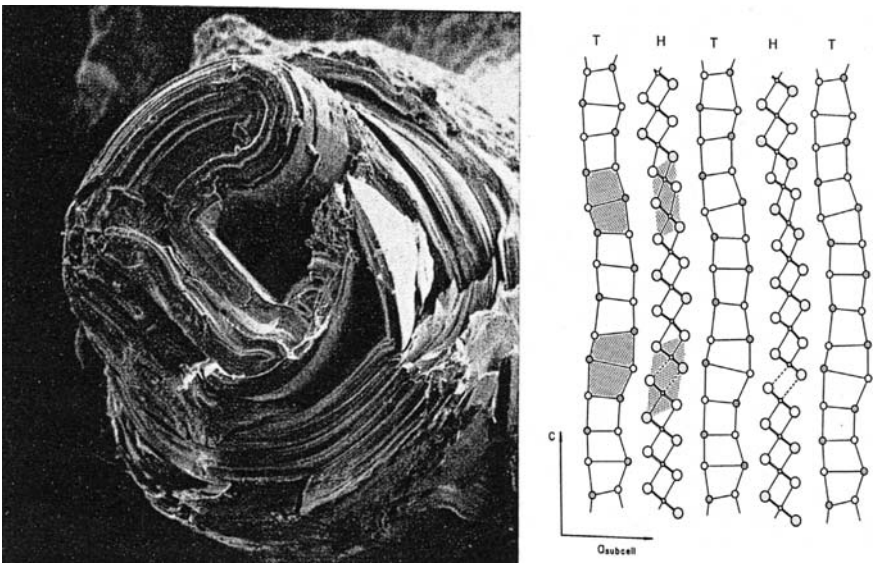

Fig. 1 *Left*: SEM photo of a tubular cylindrite aggregate. The diameter of the cylinder is about 0.5 mm. Reproduced with permission from Makovicky (1971). *Right*: Projection of the structure of cylindrite along the b axis. In the H sheets, cation and anion positions are indicated by small and large circles, respectively; in the T sheets, circles indicate cation positions. Reproduced with permission from Makovicky (1974)

cylindrite is slightly larger than the b parameter of berndtite, 3.62–3.65 Å. The mismatch is obvious between the b and c parameters of the two modules with the $\Delta b = 2.12$ and $\Delta c = 0.51$ Å. The misfit between the T and H modules permits curling of the HT double layer into a cylinder parallel to the c axis with the b axis as its tangent (the mismatch is more dramatic along the [010] direction). Wang and Kuo (1991) and Wang and Buseck (1992) examined interactions between the H and T sheets and described the structure of cylindrite as incommensurately modulated with a modulation vector **q** depending upon the curvature of the cylindrite crystals (see also Williams and Hyde 1988). It was observed that, with increasing radius of the sheet and decreasing Gaussian curvature, the crystal develops planar segments, whereas, near the core of the cylinder, the sheets may display kinking. The nature of the cylindrical morphology may vary from crystal to crystal depending upon the chemical composition. To our knowledge, there are no reports in the literature on the synthesis of cylindrite.

Oxide-Based Nanotubes

Chrysotile

Chrysotile, $Mg_3Si_2O_5(OH)_4$, is probably the most investigated natural nanotube material known so far. Its occurrence and structure have been reviewed by Wicks and

O'Hanley (1988). The first note concerning the tubular structure of chrysotile was by Pauling (1930) who suggested that the Mg-analogue of kaolinite should have a curved structure because of the misfit between the octahedral and the tetrahedral sheets. Later investigations by Noll and Kircher (1951), Bates et al. (1950a), Yada (1967, 1971), etc. confirmed this hypothesis, and the tubular structure of chrysotile fibers was demonstrated by electron diffraction and transmission electron microscopy (TEM). The structure itself was solved by Whittaker (1953, 1956a,b,c) and subsequently refined on the basis of synthetic material by Falini et al. (2002, 2004). It is based upon double layers consisting of mica-like $[Si_2O_5]$ sheets of corner-sharing SiO_4 tetrahedra and brucite-like $(MgO_2(OH)_4)$ trioctahedral sheets (Fig. 2, left). There is a misfit between the tetrahedral and octahedral sheets (usually described in terms of difference in the a_{tetr} and a_{oct} parameters specified in Fig. 2, left). This misfit results in a strain that can be relieved by curling of the double layer with the tetrahedral part on the inner surface and the octahedral part on the outer surface. As calculated by Whittaker (1955), the misfit is completely compensated at the ideal radius-of-curvature of 8.8 nm. There are several varieties of chrysotile; they differ mainly in the stacking of the double sheets and in the direction around which the sheets are rolled. Clinochrysotile and orthochrysotile are rolled around [100] but correspond to 2*M* and 2*O* polytypes, respectively. Parachrysotile is rolled around the *b* axis. There are also helical varieties of chrysotile with a helicity angle of up to 10° (e.g. Yada 1971).

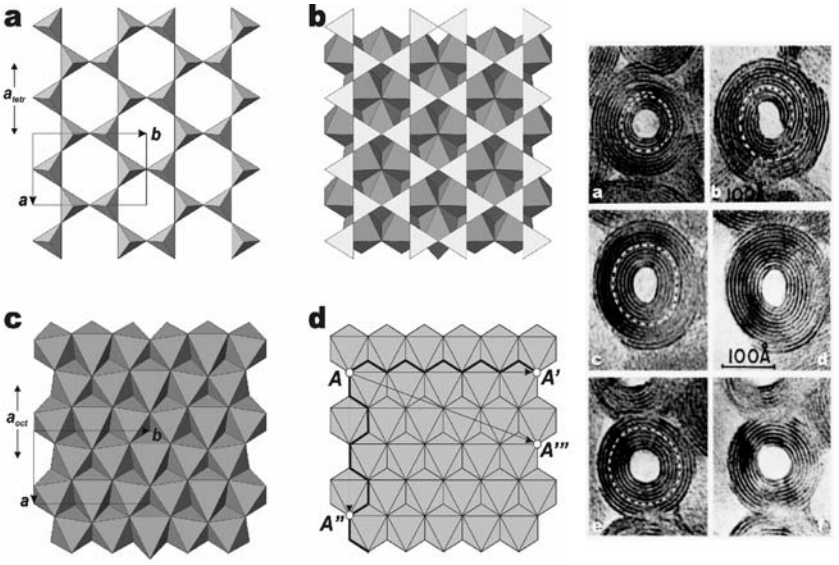

Fig. 2 *Left*: The structure of chrysotile (**b**) is based upon double layers consisting of mica-like $[Si_2O_5]$ sheets of corner-sharing SiO_4 tetrahedra (**a**) and brucite-like $(MgO_2(OH)_4)$ trioctahedral sheets (**c**). Scheme (**d**) shows directions of curling of the octahedral sheet. *Right*: Cross sections of chrysotile nanotubes with spiral **(a, b)** and concentric structures (**c–f**). Reproduced from Yada (1971)

Natural chrysotile nanotubes occur in different dimensions and morphologies. Figure 2 (right) shows both scroll and cylindrical nanotube morphologies of natural chrysotile (Yada 1971). Typical natural chrysotile nanotubes are 22–27 nm in outer diameter and 5–8 nm in inner diameter, though non-hollow morphologies are also common. Synthetic chrysotile was investigated by a number of authors (Yada and Iishi 1977; Falini et al. 2002, 2004; Korytkova et al. 2004). Falini et al. (2004) reported synthetic chrysotile nanotubes with 49 ± 1 nm outer and 7 ± 1 nm inner diameters.

Recently, Zega et al. (2004) described serpentine nanotubes from the Mighei and Murchison chondrite meteorites. The tubes are 20–230 nm in length and 2–9 nm in inner diameter (Fig. 3). Zega et al. (2004) suggested that, due to their high surface areas and hollow morphology, serpentine nanotubes could have served as containers of primordial fluids.

Chrysotile nanotubes have a high potential for nanotechnology applications. For instance, Romanov et al. (1997) used chrysotile aggregates for construction of self-assembled arrays of indium phosphide (InP) quantum wires with interesting optical properties. Chrysotile nanotubes were chosen as a matrix material because of their dielectric properties and large inter-channel separation, which prevents interaction between individual InP nanowires.

Halloysite

Halloysite, $Al_2Si_2O_5(OH)_4(H_2O)_2$, is an analogue of kaolinite, $Al_2Si_2O_5(OH)_4$, for which tubular morphology was demonstrated by Bates et al. (1950b). The structure of halloysite is closely related to that of chrysotile, and is based upon 1:1 aluminosilicate layers consisting of a dioctahedral sheet of ($AlO_2(OH)_4$) octahedra and a mica-like silicate [Si_2O_5] sheet of corner-sharing SiO_4 tetrahedra (Mitra and Bhattacherjee 1975; Giese 1988). The tubular morphology of halloysite was explained by Bates et al. (1950b) in terms of misfit between the tetrahedral and octahedral sheets, analogous to that present in chrysotile. In contrast to chrysotile, the stacking order and orientation of the sheets are more random (Mitra and Bhattacherjee 1975). In its hydrated state, halloysite consists of tubes with internal diameter of $\sim$18 nm, thin walls of 5–6 nm thickness, and lengths of up to 20 μm. High surface area, pore dimensions and relatively low price make

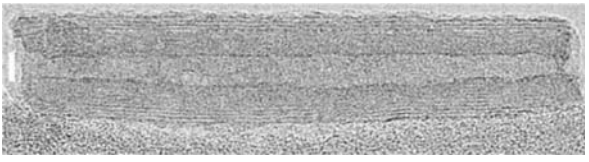

Fig. 3 HRTEM image of hollow multiwall serpentine nanotube from the Mighei CM chondrite. Reproduced with permission from Zega et al. (2004)

halloysite a promising material for preparation of molecular nanowires (Luca and Thomson 2000) and for the entrapment and release of active agents in microencapsulation applications (Price et al. 2001). Halloysite also has been described as a potential vessel for nanoscale reactions (Antill 2003).

Imogolite

Imogolite, $Al_2SiO_3(OH)_4$, was first described in soils derived from glassy volcanic ash in Japan (Yoshinaga and Aomine 1962) and later was identified as an important constituent of the B horizon of Podzol soils (see Gustafsson et al. 1999 and references therein). The status of imogolite as a separate paracrystalline mineral species was under discussion and was finally established in 1987 (Bayliss (1987). Synthesis of imogolite was reported by Farmer et al. (1977) and Wada (1987) from solutions containing hydroxyaluminium cations and orthosilicic acid. Wada and Wada (1982) prepared Ge-for-Si-substituted imogolite.

The structure of the mineral was reported by Cradwick et al. (1972) on the basis of electron-diffraction studies as containing aluminosilicate tubes with external diameter 2.1 nm. The tube walls consist of a dioctahedral gibbsite-like $Al(OH)_3$ sheet with $SiO_3(OH)$ tetrahedra attached to the sheet around an empty octahedral site (Fig. 4). The O–O distance in an ideal SiO_4 tetrahedron is smaller than the O–O distance in an AlO_6 octahedron which allows the curling of the gibbsite sheet in order to accommodate $SiO_3(OH)$ tetrahedra attached to its inner surface (Fig. 4). The structural connectivity and Q^0 character of the Si tetrahedra was confirmed by nuclear magnetic resonance (NMR) spectroscopy (Goodman et al. 1985).

In the structure of gibbsite, the $Al(OH)_3$ sheets have lateral dimensions $a_g \times b_g = 8.6 \times 5.1$ Å^2. In imogolite, the sheets are rolled around a_g as the tube axis such

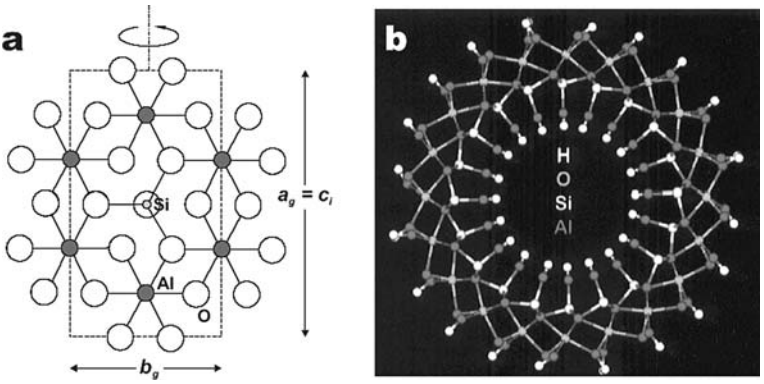

Fig. 4 Model of the aluminosilicate sheet that constitute imogolite nanotube (a_g, b_g – gibbsite unit cell parameters; c_i – c parameter of imogolite) (**a**); cross-section of imogolite nanotube (**b**; reproduced with permission from Pohl et al. (1996))

that the imogolite nanotubes are periodic with a *c* axis repeat distance of 8.4 Å (Wada 1987). Cradwick et al. (1972) suggested that a model with 10 gibbsite unit cells around the circumference is the most likely structure for imogolite nanotubes. On the basis of computer simulation studies and comparison of their results with N_2 and CH_4 adsorption isotherms, Pohl et al. (1996) concluded that 10-unit and 12-unit structures are more likely for natural and synthetic imogolite, respectively. Farmer and Fraser (1979), on the other hand, concluded that the natural material has a 12-unit structure, whereas synthetic material has a 14-unit structure. Replacement of $SiO_3(OH)$ tetrahedra by larger $GeO_3(OH)$ tetrahedra results in a 18-unit tube structure (Wada and Wada 1982). Note that, in any case, the tube found in imogolite has an achiral structure. In condensed material, imogolite nanotubes form close-packed arrangements with center-to-center separations between 2.27 and 2.62 nm. The energy of imogolite tubes versus their diameter was investigated by Tamura and Kawamura (2002) using molecular-dynamics simulations. These authors found that the total energy of imogolite has a minimum around a diameter of 2.6–2.9 nm, which corresponds to the 14- to 16-unit structure. The internal diameter of imogolite nanotubes varies from 0.6 to 1.0 nm depending upon composition (Ackerman et al. 1993; Bursill et al. 2000). Imamura et al. (1993) concluded that natural imogolite has a pore diameter of about 0.65 nm (more consistent with the 10-unit structure model of Cradwick et al. (1972)) since their samples refused adsorption of 1,3,5-triisopropylbenzene (diameter of 0.85 nm).

In general, imogolite has received considerable attention for its excellent adsorption properties that result from its large surface area. Thus, imogolite plays an important role in controlling water quality in forest soils by adsorbing anions such as AsO_4^{3-} and PO_4^{3-} (Gustafsson et al. 1998; Gustafsson 2001). Imogolite may also be a possible sorbent for other contaminants and nutrients. Johnson et al. (1988) were able to intercalate imogolite as a regular monolayer in the interlayer space of smectite clays. These intercalates, known as tubular silicate-layered silicate (TSLS) nanocomposites, may have important applications in selective absorption and catalysis (Werpy et al. 1989; Johnson and Pinnavaia (1991). Imogolite has also been suggested for use as a shape-selective catalyst (Imamura et al. 1993). Imogolite nanotubes are very rigid, which makes an acidic dispersion of imogolite an ideal lyotropic liquid-crystal system (Kajiwara et al. 1986a,b; Donkai et al. 1993). It is of interest that imogolite liquid-crystal systems contain a variety of mesostructures formed by self-assembly of imogolite nanotubes (Kajiwara et al. 1986a; Gabriel and Davidson 2003).

Mixed Sulfide–Oxide-Based Nanotubes

Tochilinite

Tochilinite, a complex layered metal sulfide/hydroxide composite mineral with composition $6FeS\bullet5(Mg,Fe)(OH)_2$, was first described by Jambor (1969) and Clark (1970) as a fibrous iron sulfide that contain Mg and H_2O. Later, this mineral

was found by S.P. Molotkov in Nizhnemamonovskoe mineral deposit, Voronezh district, Russia, and described as a new mineral species by Organova et al. (1971). On the basis of analytical electron microscopy (AEM) and high-resolution transmission electron microscopy (HRTEM) studies, Mackinnon and Zolensky (1984) identified tochilinite and its intergrowths with serpentine as important phases in carbonaceous meteorites (cf. Zolensky 1984; Tomeoka and Buseck 1985 and references therein). The cylindrical morphology of terrestrial tochilinite was described by Jambor (1976) as resembling a rolled-up newspaper, whereas cylindrical microstructures in meteoritic samples were reported by Barber et al. (1983). Zolensky and Mackinnon (1986) reported hollow tubes of tochilinite from Cornwall, Pensylvania. The individual cylinders occur up to 1 cm in length and up to 10–30 μm in outer diameter. The thickness of the cylinder walls was described as 45–75 nm (Fig. 5a).

Synthetic tochilinite nanotubes prepared by hydrothermal treatment of a mixture of Fe^{3+} sulfide gels with Mg/Al hydroxide gels at 200°C were reported by Kakos et al. (1994) (Fig. 5b). Synthetic nanotubes are 200–300 nm in length and 70 nm in outer diameter with a wall thickness of about 20–30 nm. As in the case of cylindrite, rolling of tochilinite sheets into cylinders may be explained as originating from the composite character of the mineral structure. The structure of tochilinite was investigated by Organova et al. (1973, 1974a,b, 1988) and Organova (1989) on platelike varieties. It consists of pseudotetragonal FeS mackinawite-like sulfide T sheets of edge-sharing FeS_4 tetrahedra (Fig. 6a) and brucite-like pseudohexagonal H sheets $(Mg,Fe)(OH)_2$ of edge-sharing $(Mg,Fe)(OH)_6$ octahedra (Fig. 6b). The sheets are stacked along [001] in the sequence …HTHT… (Fig. 6c).

For an equant variety of tochilinite, Organova et al. (1973) found a pseudomonoclinic unit cell, space group $C1$, $a = 5.37$, $b = 15.65$, $c = 10.72$ Å, $\alpha = 90$, $\beta = 95$, $\gamma = 90°$. The T sheet has a pseudotetragonal C-centered subcell with $a_T \sim b_T \sim$ 5.2–5.4 Å oriented so that $a = a_T$, $b = 3b_T$. The pseudohexagonal H *sub*cell has a_H close to that observed in brucite, 3.14 Å, which yields a pseudo-orthorhombic cell

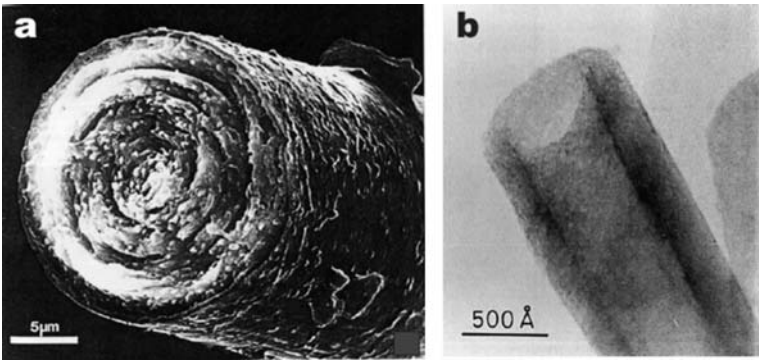

Fig. 5 SEM image of a natural tochilinite cylinder from Cornwall (**a**; reproduced with permission from Zolensky and Mackinnon 1986); HRTEM image of a synthetic tochilinite nanotube (**b**; reproduced with permission from Kakos et al. (1994))

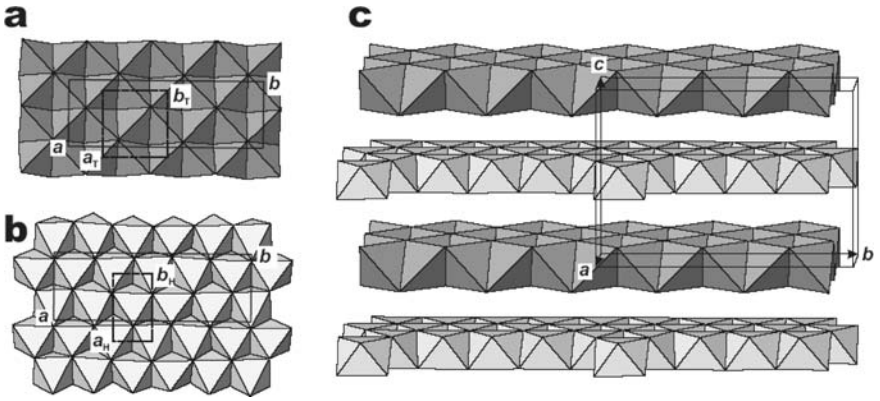

Fig. 6 Pseudotetragonal FeS mackinawite-like sulfide T sheets of edge-sharing FeS_4 tetrahedra **(a)** and brucite-like pseudohexagonal H sheets $(Mg,Fe)(OH)_2$ of edge-sharing $(Mg,Fe)(OH)_6$ octahedra **(b)**. The sheets are stacked along [001] in the sequence …HTHT… **(c)**

with parameters $a'_H = 5.43$, $b'_H = 3.14$ Å. This subcell is oriented in the tochilinite unit cell such that $a \sim a'_H \sim 5.43$, $b \sim 5b'_H$. Thus, the H and T sheets are related by $a_T = a'_H$; $3b_T = 5b'_H$.

Misfit in the [010] direction is stronger than that along [100] and permits curling of tochilinite crystals around [100] in order to accommodate mismatch along the *b* axis.

Note that mismatch and formation of either plate-like or nanotube microstructures depends upon the chemical composition of the tochilinite crystals in both natural and synthetic tochilinite (Organova 1989; Kakos et al. 1994).

As mentioned above, one of the particularly useful properties of nanomaterials is their large surface area, which make them excellent candidates for use as adsorbents. Lidzey (1995) patented a tochilinite-like synthetic compound as an inexpensive material for removal of heavy metal cations from effluent solutions. Following this idea, Watson and Ellwood (2003) proposed the use of tochilinite as an adsorbent for actinides in the Enhanced Actinide Removal Plant (EARP) attached to the Sellafield reprocessing plant of British Nuclear Fuels (BNFL), Cumbria, UK.

Formation Mechanisms

Perhaps the most important mechanism of formation of nanotubes in minerals is by misfit rolling. This mechanism functions when a structure contains at least two chemically and structurally different blocks (i.e. when the mineral has a composite structure). Mismatch in the unit-cell parameters between the two blocks results in a strain that can be relieved by curling of the specific structural layers. The structural blocks can be both two-dimensional (as in the case of cylindrite, tochilinite, serpentine-group minerals and halloysite) or, two- and zero-dimensional

(imogolite). It is the structural mismatch between the blocks, rather than their dimensionality, which plays an essential role in nanotube formation.

However, there are many cases when rolling layers into tubes cannot be explained on the basis of a misfit mechanism. The classical example is that of carbon nanotubes, for which there is no obvious composite structure. Another example is natural and synthetic molybdenite nano- and microtubes. Seifert et al. (2002) considered the stability of MS_2 nanotubes (M = Mo, W) in terms of the interplay between the strain energy in the tubes due to the bending of the layers and the energy due to unsaturated (dangling) bonds in layer tapes. These authors demonstrated that, for a small number of atoms, flat structures are more favorable than tubular. However, with increasing width of the tape, tubular structure become more stable. Thus, for molybdenite, the **A**(36,36) armchair nanotube with a diameter of 6.2 nm is energetically more favorable than a corresponding tape. The presence of unsaturated bonds on the edges of tapes is therefore a major factor driving nanotube formation. As demonstrated by Seifert et al. (2002), MWNTs have an additional stabilization force that comes from the van der Waals interactions between the adjacent layers. In general, this additional stabilization may explain the prevalence of MWNTs over SWNTs.

Acknowledgements I thank Russian Federation Ministry of Science and Education for financial support through the RNP grant (2.1.1.3077) and 'Molecular geochemistry and biogeochemistry' project of the program 'Innovative education environment in a classical University'.

References

Ackerman WC, Smith DM, Huling JC, Kim Y-W, Bailey JK, Brinker CJ (1993) Gas/vapor adsorption in imogolite: a microporous tubular aluminosilicate. Langmuir 9:1051–1057

Antill SJ (2003) Halloysite: a low-cost alternative nanotube. Aust J Chem 56:723

Banfield J, Navrotsky A (eds) (2002) Nanoparticles and the Environment. Rev Miner Geochem, vol 44. Mineralogical Society of America, Washington, DC

Barber DJ, Bourdillon A, Freeman LA (1983) Fe–Ni–S–O layer phase in C2M carbonaceous chondrite – a hydrous sulfide? Nature 305:295–297

Bates TF, Sand LB, Mink JF (1950a) Tubular crystals of chrysotile asbestos. Science 3:512

Bates TF, Hildebrand FA, Swineford A (1950b) Morphology and structure of endellite and halloysite. Am Mineral 35:463–484

Bayliss P (1987) Mineral nomenclature: imogolite. Mineral Mag 51:327

Bideaux RA (1970) Mineral rings and cylinders. Mineral Rec 1:105–112

Bursill LA, Peng JL, Bourgeois LN (2000) Imogolite. An aluminosilicate nanotube material. Philos Mag A 80:105–117

Chianelli RR, Prestridge E, Pecorano T, DeNeufville JP (1979) Molybdenum disulfide in the poorly crystalline "rag" structure. Science 203:1105–1007

Clark AH (1970) A probable second occurence of Jambor's "fibrous iron sulfide". Am Mineral 55:283–284

Cradwick PDG, Farmer VC, Russell JD, Masson CR, Wada K, Yoshinaga N (1972) Imogolite, a hydrated aluminum silicate of tubular structure. Nat Phys Sci 240:187–189

Donkai N, Hoshino H, Kajiwara K, Miyamoto T (1993) Lyotropic mesophase of imogolite. 3. Observation of liquid crystal structure by scanning electron and novel polarized optical microscopy. Makromol Chem 194:559–580

Dvurechenskaya SS, Boyarskaya RV, Amosov RA (1993) Tubular and fibrous acanthite crystals. Miner Mag 15:90–94

Falini G, Foresti E, Lesci G, Roveri N (2002) Structural and morphological characterization of synthetic chrysotile single crystals. Chem Commun 2002:1512–1513

Falini G, Foresti E, Gazzano M, Gualtieri AF, Leoni M, Lesci IG, Roveri N (2004) Tubular-shaped stoichiometric chrysotile nanocrystals. Chem Eur J 10:3043–3049

Farmer VC, Fraser AR (1979) Synthetic imogolite, a tubular silicate. Dev Sedimentol 27:547–553

Farmer VC, Fraser AR, Tait JM (1977) Synthesis of imogolite: a tubular aluminum silicate polymer. J Chem Soc Chem Commun 1977:462–463

Frenzel A (1893) Ueber den Kylindrit. Neues Jahrb Miner Geol P 2:125–128

Gabriel J-CP, Davidson P (2003) Mineral liquid crystals from self-assembly of anisotropic nanosystems. Top Curr Chem 226:119–172

Ghiurca V, Motiu A (1986) Curved jamesonite crystals from Romania. Mineral Rec 17:375–376

Giese RFJ (1988) Kaolin minerals: structures and stabilities. Rev Mineral 19:29–66

Goodman BA, Russell JD, Montez B, Oldfield E, Kirkpatrick RJ (1985) Structural studies of imogolite and allophanes by aluminum-27 and silicon-29 nuclear magnetic resonance spectroscopy. Phys Chem Miner 12:342–346

Gustafsson JP (2001) The surface chemistry of imogolite. Clay Clay Miner 49:73–80

Gustafsson JP, Karltun E, Bhattacharya P (1998) Allophane and imogolite in Swedish soils or why small, previously unknown, fibers influence the water quality in forests. Research Report TRITA-AMI 3046. Division of Land and Water Resources, Department of Civil and Environmental Engineering, Royal Institute of Technology, Stockholm, Sweden

Gustafsson JP, Bhattacharya P, Karltun E (1999) Mineralogy of poorly crystalline aluminum phases in the B horizon of podzols in southern Sweden. Appl Geochem 14:707–718

Hochella MF Jr (2002a) There's plenty of room at the bottom: nanoscience in geochemistry. Geochim Cosmochim Ac 66:735–743

Hochella MF Jr (2002b) Nanoscience and technology: the next revolution in the Earth sciences. Earth Planet Sc Lett 203:593–605

Iijima S (1991) Helical microtubules of graphitic carbon. Nature 354:56–58

Imamura S, Hayashi Y, Kajiwara K, Hoshino H, Kaito C (1993) Imogolite: a possible new type of shape-selective catalyst. Ind Eng Chem Res 32:600–603

Ivanovskii AL (2002) Non-carbon nanotubes: synthesis and simulation. Russ Chem Rev 71: 175–194

Jambor JL (1969) Coalingite from the Muskox intrusion, Northwest Territories. Am Mineral 54:437–447

Jambor JL (1976) New occurrences of the hybrid sulfide tochilinite. Geol Surv Can Paper 76-1B:65–69

Johnson LM, Pinnavaia TJ (1991) Hydrolysis of (γ-aminopropyl)triethoxysilane-silylated imogolite and formation of a silylated tubular silicate-layered silicate nanocomposite. Langmuir 7:2636–2641

Johnson ID, Werpy TA, Pinnavaia TJ (1988) Tubular silicate-layered silicate intercalation compounds: a new family of pillared clays. J Am Chem Soc 110:8545–8547

Kajiwara K, Donkai N, Hiragi Y, Inagaki H (1986a) Lyotropic mesophase of imogolite. 1. Effect of polydispersity on phase diagram. Makromol Chem 187:2883–2893

Kajiwara K, Donkai N, Fujiyoshi Y, Inagaki H (1986b) Lyotropic mesophase of imogolite. Microscopic observation of imogolite mesophase. Makromol Chem 187:2895–2907

Kakos GA, Turney TW, Williams TB (1994) Synthesis and structure of tochilinite: a layered metal hydroxide/sulfide composite. J Solid State Chem 108:102–111

Korytkova EN, Maslov AV, Pivovarova LN, Drozdova IA, Gusarov VV (2004) Formation of $Mg_3Si_2O_5(OH)_4$ nanotubes under hydrothermal conditions. Glass Phys Chem 30:51–55

Lidzey RG (1995) Separation of heavy metals from aqueous media. United States Patent Office, United States of America. Bio-Separation Limited, Middlesex, UK. US Patent 5,441,648
Luca V, Thomson S (2000) Intercalation and polymerization of aniline within a tubular aluminosilicate. J Mater Chem 10:2121–2126
Mackinnon IDR, Zolensky ME (1984) Proposed structures for poorly characterized phases in C2M carbonaceous chondrite meteorites. Nature 309:240–242
Makovicky E (1971) Microstructure of cylindrite. Neues Jb Miner Monat 1971:403–413
Makovicky E (1974) Mineralogical data on cylindrite and incaite. Neues Jb Miner Monat 1974:235–256
Mitra GB, Bhattacherjee S (1975) The structure of halloysite. Acta Crystallogr B 31:2851–2857
Noll W, Kircher H (1951) Ueber die Morphologie von Asbesten und ihren Zusammenhang mit der Kristallstruktur. Neues Jb Miner Monat 10:219–240
Organova NI (1989) Crystal chemistry of incommensurate and modulated mixed-layer minerals. Nauka, Moscow, p 143 (in Russian)
Organova NI, Genkin AD, Drits VA, Molotkov SP, Kuz'mina OV, Dmitrik AL (1971) Tochilinite, a new sulfide–hydroxide of iron and magnesium. Zapiski VMO 100:477–487
Organova NI, Drits VA, Dmitrik AL (1973) Structural study of tochilinite. I. Isometric variety. Sov Phys Crystallogr 17:761–767
Organova NI, Drits VA, Dmitrik AL (1974a) Structural study of tochilinite. II. Needle-shaped variety. Unusual diffraction patterns. Sov Phys Crystallogr 18:606–609
Organova NI, Drits VA, Dmitrik AL (1974b) Selected area electron diffraction study of a type II valleriite-like mineral. Am Mineral 59:190–200
Organova NI, Gorshkov AI, Dikov YuP, Kul'bachinskii VA, Laputina IP, Sivtsov AV, Sluzhenikin SF, Ponomarenko AI (1988) New data for tochilinite. Izv AN SSSR Geol 6:84–98
Patzke GR, Krumeich F, Nesper R (2002) Oxidic nanotubes and nanorods – anisotropic modules for a future nanotechnology. Angew Chem Int Edit 41:2446–2461
Pauling L (1930) The structure of chlorites. Proc Natl Acad Sci USA 16:578–582
Pohl PI, Faulon J-L, Smith DM (1996) Pore structure of imogolite: computer models. Langmuir 12:4463–4468
Price RR, Gaber BP, Lvov Y (2001) In-vitro release characteristics of tetracycline HCl, khellin and nicotinamide adenine dineculeotide from halloysite; a cylindrical mineral. J Microencapsul 6:713–722
Rakov EG (1999) Nanotubes of inorganic substances. Russ J Inorg Chem 44:1736–1748
Rao CNR, Nath M (2003) Inorganic nanotubes. Dalton Trans 2003:1–24
Rao CNR, Tenne R (2004) Inorganic nanotubes. Philos T Roy Soc A 362:2099–2125
Remškar M (2004) Inorganic nanotubes. Adv Mater 16:1497–1504
Romanov SG, Sotomayor Torres CM, Yates HM, Pemble ME, Butko V, Tretijakov V (1997) Optical properties of self-assembled arrays of InP quantum wires confined in nanotubes of chrysotile asbestos. J Appl Phys 82:380–385
Seifert G, Köhler T, Tenne R (2002) Stability of metal chalcogenide nanotubes. J Phys Chem B 106:2497–2501
Tamura K, Kawamura K (2002) Molecular dynamics modeling of tubular aluminum silicate: imogolite. J Phys Chem B 106:271-278.
Tenne R (2002) Inorganic nanotubes and fullerene-like materials. Chem Eur J 8:5297–5304
Tenne R (2003) Advances in the synthesis of inorganic nanotubes and fullerene-like nanoparticles. Angew Chem Int Edit 42:5124–5132
Tenne R, Homyonfer M, Feldman Y (1998) Nanoparticles of layered compounds with hollow cage structures (inorganic fullerene-like structures). Chem Mater 10:3225–3238
Tenne R, Margulis L, Genut M, Hodes G (1992) Polyhedral and cylindrical structures of tungsten disulphide. Nature 360:444–446
Tomeoka K, Buseck PR (1985) Indicators of aqueous alterations in CM carbonaceous chondrites: microtextures of a layered mineral containing Fe, S, O and Ni. Geochim Cosmochim Ac 49:2149–2164
Tremel W (1999) Inorganic nanotubes. Angew Chem Int Edit 38:2175–2179

Wada S (1987) Imogolite synthesis at 25°C. Clay Clay Miner 35:379–384
Wada S, Wada K (1982) Effects of substitution of germanium for silicon in imogolite. Clay Clay Miner 30:123–128
Wang S, Buseck PR (1992) Cylindrite: the relation between its cylindrical shape and modulated structure. Am Mineral 77:758–764
Wang S, Kuo KH (1991) Crystal lattices and crystal chemistry of cylindrite and franckeite. Acta Crystallogr A 47:381–392
Watson JHP, Ellwood DC (2003) The removal of the pertechnetate ion and actinides from radioactive waste streams at Hanford, Washington, USA and Sellafield, Cumbria, UK: the role of iron-sulfide-containing adsorbent materials. Nucl Eng Des 226:375–385
Werpy TA, Michot LJ, Pinnavaia TJ (1989) Adsorption properties of a tubular silicate – layered silicate intercalation complex formed from imogolite and montmorillonite. Clay Res 8:47–52
Whittaker EJW (1953) The structure of chrysotile. Acta Crystallogr 6:747–748
Whittaker EJW (1955) A classification of cylindrical lattices. Acta Crystallogr 8:571–574
Whittaker EJW (1956a) Structure of chrysotile. II. Clinochrysotile. Acta Crystallogr 9:855–862
Whittaker EJW (1956b) Structure of chrysotile. III. Orthochrysotile. Acta Crystallogr 9:862–864
Whittaker EJW (1956c) Structure of chrysotile. IV. Parachrysotile. Acta Crystallogr 9:865–867
Wicks FJ, O'Hanley DS (1988) Serpentine minerals: structure and petrology. Rev Mineral 19: 91–159
Williams TD, Hyde BG (1988) Electron microscopy of cylindrite and franckeite. Phys Chem Miner 15:521–544
Yada K (1967) Study of the chrysotil asbestos by high resolution transmission electron microscopy. Acta Crystallogr 23:704–707
Yada K (1971) Study of the microstructure of chrysotil asbestos by high resolution transmission electron microscopy. Acta Crystallogr A 27:659–664
Yada K, Iishi K (1977) Growth and microstructure of synthetic chrysotile. Am Mineral 62:958–965
Yoshinaga N, Aomine S (1962) Allophane in some Ando soils. Soil Sci Plant Nutr 8(2):6–13
Zega TJ, Garvie LAJ, Dodony I, Buseck PR (2004) Serpentine nanotubes in the Mighei CM chondrite. Earth Planet Sc Lett 223:141–146
Zolensky ME (1984) Hydrothermal alteration of CM carbonaceous chondrites: implications of the identification of tochilinite as one type of meteoritic PCP. Meteoritics 19:346–347
Zolensky ME, Mackinnon IDR (1986) Microstructures of cylindrical tochilinites. Am Mineral 71:1201–1209

Natural and Synthetic Minerals – Matrices (Forms) for Actinide Waste Immobilization

Tatiana Livshits and Sergey Yudintsev

Introduction

The reprocessing of irradiated fuel of nuclear power plants results in the formation of a great amount of radioactive wastes, including high-level radioactive wastes (HLW). Selection of suitable immobilizing materials is a key part of safe HLW management in the nuclear fuel cycle. The search for confinement matrices began in the 1950s with study of various glassy and crystalline materials containing silicates, phosphates, and titanates (Ewing and Lutze 1988). Only borosilicate and alumophosphate glasses are used for this purpose on an industrial scale (Hench et al. 1984; Vashman et al. 1997). These glasses are not capable of incorporating sufficient amounts of actinides (particularly, Pu) and have low resistance to chemical corrosion by water (Matzke and van Geel 1996; Laverov et al. 1997). Interaction of the vitreous matrices with underground waters will result in the formation of colloidal particles (Glass as a waste form... 1996), which can carry actinides for very long distances. The glasses also easily crystallize on aging (Vashman et al. 1997), which significantly decreases stability of the waste forms due to appearance of various soluble phases, such as alkali and alkaline-earth silicates, phosphates, and molybdates.

For efficient management of the high level radioactive wastes, they should be separated into fractions (Actinide... 1999). One of them contains tens of weight percents of actinides, zirconium, and lanthanides. U, Np, Pu, and Am dominate among the actinides, among the lanthanides light REEs (Nd, Ce, La, and Pr) are the most significant. One more group of actinide wastes is produced during conversion of weapons plutonium into nuclear fuel. Actinide-rich waste forms alternative to glasses are the crystalline matrices (Ringwood 1985; Vance et al. 1995).

Tatiana Livshits
Institute of Geology of Ore Deposits, Moscow, Russia

Sergey Yudintsev
Institute of Geology of Ore Deposits, Moscow, Russia, e-mail: syud@igem.ru

Various host phases have been proposed, differing in their capability for actinide incorporation, as well as in resistance to water attack and radiation damages (Ewing and Lutze 1988; Hench et al. 1984; Laverov et al. 1997; Ringwood 1985; Vance et al. 1995; Fielding and White 1987; Ebbinghaus et al. 1998; Wang et al. 1999; Begg et al. 1998). The pyrochlore $(Ca, Gd, U, Pu, Hf)_2T_2O_7$ was developed in the USA for immobilization of excess Pu (Ebbinghaus et al. 1998). Zircon, zirconolite, perovskite, Y–Al garnet, britholite, monazite have been proposed for immobilization of Pu-bearing wastes. Synthetic materials for immobilization of radioactive wastes have been studied for about 15 years at the Institute of Geology of Ore Deposits, Russian Academy of Sciences. In this chapter we have summarized briefly some of the results obtained.

From a structural-chemical perspective, host phases stable upon wide variations of waste compositions are preferable. Such phases can be used for immobilization of excess plutonium or more complex wastes, i.e. actinide-Zr-REE fraction of HLW, actinides, long-lived fission products (^{93}Zr, ^{99}Tc, ^{126}Sn) and so on. The search for HLW forms can be optimized by preliminary analysis of the crystal structures of promising phases. It allows reducing amount of potential compounds, which simplifies further experimental examination of the selected materials. The efficiency of such approach was demonstrated for titanates and aluminates with zirconolite and perovskite structures (Fielding and White 1987). We have applied this approach for matrices with pyrochlore- and garnet-type structures. These results helped us to select the phases with the highest capacity to incorporate actinides. Data on the irradiation behavior of natural minerals of britholite group are also discussed in this communication.

Conditions of Stability of the Pyrochlore Structure

The structural-chemical features of the pyrochlore-type phases are interrelated. In addition to the general condition of charge balance, correspondence between cation sizes in the two sites is a very important requirement for stability of the pyrochlore structure. Geometrical analysis shows that the $(A^{3+})_2(B^{4+})_2O_7$ phases crystallize in the pyrochlore structural type if the ratio $(R_A + R_O) : (R_B + R_O)$ is between 1.10 and 1.24 (Wang et al. 1999). R_A and R_B denote the radii of ions in the "A" and "B" sites, and R_O is the radius of the oxygen anion. A change in the ratio beyond this interval leads to destabilization of the pyrochlore structure and the formation of phases with other crystal structures. On the basis of these data, we can determine elements in the "A" site with coordination number, CN = 8 (including actinides) that can associate with various cations in the "B" site with CN = 6 to form a $(A^{3+})_2(B^{4+})_2O_7$ phase with the pyrochlore structure. So, for formation of titanate pyrochlores ($[B]^{VI} = Ti^{4+}$, $R_{VI} = 0.605\ \Delta$), cations in the "A" site should have radii between 0.8 and 1.0 Δ, while larger cations with radii from 0.9 to 1.2 Δ are necessary to stabilize the zirconates ($R_{VI} = 0.72\ \Delta$).

Pyrochlore-Type Phases with REEs and Actinides

Actinides (except for Th, which has a valence of +4) can occur in crystal phases in various oxidation states. Under common conditions of HLW forms synthesis (1300–1500°C in Ar, Ar + H_2, or air atmospheres), the actinide cations (An) have charges of +3 (Am, Cm) or +4 (U, Np). Plutonium occurs as Pu^{4+} (air-atmosphere synthesis), Pu^{3+} (reducing conditions), or in both forms simultaneously. Similar behavior is typical of Ce (Begg et al. 1998). However, Pu is more stable in tetravalent form, whereas Ce is more stable as trivalent ion. We estimated stabilities of $^{VIII}(An^{3+})_2\,^{VI}(B^{4+})_2O_7$ and $^{VIII}(CaAn^{4+})^{VI}(B^{4+})_2O_7$ pyrochlores, where trivalent and tetravalent actinides occupy all or half of the "A" sites with CN = 8. The ionic radii of Pu^{3+}, Am^{3+}, and Cm^{3+} with CN = 8 are 1.08–1.10 Δ and are close to the radii of the Nd^{3+}, Pm^{3+}, and Sm^{3+} cations (Shannon 1976). Thus, we can expect that the conditions of stability of the pyrochlore structure for the An phases and the REE compounds with same cations in the site with CN = 6 are similar. For $(REE^{3+})_2(B^{4+})_2O_7$ phases the VI-coordinated sites theoretically can be occupied by tetravalent cations of elements from the IV group of the Periodic Table with radii from 0.4 Δ (Si^{4+}) to 0.78 Δ (Pb^{4+}). The pyrochlore structure is not stable for the end members of this series. The optimal radius of VI-coordinated cation is 0.65–0.69 Δ. Therefore, the Sn^{4+} cation with radii within this interval forms the pyrochlore phases with all REEs, from La to Lu (McGauley 1980).

A decrease (or increase) in the radius of the VI-coordinated cation should be accompanied by corresponding changes in the radius of the VIII-coordinated cation. For example, among titanates ($Ti^{4+}{}_{VI}$ radius = 0.605 Δ), the pyrochlore-type structure is typical of phases of medium and heavy REEs (from Sm to Lu) with relatively small ionic radii. The Ge^{4+} cation has a smaller radius (0.53 Δ). As a result, germanates with the pyrochlore structure are formed with small lanthanides (from Gd to Lu) and only at very high pressure of 65 kbar. REE silicates with pyrochlore structure are not stable, because of the too small radius of the Si^{4+} (0.40 Δ). Silicates with this structure were synthesized at a pressure of 120 kbar for In and Sc, which have smaller ionic radii than HREEs. Similarly, an increase in the radius of the cation occupying the octahedral site also affects the structure stability. For example, only compounds of the light lanthanides (from La to Gd) with the largest ionic radii among the REEs form hafnates and zirconates with pyrochlore structure (the radii of Zr^{4+} and Hf^{4+} are 0.72 Δ and 0.71 Δ). Three rare-earth elements (Gd, Sm, and Nd) form phases both with pyrochlore or fluorite structures (Subramanian et al. 1983). The latter structure is a disordered high-temperature variety. The phase boundaries between these varieties are located at 1600°C for Gd zirconate, at 2100°C for Sm zirconate, and at 2300°C for Nd zirconate. The REE plumbates have a fluorite-type structure, where REE^{3+} and Pb^{4+} occupy the sites with CN = 8. This is related to the large radius of Pb^{4+} (0.78 Δ), which precludes formation of plumbates with pyrochlore structure.

Thus, radius of the "B" cation in the REE pyrochlores of $REE_2B_2O_7$ type can vary from 0.605 Δ (Ti^{4+}) to 0.72 Δ (Zr^{4+}). The results obtained for the REE pyrochlores allow us to estimate the phase stability of trivalent actinides. On the basis

of the ionic radii of actinides, we can predict the stability of pyrochlore-type phases with Cm, Am, and Pu. Unlike Cm^{3+}, the Pu^{3+} and Am^{3+} titanates have monoclinic symmetry as light REE titanates. This is related to their larger ionic radii than is necessary for the stability of the pyrochlore structure. However, regardless of the instability of $Pu_2Ti_2O_7$ and $Am_2Ti_2O_7$ pyrochlores, titanate pyrochlores with significant amounts of Pu and Am were synthesized (Shoup and Bambergher 1997). They are the solid solutions where lanthanide cations with smaller radii stabilize the pyrochlore structure. It was found that pyrochlore based on $Gd_2Ti_2O_7$ can include 16 mol % $Pu_2Ti_2O_7$. The proportion of the $Pu_2Ti_2O_7$ end member increases with decreasing radius of the rare-earth elements up to 22 mol % in pyrochlore based on $Er_2Ti_2O_7$ and up to 33 mol % in the $Lu_2Ti_2O_7$ pyrochlore. The proportion of Am end member in the $(Er, Am)_2Ti_2O_7$ pyrochlore solid solution is still higher (61 mol %). The same result can also be obtained by replacement of Ti in octahedral sites by larger cations of Sn, Hf, and Zr, which stabilize the pyrochlore structure of the $[(Pu, Am)_2(Ti, Sn, Hf, Zr)_2O_7]$ phase.

Wastes from reprocessing of irradiated nuclear fuel are dominated by elements with stable tetravalent cations (U, Np, Pu), only a small amount of which can be incorporated in $A_2B_2O_7$ pyrochlores. Because of a charge difference, substitution of actinides for REEs in the lattice increases the amount of vacancies by $4REE^{3+} = 3U^{4+}$ + [vacancy], i.e., increases the deficiency of the structure. The scale of this substitution is relatively low. According to our data, Y-Ti pyrochlore can contain up to 12 wt % UO_2, i.e., 0.2 U atoms per formula. The charge balance of the structure can be also maintained by replacement of two REE cations by pair of divalent ion (e.g., Ca^{2+}) and tetravalent actinide. Such a replacement results in formation of pyrochlore $^{VIII}(CaAn^{4+})^{VI}(B^{4+})_2O_7$ with one actinide atom per formula. Thus, the amount of actinide increases by five times compared to the previous substitution type. Phases $^{VIII}(CaAn^{4+})^{VI}(B^{4+})_2O_7$ can be predicted from comparison of radii of cations in REE pyrochlores $(A^{3+})_2(B^{4+})_2O_7$ and the effective radius of the Ca^{2+} + An^{4+} pairs, where An = Th, U, Np, Pu. An effective radius of the cationic pair falling within the interval typical of a stable pyrochlore structure can indicate the possible stability of corresponding actinide compounds. The (Ca^{2+} + U^{4+}) and (Ca^{2+} + Np^{4+}) pairs, with respective effective radii of 1.06 Δ and 1.05 Δ, which are close to the radius of Gd^{3+}, compose many phases with Ti^{4+}, Sn^{4+}, Zr^{4+}, and Hf^{4+} cations. Incorporation of larger (e.g., Th^{4+}) or smaller (e.g., Pu^{4+}) cations causes changes in the effective ionic radius and decreases the number of possible pyrochlore-type compounds. The latter are stannates, hafnates, and zirconates for Th^{4+},and only stannates and titanates for Pu^{4+}. It is theoretically possible for $Ca^{2+}$to be replaced by Sr^{2+} (1.26 Δ) in $^{VIII}(CaAn^{4+})^{VI}(B^{4+})_2O_7$ pyrochlore, which allows incorporation of fission products together with tetravalent actinides in a single-phase matrix. However, our data have showed that the synthesis of Sr–Th pyrochlores was not successful.

Pyrochlores with the compositions $CaUTi_2O_7$ and $CaCeTi_2O_7$ (Ce serves as an imitator of Pu) were synthesized (Ringwood 1985; Xu et al. 2000). The phases $Ca(Pu, U, Zr)Ti_2O_7$ and $Ca(Np, Zr)Ti_2O_7$ with 45 wt % PuO_2 and NpO_2 (or 0.8–1 Pu or Np atoms per formula) were also obtained (Vance et al. 1995). The

titanate pyrochlore is the main phase of matrices for immobilization of wastes with high actinide content, e.g., irradiated nuclear fuel. By analogy with the other materials, this ceramic was called Synroc-F (where F is an abbreviation of "fuel"). Matrices composed of 80%–90% pyrochlore are considered in the United States to be the most promising forms for immobilization of the excess weapons Pu (Ebbinghaus et al. 1998). Samples with Ce, Th, U, and Pu were obtained by cold pressing followed by sintering at the Lawrence Livermore National Laboratory in the United States. The optimal composition of such pyrochlore corresponds to a solid solution of $CaUTi_2O_7$, $CaPuTi_2O_7$, and $Gd_2Hf_2O_7$ in proportion of 2 : 1 : 1.

Garnet-Structure Matrices for High-Level Radioactive Wastes

Specialists from the Research Institute of Inorganic Materials were the first who proposed to use the garnet for HLW immobilization (Vlasov et al. 1987). They synthesized materials close in composition to andradite ($Ca_3Fe_2Si_3O_{12}$) by inductive melting in a cold crucible. However, the phase and chemical compositions of these materials have not been determined, and, therefore, the formation of garnet has not been proved. These studies were continued later and resulted in the synthesis of a matrix containing more than 80% garnet (Smelova et al. 2000). The concentration of REE and Zr oxides reached 20 wt %, actinide incorporation in the matrix has not been defined. The study of garnet ceramics as potential matrices for actinide immobilization is being carried out by specialists of the Radium Institute (Burakov et al. 2000). The basic phase for this study was a (Y, Gd) aluminate–gallate garnet. Ce and U oxides or more complex mixtures modeling actinide wastes were used as HLW imitators. Ceramics composed of the garnet-, perovskite- and hibonite-type phases, as well as rare Zr and Al oxides, are products of the experiments. Chemical compositions of the samples affect their phase composition. Perovskite dominates in the Gd_2O_3–Al_2O_3 system. Garnet is the major phase in the Gd_2O_3–Ga_2O_3 system and contains about 6 wt % Ce and <0.1 wt % U. Addition of metallic Sn (4 wt %) in the starting material increases the U content in garnet up to 5.5 wt %. Garnet includes $<10\%$ of the total uranium amount of the sample. Plutonium shows similar solubility in garnet or about 6 wt % (Burakov et al. 2000).

Synthesis of New Pyrochlore and Garnet Matrices for Actinide Wastes

We have carried out experimental research on synthesis of potential actinide hosts with pyrochlore and garnet structures. For pyrochlores fabrication starting material with composition $(A_1^{2+}A_2^{4+})_2(B^{4+})_2O_7$, where "$A_1^{2+}$" = Ca or Sr; "$A_2^{4+}$" = U or Th; and "$B^{4+}$" = Ti, Sn, or Zr, was prepared of element oxides milled to 20–30 μm.

We have also produced garnet ceramics in the Ca–Al–Si–Fe–Zr–Sn–Gd–Ce–U–T–Pu–O system (Yudintsev 2003; Yudintsev et al. 2002, 2007; Yudintseva 2005). The powders were pressed at 200–400 MPa into pellets and sintered at 1100–1550°C for 1–20 h. Equilibrium state was recognized according to invariable phase composition of final product with an increase the sintering time. The time for attaining equilibrium was 3–5 h at 1300°C, 2 h at 1400°C, and 1 h at 1500°C. Some samples were melted at 1500°C, with the formation of a layer at the crucible bottom. Other samples preserved the initial pellet shape, which indicates higher melting temperatures of their precursor. The samples were studied using XRD, scanning and transmission electron microscopy methods.

Pyrochlores

The pyrochlores with Ti and Sn were formed most rapidly, while the slowest synthesis is characteristic of Zr-based systems. Pyrochlore is the major or single phase in most of the samples (Fig. 1, Table 1). Titanate matrices contain brannerite, perovskite, and a cubic fluorite-type oxide. Pyrochlore in the zirconate matrices was found only in the Th-bearing samples. The replacement of Th by U in zirconates was resulted in the formation of a fluorite-type oxide instead of pyrochlore. Except for the phases in the Ca–U–Ti–O and Ca–Ce–Ti–O systems the other pyrochlores were synthesized for the first time.

Data on these phases are absent in the X-ray diffraction databases. Their common feature is a deficiency of cations in the VIII-coordinated site of their formulas. A part of Zr^{4+} cations could also occupy the eight-coordinated sites. The substitution of U for Th in $CaThZr_2O_7$ and $(Ca_{0.5}GdTh_{0.5})Zr_2O_7$ matrices makes the pyrochlore structure unstable. This is probably related to smaller radius of U^{4+} (1.0 Δ) as compared to radius of Th^{4+} (1.05 Δ). As a result, the ratio of ionic radii in the "A" and "B" sites decreases beyond the range characteristic of the pyrochlore-type structures. The replacement of Zr^{4+} by smaller Ti^{4+}ions increases this ratio and stabilizes $(CaU)(ZrTi)O_7$ and $(Ca_{0.5}GdU_{0.5})(ZrTi)O_7$ pyrochlores. Sr-Th pyrochlores have not been synthesized, even with the largest Sn^{4+} and Zr^{4+} cations in the six-coordinated site, regardless of the formal consistence of ratio of ionic radii to requirements of geometrical stability. From the batches with $SrThSn_2O_7$ and $SrThZr_2O_7$ stoichiometry oxides with fluorite and perovskite structures as well as SnO_2 were obtained instead of pyrochlore. Data on correlation of composition with structure should be taken into account in selecting matrices for actinide-bearing wastes, particularly for complex wastes, e.g., the actinide-Zr-REE fraction of HLW. The radii of six-coordinated cations of pyrochlore phases with REE and trivalent actinides vary from 0.55 to 0.75 Δ. The Ti^{4+}, Sn^{4+}, Hf^{4+}, Zr^{4+} as well as Tc^{4+}, with radius of 0.65 Δ, are within this interval. The capacity of pyrochlore structure to incorporate tetravalent actinides increases if it simultaneously includes Ca^{2+}.

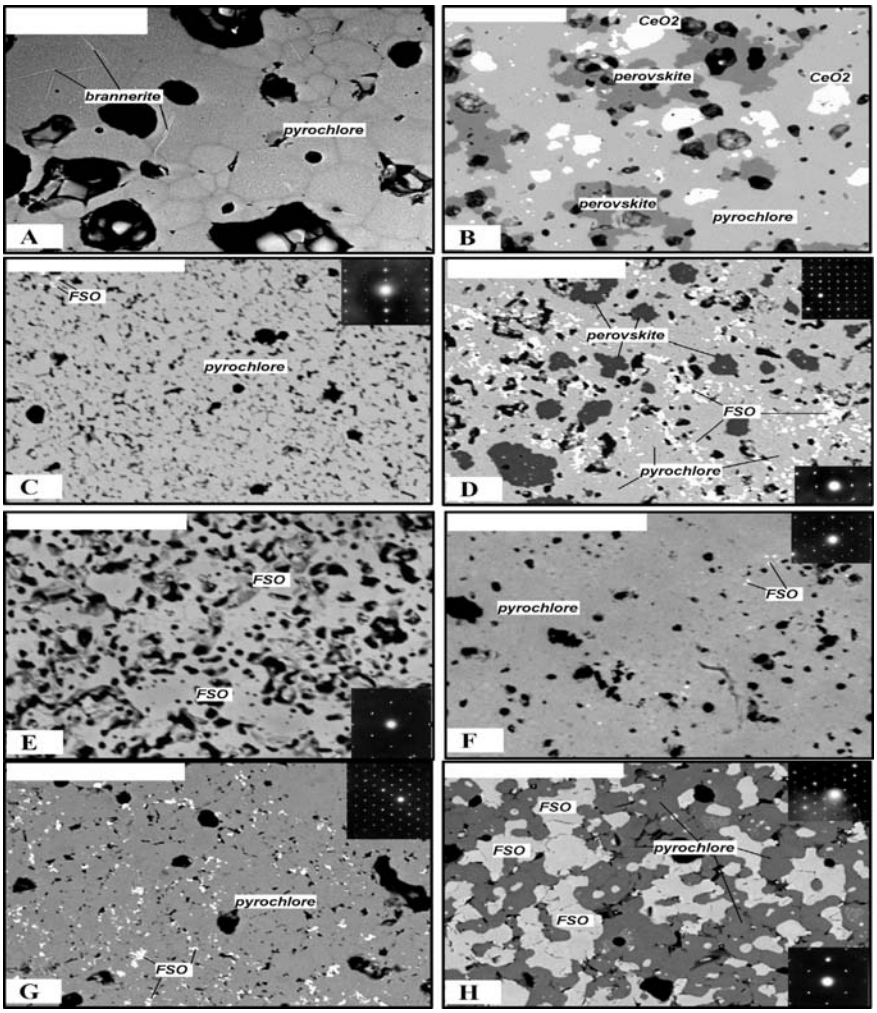

Fig. 1 SEM/bse images of ceramics with bulk composition: $CaUTi_2O_7$ (**A**), $CaCeTi_2O_7$ (**B**), $CaThSn_2O_7$ (**C**), $CaThZr_2O_7$ (**D**), $CaUZr_2O_7$ (**E**), $(Ca_{0.5}GdTh_{0.5})Zr_2O_7$ (**F**), $(Ca_{0.5}GdTh_{0.5})(ZrTi)O_7$ (**G**), and $(Ca_{0.5}GdU_{0.5})(ZrTi)O_7$ (**H**). Black – pores. Scale bars = 50 μm. Data from Laverov et al. (2002)

Garnets

Garnet structure ferrites $^{VIII}A_3^{VI}B_2[XO_4]_3$, *Ia3d*, $Z = 8$ are considered to be promising actinide host phases. U and Th contents in natural garnets don't exceed fractions of percent. Therefore, unlike some well-known phases (pyrochlore, zirconolite, etc.) garnets with actinide may be selected from synthetic phases study only. Earlier we have synthesized the garnets $(Ca, Gd, An)_3(Zr, Fe)_2[FeO_4]_3$ in which

Table 1 Phases observed in the samples and compositions (formulae) of the pyrochlores

Initial batch composition	Phases found	Pyrochlore formula, SEM/EDS data
$CaUTi_2O_7$ (A on Fig. 1)	Py > Br	$Ca_{1.06}U_{0.72}Ti_{2.22}O_{6.94}$
$CaCeTi_2O_7$ (B)	Py > Pe > Fso	$Ca_{1.03}Ce_{0.99}Ti_{1.98}O_{6.98}$
$Gd_2Ti_2O_7$	Py	$Gd_{2.04}Ti_{1.96}O_{6.98}$
$CaThZr_2O_7$ (D)	Py > Pe ~ Fso	$Ca_{0.91}Th_{0.84}Zr_{2.25}O_{7.09}$
$CaUZr_2O_7$ (E on Fig. 1)	Co	Pyrochlore phase was not found
$(Ca_{0.5}GdU_{0.5})Zr_2O_7$	Co	The same
$(Ca_{0.5}GdTh_{0.5})Zr_2O_7$ (F on Fig. 1)	Py >> Fso	$(Ca_{0.44}GdTh_{0.42})Zr_{2.13}O_{7.05}$
$(Ca_{0.5}GdTh_{0.5})(ZrTi)O_7$ (G on Fig. 1)	Py >> Fso	$(Ca_{0.47}Gd_{0.95}Th_{0.40})(Zr_{1.29}Ti_{0.89})O_{7.05}$
$(Ca_{0.5}GdU_{0.5})(ZrTi)O_7$ (H on Fig. 1)	Py ~ Fso	$(Ca_{0.62}Gd_{0.97}U_{0.23})(Zr_{0.84}Ti_{1.34})O_{6.90}$

Py – pyrochlore, Br – brannerite, Pe – perovskite, Fso – oxide with fluorite-type structure.

total REE and actinide content reached 50 wt % at actinide content of 15–20 wt % (Yudintsev 2003; Yudintsev et al. 2002, 2007; Yudintseva 2005). To study effect of impurities (Al, Na, Si) on the capacity of lattice with respect to HLW element garnets with formulae: 1: $(Ca_{1.5}GdTh_{0.5})(ZrFe)(Fe_{3-x}Al_x)O_{12}$ (x = 0–3); 2: $(Ca_{1.5}GdTh_{0.5})(SnFe)Fe_{3-x}Al_xO_{12}$ (x = 0-1); 3: $(Ca_{1.5-x}Na_x(Gd,La)Ce_{0.5})(ZrFe)(Fe_{3-x}Si_x)O_{12}$, 4: $(Ca_{1.5-x}Na_xGdTh_{0.5})(ZrFe)(Fe_{3-x}Si_x)O_{12}$($x = 0.25$–$0.75$) were fabricated at 1200–1400°C. Garnet was predominant phase in all samples (Fig. 2), ThO_2, perovskite (at high Al content), hematite, and ZrO_2-based oxides occurred as minor phases. Changes in compositions are due to contraction of the polyhedra at replacement of $^{IV}Fe^{3+}$ (r = 0.49 Å) by lower $^{IV}Al^{3+}$ (0.39 Å) or $^{IV}Si^{4+}$ (0.34 Å) and $^{VI}Zr^{4+}$(0.72 Å) by$^{VI}Sn^{4+}$ (0.65 Å). Capacity of the lattice with respect to Th depends in a greater degree on substitutions rather than temperature (Fig. 3).

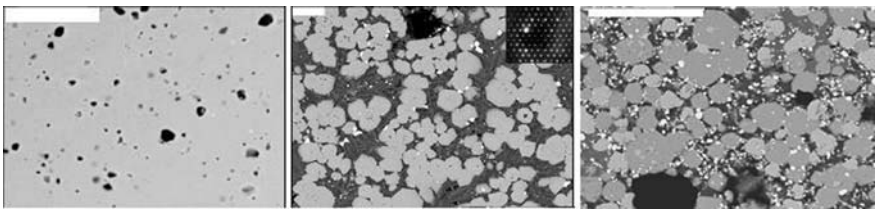

Fig. 2 SEM/bse images of the garnet samples with formulations: $(Ca_{1,5}GdTh_{0,5})(ZrFe_4)O_{12}$ (*left*), $(Ca_{1,2}Gd_{1,6}Th_{0,2})(Zr_{0,5}Fe_{1,5})(Si_{0,6}Al_{1,3}Fe_{1,1})O_{12}$ (*middle*) and $(Ca_{0.67}Na_{0.3}Gd_{1.92}Th_{0.11})(Fe_{3.88}Zr_{0.39}Si_{0.58})O_{12}$(*right*). *Left*: gray – garnet; *middle*: gray – garnet, dark – hibonite ($CaFe_{12}O_{19}$), white – ThO_2, inset – SAED pattern from plane (111)* in the garnet structure; *right*: gray – garnet, light – ZrO_2, white – ThO_2, dark – Fe_2O_3, black – pores. Scale bars = 50 μm

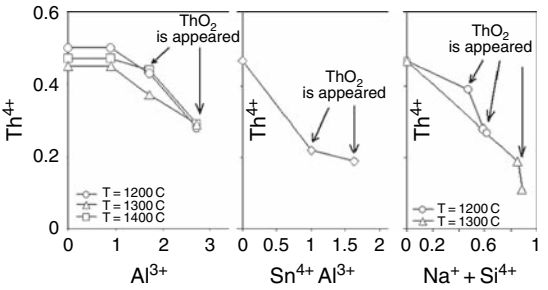

Fig. 3 Influence of temperature and impurities on Th content in garnet (atoms per formula unit)

Radiation Stability of Garnet

Amorphization due to Cm-244 incorporation (Lukinykh et al. 2007). Radiation damage was studied for the garnet with composition, wt %: 9.9 CaO; 19.4 Gd_2O_3; 2.9 Cm_2O_3 (including 2 wt % Cm-244); 15.6 ThO_2; 14.5 ZrO_2; 37.7 Fe_2O_3 which corresponds to: $(Ca_{1.5}Gd_{0.91}Cm_{0.09}Th_{0.5})(ZrFe)Fe_3O_{12}$.

Two samples were fabricated by cold pressing at 200 MPa and sintering for 5 h at 1350°C. XRD showed that the initial samples were composed of predominant

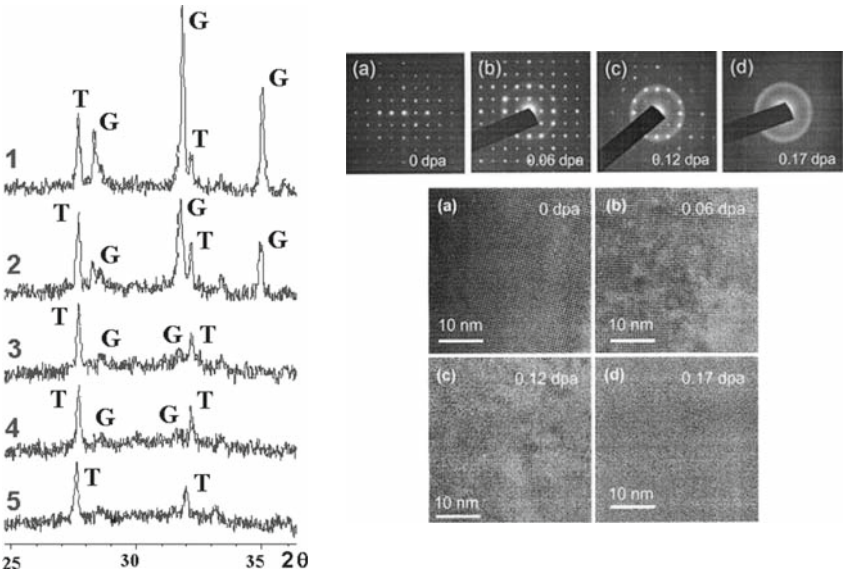

Fig. 4 *Left:* XRD patterns of garnet with 2% ^{244}Cm. G – garnet, T – ThO_2. Doses accumulated: 1 – $1.5 \cdot 10^{17}$(0.01); 2 – $4.5 \cdot 10^{17}$(0.04); 3 – $1 \cdot 10^{18}$(0.09); 4 – $1.33 \cdot 10^{18}$(0.11); 5 – $1.6 \cdot 10^{18}$ α-decays/g (0.16 dpa). It was suggested that curium entered the garnet phase only. From Lukinykh et al. (2007). *Right:* TEM and HRTEM images of garnet similar in composition before (**a**) and after irradiation with 1 MeV Kr^{2+} to doses of 0.06 dpa (**b**), 0.12 dpa (**c**), and 0.17 dpa (**d**). From Utsunomiya et al. (2005)

garnet and traces of ThO_2 (Fig. 4, left). *Kr ions irradiation* (Utsunomiya et al. 2005). Garnets $Ca_{1.50}Gd_{1.03}Ce_{0.53}Zr_{1.21}Fe_{3.82}O_{12}$, $Ca_{2.40}Ce_{0.60}Zr_{2.08}Fe_{3.03}O_{12}$, $Ca_{1.44}Gd_{0.98}Th_{0.53}Zr_{1.06}Fe_{3.92}O_{12}$, and $Ca_{2.37}Th_{0.56}Zr_{2.03}Fe_{2.96}O_{12}$ were irradiated by 1 MeV Kr^{2+} ions within 298–1073 K. Lattice damage was observed by TEM and HRTEM (Fig. 4, right). Critical dose (D_c) at 298 K was found to be 0.17 dpa and equal to results from the Cm-doping experiments. The D_c increased with temperature, and the T_c values range between 820 and 870 K (Utsunomiya et al. 2005).

Corrosion of the Garnet-Based Ceramics in Water Solutions

1. Study of the Cm–garnet using MCC-1 test (Lukinykh et al. 2007). The samples were suspended in the center of Teflon container filled with water and placed in oven heated to 90°C. Leachant was replaced after 3, 7, and 14 days. Solutions pH (4.0–4.5) are lower than for water on air (pH = 6.5) due to radiolysis. Leaching rate of Cm from the crystalline garnet is similar to Gd-Ti pyrochlore corrosion behavior (Matzke and van Geel 1996) and slightly increased (in 4–5 times) after amorphization of the sample (Table 2).

2. Corrosion of Ce–garnet (Ce used as a Pu surrogate). Garnets $(Ca_{1.5}GdTh_{0.5})ZrFeFe_3O_{12}$ (Sample 312), $(Ca_{1.5}GdCe_{0.5})ZrFeFe_3O_{12}$ (Sample 25), and $(Ca_{2.5}Ce_{0.5})Zr_2Fe_3O_{12}$ (Sample 21) were subjected to interaction with renewal water, acid (0.01M HCl) or alkaline (0.01M NaOH) solutions at 90–150°C using MCC-1 and MCC-2 tests (Yudintsev et al. 2004; Livshits and Yudintsev 2006). All specimens are composed of predominant garnet, minor perovskite and Fe_2O_3. Leaching rates of Ce or Th in 0.01M HCl from the garnets were by 3–5 orders of magnitude higher than in water (Fig. 5) and alkaline solution.

Table 2 Normalized leach rates from the initial garnet-based ceramic and after its amorphization

Element	Leaching period, days	Normalized leach rate, g / ($m^2 \times$ day)	
		Crystalline (as prepared)	Amorphous
Cm	3	$5.3 \cdot 10^{-3}$	$2.2 \cdot 10^{-2}$
	7	$2.4 \cdot 10^{-3}$	$1.1 \cdot 10^{-2}$
	14	$1.4 \cdot 10^{-3}$	$5.8 \cdot 10^{-3}$
Ca	3	$3.6 \cdot 10^{-1}$	$3.1 \cdot 10^{-1}$
	7	$2.2 \cdot 10^{-1}$	$3.8 \cdot 10^{-1}$
	14	$2.5 \cdot 10^{-1}$	$2.7 \cdot 10^{-1}$
Fe	3	$1.4 \cdot 10^{-1}$	$1.6 \cdot 10^{-1}$
	7	$2.9 \cdot 10^{-1}$	$1.9 \cdot 10^{-2}$
	14	$2.8 \cdot 10^{-1}$	$1.8 \cdot 10^{-2}$

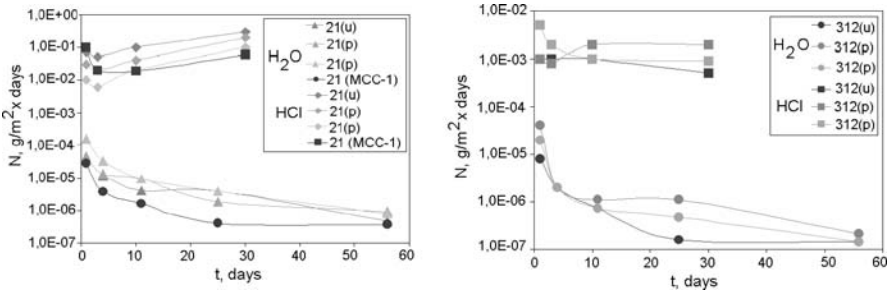

Fig. 5 *Left:* leach rates of Ce from the Sample 21 in MCC-2 (150°C) and MCC-1 (90°C). *Right:* leach rate of Th from the Sample 312 in various media in MCC-2 test at 150°C. u – unpolished surface of the pellet, p – polished surface of the sample

Study of Radioactive Minerals of Britholite Group

Britholite, Ca-REE silicate with an apatite structure, is typical actinide host in the devitrified B–Si high level waste glasses (Fig. 6). Glass-ceramics with the britholite crystalline phase are also considered to be potential matrices for an actinide fraction of HLW. A very limited number of data on radiation stability of the natural britholite exist because these minerals are commonly X-ray amorphous. Temperatures of recovery of the structure of natural (U, Th)-britholites are unknown.

Structural Chemical Properties of the Britholites and Their Behavior at Heating

The minerals of the britholite group ($P6_3/m$) belong to the apatite structure type. Their composition corresponds to a general formula $A_{10}B_6O_{24}X_2$ ("A" = Ca^{2+}, $REE^{3+/4+}$, $An^{3+/4+}$; "B" = B^{3+}, Si^{4+}, P^{5+}; "X" = F^-, OH^-, O^{2-}). "A" cations occupy nine- and seven-coordinated sites at ratio of 2:3. The lattice is formed by Ca and REE prisms linked by $(PO_4)^{3-}$ or $(SiO_4)^{4-}$ group elongated along the *c* axis.

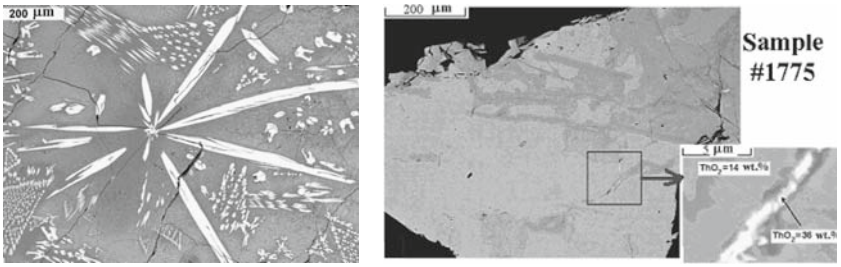

Fig. 6 Britholite in devitrified B–Si glass (*left*) and SEM images of natural mineral (*right*)

Ca atoms occupy the nine-coordinated polyhedra and REE atoms fill the seven-coordinated polyhedra. BO_4 tetrahedra are located between the nine- and seven-vertex polyhedra. Natural britholites are commonly metamict due to high Th and U content. Six britholites from alkaline rocks of various massifs in Russia were examined. Age of the minerals ranges between 320 my and 2600 my and total ThO_2+UO_2content ranges between 1 and 12 wt % (Livshits 2006). Two amorphous samples were also annealed at 750°C and 800°C for 6 h. The dynamics of structural recovery in the metamict britholite was studied with differential thermal analysis at heating rate of 10°C/min. In order to examine stages of the recrystallization process, one metamict sample (#1775) was heat-treated at temperatures of 100, 300°C for 7 h and 500, 600, 750, 800°C for 5 h. According to SEM/EDS data, the total in analysis of the britholites don't exceed 90–95 wt %, implying an occurrence of water (as OH^- or H_2O) and B_2O_3 in their compositions. Based on the data of ThO_2 and UO_2 contents and ages, the cumulative doses have been calculated (Table 3). The doses range between 0.6×10^{19} α-decays/g (0.5 dpa) and 7.7×10^{19} α-decays/g (6.6 dpa). Figure 7, left shows the XRD patterns and SAED of britholites with various doses (and degree of the lattice damage). XRD pattern of the britholite whose structure was recovered after heating at 750°C is also shown for comparison. XRD patterns for the specimens #65863 (0.5 dpa) and #1769 (1.2 dpa) reveal only two diffused peaks at the position of major britholite reflections, (211) and (210). The SAED patterns of these samples show some diffraction maxima and diffused halo. The intensity of halo is relatively high. Both XRD and SAED patterns indicate that a large volume of amorphous domains is present in the structures of these britholites. XRD pattern of the sample #1775 (2.8 dpa) reveals no diffraction maxima, SAED patterns demonstrate a broad halo, indicating that the structure is fully amorphous. Samples #89510, Brit-8, and #1771 were also characterized as amorphous. So, the minerals with cumulative dose >1 dpa ($>0.9\times10^{19}$ α-decays/g) are amorphous. Critical dose of the samples is close to the results obtained earlier for a single sample (Gong et al. 1997).

To confirm that the amorphous samples #1775 (Fig. 6, right; Fig. 7) and #65863 belong to the britholite group, these specimens were annealed at 750–800°C for 6 h. The annealing resulted in recovery of the apatite type structure without appearance

Table 3 U and Th contents in the britholites investigated and calculated cumulative doses (D)

Sample	UO_2, wt %	ThO_2, wt %	$D\times10^{19}$, α-decays/g	D, dpa
65863	< 0.2	1.9[1] (1.5–2.7)[2]	0.6 (0.3–1.5)	0.5 (0.3–1.3)
1769	< 0.6	1.4 (2.1–0.9)	1.5 (0.9–2.2)	1.2 (0.9–1.8)
Brit-8	< 0.6	4.1 (3.0–5.3)	0.9 (0.7–1.2)	0.8 (0.6–1.0)
89510	–	1.0 (0.8–2.3)	1.9 (1.5–2.2)	1.5 (1.2–1.8)
1775	0.8[1] (0.2–1.2)[2]	11.1 (9.8–12.1)	3.2 (2.3–3.7)	2.8 (2.1–3.4)
1771	< 0.7	4.1 (3.8–4.6)	7.7 (8.7–7.2)	6.6 (6.4–7.1)

[1] Average value for all analytical points.
[2] Variation range.

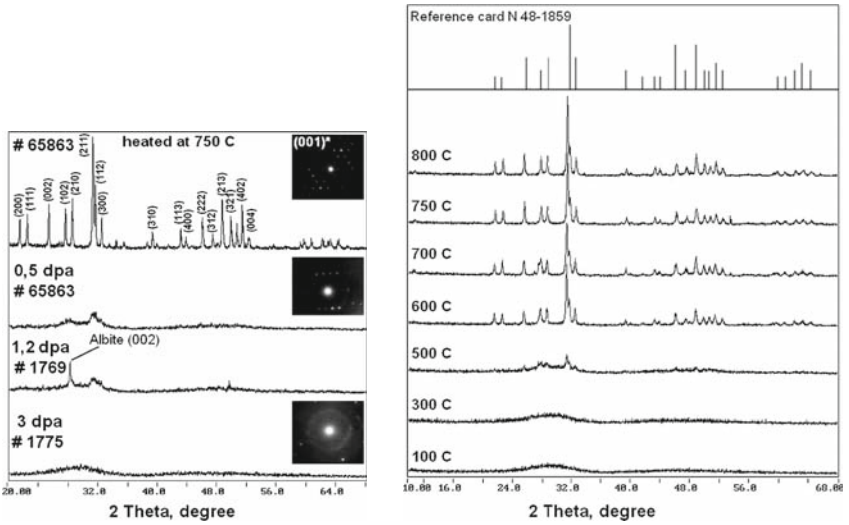

Fig. 7 XRD and SAED patterns of britholites examined (*left*) and XRD patterns for the sample #1775 after heating for 5 h at different temperatures (*right*) for recovery of the initial structure

of the other phases. A change in the chemical composition after annealing is due to decrease of fluorine content. Investigation of re-crystallization in the samples Brit-8, #1775 and #65863 by DTA method has shown that there are exothermic peaks at 480, 720–750, and 520°C due to the phases structure recovery. The difference in re-crystallization temperatures is likely due to the different degree of disordering of the initial samples. Sample #1775 is fully amorphous whereas the structures of the samples #65863 and Brit-8 are less disordered. Therefore, re-crystallization temperatures for samples #65863 and Brit-8 are lower than that for the sample #1775. At the Fig. 7 (right) a series of the XRD patterns is shown after heating at 100, 300°C for 7 h and 500, 600, 750, and 800°C for 5 h on the initially amorphous sample #1775. Peaks at XRD patterns start to appear at the temperature close to 500°C.

The structure of the mineral is completely recovered between 500 and 600°C. Above the latter XRD pattern does not change significantly. The dose required to cause amorphization in synthetic britholite by heavy ions irradiation at room temperature is about 0.2–0.4 dpa (Utsunomiya et al. 2003). Critical dose of the natural britholites is about 1 dpa (0.9×10^{19} α-decays/g) that is higher than for synthetic samples because of recovery of the structure with time in the long geological periods. The similar difference is typical of the other natural radioactive minerals (pyrochlore, zirconolite) and their irradiated synthetic analogs suggested as promising actinide hosts (Ewing and Lutze 1988; Ringwood 1984; Lumpkin 2001; Omelianenko et al. 2007).

Conclusions

Results of our research have showed that safe immobilization of the long-lived actinides can be provided with optimal selection of the durable confinement matrices (actinide waste forms), such as pyrochlore, britholite or ferrites with garnet-type structure.

Acknowledgements This work was supported by the Russian Foundation for Basic Research (05-05-64005) and US Department of Energy (RUC2-20009-MO-04). S. Yudintsev thanks organizers of the workshop "Minerals as Advanced Materials" for invitation to participate in its activity and the scientists from various Russian and American organizations collaborating in the actinide waste forms examination: M.I. Lapina, A.V. Mokhov, B.S. Nikonov, and B.I. Omelianenko (IGEM RAS), N.S. Mikhailenko, A.G. Ptashkin, O.I. Stefanovsky, and S.V. Stefanovsky (SIA Radon), A.A. Lizin, A.N. Lukinykh, S.V. Tomilin (RIIAR), R.C. Ewing, J. Lian, and S. Utsunomiya (University of Michigan, USA).

References

Actinide and fission product partitioning and transmutation (1999) In: V-th Intern Information Exchange Meeting. Nuclear Energy Agency, Paris, EUR 18898 EN

Begg BD, Vance ER, Lumpkin GR (1998) MRS Symp Proc 506:79–86

Burakov BE, Anderson EB, Zamoryanskaya MV, Petrova MA (2000) MRS Symp Proc 608: 419–422

Ebbinghaus BB, VanKonynenburg RA, Ryerson FJ (1998) Proc Intern Conf Waste Management '98. CD version Tucson Arizona USA

Ewing RC, Lutze W (1988) Radioactive waste forms for the future. Elsevier Science, NY

Ewing RC (1996) Three future for glass. Glass as a waste form and vitrification technology:8–18

Ewing RC (2006) The nuclear fuel cycle: a role for mineralogy and geochemistry. Elements 2(6):331–335

Fielding PE, White TJ (1987) Crystal-chemical incorporation of high level waste species in aluminotitanate-based ceramics: valence, location, radiation damage, and hydrothermal durability. J Mater Res 2(3):387–414

Glass as a waste form and vitrification technology (1996). Natl Acad Press, Washington

Gong WL, Wang LM, Ewing RC, Chen LF, Lutze W (1997) MRS Symp Proc 465:649–656

Hench LL, Clark DE, Campbell J (1984) High level waste immobilization forms. Nucl Chem Waste Man 5:149–175

Laverov NP, Omel'yanenko BI, Yudintsev SV, Nikonov BI (1997) Mineralogy and geochemistry of matrices of high level wastes. Geol Ore Deposit 39:211–228

Laverov NP, Yudintsev SV, Stefanovsky SV, Jang YN, Ewing RC (2002) MRS Symp Proc 713:337–344

Livshits TS (2006) Britholite as natural analog of the matrices for actinides: stability to radiation-induced damages. Geol Ore Deposit 48(5):410–422

Livshits TS, Yudintsev SV (2006) Proc 1st Eur Chem Congress, 27–31 August, Budapest, Hungary 399

Lukinykh AN, Tomilin SV, Livshits TS, Yudintsev SV, Stefanovsky SV, Lizin AA, Ewing RC (2007) Proc 11th Int Conf on Environm Remed and Rad Waste Managem, 2–6 September, Bruges, Belgium, Paper 7030

Lumpkin GR (2001) Alpha-decay damage and aqueous durability of actinide host phases in natural systems. J Nucl Mater 289:136–166

Matzke Hj, van Geel J (1996) Disposal of weapon plutonium. Kluwer, Netherlands, 93–105
McCauley RA (1980) Structural characteristics of pyrochlore formation. J Appl Phys 51(1): 290–294
Omelianenko B, Livshits T, Yudintsev S, Nikonov B (2007) Natural and synthetic minerals as matrices for actinide immobilization. Geol Ore Deposit 49(3):3–26
Ringwood AE (1985) Disposal of high-level nuclear wastes: a geological perspective. Mineral Mag 49:159–176
Shannon RD (1976) Revised effective ionic radii and systematic studies of interatomic distances in halides and chalcogenides. Acta Crystallogr 32:751–767
Shoup SS, Bambergher CE (1997) MRS Symp Proc 465:379–386
Smelova TV, Krylova NV, Yudintsev SV, Nikonov BS (2000) Silicate matrix for actinides. Dokl Russ Acad Sci 374(2):242–246
Subramanian MA, Aravamudan G, Subba Rao GV (1983) Oxide pyrochlores – a review. Prog Solid State Ch 15:55–143
Utsunomiya S, Yudintsev SV, Ewing RC (2005) Radiation effects in ferrate garnet. J Nucl Mater 336:251–260
Utsunomiya S, Yudintsev S, Wang LM, Ewing RC (2003) Ion-beam and electron beam irradiation of synthetic britholite. J Nucl Mater 322:180–188
Vance E, Begg B, Day R, Ball C (1995) MRS Symp Proc 353:767–774
Vashman AA, Demin AV, Krylova NV (1997) Phosphate glasses with radioactive wastes. Atominform, Moscow (in Russian)
Vlasov VI, Kedrovskii OL, Nikiforov AS (1987) IAEA M-294/3 Vienna 109–116
Wang SX, Begg BD, Wang LM (1999) Radiation stability of gadolinium zirconate: a waste form for plutonium disposition. J Mater Res 14:4470–4473
Xu H, Wang Y, Putnam RL (2000) MRS Symp Proc 608:461–466
Yudintsev SV (2003) Structural-chemical approach to actinide waste forms selection. Geol Ore Deposit 45(2):172–187
Yudintseva TS (2005) Study of the synthetic ferrite garnets in connection with the problem of actinide waste immobilization. Geol Ore Deposit 47(5):444–450
Yudintsev SV, Lapina MI, Ptashkin AG (2002) MRS Symp Proc 713:477–480
Yudintsev SV, Osherova AA, Dubinin AV, Zotov AV, Stefanovsky SV (2004) MRS Symp Proc 824:287–292
Yudintsev SV, Stefanovsky SV, Ewing RC (2007) Structural chemistry of inorganic actinide compounds. Elsevier, Amsterdam, B:453–490

Behavior of Actinide Host-Phases Under Self-irradiation: Zircon, Pyrochlore, Monazite, and Cubic Zirconia Doped with Pu-238

Boris E. Burakov, Maria A. Yagovkina, Maria V. Zamoryanskaya, Marina A. Petrova, Yana V. Domracheva, Ekaterina V. Kolesnikova, Larisa D. Nikolaeva, Vladimir M. Garbuzov, Alexander A. Kitsay and Vladimir A. Zirlin

Introduction

Crystalline ceramics are the most prospective materials suggested for the immobilization of long-lived radionulcides, in particular, weapons grade Pu and other actinides. The immobilization might include: (1) transmutation (burning) followed by geological disposal of irradiated materials or (2) just direct geological disposal of actinide matrices. Different durable host phases have been suggested for actinide (An) incorporation in the form of solid solutions. These are: different polymorphs of zirconia, $(Zr,An,\ldots)O_2$, in particular, one of cubic fluorite-type structure (Carroll, 1963; Heimann and Vandergraaf 1988); zircon, $(Zr,Hf,An,\ldots)SiO_4$ (Burakov, 1993; Ewing et al., 1995); monazite, $(La,An,\ldots)PO_4$ (Boatner et al., 1980; Boatner and Sales 1988); Ti-pyrochlore, $(Ca,Gd,Hf,Pu,U)_2Ti_2O_7$ (Ebbinghaus et al., 1998) etc. To investigate the resistance of actinide host phases to accelerated radiation damage, which simulates effects of long term storage the ^{238}Pu-doped samples of cubic zirconia and plutonia, zircon, La-monazite, Pu-monazite and Ti-pyrochlore have been repeatedly studied using X-ray diffraction analysis (XRD) and other methods. Main goal of this chapter was to summarize in comparison the principal features of different actinide host materials under self-irradiation from ^{238}Pu. All results described in this chapter have been obtained during last several years in Laboratory of Applied Mineralogy and Radiogeochemistry of the V. G. Khlopin Radium Institute.

Polycrystalline ^{238}Pu-doped samples of Ti-pyrochlore, $(Ca,Gd,Hf,Pu,U)_2Ti_2O_7$ (Burakov, 2002; Burakov and Anderson, 2002); gadolinia-stabilized cubic zirconia, $Zr_{0.79}Gd_{0.14}Pu_{0.07}O_{1.99}$ (Burakov et al., 2002, 2003); zircon/zirconia based ceramic,

Boris E. Burakov, Maria A. Yagovkina, Maria V. Zamoryanskaya, Marina A. Petrova, Yana V. Domracheva, Ekaterina V. Kolesnikova, Larisa D. Nikolaeva, Vladimir M. Garbuzov, Alexander A. Kitsay and Vladimir A. Zirlin
Laboratory of Applied Mineralogy and Radiogeochemistry, V.G. Khlopin Radium Institute, 2-nd Site, KIRSI-branch, 1, Roentgen Street, St. Petersburg 197101, Russia, e-mail: Burakov@peterlink.ru

$(Zr,Pu)SiO_4/(Zr,Pu)O_2$ (Burakov et al., 2003) and single crystal zircon, $(Zr,Pu)SiO_4$ (Hanchar et al., 2003), were obtained from previous research. Other ^{238}Pu-doped samples such as: La-monazite, $(La,Pu)PO_4$, and Pu-phosphate, $PuPO_4$, with monazite structure were obtained through cold pressing of co-precipitated and calcined hydroxide precursors followed by sintering in air at temperature 1200–1500°C. The repeated XRD measurements were carried out at ambient temperature after different cumulative dose using special technique developed at the V.G. Khlopin Radium Institute (Burakov, 2000). In this method, the highly radioactive sample is placed into regular XRD holder, which is then hermetically covered by thin (50–100 μm) Be-window. This avoids contamination of the X-ray diffractometer during analysis. All XRD analyses were carried out under the same conditions: Co K_α irradiation; current–40 mA; tube voltage–30 kV, scan speed–2 degrees/min, step analysis–0.01 degree.

The partial results of repeated XRD analyses collected during approximately two years are shown in Figs. 1–5.

The **Ti-pyrochlore** became amorphous at cumulative dose of $(1.1–1.3) \times 10^{25}$ alpha decays/m^3 (Fig. 1). This was accompanied by decrease of ceramic density of approximately 10% in comparison with initial fresh sample. Many cracks have been observed by optical microscope in ceramic matrix after dose 5.7×10^{24} alpha decays/m^3. Unfortunately, an initial ceramic sample has not been studied by optical microscopy immediately after synthesis. The same situation took place with electron microprobe analysis (EMPA) of this sample. At cumulative dose 5.7×10^{24} alpha decays/m^3 an essential chemical inhomogeneity of pyrochlore phase has been observed. The simplified variation of the estimated pyrochlore

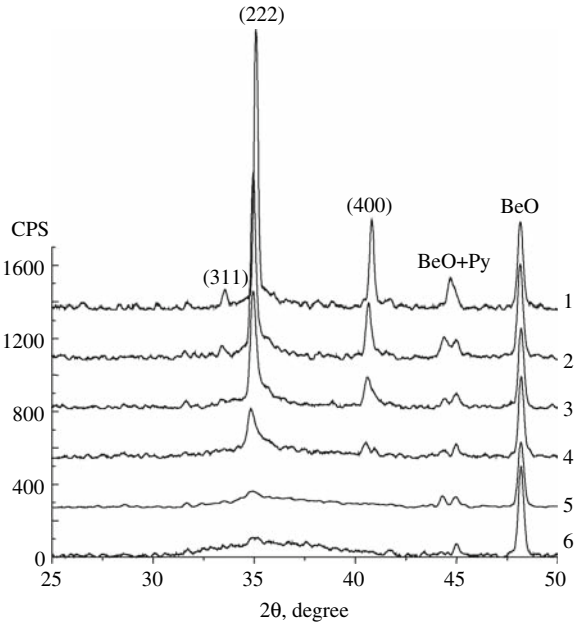

Fig. 1 X-ray diffraction patterns of titanate pyrochlore-based ceramic doped with 8.7 wt.% ^{238}Pu after cumulative doses (in alpha decays/m$^3 \times 10^{23}$) of: (1) 26; (2) 43; (3) 57; (4) 82; (5) 110; (6) 130. BeO – reflections from the Be window that covered ceramic sample; BeO+Py – overlapping of BeO and pyrochlore peaks

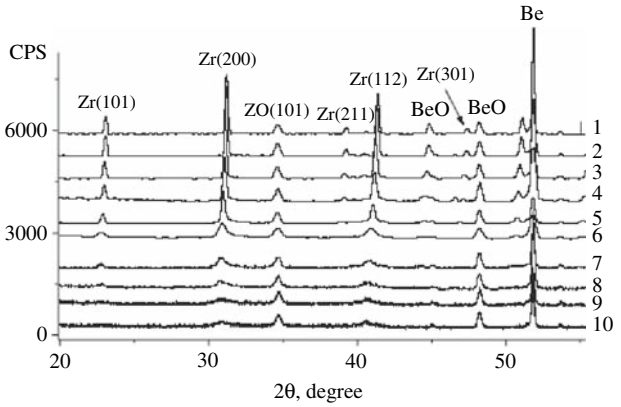

Fig. 2 X-ray diffraction patterns of ^{238}Pu-doped ceramic based on zircon (Zr) and minor phase, tetragonal zirconia (ZO), after cumulative dose (in alpha decay/m^3 $\times$ 10^{23}): (1) 3.2; (2) 13; (3) 30; (4) 51; (5) 65; (6) 91; (7) 113; (8) 134; (9) 151; (10) 166

formula was $Ca_{0.9}(U_{0.3–0.5}Pu_{0.2–0.5}Gd_{0.1–0.2}Hf_{0.1–0.2})Ti_2O_7$, however, there are no EMPA data for the initial sample. Some new-formed (?) inclusions of $(U,Pu)O_x$ and $(Hf,Ti,Ca)O_x$ were identified in ceramic matrix by scanning electron microscopy (SEM). In according to our visual observation from SEM the amount of these inclusions increased depending on cumulative dose. This correlates with shift of main pyrochlore peaks (222) and (400) depending on cumulative dose to the low angle direction (Fig. 1) that corresponds to position of pure Ti-pyrochlore phase, $Gd_2Ti_2O_7$. We assumed that self-irradiation might cause partial destruction of solid solution, $(Ca,Gd,Hf,Pu,U)_2Ti_2O_7$, into different phases such as: Ti-pyrochlore with less amount of impurities, in particular, U and Pu; $(U,Pu)O_x$ and $(Hf,Ti,Ca)O_x$.

Self-irradiation of **zircon** based ceramic caused amorphization of zircon phase at cumulative dose (1.3–1.5) $\times$ 10^{25} alpha decays/m^3 (Fig. 2).

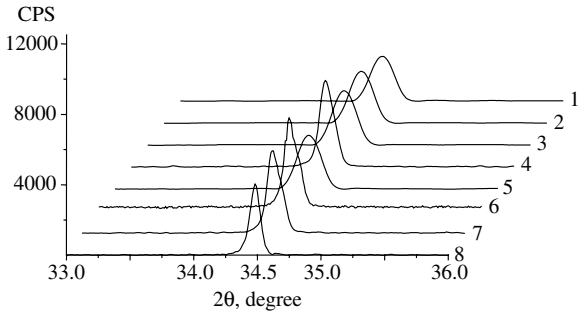

Fig. 3 Behavior of (111) XRD reflection of gadolinia-stabilized cubic zirconia doped with 9.9 wt.% ^{238}Pu after cumulative dose (alpha decay/m^3 $\times$ 10^{23}): (1) 3; (2) 27; (3) 62; (4) 110; (5) 134; (6) 188; (7) 234; (8) 277

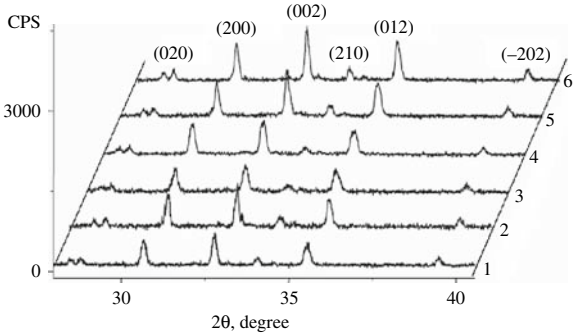

Fig. 4 X-ray diffraction patterns of La-monazite, $(La,Pu)PO_4$, doped with 8.1 wt.% ^{238}Pu depending on cumulative dose (alpha decay/m^3 $\times 10^{23}$): (1) 1.5; (2) 19; (3) 47; (4) 72; (5) 93; (6) 119

In general, such a behavior of zircon under radiation damage has been expectable and it well correlated with increase of unit cell parameters depending on cumulative dose (Table 1). However, the unusual delay of zircon amorphization has been observed between doses 9.1×10^{24} and 1.13×10^{25} alpha decays/m^3 (Fig. 2, Table 1).

Tetragonalzirconia, **$(Zr,Pu)O_2$**, which was a minor phase in zircon based ceramic, has demonstrated significantly higher resistance to radiation damage in comparison with zircon (Fig. 2). No evidence of ceramic matrix swelling or cracking was found by optical microscopy after zircon amorphization. Self-irradiation changed color of **^{238}Pu-doped single crystal zircon** from initial pink-brown to yellow-gray and caused essential crack formation in crystal matrices (Fig. 6). We assumed that main reason of crack formation in zircon single crystals was not just swelling but inhomegeneous (zoned) Pu distribution in crystal matrices.

Gadolinia-stabilized cubic zirconia, $Zr_{0.79}Gd_{0.14}Pu_{0.07}O_{1.99}$, retained crystalline structure after extremely high dose of self-irradiation, 2.77×10^{25} alpha decay/m^3 (Fig. 3). No changes in the measured ceramic density, matrix swelling,

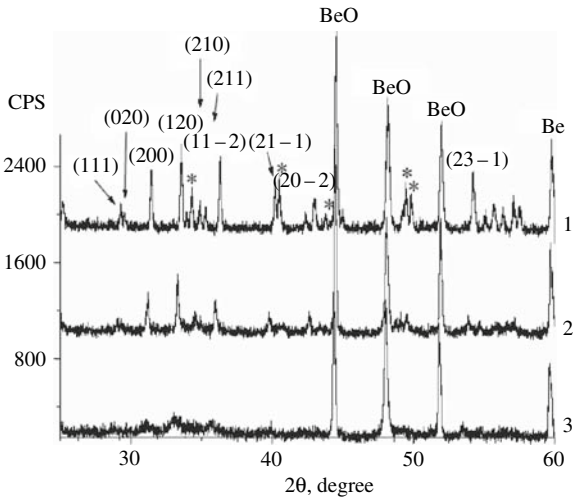

Fig. 5 X-ray diffraction patterns patterns of ceramic based on Pu-monazite, $PuPO_4$, containing 7.2 wt.% ^{238}Pu depending on cumulative dose ($\times 10^{23}$ alpha decay/m^3): (1) 1.3; (2) 17; (3) 42. Reflections from minor phase, PuP_2O_7, are marked as (∗). BeO and Be are reflections from Be-window that covered ceramic sample

Table 1 Unit cell parameters of ^{238}Pu-doped zircon, $(Zr,Pu)SiO_4$, depending on cumulative dose

Cumulative dose, alpha decay/m^3 $\times 10^{23}$	Unit cell parameters, Å	
	a	*c*
3.2	6.639(5)	6.014(10)
13	6.642(5)	6.019(10)
30	6.654(5)	6.035(10)
51	6.668(5)	6.04(1)
65	6.679(6)	6.05(1)
91	6.689(5)	6.06(1)
113	6.689(2)	6.07(1)
134, 151, 166	–	–

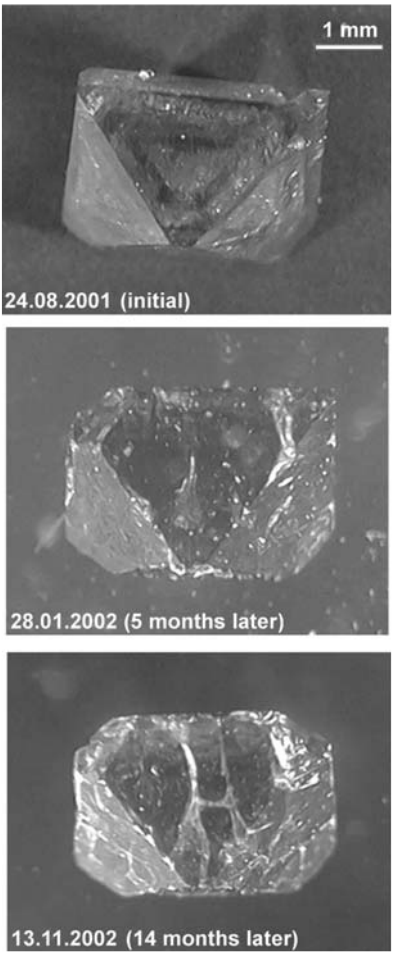

Fig. 6 Cracking of ^{238}Pu-doped zircon single crystal under self-irradiation. Average bulk content of ^{238}Pu analyzed by gamma-spectrometry is 2.4 wt.% el. The distribution of all Pu isotopes in the zircon crystals analyzed by EMPA is not homogeneous and ranges from 1.9 to 4.7 wt.% el. The lowest Pu concentrations occur in outer edge regions of the zircon crystals

or cracking were observed. No inclusions of new-formed separate Pu phases have been so far found in ceramic matrix by SEM method. Detailed XRD analysis has demonstrated unusual behavior of main (111) reflection of cubic zirconia depending on cumulative dose. At dose (in alpha decay/$m^3 \times 10^{23}$): 3; 27; 62 and 134 this peak looked nearly the same, but at 110; 188; 234 and 277 it became more narrow and its intensity increased (Fig. 3). Measurement of integrated width (Int. W) and full width of half maximum (FWHM) of XRD reflections: (111); (200) and (220) did not allow identifying difference between dose (in alpha decay/$m^3 \times 10^{23}$): 3; 27; 62; 110; 134, however, principal changes were observed at dose 188; 234 and 277 (Table 2).

We assumed that self-irradiation of cubic zirconia by is accompanied with two processes: accumulations of defects in fluorite-type crystalline structure and repeated self-annealing of those defects at ambient temperature.We assumed that self-irradiation of cubic zirconia by is accompanied with two processes: accumulations of defects in fluorite-type crystalline structure and repeated self-annealing of those defects at ambient temperature.

The **La-monazite, (La,Pu)PO_4**, remained crystalline at cumulative dose 1.19×10^{25} alpha decay/m^3 (Fig. 4). Self-irradiation caused repeated change of intensity and width of monazite XRD peaks (Fig. 4, Table 3). No essential changes of unit cell parameters depending on cumulative dose have been observed (Table 4). No swelling or crack formation in ceramic matrix have so far been observed. Under radiation damage La-monazite changed its color from initial light blue to gray.

The **Pu-phosphate, $PuPO_4$**, with monazite structure became nearly completely amorphous at a relatively low dose 4.2×10^{24} alpha decay/m^3 (Fig. 5). Minor phase in the in Pu-phosphate ceramic, e.g. **PuP_2O_7**, became amorphous earlier than $PuPO_4$. Swelling and crack formation as a result of self-irradiation damage were observed in this ceramic. Also, under self-irradiation this sample completely changed color from initial deep blue to black. Main features ^{238}Pu-doped ceramics are summarized in Table 5.

Table 2 Features of main XRD reflections of ^{238}Pu-doped gadolinia-stabilized cubic zirconia depending on cumulative dose (CD). FWHM is full width on the half maximum and Int. W is integrated width, degrees

CD, $\alpha/m^3 \cdot 10^{23}$	Unit cell parameters, Å	Miller indices					
		(111)		(200)		(220)	
		Int. W	FWHM	Int. W	FWHM	Int. W	FWHM
3	5.212(20)	0.221	0.215	0.238	0.230	–	–
27	5.213(20)	0.224	0.216	0.235	0.227	0.246	0.228
62	5.214(20)	0.224	0.218	0.233	0.225	0.248	0.230
110	5.215(20)	0.225	0.220	0.240	0.232	0.248	0.230
134	5.216(20)	0.223	0.216	0.231	0.223	0.246	0.227
188	5.216(20)	0.103	0.093	0.102	0.092	0.103	0.094
234	5.216(20)	0.105	0.094	0.102	0.092	0.102	0.093
277	5.216(20)	0.107	0.095	0.102	0.880	0.106	0.095

Table 3 Features of main XRD reflections of ^{238}Pu-doped La-monazite, (La,Pu)PO_4, depending on cumulative dose (CD). FWHM is full width on the half maximum and Int.W is integrated width, degrees

CD, α /m$^3 \cdot 10^{23}$	Miller indices							
	(200)		(002)		(012)		(−202)	
	Int. W	FWHM	Int.W	FWHM	Int. W	FWHM	Int. W	FWHM
1.5	0.164	0.163	0.138	0.148	0.194	0.192	0.118	0.113
19	0.143	0.155	0.127	0.130	0.132	0.142	0.114	0.110
47	0.145	0.158	0.181	0.180	0.179	0.198	0.126	0.135
72	0.175	0.179	0.192	0.194	0.234	0.230	0.145	0.146
93	0.151	0.128	0.158	0.146	0.201	0.204	0.140	0.130
119	0.159	0.145	0.156	0.147	0.185	0.171	0.156	0.141

The results obtained allowed us to make the following conclusions:

1. The Ti-pyrochlore, $(Ca,Gd,Hf,Pu,U)_2Ti_2O_7$, doped with ^{238}Pu became amorphous at the cumulative dose $(1.1–1.3) \times 10^{25}$ alpha decays/m^3. This was accompanied by decrease of ceramic density of approximately 10% in comparison to the initial sample. Self-irradiation caused essential chemical inhomogeneity of ceramic matrix.
2. The zircon, (Zr,Pu)SiO_4, doped with ^{238}Pu became amorphous at the cumulative dose $(1.3–1.5) \times 10^{25}$ alpha decays/m^3. At the same dose tetragonal zirconia, (Zr,Pu)O_2, which is a minor phase in zircon-based ceramic, has demonstrated significantly higher resistance to radiation damage and remained crystalline.
3. Self-irradiation changed color of ^{238}Pu-doped single crystal zircon from initial pink–brown to yellow–gray. Radiation damage caused essential crack formation in matrices of ^{238}Pu doped zircon single crystals, although no matrix swelling or cracking was visually observed for completely amorphous polycrystalline zircon sample doped with two times higher amount of ^{238}Pu.
4. Zircon based ceramic doped with ^{238}Pu remains chemically durable after significant damage of zircon crystalline structure caused by self-irradiation.

Table 4 Unit cell parameters of ^{238}Pu-doped La-monazite, (La,Pu)PO_4, depending on cumulative dose

Cumulative dose, alpha decay/m$^3 \times 10^{23}$	Unit cell parameters, Á		
	a	*b*	*c*
1.5	6.89(1)	7.08(1)	6.57(1)
19	6.89(1)	7.10(1)	6.57(1)
47	6.92(1)	7.10(1)	6.55(1)
72	6.93(1)	7.11(1)	6.54(1)
93	6.89(1)	7.10(1)	6.57(1)
119	6.90(1)	7.11(1)	6.53(1)

Table 5 Principal features of ^{238}Pu-doped ceramics under self-irradiation

Ceramic, formula of main phase	Minor phases (method of analysis)	^{238}Pu content, wt.% el.	Initial geometric density, g/cm^3	Dose of amorphization, alpha decay/m$^3 \times 10^{23}$
Zircon, (Zr,Pu)SiO_4	15% tetrag. zirconia, (Zr,Pu)O_2 (XRD and SEM)	4.6	4.4	130–150 for zircon, but not for tetragonal zirconia
Cubic zirconia, $Zr_{0.79}Gd_{0.14}Pu_{0.07}O_{1.99}$	No (XRD and SEM)	9.9	5.8	No at 277
Ti-pyrochlore, (Ca,Gd,Hf,Pu,U)$_2Ti_2O_7$	1–3% rutile, TiO_2 (XRD and SEM); new-formed (?) under self-irradiation inclusions of (U,Pu)O_x and (Hf,Ti,Ca)O_x (SEM)	8.7	4.9	110–130
Ln-monazite, (Ln,Pu)PO_4	No (XRD)	8.1	4.7	No at 119
Pu-monazite, $PuPO_4$	30–40% PuP_2O_7 (XRD)	7.2	4.9	42–45 for Pu-monazite, but less for PuP_2O_7

5. The cubic zirconia of fluorite-type structure has confirmed extremely high resistance to self-irradiation. No change of phase composition, matrix swelling, or cracking in the gadolinia-stabilized cubic zirconia, $Zr_{0.79}Gd_{0.14}Pu_{0.07}O_{1.99}$, were observed after cumulative dose 2.77×10^{25} alpha decay/m^3.
6. The ^{238}Pu-doped La-monazite, (La,Pu)PO_4, remained crystalline at cumulative dose 1.19×10^{25} alpha decay/m^3. Under self-irradiation this sample changed the color from initial light blue to gray. No swelling or crack formations have so far been observed.
7. The Pu-phosphate of monazite structure, $PuPO_4$, became nearly completely amorphous at a relatively low dose 4.2×10^{24} alpha decay/m^3. Minor phase in the Pu-phosphate ceramic, e.g. PuP_2O_7, became amorphous earlier than $PuPO_4$. Under self-irradiation Pu-phosphate sample completely changed color from initial deep blue to black. Essential swelling and crack formations as a result of accelerated radiation damage were observed in this ceramic.
8. It is assumed on the basis of XRD data that self-irradiation of cubic zirconia, $Zr_{0.79}Gd_{0.14}Pu_{0.07}O_{1.99}$ and La-monazite, (La,Pu)PO_4, is accompanied with two processes: accumulation of defects in crystalline structures and repeated self-annealing of those defects at ambient temperature.

9. It is assumed that increase of Pu content in monazite structured solid solutions, (REE,Pu)PO_4, decreases resistance of monazite to self-irradiation.

Acknowledgements This work was supported in part by V.G. Khlopin Radium Institute. Work on pyrochlore investigation performed under the auspices of the U.S. DOE by the Lawrence Livermore National Laboratory under Contract W-7405-Eng-48. Authors thank Prof. Sergey V. Krivovichev for inviting them to present this paper at the workshop "Minerals as Advance Materials I.

References

Boatner LA, Beall GW, Abraham MM (1980) Scientific basis for nuclear waste management. In: Northrup CJM Jr (ed). vol 2. Plenum Press, New York, pp 289–296

Boatner LA, Sales BC (1988) Monazite In: Lutze W, Ewing RC (eds) Radioactive waste forms for the future, vol B. Elsevier Science Publishers, Amsterdam, pp 495–564

Burakov B (1993) A Study of high-uranium technogeneous zircon (Zr,U)SiO_4 from chernobyl "Lavas" in connection with the problem of creating a crystalline matrix for high-level waste disposal. Proc SAFE WASTE'93 13-18/06/1993 Avignon France 2:19–28

Burakov BE, Anderson EB (2000) Excess weapons plutonium immobilization in Russia. In: Jardine JL, Borisov GB, (eds). UCRL-ID-138361, Proc. Meeting for Coordination and Review of Work, St. Petersburg, Russia, 1-4/11/1999, 167-179 and 251–252

Burakov B, Anderson E (2002) Summary of Pu ceramics developed for Pu immobilization (B506216, B512161). In: Jardine LJ, Borisov GB (eds) Review of excess weapons disposition: LLNL contract work in russia, Proc 3-rd Ann Meeting Coord Review of LLNL Work, St. Petersburg, Russia, January 14–18, 2002, UCRL-ID-149341, pp 265–270

Burakov B, Anderson E, Yagovkina M, Zamoryanskaya M, Nikolaeva E (2002) Behavior of ^{238}Pu-doped ceramics based on cubic zirconia and pyrochlore under radiation damage. J Nucl Sci Technol 3:733–736

Burakov BE, Anderson EB, Zamoryanskaya MV, Yagovkina MA, Nikolaeva EV (2002) Synthesis and characterization of cubic zirconia, (Zr,Gd,Pu)O_2, doped with ^{238}Pu. Mater Res Soc Symp Proc, Scientific Basis for Nuclear Waste Management XXV 713:333–336

Burakov BE, Yagovkina MA, Pankov AS (2003) Behavior of zircon-based ceramic doped with ^{238}Pu under self-irradiation. CD-ROM Proceedings of International Conference Plutonium Future – The Science, Albuquerque, New Mexico, USA, July 6-10, 2003, CP673, pp 274–275

Carroll D (1963) The system PuO_2-ZrO_2. J Am Ceram Soc 46(4):194

Ebbinghaus B, VanKonynenburg R, Ryerson F (1998) Ceramic formulation for the immobilization of plutonium. Proc Intern Symp WASTE MANAGEMENT-98, Tucson, AZ, USA, 1998, CD version, Rep 65–04

Ewing R, Lutze W, Weber W (1995) Zircon: A host-phase for the disposal of weapons plutonium. J Mater Res 10:243–246

Hanchar JM, Burakov BE, Anderson EB, Zamoryanskaya MV (2003) Investigation of single crystal zircon, (Zr,Pu)SiO_4, doped with ^{238}Pu and ^{239}Pu. Materials Research Society Symposium Proceedings, Scientific Basis for Nuclear Waste Management XXVI, pp 215–225

Heimann R, Vandergraaf T (1988) Cubic zirconia as a candidate waste form for actinides: dissolution studies. J Mater Sci Lett 7:583

Stabilization of Radioactive Salt-Containing Liquid and Sludge Waste on the Ceramic Matrices

Ivan G. Tananaev

Vernadsky Institute of geochemistry and analytical chemistry, Frumkin Institute of physical chemistry and electrochemistry Russian Academy of sciences, PA "Mayak" and Argonne National Laboratory (ANL) has worked since 2003 on a number of waste treatment applications for the Ceramicrete technology based on $KMgPO_4$ compound invented and patented at ANL. These include low level inorganic residues at Rocky Flats, and also TRU level waste organics, aqueous solvents, acids, and salts at PA Mayak. The study showed that high level wastes (and low activity wastes derived therefrom) could be treated to meet the waste acceptance criteria (WAC) for the waste repository at Yucca Mountain in Nevada and the Hanford waste disposal facility in Washington. Also, an improvement has been identified that would lead to a new class of ceramic waste forms.

Those studies were conducted on simulants of high level liquid and sludge streams that comprise the chemical and radiological constituents that have proven to be most challenging for vitrification and other treatment technologies. The simulants contained isotopic and chemical surrogates for the radionuclides. Russia shares with the U.S. similar wastes and interests in finding cost-effective, simple, reliable treatment methods.

Vernadsky Institute and PA Mayak worked on the following purposes:

(1) to demonstrate the currently developed treatment methods using high level waste simulants containing the actual radioisotopes;
(2) to further develop the potential improved ceramic formulation;
(3) to develop a pilot scale facility for high level waste treatment;
(4) to treat actual wastes at the pilot facility. In general, the laboratory work will be conducted at the Vernadsky Institute and the pilot plant work will be conducted at the PA Mayak site.

Ivan G. Tananaev
Vernadsky Institute of Geochemistry and Analytical Chemistry, Russian Academy of Sciences, Moscow, Russia; Frumkin Institute of Physical Chemistry and Electrochemistry, Russian Academy of Sciences, Moscow, Russia, e-mail: Tananaev@geokhi.ru

Testing of ceramicrete samples produced using improved process technique has been carried out. It has been shown that the proposed scheme of solution preparation permits reliable stabilization of such waste elements as Cs, Sr, Ce, Ni, Cr and I. Degrees of leaching of structure-forming matrix components varied within the range of 0.8%–1.0% for Mg; 5%–13% for PO_4^{3-}; and 18%–33% for K. Tests on leaching of structure-forming matrix components from Ceramicrete samples with surrogate intermediate sludge have shown their minimal leaching. Weight loss of these samples was only 7.5%. One should note, that phosphate neutralization (as a method of preliminary preparation of solutions) permitted to reduce weight loss for stream solutions almost two times from 20% to 11%. In general, it may be stated that application of phosphate neutralization, ionites for sorption of iodine, and nickel ferrocyanide for sorption of cesium allows effective stabilization of radionuclides and toxic elements. No presence of I, Ce, and Cs was determined in leaching mediums. Leachability index for Sr, Cr, and Ni is 11.9, 10.2–12.2 and 12.9, respectively. Fixation strength of cesium, iodine and alpha-emitting elements is so high that radioactive tracers are needed to determine leaching parameters.

The Role of Organic Matter in Peralkaline Pegmatites: Comparison of Minerogenetic and Technological Processes

Nikita V. Chukanov, Igor V. Pekov and Vera N. Ermolaeva

Solid bituminous substances (SBS) are known as usual components of late hydrothermal parageneses in peralkaline pegmatites of the Khibiny and Lovozero agpaitic massifs at Kola peninsula, Russia (Antonov et al., 1933; Labuntsov, 1937; Petersil'e, 1959, 1960, 1964; Linde, 1961; Sokolova, 1965; Zezin and Sokolova, 1967; Florovskaya et al., 1968; Loskutov and Polezhaeva, 1968; Pekov, 1998, 2001; Chukanov et al., 2005, 2006; Kartashov et al., 2006). The following occurrences of SBS are the most common:

1. Macroscopic (from 0.1 mm to 1–2 cm) spheroidal or drop-like segregations of black or dark-brown bituminous substance overgrowing (or included in) aggregates of different minerals of late hydrothermal assemblages. Very often microporous hetero-framework zeolite-like silicates (MHFZ) with Ti, Nb or Zr (elpidite, labuntsovite- and hilairite-group minerals, umbite, paraumbite etc.) are substrates for SBS. Association of bitumen-like substances with aluminosilicate zeolites and alkaline heterophyllosilicates (murmanite, lomonosovite, astrophyllite- and lamprophyllite-group minerals) is also typical. Sometimes abundant organic substances are present in cavities with MHFZ whereas in neighbouting cavities without MHFZ, bituminous substances are absent.
2. SBS are habitual microscopic inclusions in thorium minerals formed in peralkaline pegmatites of the Khibiny and Lovozero massifs on hydrothermal stage: thorite, steacyite, Na,Th- and Na,Ti,Th-silicates, Th-phosphate, Th-bearing karnasurtite-(Ce).

Nikita V. Chukanov
Institute of Problems of Chemical Physics Russian Academy of Science, Chernogolovka, Moscow region, Russia, e-mail: Chukanov@icp.ac.ru

Igor V. Pekov
Faculty of Geology, Moscow State University, 119991 Moscow, Russia
Institute of Geochemistry and Analytical Chemistry, 119991 Moscow, Russia

Vera N. Ermolaeva
Institute of Geochemistry and Analytical Chemistry, 119991 Moscow, Russia

3. In hydrothermal bodies of the Lovozero massif, abundant SBS have been detected in micro-heterogeneous aggregates forming rims around grains of Th- and *REE*-minerals (karnasurtite-(Ce), Na,Th-silicate, belovite-(Ce), etc.).
4. High concentrations of microscopic inclusions of SBS are typical for polymineral pseudomorphs after steenstrupine-(Ce) formed on hydrothermal stage (Shkatulka pegmatite, Lovozero).
5. Often films of SBS cover surfaces of mineral aggregates in cavities. Close association of SBS with MHFZ is very typical.

By IR spectroscopic and X-ray diffraction data (Chukanov et al., 2005), macroscopic aggregations of bituminiferous substances in pegmatites of the Lovozero massif are usually characterized by high contents of aliphatic hydrocarbons. They are enriched by sulfur and sodium but depleted in oxygen and rare elements. More rarely aromatic organic substances are also present in rather high concentrations.

SBS from the pegmatites of the Khibiny massif have lower average sulfur content and are enriched by derivatives of polycyclic aromatic hydrocarbons containing hydroxyl, carbonyl, carboxyl and carboxylate groups, as well as water molecules. Usually they contain alkaline-earth and other elements in the form of carboxylate salts $M^{2+}(ArCOO^{-})_2$ (where *Ar* is a polycyclic aromatic radical; *M* = Ca, Sr, Ba, Pb, *REE*) and microscopic inclusions of mineral phases with Th, *REE*, Nb and Ti.

Carbon-bearing substances in peralkaline pegmatites of the Khibiny massif are known as concentrators of rare-earth elements for a long time. The most known example is so-called "carbocer" that was first described in natrolitized pegmatite located in Loparskaya valley. Soluble part of solid rest after combustion of this substance contained 8.2 wt.% REE_2O_3 (Antonov et al., 1933). The typical "carbocer" (Table 1) contains 71.94 wt.% C, 7.01% H, 1.12% N, 0.12% S and 18.89% O, the solid rest after combustion reaching 15% (Florovskaya et al., 1968). Our investigation of a bitumen enriched by heavy metals collected in a natrolitized pegmatite vein at the Kukisvumchorr Mt., Khibiny, has demonstrated that it contains 7.2% ThO_2 and only 1.1% REE_2O_3 (Loskutov and Polezhaeva, 1968). Amorphous organic substance (with 57–60% C and 5.1% H) and H_2O (22–33%) are the main components of this bitumen.

We have investigated original "carbocer" collected by A.N. Labuntsov in the period from 1931 to 1939 in the pegmatites of Loparskaya valley, Khibiny (## 40749, 41156, 41426, 44322 in the collection of Fersman Mineralogical Museum of the Russian Academy of Sciences, Moscow).

All samples investigated give similar IR spectra containing strong bands at 1571–1576, 1378–1414 and 1250–1260 cm^{-1} and weaker bands in the range of 600–670 cm^{-1}. All these bands are assigned to vibrations of carboxylate groups connected with polycyclic aromatic systems. Prevailing of condensed aromatic structures in "carbocer" was demonstrated also by X-ray powder diffraction patterns. Along with carboxylate groups, carboxyl and/or carbonyl ones are present in all samples (corresponding bands are observed in the range of 1695–1700 cm^{-1}). Bands of C–H stretching vibrations of aliphatic hydrocarbonic groups (the range of 2870–2970 cm^{-1}) are very weak; in the IR spectrum of the sample #40749 these bands are absent.

Table 1 Mean contents of elements with atomic numbers >10 in "carbocer"

Sample	40749	41426	41156
Na_2O	0.08	0.12	–
K_2O	0.03	0.10	0.06
CaO	3.38	4.82	1.36
SrO	0.07	0.16	0.15
MgO	–	–	0.07
FeO	0.03	–	–
ZnO	–	–	–
Al_2O_3	0.12	0.08	0.13
ThO_2	2.72	0.25	1.73
TiO_2	1.06	0.99	1.26
SiO_2	1.26	0.27	0.97
SO_3	0.43	0.64	0.28
Total	9.18	7.43	6.06

Note: "–" means that the content of a constituent is below detection limit.
In all samples listed in the table *REE* elements are absent.

In the IR spectra of all investigated "carbocer" samples, very strong and broad bands of water molecules are observed in the range of 3345–3370 cm^{-1}.

Bands of mineral phases (silicate, at 910 and 450 cm^{-1}, and carbonate, at 875 cm^{-1}) are very weak and are absent in some samples. Bands of stretching vibrations of the CO_3^{2-} groups are not observed since they overlap with much stronger bands of the carboxylate groups, R–COO^-.

Comparative analysis of IR spectroscopic, electron microprobe and X-ray diffraction data shows that among silicate phases thorite is most common and the main carbonate phase is calcite. Prevailing part of thorium, lanthanides, yttrium and other heavy elements are present as metallo-organic complexes with carboxylate polycyclic aromatics and water molecules as ligands. Thorium (but not rare-earth elements as it was treated earlier) is the prevailing complex-forming metal. Silicon is distributed between silicate phases with sizes >1 μm and dispersed forms (probably silico-organic groups or submicroscopic phases). Distribution of heavy elements in the metallo-organic matrix is non-uniform; maximal local contents are (wt.%): 15.8 for Th, 1.4 for La; 2.6 for Ce; 2.25 for Nd; 3.4 for Y.

Mean contents of elements with atomic numbers >10 in three samples have been obtained by electron microprobe analysis using defocused electron beam (see Table 1). These data demonstrate that Ca, Th, Ti and Si are the main heavy components of "carbocer".

Abundant bitumen-like substances similar to "carbocer" in their chemical composition and physical properties have been found by us in numerous peralkaline pegmatites at the Mts. Koashva and Kukisvimchorr in Khibiny massif, together with minerals formed on the hydrothermal stage. Thus solid organic substances enriched by oxygen and water are common components of different late assemblages in the Khibiny massif. These substances are effective concentrators of Th, *REE*, Y, Ca. In organic phases, Th is present in the form of carboxylate salts in which carboxyl

groups are bonded to polycyclic hydrocarbon residuals of the naphthalene series (to note: similar substances are often cancerogene). In most cases (including original samples of "carbocer" collected by A.N. Labuntsov 70 years ago), Th strongly prevails over *REE* and Y. For this reason, the name "carbocer" seems non-reflecting real composition of these bitumen-like substances.

Most SBS enriched in oxydized aromatic compounds from aklaline pegmatites of Khibiny are complex microheterogenous aggregations containing mineral, metalloorganic (with *REE*, Ca, Sr, and Ba) and essentially organic phases. Among inorganics, the following phases have been detected in such aggregates: calcite, *REE* carbonates, thorite, steacyite, Na,Th-silicates $Na_{2–5}ThTiSi_8(O,OH)_{24}\cdot nH_2O$ and $Na_2Th_3Si_8O_{23}\cdot nH_2O$, Th- and U-silicates $(Th,REE,Ca)_{1-x}Si(O,OH)_4\cdot nH_2O$, (Th,*REE*,Ca)(Ti,Nb) $SiO_6\cdot nH_2O$, $NaUSi_6O_{14}(OH)\cdot nH_2O$, $Na_2U_2Si_3O_{11}\cdot nH_2O$, $Na_2USi_4O_{11}\cdot nH_2O$, $(K,Ba)_{1.5}(Ca,Na)(Th,REE)(Ti,Nb)_3(Si,Al)_8(O,OH)_x\cdot nH_2O$, (Th,*REE*)(Ti,Nb)-(Si,P)$O_6\cdot nH_2O$, $NaCaK_{0.5}MnTh_4REE_{1-x}(Ti,Nb)_2Si_8(O,OH)_x\cdot nH_2O$, $(Na,Ca,K)_2(Zn,Ti)_2Th_4REE$-$(Si,Al)_8(O,OH)_x\cdot nH_2O$, an analog of seidite-(Ce) with Th > *REE*, the phases $Na_5REE_2(Si,P)_6O_{18}\cdot nH_2O$, $(Na,Ca)_4(Mn,Fe)(Y,HREE,Th,U)_2Si_{12}O_{30}\cdot nH_2O$, alkaline niobosilicates with (Nb+Ti):Si varying from 3:2 to 3:1, rhabdophane-(Ce), rhabdophane-(Nd), monazite-(La), sazhinite-(Ce), vitusite-(Ce) etc. (Chukanov et al., 2005, 2006; Ermolaeva et al., 2007, in press). Separation of Y (+*HREE*), Ce, La, Nd, Th and U between organic and different mineral phases is an important distinctive feature of microheterogeneous aggregates containing SBS from the hydrothermal parageneses of peralkaline pegmatites.

Thus, close association of SBS with specific mineralization (minerals of lanthanides, yttrium, thorium and uranium on the one hand, and with MHFZ on the other hand) is a well-established fact. In low-temperature assemblages of the Khibiny and Lovozero agpaitic massifs, the highest concentrations of bitumen-like substances are distinctly confined to large accumulations of microporous Ti-, Nb- and Zr-silicate minerals, namely elpidite, labuntsovite-group minerals and others. Bright examples illustrating this conclusion are pegmatites Shomiokitovoye and Elpiditovoye at the Alluaiv Mt., Lovozero massif. Both pegmatite bodies were intensively altered by late peralkaline hydrothermal solutions. Shomiokitovoye is remarkable as an "yttrium anomaly", the outstanding accumulation of Y and *HREE* concentrated in shomiokite-(Y), $Na_3Y(CO_3)_3\cdot 3H_2O$, forming giant crystals. Yttrium mineralization is accompanied by abundant SBS, oxalates (mainly natroxalate, $Na_2C_2O_4$) and MHFZ (elpidite, korobitsynite etc.). The Elpiditovoye pegmatite is remarkable as one of the largest and richest occurrences of MHFZ in the Lovozero massif, mainly elpidite and recently described mineral caryochroite, $(Na,Sr)_3(Fe^{3+},Mg)_{10}(Ti_2Si_{12}O_{37})(H_2O,O,OH)_{17}$. Besides it is characterized by a very high concentration of SBS forming abundant macroscopic segregations on MHFZ.

In the present work, a representative collection of Th- and *REE*-minerals from hydrothermal assemblages of the Khibiny and Lovozero massifs has been investigated. All samples of these minerals show in IR spectra distinct bands of oxidized aromatic compounds due to abundant disperse inclusions of SBS. Some samples contain also aliphatic hydrocarbons. Associated Th- and *REE*-free minerals (zeolites,

pectolite, MHFZ etc.) do not contain inclusions of SBS detectable by routine IR spectroscopy method. It is worth to mention that thorium minerals from high-temperature (magmatic and early pegmatitic) assemblages (thorite, sodim–thorium silicate, umbozerite, steacyite–turkestanite and steenstrupine–thorosteenstrupine series minerals) do not contain SBS or contain them in trace amounts.

Basing on the facts given above, we bring up the following concept of the evolution of organic matter in peralkaline pegmatites:

Sorption of small carbon-bearing molecules (CO, CO_2, CH_4, C_2H_6, C_2H_4 etc.), their polymerization, transformation into aromatic compounds (the reforming process) and selective oxidation proceed on MHFZ playing the role of selective absorbents and catalysts.

Oxygen-bearing aromatic substances with hydrophilic substituents like –OH, –C=O, –COOH, $–COO^-$ act as complexing agents towards Th, *REE*, U, Zr, Ti, Nb, Ba, Sr, Ca and facilitate transportation of these elements under low-temperature hydrothermal conditions in the form of water-soluble micelle-type associates.

Accumulation of Th, *REE* (and, to a less extent, U, Zr, Ti, Nb) on the late stages of the hydrothermal process proceeds on the form of microphases impregnating aggregations of SBS or in the form of crystals of Th and *REE* minerals. In the latter case SBS can be captured by a growing crystals (forming disperse inclusions) or displaced on the surface of a growing crystal (forming SBS-rich rims).

On the latest stages of the pegmatite formation, phase separation in initially homogeneous metal-organic substance takes place. In particular, phase separation in bitumen-like substances containing metal-organic complexes leads to the formation of microphases of Ti- and Nb-silicates with Th, Ca, *Ln*, Y, Na and K.

The above concept is based not only on close association of organic and mineral phases in pegmatites but also on direct analogies in technological processes.

Light hydrocarbons (methane, ethane, ethylene) are common components of inclusions in minerals forming alkaline rocks (Ikorskii, 1977; Nivin, 1985). On the contrary, in Pre-Cambrian metamorphic rocks hosting the Khibiny massif, contents of hydrocarbons and other organic substances are below their detection limits or, at least, much lower than that in magmatic alkaline rocks (Petersil'e, 1964; Florovskaya et al., 1968). For example, the mean content of "organic carbon" in magmatic rocks of the Khibiny massif is 0.04% (the maximum content is 0.4%) whereas for hosting Pre-Cambrian rocks corresponding values are 0.005–0.01% and 0.04% respectively (Florovskaya et al., 1968). In young veins related to late faults within the Khibiny and Lovozero massifs, concentrations of gaseous hydrocarbons are also much lower than those in primary magmatic rocks and pegmatites (Petersil'e, 1964).

The enhancement of concentrations of organic substances in alkaline rocks enriched by Al as compared with Al-poor alkaline rocks was explained by catalytic activity of Al in the reactions of methane formation: $C+2H_2 \rightarrow CH_4$ (Petersil'e, 1964) and $4CO+2H_2O \rightarrow CH_4+3CO_2$ (Kravtsov, 1961).

Light hydrocarbons can be possible precursors of bitumen-type substances. Indeed, microporous catalysts with transition elements bearing basic active sites can selectively absorb small molecules from gases and solutions and concentrate them

near catalytic sites. For example, synthetic zeolite-like titanosilicate ETS-10 and its ion-exchanged derivatives have been found to absorb H_2, CO, N_2, NO, C_2H_4 and NH_3 (see review: Chukanov et al., 2004). Elpidite and kuzmenkoite-Mn (i.e. MHFZ that are often accompanied by bitumen-type substances in alkaline pegmatites) behave as gas sorbents even under mild conditions (Chukanov and Pekov, 2005).

On the other hand, results of our recent investigations demonstrate significant geochemical role of microporous Ti-, Nb- and Zr-silicates on late stages of the formation of alkaline massifs as ion-exchangers (Pekov and Chukanov, 2005) and promotors of abiogenic formation of organic compounds, the latter being complexing agents performing transport and concentration of rare and radioactive elements.

Synthetic micro- and mesoporous materials bearing transition elements, especially titanosilicates, are known as promising heterogeneous catalysts and catalyst carriers for selective oxidation, reforming, polymerization and other reactions in organic chemistry. In particular, modified microporous titanosilicates ETS-10 and ETAS-10 are efficient catalysts of *n*-hexane reforming; ETS-10 was used as catalyst of alkyne polymerization. Different reactions of selective oxidation of organic substrates on synthetic microporous Ti- and Nb-silicate catalysts have been described recently (Chukanov et al., 2004). Various transition metals forming complexes with aromatic hydroxyl compounds catalyze their reactions with O_2 and CO to form aromatic carbonyl compounds (US Patent 6380417). Similar catalytic processes could lead to the formation of different oxygen-bearing derivatives of naphthalene-series hydrocarbons which are present in alkaline rocks.

Different oxygen-bearing organic, especially aromatic compounds are known as effective complexing agents toward U, Th and *REE*. In particular, a new calyx[4]resorcinarene bearing 8 hydroxamic acid groups was shown to have high affinity and selectivity towards Th (Jain et al., 2005); thorium and uranium complex of *o*-carboxy $N-N$'-domethylbenzylamine was prepared by Khan and Anwar (2006); formation of thorium and uranium complexes with 4,5-dihydroxy-3,5-benzenedisulfonate in aqueous solution was investigated by Silvester et al. (2001) etc. Oxygen-rich aromatic components of heavy oil fractions ("asphaltogenetic resins"), that are structurally similar to oxidized SBS from peralkaline pegmatites, show strong affinity toward Th and U and extract these elements from aqueous solutions (Efendiev et al., 1964). Stability constants of Th(IV) to strong organic ligands present in seawater are $10^{6.6}$–10^8 (Santschi et al., 2006).

The formation of organic substances is possible only under sufficiently reductive conditions. The main redox pairs in alkaline fluids are Fe^{2+} – Fe^{3+}, H_2O – H_2, C – CO и CO – CO_2. Typically, mass crystallization of aegirine precedes the formation of most abundant segregations of SBS. Obviously crystallization of aegirine promotes reduction of carbon in the fluid. The simplified mechanism of this reduction can be described by the following reactions in which oxidation degree of carbon lowers from 4 to 2 and even to 0:

$$Na_2O + 2FeO + 4SiO_2 + CO_2 \rightarrow 2NaFe^{3+}Si_2O_6 \downarrow + CO;$$
$$Na_2O + 2FeO + 4SiO_2 + 0.5CO_2 \rightarrow 2NaFe^{3+}Si_2O_6 \downarrow + 0.5C.$$

In a more common case the reduction processes can involve water molecules, with the formation of organic substances instead of carbon. In such processes, catalysts containing transition elements (titanium, zirconium, iron etc.) can play a key role. For example, water–gas-shift reaction $H_2O+CO \leftrightarrow CO_2+H_2$ is known to be catalyzed by La-doped titanium oxide (US patent 037528) and by supported iron–copper catalysts (Barrault et al., 1981). Ce–Zr-supported non-noble metal catalysts have been recently shown to give very high water–gas shift activity at short contact times at the temperatures 473–973 K (Kumar and Khan 2007).

These data show that the pair of reagents H_2+CO (known in chemical technology as synthesis gas) can be formed in a reduced fluid under mild conditions. In industrial processes, synthesis gas is widely used for the synthesis of various organic compounds (see Bukur and Lang, 1999; Ruettinger et al., 2003; Pennline and Pollack, 1986; Ge et al., 1997).

The above described facts indicate that organic substances are syngenetic with alkaline rocks. Natural processes of their selective sorption, catalytic formation and thansformations proceed in peralkaline pegmatites, hydrothermal bodies and residual interstitial fluids being promoted by zeolite-like microporous Ti-, Nb- and Zr-silicates, as well as the formation of mobile complexes of rare and radioactive elements with components of SBS have close analogies in some technological processes.

Acknowledgements This work was supported by the Russian Foundation for Basic Research (grant 07-05-00130a), grant 4818.2006.5 of Leading Scientific School and grant MD-7230.2006.5 of the Foundation of the President of Russian Federation.

References

Antonov LB, Borneman-Starynkevich ID, Chirvinskii PN (1933) New veins with rare-earth minerals at the Kukisvumchorr Mt. in the Khibiny Tundras. In: The book: rare elements and pyrrhotites of Khibiny, vol 5. Goskhimtekhizdat, Leningrad, pp 173–180 (in Russian)

Barrault J, Forquy C, Menezo JC, Maurel R (1981) Heterogeneous enantioselective hydrogenation. React Kinet Catal L 17(3–4):373–378

Bukur DB, Lang X (1999) Highly active and stable iron Fischer–Tropsch catalyst for synthesis gas conversion to liquid fuels. Ind Eng Chem Res 38(9):3270–3275

Chukanov NV, Pekov IV, Rastsvetaeva RK (2004) Crystal chemistry, properties and synthesis of microporous silicates containing transition elements. Russ Chem Rev 73(1):227–246

Chukanov NV, Pekov IV (2005) Heterosilicates with tetrahedral–octahedral frameworks: mineralogical and crystal-chemical aspects. In: Ferraris G, Merlino S (eds) Mineralogy and geochemistry, vol 57. Rev Mineral Geochem, pp 105–143

Chukanov NV, Ermolaeva VN, Pekov IV, Sokolov SV, Nekrasov AN, Sokolova MN (2005) Rare-metal mineralization connected with bituminous matters in late assemblages of pegmatites of the Khibiny and Lovozero massifs. New Data Minerals 40:80–95

Chukanov NV, Pekov IV, Sokolov SV, Nekrasov AN, Ermolaeva VN, Naumova IS (2006) On the problem of formation and geochemical role of bituminous matter in pegmatites of the Khibiny and Lovozero alkaline massifs, Kola Peninsula, Russia. Geochem Int 44(7):715–728

Efendiev GKh, Alekperov RA, Nuriev AN (1964) Problems of geochemistry of radioactive elements of oil deposits. Edition of Academy of Sciences of Azerbaijan SSR, Baku (in Russian)
Ermolaeva VN, Chukanov NV, Pekov IV, Shlyukova ZV (2007) Mineral formation processes involving bituminous substances in pegmatites of Khibiny massif: new data. New Data Minerals, vol 42 (in press)
Ermolaeva VN, Chukanov NV, Pekov IV, Kogarko LN (2008) On the role of organic substances in the concentration of rare elements in postmagmatic differentiates of peralkaline complexes. Zapiski RMO (in press) (in Russian)
Florovskaya VN, Zezin RB, Ovchinnikova LI (1968) Diagnostics of organic substances in the rocks and minerals of magmatic and hydrothermal origin. Nauka, Moscow (in Russian)
Ge Q, Huang Y, Qiu F (1997) A new catalyst for direct synthesis of dimethyl ether from synthesis gas. React Kinet Catal L 63(1):137–142
Ikorskii SV (1977) On the laws of distribution and the time of accumulation of hydrocarbon gases in rocks of the Khibiny alkaline massif. Geokhimiya 11:1625–1634 (in Russian)
Jain VK, Pillai SG, Pandya RA, Agraval YK, Shrivastav PS (2005) Selective extraction, preconcentration and transport studies of thorium (IV) using octa-functionalized calyx[4]resorcinarene-hydroxamic acid. Analyt Sci J Jpn Soc Analyt Chem 21(2):129–136
Kartashov PM, Ferraris G, Soboleva SV, Chukanov NV (2006) Caryochroite, a new heterophyllosilicate mineral species related to nafertisite, from the Lovozero massif, Kola Peninsula, Russia. Can Mineral 44:1331–1339
Khan S, Anwar CJ (2006) Studies on thermal decomposition of uranium (VI) and thorium (IV) complexes of *o*-carboxy *N*-*N*'-domethylbenzylamine by means of thermoanalytical techniques in static air atmosphere. Radiochim Acta 94(1):23–28
Kravtsov AI (1961) Gases in apatite deposits of Khibiny. In: Problems of geology, mineralogy and petrography of Khibiny Tundras. Edition of the Academy of Sciences, pp 77–88 (in Russian)
Kumar P, Khan I (2007) A comparative study of copper-promoted water–gas-shift (WGS) catalysts. Energ Fuel 21(2):522–529
Labuntsov AN (1937) Carbocer. In: Minerals of the Khibiny and Lovozero Tundras (Mineraly Khibinskikh i Lovozerskikh Tundr). Edition of Acad Sci USSR, pp 445–447 (in Russian)
Linde IF (1961) About natural gases in rocks of the Khibiny alkaline massif. Izv Vuz Geol Razved 9:78–93 (in Russian)
Loskutov AV, Polezhaeva LI (1968) About the problem of a nature of carbocers from Khibiny (in Russian). In: Materials on mineralogy of the Kola Peninsula, vol 6. Nauka, Leningrad, pp 276–281
Nivin VA (1985) Structure and distribution of a gas phase in rocks of the Lovozero deposit (in Russian). Geologiya Rudnykh Mestorozhdenii 27(3):79–83
Pekov IV (1998) Yttrium mineralization in the Khibiny–Lovozero alkaline complex (Kola Peninsula). Zapiski VMO 5:66–85 (in Russian)
Pekov IV (2001) Lovozero massif: history of research, pegmatites, minerals. Zemlya, Moscow (in Russian)
Pekov IV, Chukanov NV (2005) microporous framework silicate minerals with rare and transition elements: minerogenetic aspects. In: Ferraris G, Merlino S (eds) Mineralogy and geochemistry, vol 57. Micro-and Mesoporous Mineral Phases, pp 145–171
Pennline HW, Pollack SS (1986) Deactivation and regeneration of a promoted transition-metal-zeolite catalyst. Ind Eng Chem Prod Res Dev 25:11–14
Petersil'e IA (1959) Hydrocarbon gases and bitumens from intrusive massifs of the central part of the Kola Peninsula. Izv AN SSSR Ser Geol 1:56–62 (in Russian)
Petersil'e IA (1960) Gases and dispersed bitumens of the rocks of some intrusive massifs of the Kola Peninsula. Edition of Kola Filial of Acad Sci USSR, Apatity (in Russian)
Petersil'e IA (1964) Geology an geochemistry of natural gases and dispersed bitumens of some geological formations of Kola peninsula. Nauka, Moscow Leningrad (in Russian)
Ruettinger W, Ilinich O, Farrauto RJ (2003) A new generation of water gas shift catalysts for fuel cell applications. J Power Sources 118:61–65

Santschi PH, Murray JW, Baskaran M, Benitez-Nelson CR, Guo LD, Hung C-C, Lamborg C, Moran SB, Passow U, Roy-Barman M (2006) Thorium speciation in seawater. Mar Chem 100:250–268

Silvester ER, Allen PG, Dharmawardana UR, Sutton M (2001) Structural studies of uranium and thorium complexes with 4,5-dihydroxy-3,5-benzenedisulfonate (Tiron) at low and neutral pH by X-ray absorption spectroscopy. Inorg Chem 40(12):2835–2841

Sokolova MN (1965) To mineralogy of deep horizons of the Kukisvumchorr apatite deposit in the Khibiny Tundras. Dokl Akad Nauk SSSR 160(1):193–203 (in Russian)

Zezin RB, Sokolova MN (1967) Macroscopic accumulations of carbonic substances in hydrothermal formations of the Khibiny massif. Dokl Akad Nauk SSSR 177(4):921–924 (in Russian)

Structure, Chemistry and Crystallization Conditions of Calcium Oxalates – The Main Components of Kidney Stones

Alina R. Izatulina and Vladislav Yu. Yelnikov

Introduction

The present work contains the results of studies of crystal chemistry and crystallization of calcium oxalates from human renal stones (whewellite and weddellite). These minerals are the most frequently occurring components of these pathogenic stones. The whewellite-dominant stones usually occur as polynuclear spherulite aggregates with characteristic radial microstructure (Fig. 1a). On the surface of whewellite stones, bipyramidic structures of weddellite have been observed (Fig. 1b).

In order to develop methods revealing incipient states and making prophylaxis of the stone diseases, it is necessary to study in details the crystalline substance of biomineral aggregates and mechanisms of their formation. However, detailed investigations of crystal chemistry and, in particular, isomorphous substitutions in urolithic minerals are almost absent. In addition, the mechanisms of the formation of renal stones are presently unclear. Essential progress in studying of formation of pathogenic biominerals in human organism may be achieved as a result of simulation experiments on crystallization of their analogues under laboratory conditions. This may allow to establish influence of organic and inorganic admixtures present in a normal urine solution on formation of the renal stones.

The aim of this work is to reveal variations of chemical composition and crystal structures of calcium oxalates of renal stones and study of the effects of components of urine solution on a whewellite crystallization.

Alina R. Izatulina
Department of Crystallography, Faculty of Geology, St. Petersburg State University, University Emb. 7/9, St. Petersburg, Russia, e-mail: Alina.Izatulina@mail.ru

Vladislav Yu. Yelnikov
Department of Crystallography, Faculty of Geology, St. Petersburg State University, University Emb. 7/9, St. Petersburg, Russia

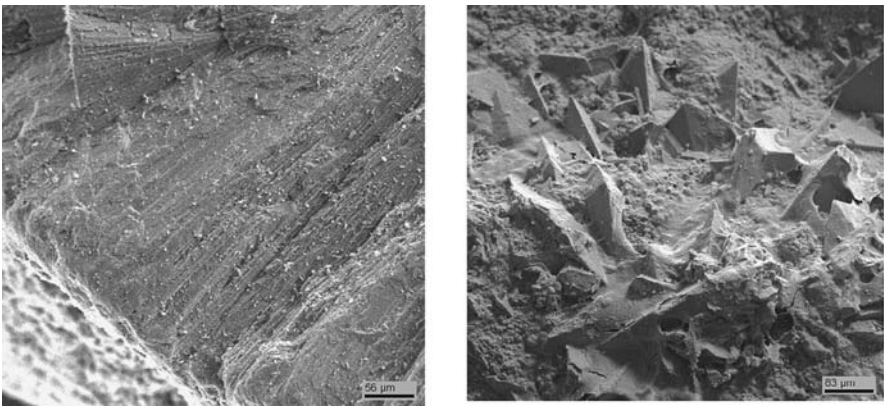

Fig. 1 Radial aggregate of whewellite (**a**) and bipyramidal crystals of weddellite (**b**)

Experimental

Thirty nine samples of calcium oxalates from renal stones were studied by X-ray powder diffraction using DRON-2 powder diffractometer withCuK_α radiation, electron microprobe analysis (electron microscope ATB-55 with analytical attachment LINK AN 10000/S85), and thermogravimetry (complex STA-449C, "NETZSCH"). The detailed structural information has been obtained by single crystal X-ray diffraction method (Table 1). Composition of solution for simulation experiments was selected according to physiological conditions present in a human organism. We studied influence of amino acids, Mg ions and crystals of hydroxylapatite. Amino acids are very important components of physiological solutions that can form a part

Table 1 Detailed information on single-crystal X-ray diffraction experiments

Mineral	Whewellite		Weddellite	
Crystal no.	1	2	1	2
Diffractometer	Nicolet P3			
Radiation	MoKα, λ=0.71069			
Space group	$P2_1/c$	$P2_1/c$	$I4/m$	$I4/m$
a, Å	6.296(1)	6.293(1)	12.364(2)	12.344(5)
b, Å	14.598(2)	14.590(3)	= a	= a
c, Å	10.115(1)	10.125(2)	7.362(1)	7.358(2)
β,°	109.50(1)	109.46(2)	–	–
V, Å^3	876.3(4)	876(1)	1125.4(5)	1121(1)
μ, cm^{-1}	12.95		10.60	
Refl. measured	3996	8243	2828	2817
Unique refl. with ($F>4\sigma_F$)	1169	3856	1319	1314
R_F	0.036	0.030	0.033	0.036
R_w	0.050	0.039	–	0.040

of nephroliths, as long as free carboxylic groups of limiting amino acids cooperate with a surface of the crystals formed. Mg^{2+} cations can also influence upon crystallization of calcium oxalates, due to the competing role of Mg relative to Ca in human organism (Sokol et al. 2003).

Besides soluble impurity, hard particles of other phases present in a physiological solution can have an impact on crystallization of calcium oxalate. From the electron microscopy and microprobe data, it is known that practically in all oxalate stones there are impurities of poorly crystalline apatite. For this reason, it is important to study their effects on crystallization of whewellite.

Thus, the research of crystallization processes was done in solutions of both pure calcium oxalate and in presence of Mg-ions and amino acids that are present in renal stones (Golovanova et al. 2002) and urine [aspartic ($HOOCCH(NH_2)CH_2COOH$), glutamic ($HOOCCH(NH_2)CH_2CH_2COOH$), alanine ($CH_3CH(NH_2)COOH$), glycine ($CH_2(NH_2)COOH$), and proline (-$CH(COOH)CH_2CH_2CH_2$)-NH] with the concentration range of (10^{-5}–10^{-2} mol/l). Investigations of crystallization of calcium oxalates were made according to the reaction:

$$CaCl_2 + (NH_4)_2C_2O_4 \rightarrow Ca_2C_2O_4 \downarrow + 2NH_4Cl$$

The precipitates were separated from soluble calcium chloride and ammonium oxalate by draining equal volumes of initial $7{,}06 \cdot 10^{-3}$M solutions.

The process of crystallization was studied at one basic supersaturation range of a calcium oxalate solution $\gamma = C_0/C_s = 7$ (C_0 – concentration of calcium and oxalate ions in a supersaturated solution, C_s – solubility of calcium oxalate monohydrate, equal to $0{,}7 \cdot 10^{-4}$ mol/l). In order to get more complete information, additional experiments were carried out at larger ranges of supersaturation $\gamma = 12, 15, 20, 25$. The choice of the major value of γ was made according to the presence of such supersaturations in biological environments, e.g. in urea of the healthy adult average man (Tiktinskiy and Aleksandrov 2000) The pH of the solution was held equal to 6.5 by the addition of 10% solution of NaOH. The value of an ionic force was reached by addition of 0,3 mol/l NaCl to the solution.

Crystallization phenomena were studied by a laser diffraction analyzer of the particle size (SALD 2101, Mastersizer 2000). As a result, we obtained distribution curves of particle sizes that are directly connected with the parameters that define mechanisms of nucleation and crystal growth. Crystallization products were studied by X-ray diffraction analysis.

Results and Discussion

Variable Composition and Non-stoichiometry of Whewellite and Weddellite

According the data obtained, calcium oxalates from uroliths demonstrate significant variations of unit-cell parameters that points out on their variable composition:

whewellite (S. G. $P2_1/c$): a = 6.286–6.292(1), b = 14.560–14.588(4), c = 10.094–10.132(4), Å; β = 109.39–109.49(2)°; weddellite (S. G. I4/m): a =12.344–12.365(3), c = 7.348–7.360(2) Å.

Results of X-ray microprobe and series of crystal structure refinements of calcium oxalates from renal stones (Table 1) have shown that these variations are not due to isomorphous substitutions in the Ca sites. This fact indicates that both whewellite and weddellite can keep variable quantities of water in their structures. This suggestion is in agreement with the previous investigations of weddellite (Tazzoli and Domeneghetti 1980; Naumov et al. 1996). Its structure contains "zeolitic" water with incomplete occupancy of crystallographic sites.

The crystal structure of *whewellite* consists from two types of alternating layers, parallel to (100) (Fig. 2). The calcium cations are at the center of a distorted square antiprism. Each antiprism shares three edges with adjacent antiprisms and, as a result, a layered hexagonal motif is formed. The second type of layers consists of ribbons that are formed by alternating oxalic ions and water molecules bonded by hydrogen bonds laying in the (010) plane and extending along the c axis.

H_2O molecules occupy two independent crystallographic sites, W(1) and W(2). On difference Fourier maps, the positions of water molecules are disordered over the W(1), W(11), W(2), W(21), and W(22) sites (Fig. 2). The sums of occupancies of both splitting sites are close to one (Table 2).

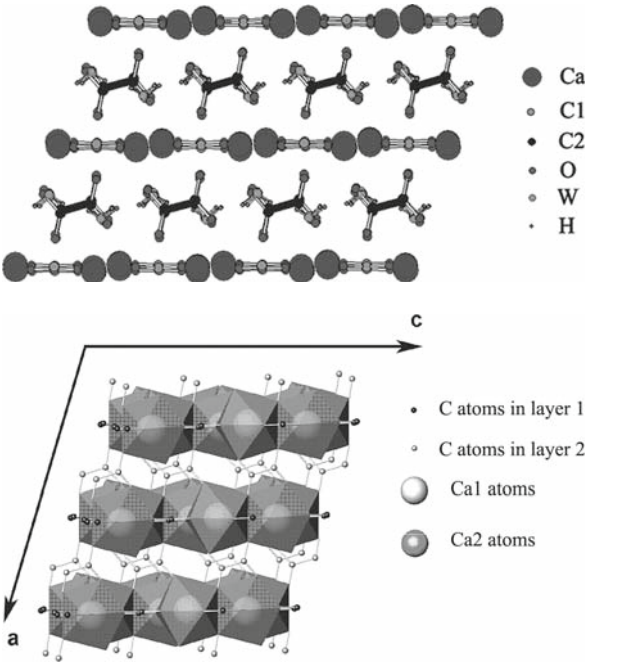

Fig. 2 Crystal structure of whewellite in ball-and-stick (*up*) and polyhedral (*below*) representations

Table 2 Occupancies of sites occupied by water molecules in the structure of whewellite

Sample	W(1) / W(11)	W(2) / W(21) / W(22)
1	0.78 / 0.23	0.67 / 0.21 / 0.19
2	0.85 / 0.17	0.80 / 0.14 / 0.08
Literature data (Tazzoli and Domeneghetti 1980)	0.85 / 0.15	0.86 / 0.14 / –

Disordered distribution of water molecules in structure of whewellite allows to assume the presence of additional water molecules, W(3), in the sites (½ 0 0), (½ 0 ½), and (½ ¼ 0) that are in the cavities between the "C_2O_4 – W(1) – W(2) – C_2O_4" chains (Fig. 3). Distances between additional water molecules are: W(1)(11)–W(3) = 2.60–2.65, W(21)(22) – W(3) = 2.86 – 2.69 Å. This hypothesis allows to explain the thermogravimetric data of urinary and synthetic whewellites. As result, a general formula of whewellite can be written as $Ca_2C_2O_4(H_2O)_{1+x}$, where $0 \leq x \leq 0.07$.

In *weddellite*, as well as in whewellite, the Ca coordination polyhedron is a distorted square antiprism. Every antiprism is linked to two adjacent antiprisms to form chains extended along the *c* axis. The chains are connected by oxalate-water ribbons parallel to (100) and (010) (Fig. 4). As result of operation of the 4-fold axis, the Ca-chains and oxalate-water ribbons form channels occupied by "zeolitic" water molecules.

We studied the crystal structures of weddellite samples that have significantly different unit-cell parameters that revealed direct dependence between the quantity *x* of "zeolitic" water and the *a* unit-cell parameter and the unit-cell volume. It allowed us to estimate variations of "zeolitic" water in the structure of weddellite as from 0.13 to 0.33. In most cases, the *x* values are close to an upper bound. The formula of the mineral can be written as $Ca_2C_2O_4(H_2O)_{2+x}$, where $x = 0.13–0.33$.

Thus, the calcium oxalates from uroliths are characterized by variable non-stoichiometric composition related to the variable quantity of water in their structures and vacancies in water-occupied sites.

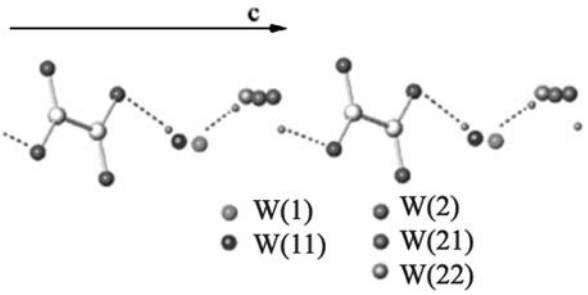

Fig. 3 Disordered distribution of water molecules in the structure of whewellite

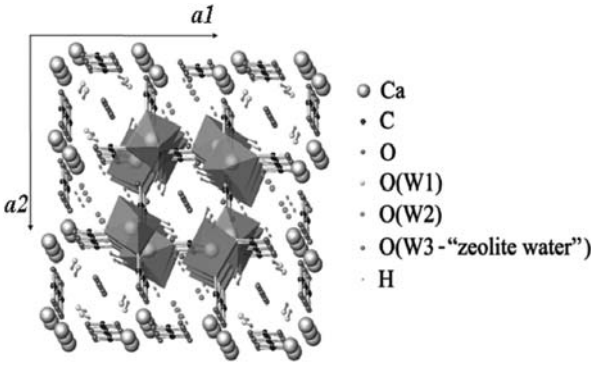

Fig. 4 Crystal structure of weddellite projected onto the (001) plane

The Influence of Impurities on the Crystallization of Calcium Oxalate

X-ray analysis of the crystallization products demonstrated that, in all experiments, the only obtained product was a calcium oxalate monohydrate.

The study of the influence of *amino acids* showed that the average size of formed crystals of calcium oxalate monohydrate decreases with the amount of amino acids in solution (Fig. 5). The greatest effect is observed at largest concentrations. Full stagnation of crystallization, with supersaturation equal to $\gamma = 7$, was induced by the increase of aspartic and glutamic amino acid concentrations up to 10^{-2} mol/l.

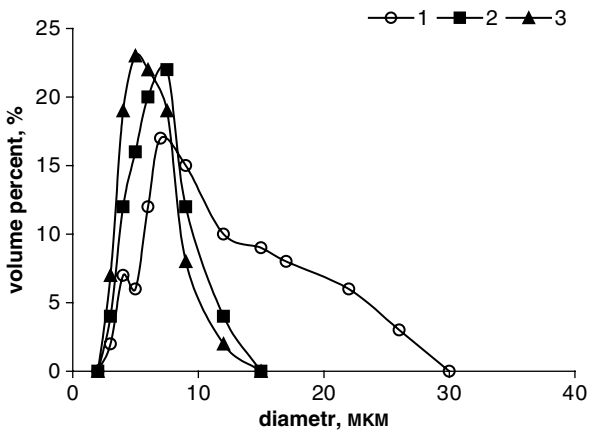

Fig. 5 Curves of distribution of sizes of calcium oxalate monohydrate crystals. Crystallization in bidistillate (1), in solution (glu)=10^{-6} mol/l (2), in solution (glu)=10^{-5} mol/l (3), supersaturation is equal to $\gamma = 7$

It follows that aspartic and glutamic aminoacids inhibit growth of calcium oxalate crystals, with the effect of the glutamic acid being much stronger.

The experiments with higher supersaturation showed that crystallization of calcium oxalate in a solution with glutamic acid with C = 10^{-2} mol/l concentration will take place only if the initial concentration of calcium oxalate is increased up to 1.5 times. Once again, it demonstrates the strong concentration dependence of the inhibit action of aminoacids.

The experiments on crystallization with impurities of alanine, proline and glycine were carried out in order to study the influence of aminoacid structure on a degree of stagnation of calcium oxalate monohydrate crystal growth. The results are shown in Table 3. It is clear that the inhibit degree on the crystal growth increases with the increase of amino acid concentration and its structure.

It can be suggested that the inhibit action of amino acids is due to their adsorption on the active centers of a growing crystal's surface. Amino acids that can be adsorbed on the surface of calcium oxalate monohydrate are inhibiting crystallization of essentially calcium oxalate monohydrate. According to the results aminoacids can be placed in the following row with increasing inhibition effect:

Glycine < Alanine < Proline < Aspartic acid < Glutamic acid

Experiments that we carried out to understand the role of *magnesium ions* during the calcium oxalate monohydrate crystallization displayed strong stagnation of crystallization in the presence of Mg ions in the solution. Being added to the solution with supersaturation equal to $\gamma = 7$, Mg ions with the concentration $= 10^{-3}$ mol/l reduced the size of calcium oxalate crystals up to 2.5 times, i.e. very strong stagnation of the crystals growth has been observed. If concentration of Mg^{2+} ions in the solution increases up to $C_{Mg} = 10^{-2}$ mol/l (that corresponds to physiological concentration) under supersaturation ($\gamma = 7$), the crystallization of calcium oxalate fully stops. Crystallization of calcium oxalate in the solution with the presence of Mg^{2+} ions with the concentration $C = 10^{-2}$ mol/l is observed only if the initial concentration of calcium oxalate is increased up to 3 times.

Studies of the influence of an ionic force (I = 0.3) showed that with the supersaturation ($\gamma = 7$), crystals of calcium oxalate can not be detected by the dispersion method two hours after crystallization starts, i.e. the diameter of crystals was less than 0.03 μm. Moreover, the absence of crystallization of calcium oxalate monohydrate from the solution with ionic force $I = 0.3$ and $\gamma = 7$ during two months was

Table 3 Average size of the calcium oxalate crystals with the amino acid impurities

Aminoacid (mol/l)	10^{-5}	10^{-2}
Glutamic acid	3.88 ± 0.09 μm	lower than 0.03 μm
Aspartic acid	5.08 ± 0.06 μm	lower than 0.03 μm
Glycine	6.11 ± 0.07 μm	3.95 ± 0.05 μm
Alanine	5.52 ± 0.04 μm	4.32 ± 0.06 μm
Proline	5.30 ± 0.07 μm	4.73 ± 0.04 μm
Calcium oxalate without impurities	10.31 ± 0.07 μm	

established that confirms stability of this solution. Crystallization of calcium oxalate from the solution with the given ionic force $I = 0.3$ is observed only if supersaturation is increased up to $\gamma = 10$.

The studies of calcium oxalate monohydrate crystallization in the presence of *hydroxylapatite,* $Ca_5(PO_4)_3OH$, showed that the presence of hydroxylapatite crystals in the solution initiates the process of calcium oxalate monohydrate crystallization. As it was demonstrated (Table 3), in the solution of glutamic acid with concentration $C_{Glu} = 10^{-2}$ mol/l with supersaturation equal to $\gamma = 7$, calcium oxalate monohydrate crystallization does not happen. The results of dispersion analysis showed that calcium oxalate monohydrate crystallization takes place with addition of crystals of hydroxylapatite into the solution ($d_{mid} = 5.29 \pm 0.06$ μm), and the average size of particles of the solid phase increases from 5.29 ± 0.06 to 9.14 ± 0.29. As hydroxylapatite is almost insoluble, the increase of the size of particles should be attributed to the formation and growth of calcium oxalate monohydrate crystals. As a whole, these results confirm the assumptions that the crystals of hydroxylapatite can represent itself as nuclei of heterogeneous nucleation of calcium oxalate monohydrate. From the literature, it is known, that, in oxalate stones, nuclei are represented by calcium phospates and an organic matrix. Therefore, it is possible to suggest, that in the presence of hydroxylapatite, formation and growth of calcium oxalate monohydrate crystals occurs even at high concentration of amino acids.

Conclusions

The main results of our studies can be summarized as follows:

1. Amino acids inhibit crystal growth of monohydrate calcium oxalate and reduce average size of the crystals. The inhibition effect of amino acids depends upon their molecular structure and increases with the extension of carboxyl groups and concentration.
2. Mg ions can also inhibit crystallization by increasing the critical supersaturation up to $\gamma = 20$ for the concentration of ions corresponding to that of a physiological solution (urea).
3. The ionic force ($I = 0.3$) of the biological fluid is a factor of stable supersaturated solution of calcium oxalate.
4. The presence of crystals of hydroxylapatite in the solution induces the calcium oxalate crystallization processes.

The results obtained indicate direction of a further research aimed at the detection of a true role of proteins and hydroxylapatites in the formation of nephroliths and potential development of a synthetic peptides for use in urolithiasis therapy.

Acknowledgements This work was supported by RFBR (## 06-05-65165, 05-05-64289). We thank Prof. O.V. Frank-Kamenetskaya, Dr. O.A. Golovanova, and Prof. Yu.O. Punin for assistance and advices during research.

References

Golovanova OA, Pyatanova PA, Rosseeva EV (2002) Definition methods of protein component of kidney stones. Materials of the I Russian Meeting on Organic Mineralogy, St.-Petersburg 36–37

Naumov DYu, Podberezskaya NV, Boldyreva EV (1996) Crystallochemical analysis of structures of oxalic acid and its salts $M_x(C_2O_4)_y nH_2O$ (n=0–3). J Struct Chem 37(3):550–577

Sokol EV, Nigmatulina EN, Maksimovna NV (2003) The spherulites of calcium oxalate in a kidney stones: morphology and formation conditions. Chemistry in Stable Evolution Interests 11:547–558

Tazzoli V, Domeneghetti C (1980) The crystal structures of whewellite and weddellite: re-examination and comparison. Am Mineral 65:327–334

Tiktinskiy OL, Aleksandrov VP (2000) Urolithiasis. Medicine, St.-Peterburg

Structure, Chemistry and Synthesis of Carbonate Apatites – The Main Components of Dental and Bone Tissues

Olga V. Frank-Kamenetskaya

Introduction

Nonstoichiometric carbonate-doped or carbonate apatites are the main mineral components of human and animal hard tissues (bones and teeth). They are increasingly used as biocompatible materials for medical purposes. Besides, dispersed systems based on apatite-like compounds are characterized by highly developed surface ($400\,m^2/g$) and used as high effective ion-exchanger matrixes.

The basic structure of apatite $Ca_5(PO_4)_3(OH, F, Cl)$ had been determined in 1930 (Mehmel 1930). It can be described (Fig. 1) as the three-dimensional network of PO_4-tetrahedra, which are linked together by columns of nine-fold coordinated Ca1 atoms (Fig. 2a). The channels passing through the network have the axes coinciding with the six-fold screw axes and contain the triangles of seven-fold coordinated Ca2 atoms (Fig. 2b) and OH^-, F^- or Cl^- ions.

The location of CO_3^{2-} ions in apatite structure is an important question because it usually increases the reactivity of apatites, for example, in the processing of dissolution of dental enamel in caries. It is now generally accepted that the principal possibly sites for CO_3^{2-} ions are on the hexad axis replacing OH^- ion in channel (A-type) or replacing a PO_4^{3-} ion (B-type). These substitution types are resulting in characteristic infrared (IR) signatures. In biological apatites the predominant substitution appears to be CO_3 – triangles for PO_4 – tetrahedral, but frequently a small amount of OH^- ion replacement also occurs.

A-type carbonate substitution results in progressive increase in ***a*** and decrease in ***c*** parameters (LeGeros et al. 1969; Bonel 1972) whereas substitution of phosphate by B-type carbonate results in progressive decrease in ***a*** and increase in ***c*** (Nelson and Featherstone 1982; Vignoles et al. 1988). However, many of B-type apatites have somewhat increased lattice constants ***a*** due to entering of water molecules.

Olga V. Frank-Kamenetskaya
Department of Crystallography, Faculty of Geology, St. Petersburg State University, University Emb. 7/9, St. Petersburg, Russia, e-mail: OFrank-Kam@mail.ru

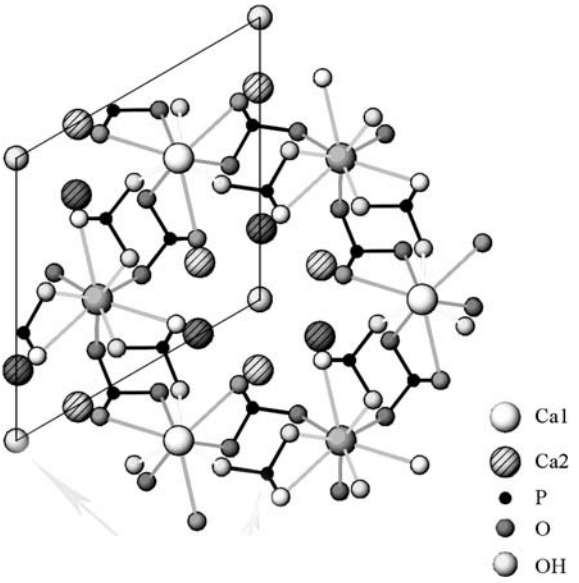

Fig. 1 Crystal structure of apatite. Projection onto (0001) plane

The numerous possibilities of charge-balance mechanisms associated with the incoporation of CO_3-ions into the apatite structure have not been fully clarified. The question of how the CO_3^{2-}ion is incorporated into the structure remains under discussion. So, there are many uncertainties about the substitutions in carbonate apatites, including biological apatites.

The present work is devoted to the research results on various carbonate apatites that have been obtained in Saint Petersburg University over many years. The main aim of this work is to reveal the regularities of complicated substitutions in crystal structures of carbonate apatites and to develop synthesis of analogues of biological apatites.

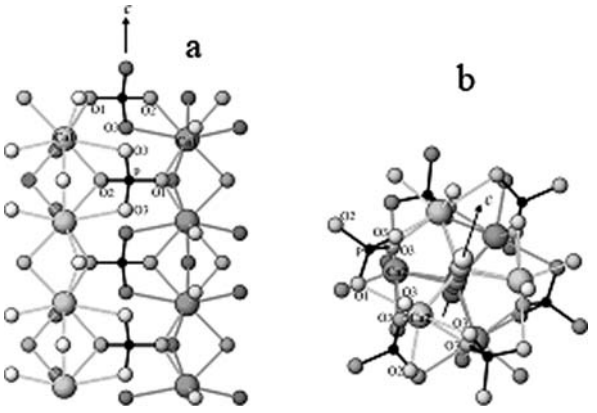

Fig. 2 Types of calcium polyhedra in the structure of apatite: columns of nine-fold coordinated Ca1 polyhedra (**a**) and triangles of seven-fold coordinated Ca2 polyhedra (**b**)

Experimental

The study of crystal chemistry of biological and synthetic carbonate apatites has been carried out by powder (including high-temperature measurements) and single-crystal X-ray diffraction methods, IR-spectroscopy, thermal analysis and various chemical analytical techniques.

Biological samples used in this study were physiogenic and pathogenic carbonate apatites formed in a human organism (in teeth, bone hard tissues and in renal, salivary and dental stones) and apatites from fossils of different taxonomic families (brachiopods, conodonts, fishes, reptiles, mammal) with different geological ages and burial conditions.

Synthesis of apatites was realized by precipitation methods and under hydrothermal conditions (from flux and by calcite treatment).

Results and Discussion

Location of Carbonate Ion of the B Type

The Rietveld refinement of the crystal structures of two synthetic hydrothermal Ca-deficient carbonate apatites (sp.gr. $P6_3/m$) allowed to determine two orientations of triangular carbonate ions (Ivanova et al. 2001, 2004) (Fig. 3).

In crystal structure of K^+-doped hydrohyapatite with 7.7 wt% of CO_2 (***a*** = 9.401(1), ***c*** = 6.898(1) Å; Rp = 4.82, Rwp = 5.17, Rexp = 4.95%), the splitting of all tetrahedra oxygen sites was revealed. The refined unit cell content is $[Ca_{8.40}K_{0.34}\square_{1.26}][(PO_4)_{3.15}(HPO_4)_{1.30}(CO_3)_{1.55}](OH)_2$. Carbonate triangles are located at the centers of the PO_4 tetrahedra so that the positions of the C atoms coincide with those of the P atoms, and the O3c–O3c edges of the triangles are parallel to the O3p–O3p edges of the tetrahedra (Fig. 3a). The O3c atoms coordinating carbon atoms are shifted by 1.14 Å from the O3p atoms belonging to the PO_4 tetrahedra,

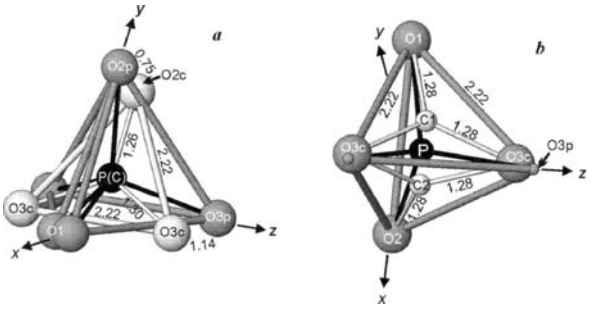

Fig. 3 PO_4 tetrahedron with CO_3-triangles crossing it (**a**) and located on its vertical faces(**b**). C–O and O–O distances (in angstroms) are indicated

and the O2c atoms are shifted by 0.75 Å from the O2p atoms. There are six symmetrically equivalent CO_3 groups in the unit cell, all with the triangle plane parallel to the *z*-axis. In four of them, one of the symmetrically equivalent coordinate axes (*x* or *y*) lies in the triangle plane, whereas the other makes 60 deg with it. The planes of the other two triangles make 60 deg with both *x*- and *y*-axes. Such orientation of the triangles should induce significant reduction of the *a* lattice constant in comparison to hydroxyapatite (OH-AP).

In crystal structure of NH_4-doped hydrohyapatite with 4.4 wt% of CO_2 and 1.4 wt% of water (***a*** = 9.437(1), ***c*** = 6.888(1)Å; Rp = 4.85, Rwp = 5.23, Rexp = 5.05%), the O3 position is splitting. The final unit cell content is $[Ca_{9.30}(NH_4)_{0.10}\square_{0.60}][(PO_4)_{4.95}(CO_3)_{1.05}][(OH)_{1.65}(H_2O)_{0.35}](H_2O)_{0.30}$. Carbonate ions randomly occupy adjacent faces of the PO_4 tetrahedra, which are parallel to the *c*-axis (Fig. 3b). Consequently, there are two positions, C1 and C2, of carbon atoms with the equal occupations of about 0.1. They are located at the equal distance of 0.6 Å from the position of the P atom. Each of them has in their coordination one of two oxygen atoms (O1 or O2) which retains their positions in the structure. Two other coordinating oxygen atoms O3c are common for both carbon atoms. The O3c atoms are shifted by 0.37 Å from the O3p atoms belonging to the PO_4 tetrahedron.

The isomorphic substitution $(K^+, NH_4^+) \rightarrow Ca^{2+}$ is limited because of the rather different ionic radii of these ions and, therefore, in both structures under considerations, there is a charge disbalance associated with the replacement of the $[PO_4]^{3-}$ groups by CO_3^{2-} and HPO_4^{2-}. This disbalance is compensated by the vacancies in the cation sites through the scheme:

$$0.5Ca^{2+} + (PO_4)^{3-} = 0.5\square_{Ca} + A^{2-},\ A^{2-} = {CO_3}^{2-},\ {HPO_4}^{2-},\ \square_{Ca}\text{ - vacancies.}$$

In NH_4-doped apatite charge disbalance is associated also with the replacement of the part of OH^- anions by vacancies and water molecules:

$$0.5Ca^{2+} + OH^- = 0.5\square_{Ca} + (\square_{OH,}\ H_2O),\ \square_{OH^-}\text{ vacancies.}$$

This mechanism is usual for carbonated apatites and results in the dominance of vacancies in the calcium sites. The vacancies in the channel sites in the structure of K^+-doped apatite are absent. The data of IR-spectroscopy, thermal analysis and changes of lattice constant ***a*** at elevated temperatures (Fig. 4) demonstrate also the absence of water in the structure of this apatite. Therefore, in the K^+-doped structure the positive extra charge is completely compensated through the scheme $0.5Ca^{2+} + (PO_4)^3 = 0.5\square_{Ca} + A^{2-}$.

The Rietveld refinement (synchrotron radiation, high-resolution diffractometer, Siberian Synchrotron Center) of the crystal structures of human tooth enamel apatite with 2.9 wt% of CO_2 and 0.22 wt% of F (sp gr. $P6_3/m$, ***a*** = 9.4486(2), ***c*** = 6.8875(3) Å; Rp = 0.047, Rwp = 0.062, RBragg = 0.025) allowed to propose "average" structural model of the human tooth enamel apatite of the elder age group (Ivanova et al. 2005). The sample was prepared from the enamels of five molars of consent Saint Petersburg 50–60 years inhabitants. The occupancy of phosphorous site is lower than it could be expected with C replacing P without vacancies in this site. Therefore, the shift of carbon atom from phosphorous site is quite believable. The geometry of a tetrahedron is closer to that in the structure of stoichiometric

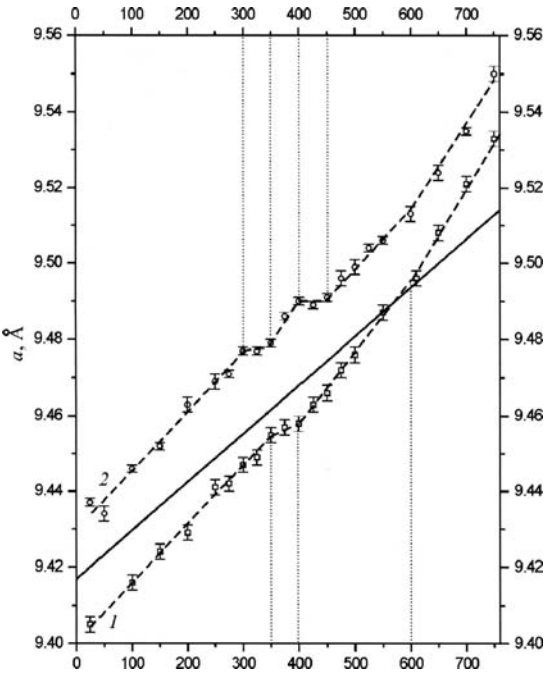

Fig. 4 The changes of lattice dimensions ***a*** of the synthetic calcium-deficient carbonated hydroxyapatites at elevated temperatures: *1*– K^+-doped water free hydroxyapatite, *2* – NH_4^+-doped water containing hydroxyapatite. Dots with error bars and dashed lines represent the experimental data, solid line – the averaged data on the thermal expansion of stoichiometric hydroxyapatite lattice (Trombe and Montel 1978; Perdok et al. 1987; Kondratyeva and Filatov 1989). The plateaus from 300 to 400 °C and from 400 to 450 °C connected with loss of water and with re-location of CO_3 ions on the curve 1 are absent

hydroxyapatite (Sudarsanan and Young 1969), than to those in the structures of human (Wilson et al. 1999) and modern deer (Michel et al. 1995) tooth enamels. The distribution of vacancies over tetrahedral oxygen sites (0.05–0.08 at.un.) appears to be random. Thus, it may be concluded that carbonate groups can occupy any of tetrahedral faces with the same probability, that is the consequence of enamel "averaging" during the sample preparation.

The different orientation of the carbonate triangles certainly determined by us and other researchers (Ivanova et al. 2001, 2004, 2005; Leventouri et al. 2000a, b; Wilson et al. 2004, 2005, 2006; Fleet and Liu 2004, 2005; Fleet et al. 2004) opens up a new path for the development of a conception of the crystal chemistry of carbonate apatites. The question which has to be clarified is the reason(s) of this phenomenon. There are several ideas knitted from the composition of apatite, the charge-balance compensation mechanism, their synthesis or natural formation etc. As demonstrated above, the most believable hypothesis is thought to be the carbonate content.

Isomorphic Substitutions in Biological Apatites

Carbonate Apatites Formed in a Human Organism

According to our data, among the carbonate apatites forming in a mouth cavity, only dental enamel mineral belongs to the B type and the others (of dentin, salivary and

dental stones) belong to the A – B type (B > A). Renal stone apatites may be both A–B and B types.

According to the variations in the unit-cell parameters, isomorphic replacements in crystal structures of the apatites of pathogenic origin (in renal, salivary and dental stones) are more intensive in comparison with physiogenic dental enamel apatites (Fig. 5). Among the pathogenic apatites, the most considerable compositional variations are observed for the renal stone apatites that indicates strong variability of conditions of their formation. The changes in the unit-cell parameters of bone apatites are not completely interpretable, because these apatites consist of nanosized crystals that are smaller than those of other biological apatites.

The age variations of the crystal lattice parameters of human enamel apatites (Table 1) are related to the complicate processes of de- and remineralization, which result in the increase or reduction of vacancies in the Ca positions and in the respective changes of CO_3^{2-}, H_2O and $[HPO_4]^{2-}$ content in the unit cell:

$$(n+m/2)Ca^{2+} + n(PO_4)^{3-} + mOH^- = (n+m/2)\square_{Ca} + nA^{2-} + m(\square_{OH,}H_2O)$$

where A^{2-}=$[CO_3]^{2-}$ or $[HPO_4]^{2-}$-; $\square_{Ca}$, $\square_{OH}$ – vacancies (Frank-Kamenetskaya et al. 2004).

Till 50 years age, values of the ***a*** and ***c*** parameters of enamel apatites change considerably without any dependence on concrete age that may be explained by the essential fluctuations of the Ca content in human organisms. After 50 years age, the significant direct correlation between the ange and the ***a*** parameter has been revealed (Fig. 6).

Relationships between the chemical composition and human age (Table 2, Fig. 7) point out to the fact that, at the age of 50, remineralization processes are damping. Changes in the unit-cell parameters of biological apatites connect mainly with the age demineralization resulting primarily in the increase of Ca-site vacancies, and

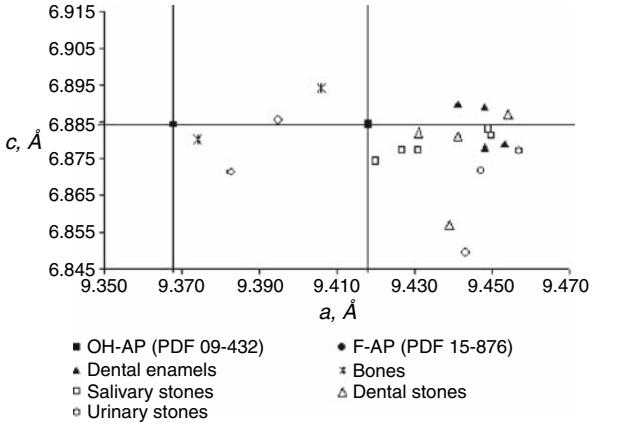

Fig. 5 Unit cell parameters of apatites forming in human organisms. See text for details

Table 1 Unit cell constants of dental enamel apatites of the of St. Petersburg residents of different ages and sex

Age, years	Sex	***a***, Å	***c***, Å
5–10	Male	9.446–9.447	6.886–6.891
11–30	Male	9.446–9.453	6.878–6.886
	Female	9.442–9.451	6.878–6.887
31–50	Male	9.443–9.453	6.879–6.887
	Female	9.441–9.450	6.880–6.890
51–65	Male	9.443–9.453	6.880–6.888
	Female	9.441–9.449	6.879–6.888

Note: Standard deviation of determination = ± 0.001 Å.

the content of H_2O molecules and divalent oxyanions ($[CO_3]^{2-}$ and $[HPO_4]^{2-}$). Even more significant direct correlation between the a/c value and the human age (Fig. 6) is probably connected to a weak feedback between human age and value of the ***c*** parameter, that specified prevalence of the $[HPO_4]^{2-}$ groups among the divalent oxyanions.

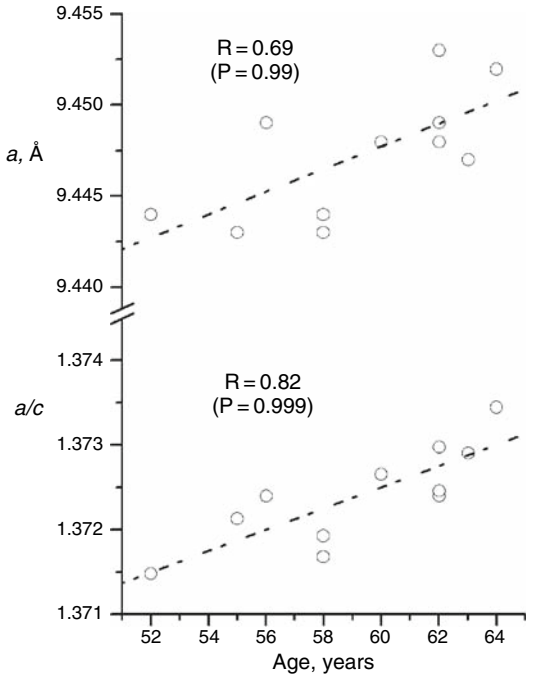

Fig. 6 Unit-cell parameters (a and a/c) of the enamel apatite after 50 years versus age

Table 2 Pair correlation coefficients (R) between the human age and the chemical composition of the enamel apatite

Parameter	Age, years	n	R	P
Ca/P	15–58	9	−0.68	0.95
Ca+Na+Mg/P	15–58	9	−0.77	0.99
F, mass%	12–48	10	0.63	0.95
CO_2, mass%	30–58	9	0.86	0.999

Carbonate Apatites of Fossils

By the data of study of skeletal reliquiae (teeth, tusks, bones) of mammals from continental and marine deposites of the Pleistocene and Neogene formations (geological age from 2 up to 1000 thousand years), the mineral composition of hard tissues by fossilization processes changes essentially (Frank-Kamenetskaya et al. 2005). The following secondary minerals were found: quartz, carbonates of calcium (calcite, aragonite, vaterit), ferriferous calcite, hematite and others iron oxides; only in sea deposites: rhodochrosite and Mn-bearing calcite. The quantity of carbonate apatite decreases. Simultaneously, the intensive substitutions in carbonated hydroxyapatite crystal structure associated with the decrease of the H_2O content and the increase of the F concentration occurs that results in a gradual decrease of the a parameter (compared to values characteristic for carbonate F-apatite). The possibility to use the **a** parameter for the determination the geological age is restricted

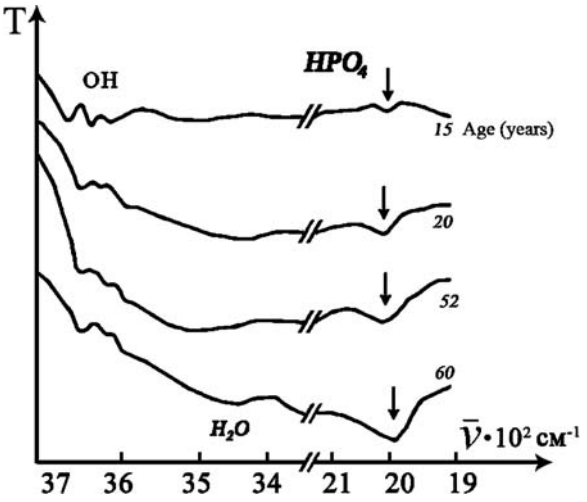

Fig. 7 Examples of IR spectrums of human different age enamel apatite in region 1900 – 3700, cm^{-1}

Table 3 The beginning of fossilization of skeletal reliquiaes from continental deposits

Processes	Geological age (1000 years)		
	Dental enamel	Dental dentin	Tusk dentin
Apatite dissolution	400	14–20	20–40
Carbonation	4.5	4.5	20–40
Fluorine increasing	600–800	400	20–40
Ferrugination	600–800	600–800	20–40
Silicification	4.5	14–20	20–40

over influence of the burial conditions and hard tissue structure on the destruction processes (Table 3).

Apatites of skeletal reliquiae representing invertebrates and chordata (brachiopods, conodonts, fishes, reptiles) from Cretaceous, Jurassic Carbon, Devonian and Ordovician formation (geological age more than 60 million years) are carbonate fluoroapatites of the A–B (B > A) and B types (see, e.g., Panova et al. 2001). Among these minerals, for the first time a single crystal of biological apatite – the element of conodontous of the Ozarkodinida class (from Devon formation nearby Ilmen Lake) has been found (sp.gr. $P6_3/m$, $\boldsymbol{a}$ = 9.374(2), $\boldsymbol{c}$ = 6.882(2) Å). The refinement of the conodontous apatite structure (single-crystal X-ray diffraction, MoKα X-radiation, R = 0.017, Rw = 0.022) confirmed its close relationships to the stoichiometric fluoroapatite structure. Bond lengths in the PO_4 tetrahedra are: P–O1 $\approx$ P–O3 = 1.535(2) $<$ P–O2 = 1.543(2) Å. The positions of all tetrahedral oxygen sites are partly vacant (the quota of vacancies = 0.03–0.01 at. un.). Large values of the anisotropic displacement parameters indicate the possible splitting of the tetrahedral O sites: O2 along the Z-axis and O3 along the X-axis.

Development and Realization of Synthesis Methods for the Analogues of Biogenic Apatite

The possibilities of different methods of synthesis of carbonate apatites B and A–B (B > A) types with different substitutions in the crystal structures were experimentally analyzed (Kol'tsov et al. 2000, 2002).

By chemical methods (at P-T parameters and pH close to the formation conditions of living organism apatites), calcium-deficient water-containing carbonate hydroxyapatites which are the analogues of human teeth and bone apatites have been obtained. The $\boldsymbol{a}$ parameter of as-synthesized apatites are larger than those of the stoichiometric hydroxyapatite. Direct correlation between the $\boldsymbol{a}$ parameter and the amount of vacancies in the Ca site has been observed (the $(Ca^{2+} + R^{+})$ / $(P^{5+} + C_B{}^{4+})$ ratio, where R is the amount of monovalent cations at Ca-position, $C_B{}^{4+}$ is the amount of the C atoms of the B-type at the P site). It indicates that

the incorporation of water into the structure of these apatites and their biogenic analogues occurs simultaneously with the advent of vacancies in calcium position and carbonate – ion replacements of PO_4-groups according to scheme:

$$\begin{aligned}(n+m+r/2)Ca^{2+} + (n+m)(PO_4)^{3-} + rOH^- \\ = (n+m+r/2)\square_{Ca} + nCO_3^{2-} \\ + m[HPO_4]^{2-} + r(\square_{OH}, H_2O),\ r+m > n.\end{aligned}$$

Na-containing carbonate fluorineapatites with the excess of F (more than 2 *apfu*) obtained under the wide interval of conditions are the analogues of apatites from the skeletal reliquiae with high fossilization degree as well as of the apatites from the bedded and nodular phosphorites. The ***a*** parameter of such apatites is equal or less than the ***a*** parameter of fluoroapatite. Inverse correlation between the ***a*** parameter and the carbonate amount results from the replacement:

$$Ca^{2+} + [PO_4]^{3-} = Na^+ + [CO_3]^{2-}.$$

Conclusion

Crystal chemistry of carbonate apatites is important for the development of the conception of biomineralization and for the creation of scientific bases for the new biocompatible materials for medical purposes.

Small crystallite sizes (about tens to hundreds of Angstroms) and great complexity of substitutions have made definitive determinations of the crystal structure and chemistry of carbonate apatite quite difficult. For this reason, there are many unanswered questions concerning replacements in the crystal structures of carbonate apatite.

Undoubtedly, the crystal structures of carbonate apatite are highly disordered. Recent success in the synthesis of single crystal of the A-B apatite at high pressure and in the location of carbonate ion in the *c*-axis channel of apatite structure (Fleet and Liu 2004, 2005; Fleet et al. 2004), and the essential progress of diffraction and microscopy methods opens up new perspectives in crystal chemistry of carbonate apatites, first of all, of biological origin.

Acknowledgements The work was supported by RFBR projects (98-05-65578, 03-05-65278, 06-05-65165). The authors are grateful to the late Prof. N.V. Kotov, Prof. A.B. Kol'tsov, Dr. T.I. Ivanova, Dr. M.A. Kus'mina, Dr. M.L. Zorina, Dr. L.G. Poritskaya, Mrs. T.N. Kaminskaya, Dr. O.A. Golovanova, Dr. Yu.V. Plotkina, Dr. O.L. Pichur, Dr. A.V. Volkov, Mrs E.V. Rosseeva, Mr. V. Sapega, Mr. V.V Golubtsov, Mr. N.Yu. Vernigora, Mrs. D.A. Kotlyarova (St. Petersburg State University) and Dr. A.N. Shmakov (Siberian Synchrotron Center, Novosibisk) for active collaboration in this work.

References

Bonel G (1972) Contribution a l'etude de la carbonatation des apatites. 1. Synthese et etude des properietes physico-chimiques des apatites carbonatees de type A. Ann Chim 7:65–87

Fleet ME, Liu X (2004) Location of type B carbonate ion in type A–B carbonate apatite synthesized at high pressure. J Solid State Chem 177:3174–3182

Fleet ME, Liu X (2005) Local structure of channel ions in carbonate apatite synthesized at high pressure. Biomaterials 26:7548–7554

Fleet ME, Liu X, King PL (2004) Accomadation of the carbonate ion in apatite: An FTIR and X-ray structure study of crystals synthesized at 2–4 GPa. Am Mineral 89:1422–1432

Frank-Kamenetskaya OV, Golubtsov VV, Pikhur OL, Zorina ML, Plotkina YuV (2004) Nonstoichiometric apatite of the human dental hard tissues (the age alterations). Proc All-Rus Miner Soc 5:120–130 (in Russian)

Frank-Kamenetskaya OV, Zorina ML, Kotl'yarova DA, Plotkina JuV, Polyarnaya ZhA, Garutt NV (2005) Apatites of skeletal reliquiae of mammals of different geological age. Mineralogical museums Saint Petersburg SPbGU 190–191 (in Russian)

Ivanova TI, Frank-Kamenetskaya OV, Kol'tsov AB, Ugolkov VL (2001) Crystal structure of calcium-deficient carbonated hydroxyapatite. Thermal decomposition. J Solid State Chem 160:340–349

Ivanova TI, Frank-Kamenetskaya OV, Kol'tsov AB (2004) Synthesis, crystal structure and thermal decomposition of potassium-doped carbonated hydroxylapatite. Z Kristallogr 219:479–486

Ivanova TI, Golubtsov VV, Frank-Kamenetskaya OV, Shmakov AN (2005) Crystal structure Refinement of human tooth enamel apatite of elder age group. Mineralogical museums Saint Petersburg SPbGU, p 246

Kol'tsov AB, Frank-Kamenetskaya OV, Zorina ML, Kaminskaya TN, Vernigora NYu (2000) Complicate isomorphism in synthetical carbonate apatites. Proc All-Rus Miner Soc 2:109–116 (in Russian)

Kol'tsov AB, Poritskaya LG, Frank-Kamenetskaya OV, Kaminskaya TN, Zorina ML (2002) Methods of synthesis of biogenic apatite analogues and results of its study. Organic Mineralogy Saint-Petersburg 41–42 (in Russian)

Kondratyeva IA, Filatov SK (1989) Thermal and chemical deformations of fluorhydroxyapatite crystals on X-ray diffraction of raw minerals. Proceeding of the XI-th All-Union Conference, Sverdlovsk, p145 (in Russian)

LeGeros RZ, Trautz OR, Klein E, LeGeros JP (1969) Two types of carbonate substitution in the apatite structure. Experimentia 25(1):5–7

Leventouri Th, Chakoumakos BC, Moghaddam HY, Perdikatsis V (2000a) Powder neutron diffraction studies of a carbonate apatite. J Mater Res 15:511–517

Leventouri Th, Moghaddam HY, Papancarchou N, Bunaciu CE, Levinson RL, Martinez O (2000b) Atomic displacement parameters of carbonate apatites from neutron diffraction data. Mater Res Soc Symp Proc 599:79–84

Mehmel M (1930) Uber die structur des apatites. Z Kriststallogr 75:323–331

Michel V, Ildefonse P, Morin G (1995) Chemical and structural changes in Cervus elaphus tooth enamel during fossilization (Lazaret Cave): a combined IR and XRD Rietveld analysis. Appl Geochem 10:145–159

Nelson DGA, Featherstone JDB (1982) Preparation, analysis and characterization of carbonated apatites. Calcified Tissue Int 34:69–81

Panova EG, Ivanova TI, Frank-Kamenetskaya OV, Bulach AG, Chukanov NV (2001) Apatite of bone detritus of testaceous fishes from devon formation of north -west Russian platform. Proc All-Rus Miner Soc 4:97–107 (in Russian)

Perdok WG, Christoffersen J, Arends J (1987) The thermal lattice expansion of calcium hydroxyapatite. Cryst Growth 80:149–154

Sudarsanan K, Young RA (1969) Significant precision in crystal structural details: Holly Springs hydroxyapatite. Acta Crystallogr B 25:1534–1543

Trombe JC, Montel G (1978) Some features of the incorporation of oxygen in different oxidation states in the apatite lattice.1. On the existence of calcium and strontium oxyapatites. J Inorg Nucl Chem 40:15–21

Vignoles M, Bonel G, Holcomb DW, Yong RA (1988) Influence of preparation conditions on the composition of type B carbonated hydroxyapatite and on the localization of the carbonate ions. Calcified Tissue Int 43:33–40

Wilson RM, Elliott JC, Dowker SEP (1999) Rietveld refinement of the crystallographic structure of human dental enamel apatites. Am Mineral 84:1406–1414

Wilson RM, Elliott JC, Dowker SEP, Smith RI (2004) Rietveld structure refinement of precipitated carbonate apatite using neutron diffraction data. Biomaterials 25:2205–2213

Wilson RM, Elliott JC, Dowker SEP, Rodriguez-Lorenzo LM (2005) Rietveld refinement and spectroscopic studies of the structure of Ca- deficient apatite. Biomaterials 26:1317–1327

Wilson RM, Dowker SEP, Elliott JC (2006) Rietveld refinements and spectroscopic structural studies of a Na-free carbonate apatite made by hydrolysis of monetite. Biomaterials 27:4682–4692

Index